UNIVERSITY OF SOUTHAMPTON

Investigation of Tip-Driven Thruster and Waterjet Propulsion Systems

Adam William Hughes

Doctor of Philosophy

FACULTY OF APPLIED SCIENCE AND ENGINEERING
SCHOOL OF ENGINEERING SCIENCES

April 2000

UNIVERSITY OF SOUTHAMPTON

ABSTRACT

FACULTY OF APPLIED SCIENCE AND ENGINEERING

SCHOOL OF ENGINEERING SCIENCES

Doctor of Philosophy

INVESTIGATION OF TIP-DRIVEN THRUSTER AND WATERJET PROPULSION SYSTEMS

by Adam William Hughes

Experimental and computational techniques have been used to study the performance of a tip-driven propeller (TDP) and a waterjet intake duct for the purpose of assessing the practical implications of using a tip-driven impeller in a waterjet propulsion system. A prototype electromagnetic tip-driven propeller has been successfully designed and built for the specific purpose of experimental analysis. This unit has been tested in towing tanks for a range of propeller speeds, advance speeds and duct shapes. In conjunction with the towing tank tests a potential-flow panel model (with viscous coupled duct) has been developed in order to predict the likely performance of the prototype thruster. The model has been validated against both the towing tank results, and against published data for standard ducted propeller units.

A representative waterjet intake duct has been tested using an open-circuit wind tunnel. Velocity profiles and surface pressure distributions have been obtained for three different flow regimes. In addition, a CFD model of the same inlet duct geometry has been developed using a fully viscous, commercial RANS flow solver. This model is validated against the wind tunnel test data and has been further developed to study the influence of trim and drift on the flow through the duct. In addition, a brief study on duct-hull interaction is presented.

Results from the experimental and computational tests on both the tip-driven propeller and waterjet intake duct are presented. The two validated CFD models are subsequently coupled together to investigate the performance implications of using a tip-driven, rather than shaft-driven, axial-flow waterjet impeller. It is shown that the use of a tip-driven impeller in a waterjet propulsion system has the potential to increase hydrodynamic performance. Removing the drive shaft from the system resulted in an increase in predicted impeller thrust of approximately 28%. Finally, the practical implications of such a drive mechanism are discussed. It is seen that the use of an electromagnetic tip-drive is limited by the physical size of the motor.

ACKNOWLEDGEMENTS

I would like to express my thanks to all those who have provided help and support throughout this work. Particular thanks go to my supervisor, Dr Steve Turnock, for his help, guidance and enthusiasm, even when overwhelmed by yet another chapter to proof-read. I wish also to thank Dr Suleiman Abu-Sharkh for his great assistance with the work on the prototype thruster. Thanks must also go to Paul Kinsey and other technicians in the physics workshop who managed to decipher my design drawings and make an excellent job of machining and constructing the TDP.

Thanks also go to friends and colleagues in the Department of Ship Science, who through their good humour, friendship and support, have made my time in Southampton enjoyable. I thank also, my close friends for their patience and understanding when faced with a grumpy Mancunian trying to write this dissertation, and for the many excuses to go for a coffee break.

My utmost thanks must, however, go to my Mother, for without her never ending love, support and encouragement I would not have got this far. It is to her that I dedicate this thesis.

Investigation of Tip-Driven Thruster and Waterjet Propulsion Systems

TABLE OF CONTENTS

LIST OF FIGURES

LIST OF TABLES

NOMENCLATURE

A	Electric loading (A/m).
B	Magnetic flux density (T).
C	Aerofoil chord length (m).
C_f	Skin friction coefficient.
Cp	Pressure coefficient.
D	Diameter of propeller or impeller (m).
f	Motor frequency (Hz).
F	Function used in boundary layer calculations.
F_n	Froude number.
g	Gravitational acceleration (m/s^2).
H	Shape parameter used in boundary layer calculations.
H	Betz manometer water height measurement (m).
I	Current (A).
I_m	Motor current (A).
J	Advance coefficient.
K_Q	Torque coefficient.
K_T	Thrust coefficient.
l	Function used in boundary layer calculations.
L	Active motor length (m).
L_c	Stator core length, or thickness (m).
M	Mach number.
$\dot{m}$	Mass flow rate through waterjet (kg/s).
n	Motor or propeller speed (revolutions per second).
N	Motor or propeller speed (rpm).
N_c	Number of conductors around stator diameter.
N_p	Number of poles in motor.
P	Pressure (N/m^2).
P_{bc}	Motor bearing and core loss (watts).
P_m	Motor input power (watts).
P_p	Motor output power, or propeller input power (watts).
Q	Torque (Nm).
r	Local section radius (m).
R	Radius of propeller or impeller (m).
R_{CFD}	Aft hull resistance from CFD prediction with waterjet present (N).
R_{ph}	Motor phase resistance (ohms).
R_R	Hull residuary resistance (N).
R_T	Total hull resistance with no waterjet present (N).
R_{T2}	Total hull resistance with waterjet present (N).
R_V	Hull viscous resistance (N).
R_θ	Reynolds number based on boundary layer momentum thickness.
t	Thrust deduction fraction.
T	Thrust (N).
Uo	Reference velocity, usually free-stream (m/s).
u	Velocity in the x direction (m/s).
u_e	Velocity outside the boundary layer (m/s).
v	Velocity in the y direction (m/s).

Ve	Waterjet exit velocity (m/s).
Vi	Waterjet inlet velocity (m/s).
w	Velocity in the z direction (m/s).
δ	Boundary layer thickness (m).
δ^*	Boundary layer displacement thickness (m).
ϕ	Magnetic flux.
θ	Boundary layer momentum thickness (m).
λ	Boundary layer shape parameter.
μ	Fluid dynamic viscosity (Ns/m^2).
ρ	Fluid density (kg/m^3).
υ	Fluid kinematic viscosity (m^2/s).
τ_w	Wall shear stress (N/m^2).
ω	Angular velocity (radians/s).
BAR	Blade Area Ratio
CFD	Computational Fluid Dynamics.
ETDI	Electromagnetic Tip-Driven Impeller.
ETDP	Electromagnetic Tip-Driven Propeller.
IVF	Interaction Velocity Field.
IVR	Inlet Velocity Ratio.
OD	Outer diameter (m).
PM	Permanent Magnet.
RANS	Reynolds Averaged Navier Stokes.
ROV	Remotely Operated Vehicle.
rpm	Revolutions per minute.
SD	Standard Deviation.
TDC	Top Dead Centre.
TDI	Tip-Driven Impeller.
TDP	Tip-Driven Propeller.
TUUV	Tethered Unmanned Underwater Vehicle.

1. INTRODUCTION

The conventional method of propelling a water-borne craft is through the use of a screw propeller mounted at its centre hub on a drive shaft. The screw propeller can be regarded as part of a helicoidal surface which, when rotated, drives the water aft and the vessel forward. The force acting on the vessel arises from the rate of change of momentum induced in the fluid [1.1]. Some propellers have adjustable blades, *controllable pitch propellers*, which can be moved to vary the thrust and torque whilst maintaining a constant shaft speed. It is necessary to ensure the machinery can always develop enough torque to turn the propeller at the revolutions appropriate to the power being developed [1.1]. If the blade movement is large enough the propeller can produce a reverse thrust while still rotating in the same direction, hence a reversing gearbox is not necessary. In addition, the blades can be moved to maintain good efficiencies when the vessel is operating under different regimes, e.g. a tug towing or free running. However, the majority of propellers have fixed blades, *fixed pitch propellers*.

Several developments from the basic propeller have been seen over the years, these include ducted or shrouded propellers, ring-propellers, tip-driven propellers (TDP) and, more recently, waterjet propulsion systems. This thesis combines two of these areas, tip-driven propellers and waterjets, and assesses the implications and practicality of using a tip-driven impeller in a waterjet duct.

1.1 AIMS, METHODS AND OBJECTIVES

There were several aims to this study, most of them centred around the concept of tip-driven propellers, for which little useful data has been previously published. Some of the literature has only presented a review of such techniques, or has only proposed conceptual designs. Others have built and tested propeller units but have not produced much useful performance data, possibly due to commercial and industrial constraints. For this reason, one of the major aims of the study is to design, build and test a prototype TDP. To assess the benefits and limitations, and to provide a reliable set of performance data for the public domain. The reasoning behind this has originated from the author's contract work on an EPSRC/CMPT managed programme on Tethered Unmanned Underwater Vehicles

(TUUV). As such, the ducted propeller in question is relatively small, of the size that might be seen on underwater vehicles.

A further aim, motivated by the author's other research interests, has been to assess the possible benefits of using a tip-drive in an axial-flow waterjet pump. Waterjets are often regarded as propulsion units without appendages, which is true when considered from the overall hull design. However, an intake grill is located at the duct opening in the hull to prevent the ingress of debris, and an unavoidable impeller drive shaft is located within the inlet duct which causes unfavourable velocity fields for the impeller to operate in. One method of overcoming this problem would be to drive the waterjet impeller via the blade tips. A tip-driven impeller eliminates the presence of the drive shaft protruding through the waterjet duct walls and upsetting the onset flow to the impeller. Furthermore, the length of the waterjet inlet duct must be kept as short as possible, to avoid additional added weight from the entrained water, and the ramp angle of the duct must be as shallow as possible, to avoid excessive flow distortion. In conventional waterjet systems, with shaft driven impellers, these two dimensions are constrained by the position of the engines, however, a tip-driven impeller may result in more flexibility with duct design.

It was evident from previous papers that flow non-uniformity at the waterjet impeller plane must be minimised in order to achieve good propulsive efficiency and reliability. The presence of the drive shaft can create detrimental 'shadows' at the impeller plane resulting in rapidly varying pressure gradients and fluctuating blade loadings, reducing impeller efficiency and increasing the susceptibility to fatigue. The use of a tip-driven impeller would result in the elimination of the drive shaft and its bearing through the inlet wall, producing a more uniform inflow. There is also the potential to reduce flow alignment losses due to trim and drift of the vessel.

To reach these goals, the specific objectives are to develop the necessary research tools, both experimental and computational, for the investigation of propeller and waterjet duct systems. These tools offer an aid to ducted propeller design and optimisation in the future.

1.1.1 Analysis Techniques

Traditional analysis methods for testing propulsion units make use of experimental facilities. However, to be able to test different configurations under different operating conditions can be time consuming and expensive. For this reason modern analyses often involve the use of computational techniques, which provide comprehensive solutions in relatively short time periods. However, the use of experimental tests should not be dismissed. Data from these tests is still necessary to validate the reliability of the computational predictions. To achieve the aims stated in the introduction, it was planned to undertake both experimental and computational analyses of a tip-driven propeller and a waterjet inlet duct. For each case there are several possible methods or tools that can be used.

Two fluid domains, water and air, in the form of towing tanks and wind tunnels were available for experimental testing. Towing tanks have been used for testing the prototype TDP, facilities were available that enabled the propeller to be investigated at several advance speeds. Many propellers are tested in water tunnels, or cavitation tunnels, however, this method was not available for this study.

Tests on waterjet inlet ducts are generally carried out using either water tunnels, towing tanks or on specifically designed test rigs, usually operated by waterjet manufacturers. During water tunnel tests, the jet is usually mounted on the side of the working section, drawing water from the tunnel, which has to be replenished later on in the tunnel cycle. Towing tank tests usually comprise of a model vessel being propelled by a scale model of a waterjet system. However, because of the small size, only a limited amount of data can be measured. For this investigation, wind tunnel tests have been carried out on a representative inlet duct. Wind tunnel testing allows the use of a large model, which offers good access and makes measurements easier to take. More information on this is given in Chapters 2 and 6.

In addition to experimental testing, predictions of the performance of both the TDP and waterjet inlet are necessary. Recent advances in Computational Fluid Dynamic (CFD) flow solvers offer the ability to model relatively complex flows. Furthermore, if a novel propulsion design is to be proposed, CFD provides a means of investigating relative

performance gains or losses. Two computational modelling programs were available, a potential-flow lifting surface panel code, and a viscous Reynolds averaged Navier Stokes (RANS) flow solver. Once validated against experimental data, these codes allow operating regimes, which are not possible in the laboratory, to be modelled, and means any future designs can be investigated.

The panel code models non-viscous flows, i.e. neglecting boundary layer development and flow separation, as a result lift is over predicted and drag is under predicted. So long as the user is aware of the limitations, potential-flow codes have been shown to provide reasonable initial solutions with good relative differences between different conditions [1.2]. If a more accurate prediction of the flow is required, a boundary layer and separation prediction program can be written, which can run in conjunction with the panel code. It was necessary to develop such a program during the course of this study.

The panel code allows complex geometries to be defined much more easily than the RANS package, and it offers a relatively straightforward method of modelling rotating bodies. The solution is also reached in a fraction of the time taken by a fully viscous code. For these reasons the panel code was chosen to model the tip-driven ducted propeller.

In contrast the RANS flow solver provides a fully viscous prediction of the flow, but at the cost of a significant increase of computational time. It is suited to modelling internal flows and it presented a means of modelling the flow through the representative waterjet inlet duct, within which separation can readily occur.

For the purposes of this work it was not practical to carry out an in-depth study of how various CFD parameters and boundary conditions affect the flow solution. An entire thesis could be written on the CFD modelling of either one of these propulsion units alone, studying turbulence models, interpolation schemes, orders of accuracy, block structures, cell structures and so forth. This area of work has been undertaken by a number of authors [1.3,1.4], however, it is not the aim of this study. These programs are used as tools, providing a means to an end. Further details on these codes and how they were developed for use in this context are given in Chapters 2, 5, and 7.

1.1.2 Objectives

In summary, the objectives of the work are:

1. To design and build a prototype electromagnetic tip-driven ducted propeller, to be used for experimental testing.
2. To carry out detailed tests on the prototype TDP and to obtain a comprehensive set of performance data.
3. To develop a panel code model of the ducted propeller, which can be used to predict the performance of the prototype, and any future ducted units.
4. To develop a program which can estimate the growth of the boundary layer and can be run in conjunction with the panel code.
5. To test a model waterjet inlet duct in order to obtain flow characteristics and gain information which can be used to analyse the reliability of a computational model of the duct.
6. To develop a computational model of the typical waterjet duct, with and without the presence of a drive shaft, which can be used to reliably predict the flow through the inlet duct under varying conditions.
7. To couple the two computational models together and create a method to model the waterjet inlet duct with the presence of an axial-flow impeller. The potential benefits of driving the impeller without the shaft can then be studied.

This study primarily deals with the use of propeller tip-drives in ducted propulsion units. Ducted units are considered due to their characteristic shroud around the propeller, which can be adapted to house a drive mechanism. Although controllable pitch propellers have not been studied in this context, the use of tip-driven controllable pitch propellers should not be dismissed, but noted as a possible area of further study.

1.2 DUCTED AND SHROUDED PROPELLER SYSTEMS

1.2.1 Ducted Propellers

It can be shown (Appendix B) that for propellers, high thrust loading gives low efficiency and low thrust loading gives high efficiency. It is therefore possible to raise the efficiency by lowering the thrust loading. One means of achieving this is by using a larger diameter propeller, however, this is often constrained by the vessel dimensions. A second method is

to arrange a ring aerofoil around the propeller to form what is called a *ducted propeller unit*, or propeller in a nozzle. This method is not new, Ludwig Kort developed the first nozzle designed for use on a ship in the early 1930s, and these devices are sometimes referred to as Kort nozzles. In addition to improved efficiency, under certain conditions, the duct also protects the propeller from physical damage. Figure 1.1 illustrates a schematic representation of a ducted propeller.

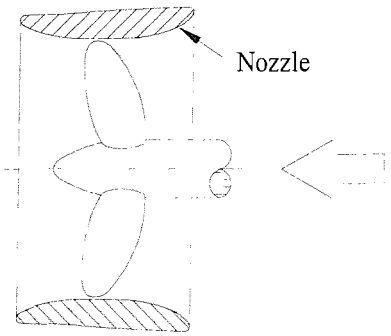

Figure 1.1 - Schematic representation of a ducted propeller.

The nozzle entrance has a larger diameter than the propeller so more water is drawn in than the corresponding open propeller. Thus for a given thrust a larger quantity of water is given a smaller acceleration, which makes for greater efficiency [1.5]. In addition to altering the propeller loading, the aerofoil section shape of the duct is also used to produce additional thrust. Due to the acceleration of the water entering the nozzle, the pressure over the inside surface of the leading part is lower than that over the outer surface, as a result there is a forward thrust developed on the nozzle, which augments the propeller thrust. However, this is only of benefit in the forward direction up to a certain advance speed, after which the drag of the duct and its supports offset any thrust produced by it.

The use of a duct can either accelerate or decelerate the flow to the propeller. Accelerating ducts reduce the thrust loading and therefore increase efficiency. Decelerating ducts generally improve cavitation problems, but at the cost of efficiency, they are rarely used on anything other than occasional military craft, when they are used to suppress propeller noise. The risk of cavitation on the propeller blades can be minimised by giving the blade tip a wide span [1.6]. This shape of blade is commonly referred to as a K-series or a Kaplan blade, Figure 1.2.

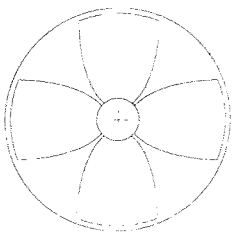

Figure 1.2 - Schematic representation of a Kaplan propeller.

Tests have also shown [1.5] that whereas the optimum diameter of a conventional propeller in a nozzle was 10% less than the equivalent open propeller, the optimum Kaplan propeller had 30% less diameter.

In a similar manner to finite span foils, the propeller blade generates trailing vortices at the tip, which increase drag and reduce performance. The duct wall in proximity to the blade has the effect of reducing the strength of these vortices. Harvald [1.6] suggests that in order to attain as high efficiency as possible the clearance gap should perhaps be about 0.1% of the propeller diameter. However, the smaller the gap, the more difficult it is to ensure a uniform clearance between the propeller and duct, which are often mounted independently of each other. For this reason, tip vortex problems still persist.

The efficiency of a ducted propeller in the forward direction can be up to 6% higher than that of an equivalent screw propeller, at high loading coefficients. This corresponds to a gain in power of about 15% [1.6]. Ducts are of little benefit in the reverse direction, however, some sections have been designed with larger trailing edge radii to give improved reverse performance over standard ducts. For most cases, the ducted propeller has been used for small vessels such as tugs and trawlers, and increasingly on small underwater vehicles.

1.2.2 Ring-Propellers

Many tests have been carried out on ducted units and, as a consequence, much performance data has been published. The efficiency gains tend to occur at the higher propeller loads, where the gain in ideal efficiency outweighs the loss in efficiency due to nozzle frictional drag. As stated above, ducted units require a very small clearance between the propeller tip and the encasing body to minimise the onset of tip vortices,

which are sources of efficiency loss. Locating the propeller centrally and maintaining the small tip clearance can sometimes be difficult, given the fact that the duct is mounted from the hull of a vessel and the propeller on a horizontal shaft.

In an attempt to eliminate tip vortices, the use of ring-propellers was studied [1.7] whereby the propeller blades were attached to a profiled ring, which rotated with the propeller, Figure 1.3. Clearance problems were eliminated, however, the overall efficiency of the ring-propeller tended to be lower due to an additional circumferential frictional drag on the rotating nozzle. Further developments of the ring-propeller led to the ducted ring-propeller in which the propeller was attached to a thin ring, which sat flush within an external duct, Figure 1.3. This did offer an improvement in efficiency over the open ring-propeller, but not to the extent of matching that of a standard ducted propeller, which still remained the most efficient.

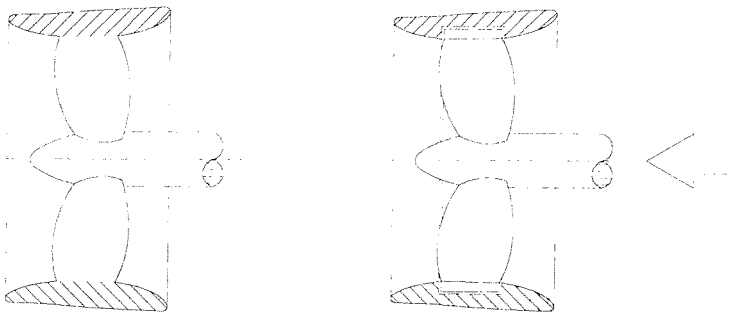

Ring-Propeller Ducted Ring-Propeller

Figure 1.3 - Schematic representation of a ring-propeller and ducted ring-propeller.

It is worth noting that the total thrust is transmitted through the shaft of a ring propeller, whereas in a ducted propeller, ducted ring-propeller or waterjet, the nozzle or waterjet duct takes part of the thrust. This may therefore result in changes to the mechanical design of the propulsor, which could be of benefit or detriment to its application. Small electric propulsor designs have been forthcoming whereby the electric motor driving the shaft is supported from the nozzle using a 'spider' type bracket arrangement as shown in Figure 1.4. In this case all the developed thrust is transmitted through the nozzle and its support bracket. This type of drive arrangement has been widely used for specialist applications such as Remote Operated Vehicles (ROVs), or Tethered Unmanned Underwater Vehicles (TUUVs), where the design has offered relatively light weight and good flexibility for

positioning of the thrusters. However, one drawback is the position of the motor, which disrupts the flow of water into the propeller, and is also susceptible to damage.

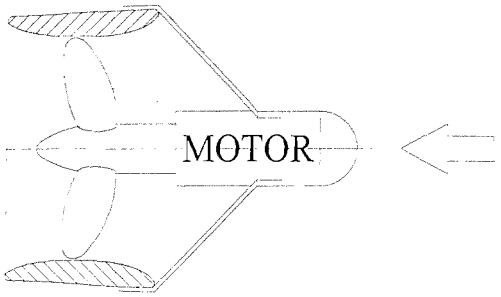

Figure 1.4 - Typical TUUV thruster with drive supported from spider frame.

1.2.3 Tip-Driven Propellers

A natural progression, drawn from the basis of ducted ring-propellers, has been the idea of tip-driven propellers (TDPs). As the propeller is attached to a ring, why not drive it via the ring and remove the imposing drive motor from the inflow. The concept involves having an electric motor, or possibly mechanical drive, encased within the nozzle walls. Although this effectively involves a step back to the slightly less efficient ducted ring-propeller design, the integrated thruster does have the advantage of little or no appendages upstream to disturb the flow (Figure 1.5).

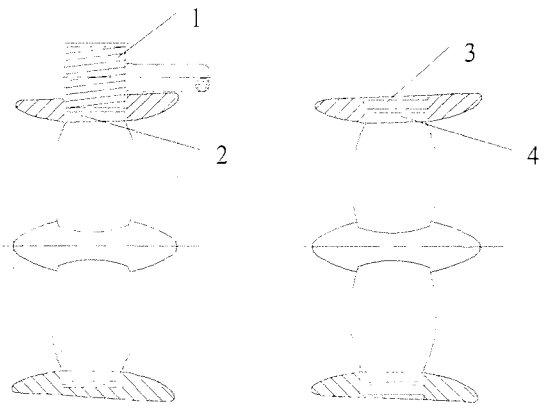

Figure 1.5 - Schematic diagram of a tip-driven propeller.

Prior Art

The idea of tip-driven propulsors has existed for several years. Some research has been carried out and some prototypes have been constructed and tested [1.8,1.9,1.10], to varying degrees of success, but there is only a limited amount of work which has been published on the performance, efficiencies and practicalities of building and using such units. Chapter 3 describes previous work on tip-driven propellers in more detail. Drawbacks with the concept have included poor system efficiencies and friction losses from bearings and seals [1.11]. Because of these problems, few designs have come to fruition and tip-driven units have not been seen in general applications. However, there are some specialised applications for which TDPs would be of benefit. Typical examples are ROVs and TUUVs, which often require vectored thrust units for positional accuracy. Using an efficient electrical motor encased and protected within the walls of the duct, which offers little flow distortion, TDPs offer a self contained drive system that allows for great flexibility when attaching the unit to a vehicle.

Radojcic [1.11] highlighted that latest developments in seal design now make mechanical tip-driven propellers a practical proposition, but there still remains concern as to whether the gains in efficiency due to the removal of the drive shaft, boss and relevant appendages would be curtailed by larger friction losses in the seals around the duct periphery. However, the use of an electromagnetic drive (Figure 1.5), with the absence of any physical contact between the drive system and the propulsor, overcomes some of the sealing problems associated with mechanical drives. Such units have been proposed in the past for underwater vehicle applications, but general conclusions have indicated lower efficiencies, compared to standard ducted units, because the electromagnetics and hydrodynamics have not been optimised. Modern developments in permanent magnet motor design now mean high efficiencies are achievable.

1.2.4 Waterjets

Waterjets are often regarded as ducted propulsors and they are one of the most popular types of shrouded systems in use today. They are not a new idea, as early as the seventeenth century, at a time when there was much interest in using steam to raise water, a patent was acquired which included an invention to propel vessels against strong wind and tide [1.12]. However, early proposed waterjet devices were not able to compete with

paddle wheels and propellers because of the limited technology and lack of understanding of the theory of propulsion. It is only in recent decades that advances in propulsion technology have enabled systems to be fitted on large-scale vessels.

By the 1950's pumps had improved in efficiency and were used successfully in marine vehicles for this purpose. Hamilton introduced the stern mounted flush units, expelling water through the transom against the air, rather than water, resulting in a high speed jet [1.13]. Since the mid-1970's waterjets have grown in popularity and now provide a useful means of propulsion in a speed range of direct relevance to fast craft. They are now seen in many applications, from small one-man jet skis to large passenger ferries.

The increasing popularity of waterjets as a propulsion device is due to a number of advantages including [1.12,1.13];

- Shallow draft - depending on hull type, but often an advantage if the vessel is to work in shallow water.
- No reversing gear required.
- Good fuel economy - usually competitive with propeller propulsion above 20-25 knots, depending on the type of vessel.
- Reduced internal noise and lower vibration levels compared to propeller installations - characteristics valued in passenger ferries.
- Improved manoeuvrability over the whole speed range.
- Protected propulsion components and lack of beneath-hull appendages.
- Good acceleration and outstanding crash stop capability.

However, disadvantages of waterjet systems include [1.12,1.13];

- Lower efficiency than the equivalent propeller at low speeds, although the acceleration is better.
- Air ingestion in a seaway can be a problem on some hull types.
- Inlet plugging from weeds and debris, resulting in the use of inlet grills.
- Although there are no appendages beneath the hull, there are in the inlet duct, which disrupt the flow to the impeller.

- Corrosion problems, though this is being overcome with the use of modern composite materials.
- More complex integration into the hull, requiring some additional design development.
- Higher initial costs.

Since the first waterjets were used as propulsion devices the general form has not altered. A convenient impeller-engine mating method, using a horizontal shaft, has ensured that the intake duct rises from the hull bottom and turns through a bend to form a horizontal duct section in which the impeller is situated. Figure A1.6 illustrates a schematic view of a flush-type waterjet system and lists the relevant terminology. The pump or impeller is basically a propeller, used to increase the momentum of the flow. The main difference only really exists in the use of the terminology. *Impeller* tends to be used when some form of duct or casing encloses the device. For this reason, the propeller within a ducted propeller is occasionally referred to as an impeller.

Although details of the duct geometry itself, e.g. lip radius and ramp angle, have been investigated, the generic form has remained unchanged - with a drive shaft imposing into the fluid flow. There are a number of key areas where the ability to understand more fully the complex nature of the fluid flow through the waterjet, and the interaction of the whole unit, would enable further improvements in performance to be made and lead to a more effective design of waterjet system. The quality of the onset flow into a waterjet inlet can strongly influence impeller pump performance. Additionally, at the preliminary design stage the influence on hull thrust deduction due to the waterjet inflow still has a high level of uncertainty associated with it.

Operating Principle

The basic operating principle of waterjet propulsion is similar to that of a screw propeller system. The propelling force is generated by adding momentum to the water by accelerating a flow of water in an astern direction. Water from beneath the vessel's hull is scooped into the inlet duct and fed to a pump, which adds head to the water. The fluid is decelerated in the intake duct, increasing the static pressure to delay cavitation. Head is applied to increase the velocity, hence momentum, and finally the fluid passes through an

outlet nozzle, usually mounted on the transom [1.14]. The normal head of water in the duct varies at different speeds. Careful design of the shape, usually ranging from an elliptical form on the hull bottom to a circle on the transom (for a flush intake) is necessary to avoid 'choking' and to ensure a regular flow with minimal losses [1.14].

Typical components making up a marine waterjet are illustrated in Figure A1.6, they include an intake duct, a pump element, a nozzle and a steering/reversing mechanism. Deflecting the jet with a bucket gear, which is normally operated by hydraulics, generates steering and reversing forces. Achieving the best efficiency requires the tuning of all these components to the working conditions of the specific application.

Inlet Ducts

Waterjet inlets can be divided into two main categories; pod inlets and flush inlets. Pod inlets, sometimes called ram inlets (Figure 1.7), are generally used for more specialised applications such as hydrofoils and vessels where air ingestion may occur regularly. The pods are mounted below the hull of the vessel, often within a hydrofoil structure, and the water is drawn up to the hull and impeller via a ducting arrangement. Recent literature has seen initial research into the potential of using pod inlets with translating inlet spikes as a means of propelling vessels at speeds in excess of 100 knots [1.15]. Flush inlets (Figure A1.6) are far more common and tend to be used on all other craft including conventional planing craft, monohulls, catamarans and surface effect ships.

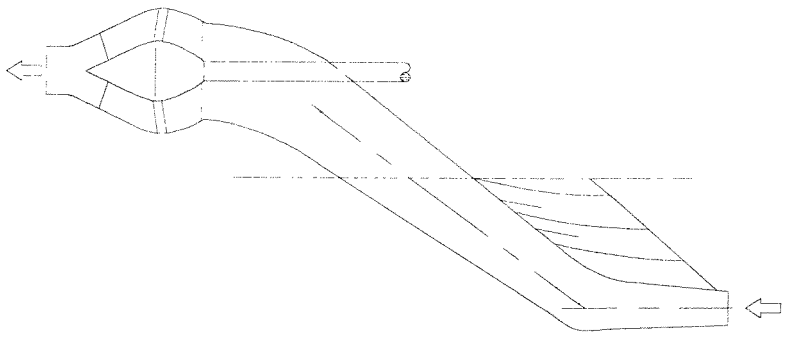

Figure 1.7 - Schematic diagram of a typical pod waterjet inlet duct, mounted beneath the hull in a hydrofoil structure.

Waterjet pump units have been known to be either axial, centrifugal or mixed-flow types. Figure A1.8 illustrates the relative design differences between the three types. Axial-flow

pumps are the most simple and produce axial flow, parallel to the pump axis, through the impeller, which is shaped like a propeller. Guide vanes are usually situated beyond the impeller. Note how similar the axial-flow pump is to the ducted propeller. Mixed-flow pumps produce both radial and axial flow. An axisymmetric guide ring is an integral part of the pump casing and guide vanes connect the pump casing with an appropriately shaped boss in the centre. This type is sometimes called a bowl pump. Centrifugal pumps produce a radial flow from the shrouded impeller, i.e. an impeller consisting of a series of blades set between two discs [1.16].

Centrifugal pumps were used on some early waterjet-propelled vessels, partly because they were readily available, however, they are no longer in use on modern waterjet applications [1.12]. Conventional axial-flow type pumps produce good mass flow, but at lower pump efficiencies, ≈80% [1.17], and the head developed with a single stage axial impeller without deleterious cavitation is limited [1.18]. An answer to this problem was the development of mixed-flow pumps, in which part of the head is developed by centrifugal action. The main penalty of using mixed-flow pumps is weight, increasing craft displacement. Normally, the total weight of a waterjet installation, including entrained water, amounts to 4.5-5.5% of the displacement [1.19]. However, mixed-flow pumps are competitive with lighter pump designs because the achievable propulsive efficiency compensates for any resistance increases due to the weight. The majority of waterjet propulsors today are mixed-flow impellers, although a small number remain axial-flow types [1.12]. The axial-flow units possess a smaller diameter and are therefore potentially lighter than mixed-flow pumps. For the purpose of this work the impeller was considered to be an axial-flow impeller, more detail of which is given in Chapter 8.

Prior Art

Increasing popularity in the use of waterjets as a propulsive device has seen a rise in the amount of research being conducted on them. The main body of the work has been to determine the characteristic behaviour of such units in an attempt to increase their efficiency and to understand interaction effects with the surrounding hull. Work has involved both experimental and computational analysis and Chapters 5 and 6 discuss this in more detail.

Experimental methods, used for the testing of waterjets, have been shown to be successful, however, they are expensive and time consuming. It is for this reason that more research is being carried out with the use of CFD, and as computer technology advances, there exists a greater ability to model more complex flows. However, experimental results are still required in order to validate the CFD predictions. The majority of papers reviewing CFD research have compared their results with existing test data. On the whole, the comparisons have been good, however, some discrepancies have also come to light due to limitations with CFD geometry modelling techniques.

1.3 BACKGROUND TO THE WORK

It is worth highlighting the author's background and reasons for the work. The author's research initially concentrated on modelling the flow through a waterjet intake duct in an attempt to improve techniques for the modelling of realistic waterjet geometries, to facilitate design modifications. The work involved the use of both wind tunnel testing and computational analysis using a viscous, RANS flow solver.

Having spent one year studying waterjets, the author was employed as a research assistant on a project which involved the design of a novel electromagnetic tip-driven propeller unit for use on work-class Tethered Unmanned Underwater Vehicles (TUUVs). The Department of Electrical Engineering carried out the design of the electromagnetic motor to drive the propeller, and the author concentrated on the hydrodynamic and mechanical design of the unit. Both theoretical and experimental techniques were adopted and the work was found to be analogous to the original waterjet research, i.e. modelling fluid flow through a duct or tube to a propeller or impeller. This similarity led to the concept of possibly using such a tip-drive unit in a waterjet application.

To this end, the work presented in this thesis is a combination of the two study areas (waterjet ducts and tip-driven propellers) for the purpose of assessing the implications and practicality of using a tip-driven impeller in a waterjet duct.

1.4 THESIS LAYOUT

Chapter 2 introduces the analysis tools, both computational and experimental, in more detail and describes how they have been used or modified to suit this particular field of study. Following this, the mechanical design of the prototype electromagnetic tip-driven thruster is detailed in Chapter 3, and the results from its tank tests are given in Chapter 4. Computational analysis of the thruster is carried out in Chapter 5, when the results from the panel code are compared to those from the experimental results. The confidence gained from this comparison means the code can be further used to model an axial-flow waterjet impeller in Chapter 8.

Details and results of the wind tunnel tests on the waterjet inlet duct are given in Chapter 6, and these results are subsequently used in Chapter 7 to verify predictions made by the RANS code model of the inlet duct. Having been validated, both CFD models of the waterjet intake duct and propeller are coupled together in Chapter 8, the propeller now being replaced by a simple axial-flow impeller, and the interaction effects are studied. Chapter 9 proposes an electromagnetic drive system for waterjet impellers and discusses the possible implications. Finally, conclusions are drawn in Chapter 10 and future areas of research are proposed.

Throughout the thesis smaller illustrations, used to aid descriptions, have been embedded within the text of each Chapter. These are referred to by the relevant chapter number and figure number, e.g. Figure 2.1 is the first figure in Chapter 2. Larger figures and graphical illustrations have been placed in Appendix A and references to these are prefixed with the letter A, Figure A2.2, for example.

2. ANALYSIS TOOLS AND PACKAGES - DESCRIPTION AND DEVELOPMENTS

This chapter presents an overview of the analysis tools and equipment, both experimental and computational, which are later used to investigate the tip-driven ducted propeller, waterjet inlet duct and impeller. It is an extension of Section 1.1.1, which introduced the analysis methods. In addition to a general description, the development of the facilities to suit the needs of this investigation is also presented.

Firstly, the experimental facilities used during this investigation are discussed; the prototype TDP has been tested in towing tanks and a wind tunnel was used to study the waterjet inlet duct. Following this, the computational packages, and the modifications and developments made to them for the purpose of this study, are described.

2.1 EXPERIMENTAL TESTING OF A TIP-DRIVEN PROPULSOR

An accurate and reliable set of experimental data was required for the prototype TDP. The test apparatus therefore had to be capable of measuring the thrust, torque and power requirement under various operating conditions including different propeller speeds, advance speeds, duct shapes and angles of yaw. General methods for testing propellers include cavitation tunnels, or water tunnels, towing tanks and full-scale trials, when the propeller is mounted on a vehicle. Open-water tests on ducted propellers are usually carried out in towing tanks [2.1], the propeller and nozzle are mounted on separate dynamometers and the drive shaft is attached to the downstream side of the propeller, so nothing disrupts the inflow. The only method available to test the TDP was the use of a towing tank. This facility provided the opportunity to test the prototype under the various conditions listed above, although a dynamometer and support framework had to be designed specifically for this purpose. The facilities comprised of two towing tanks, one at the University of Southampton and one at Southampton Institute. The tank dimensions are given in Table 2.1.

Table 2.1: Tank Dimensions.

	Length (m)	Width (m)	Depth (m)
University Lamont Tank	25	2.4	1.2
Institute Tank	60	3.7	1.85

Due to the size and total mass of the thruster, associated framework and dynamometer, it was not possible to attach the unit to the carriage over the towing tank at the University. For this reason, only commissioning and bollard pull tests were carried out in this tank. The facility at the Institute towing tank offered a large towing carriage, which could easily support the thruster, framework, and all necessary measuring equipment. The carriage was capable of running at an advance speed of up to 4.6m/s which was more than adequate for these tests, for which the maximum advance speed investigated was a full-scale 2.5m/s.

2.1.1 Support Bracket

The design work described in Chapter 3 focuses on the thruster itself and the assembly jig, which was required to build it. However, a framework was also required to support the thruster in the tank for experimental tests. Because the propeller and duct were an integrated unit there was no need to design a separate dynamometer mechanism for the two individual components. It was necessary to attach the support to a set of dynamometers to allow the resultant thrust to be measured. The requirements listed for the framework included;

- The ability to support the thruster in the water to a depth of 1m.
- To be strong enough to withstand the loadings predicted.
- To provide a mounting for a set of dynamometers to measure the loads.
- To provide a means of altering the angle of attack of the thruster.

The solution devised was to use a hollow circular-section steel tube with two flanges welded to either end (Figure A2.1). Using a circular section support with no fairing meant that if the thruster was tested at an angle of yaw, i.e. by turning the support, it could be assumed that the drag of the cylinder remained constant. The lower flange bolted to the thruster, while the upper flange had two channels milled through it, which located on two bolts screwed into a steel plate, thus providing a method of altering the angle of attack. The steel plate bolted onto four identical two-component strain gauge dynamometers, one

at each corner, which were themselves bolted on two channel sections spanning the width of the tank. Steel was chosen, rather than aluminium, as the construction material because a smaller cylindrical section could be used to withstand the large bending moment applied by the thruster. The length of the cylinder was 1.5m, its outer diameter was 4", and the wall thickness was 0.25". With these dimensions it could withstand the maximum predicted thrust loads with minimum deflection. For a thrust of 800N, the maximum deflection of the cylinder, at the position of the thruster, was calculated to be 2.0mm. Figure A2.2 illustrates a photograph of the TDP supported from the towing carriage in the Institute tank.

Flower et al [1.8] employed a similar arrangement to test a switched reluctance tip-driven propeller. Their unit was immersed in a relatively small tank and was tested at bollard pull conditions. However, results for the propeller at full speed were not achieved because of the presence of excessive turbulence above 750rpm. In addition, the results obtained were somewhat lower than those expected. It was thought this was due to a circulatory flow being initiated in the tank, meaning the propeller experienced an effective advance speed. Underwater vehicle manufacturers have reported similar phenomena when testing ducted propeller units [2.2]. This highlights the limitations caused by the confines of test tanks and, to a certain extent, wind tunnels also.

2.1.2 Dynamometers

The dynamometers were originally used for a wind tunnel propeller rig [2.3] and were designed for a total force of 800N in both the axial and normal directions. Each of the four dynamometers therefore had to withstand a quarter of this, i.e. 200N.

The individual dynamometer cages, illustrated in Figure 2.3, consisted of four identical flexures machined from aluminium alloy (HE30). The flexures were mounted, top and bottom, to 12.5mm thick steel plates, the stiffness of which minimised possible distortion of the flexures which would result in a non-linear response.

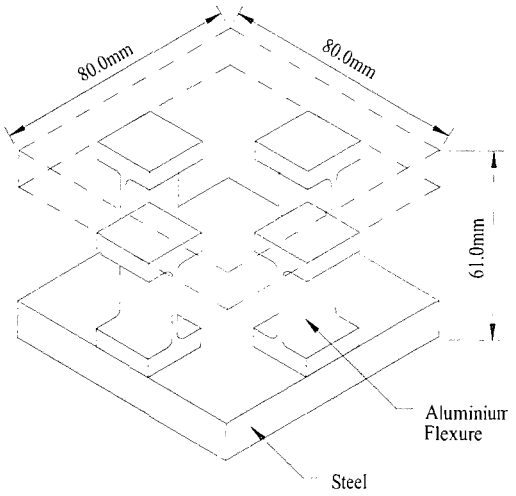

Figure 2.3 - Individual dynamometer cage.

Shear gauge flexures were originally chosen [2.4] because;

a) End fixing conditions are not critical, allowing fabricated construction.
b) Shear flexures offer little resistance at right angles to the principal measuring direction.
c) The gauge is located at the position of maximum strain and where the strain gradient is small.
d) Contra-flexures may suffer interaction due to superimposed compressive forces and moments.

Prior to testing, the dynamometer and thruster support were calibrated on a secure steel framework in the same manner as they were to be used in the experiments. Each dynamometer had previously been calibrated individually. Details of calculations for the dynamometer calibration are given in Appendix C.

However, once testing was underway, there was concern that the calibration of the dynamometers had altered having been reassembled in the tank. The resultant trend lines for the thrust agreed with theory, and the results were repeatable to within 5% which, noting the unsteady flow and varying velocities in the tank, was satisfactory. However, the absolute values were over predicted. Even so, conclusions could still be made about the relative changes between test cases. In light of these problems, tests were also carried out using a simple load cell, provided by Seaeye Marine [2.2], which was mounted on a

cantilever type arrangement, Figure A2.4. Only forces in the thrust direction could be recorded using this load cell, but the calibration was checked and it was found to be reliable and accurate. A maximum error of 3.5% in the force measurement was recorded, and the cell tended to under read the applied force. Analysing the thrust data obtained from the Seaeye load cell, alongside the results from the dynamometer, it was clear that the dynamometer results could be corrected using a linear scaling factor. This correction factor has been taken into account for the results presented in this study.

2.1.3 Data Acquisition and Instrumentation

Figure 2.5, below, illustrates a schematic diagram of the acquisition apparatus and arrangement used for the force measurements.

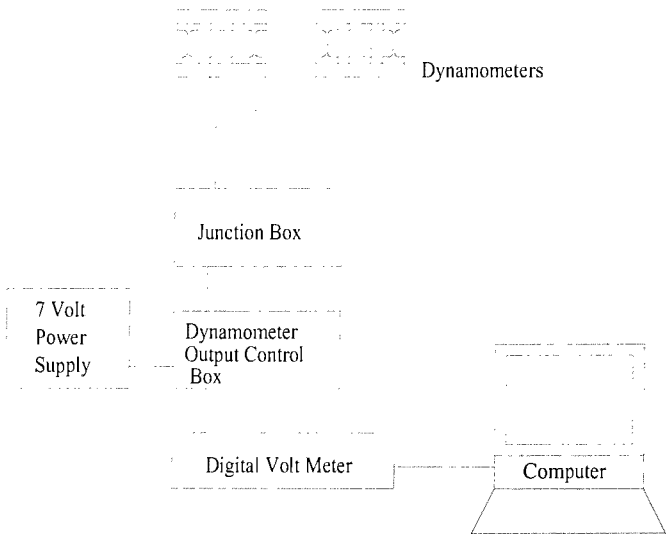

Figure 2.5 - Force data acquisition arrangement.

The four two component dynamometers were connected via a common 32-way cable to a junction box which allowed the side and axial force of each dynamometer to be measured simultaneously. The output from the junction box was connected to input channels on a Schlumberger 7061 integrating digital volt-meter (DVM) capable of reading time averaged DC voltages to an accuracy of 0.1μV. The DVM was connected to a PC which collected and stored the data.

The arrangement of the gauges was such that they react to shear stress, but cancel when subjected to tensile or compressive stresses, this was confirmed during the calibration

tests, Appendix C. The wiring of the bridge circuits is shown in Figure 2.6. A maximum bridge voltage of 7V was assumed, which gave the circuit equivalent resistance of 120Ω, and a total current I=58.3mA, with a current per bridge arm of 29.15mA. Using these values also meant that the heat dissipation from the gauges was at an acceptable level for the aluminium flexures. Tests also indicated that this level of supply voltage produced output signals, which were within the measurement range of the DVM. During testing, the supply voltage was monitored, using the DVM, and the variation was never more than ±20mV.

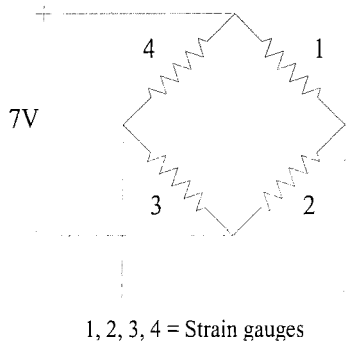

Figure 2.6 - Wiring of the strain gauge bridge circuits.

2.1.4 Power Measurement

The voltage, current and power into both the inverter and motor were measured using a Voltech PM3000A Universal Power Analyser, and the propeller speed obtained from the motor frequency, measured using a Gould digital 200MHz 1GS/s oscilloscope.

Knowledge of the motor *rms* current and the phase resistance at the operating temperature enabled the calculation of motor copper loss. The motor output power, or propeller delivered power, was calculated by subtracting core loss, bearing friction loss and copper loss from the motor input power [2.5]. Details of this are given in Appendix D.

2.2 EXPERIMENTAL TESTING OF A WATERJET INLET DUCT

Water tunnels or specially designed test rigs are often used to study complete waterjet units. However, these methods are expensive and are usually only employed by the waterjet manufacturers. Model self-propulsion tests in towing tanks can be used to study the jet-hull interaction, and wind tunnel tests are often used to study the flow through the

inlet duct alone. Further details on past experimental methods are presented in Chapter 6. In this instance, a wind tunnel model of a representative waterjet inlet duct was already in existence, at the University of Southampton, and this offered the most convenient method of studying the internal flow through the duct. Tests using this model had previously been conducted by Moss [2.6], however, problems existed with the impeller fan used at the time. Since then an improved impeller system has been devised [2.7] and has been used for these tests.

2.2.1 The Representative Waterjet Duct

The waterjet duct considered for this research was a flush-type inlet and the general form followed that used by Okamoto et al [2.8] for their model self-propulsion tests (Figure A2.7). A flush-type inlet was chosen partly because there was an existing model to test, and partly because they are the more common of the two inlet duct designs. Although based on Okamoto's [2.8] duct, a few minor alterations had been made to ease construction of the wind tunnel model. Most noticeably these occurred in the region of the inlet lip which, due to the construction techniques employed, possessed a very small radius.

The inclination of the duct centreline was 25 degrees and the lower half of the duct was semi-circular. The front-end of the upper half was rectangular in cross-section, which changed gradually into a half circle. The overall length of the duct from the base of the inlet ramp to the impeller plane, or exit plane, was 1.2m and the diameter of the waterjet outflow plane was 250mm, compared to 65mm used by Okamoto. Appendix G lists the co-ordinates of the vertical sections, which defined the geometry of the waterjet intake duct. The model was built from faired thin strips of 1.5mm plywood attached to a base plate by a series of ribs, which defined the outline shape. The flat upper surface of the unit allowed it to be constructed partially from perspex, which aided detailed flow visualisation using wool tufts taped to the inside of the duct. It also facilitated the use of a clamping and traversing device for pitot probes.

2.2.2 Test Set-Up

The duct base plate was designed to fit exactly onto the side of the working section of a 0.9m x 0.6m open circuit wind tunnel and the duct sat centrally on the wall. The overall

tunnel length, including inlet, contraction, test section, diffuser and deflector was 8.7m. The length of the test section was 1370mm. Attaching the duct to the side of the wind tunnel meant the duct was actually tested in a horizontal position rather than vertically, as it would operate in reality. However, as the fluid used was air rather than water, gravitational effects can be assumed negligible. A total of eighty five static pressure tappings were fitted to the wall of one half of the jet unit, along a number of radial and longitudinal sections. In addition, eight ports were located along the top wall of the model allowing pitot probes to be traversed through the duct.

Air was drawn through the wind tunnel by a fan situated at the end. The use of an open (non-return) wind tunnel results in the pressure within the working section of the tunnel being below atmospheric pressure. A variable speed 30kW impeller was installed aft of the jet unit in order to overcome the negative pressure within the working section and to allow the flow rate through the duct to be controlled. Due to restrictions in the space available, the impeller had to be connected to the jet unit via a flexible tube of similar diameter to the duct exit. Figure A2.8 provides a schematic layout of the experimental set-up and Figure A2.9 is a photograph of the actual apparatus.

2.2.3 Data Acquisition

The large number of individual data readings required the use of an automated system for data acquisition. The pressure tappings around the duct wall were connected via a rotary 1psi scanivalve to an automated system, which converted pressures into voltages. These voltages could then be read by a voltmeter connected to a PC, which collected and stored the data. The reference pressure used, P_A, was taken at the top centreline port at the outflow plane (A: X=*-0.3*) of the waterjet, see Figure A2.10, and made non-dimensional using the total head P_T measured at the centre of the outflow relative to the wall static P_A. The non-dimensional pressure coefficients (Cp) were calculated from the local pressure P using:

$$C_p = \frac{P - P_A}{P_T - P_A} \tag{2.3}$$

A boundary layer probe with a swan neck and flattened end was used to obtain velocity profiles through several sections along the duct. The probe used standard hypodermic stainless steel tubing with an external diameter of *1.65mm* and an internal diameter of *1.25mm*. A Betz manometer was used to measure the pressures from the probes at various distances into the duct. Velocities were defined relative to the local top wall static pressure measurement and were obtained from the Betz manometer readings using:

$$\rho_w g H = \tfrac{1}{2} \rho_a U^2$$

$$\therefore \qquad U = \sqrt{\frac{2\rho_w g H}{\rho_a}} \tag{2.4}$$

The flow quality of the wind tunnel has been improved, since Moss [2.6] carried out some tests on the waterjet duct model, through the installation of a new sheet of honeycomb at the tunnel intake. Measurements have shown that this made a vast improvement in the flow uniformity and stability through the tunnel, and the walls of the test section showed minimal disturbance [2.9].

2.3 COMPUTATIONAL MODELLING OF TDPs AND WATERJET DUCTS

Computational techniques are becoming increasingly popular as analysis tools. They offer comprehensive solutions for relatively little expense and allow rapid turnaround times between successive tests. They also provide a means of analysing the problem under test conditions, which would be too difficult, expensive or time consuming to achieve in the laboratory. However, CFD codes only provide a prediction of the flow, based on pre-defined boundary conditions, and experimental data is still required to assess the accuracy and reliability of the predictions. Once validated, codes can be used to study further problems with increased confidence, but the final solution can still only be taken as an estimate. Two CFD codes have been used during this investigation. A commercially available viscous RANS flow solver [2.10], which was used to model the waterjet inlet duct, and a non-viscous, lifting surface panel code [2.11], which has been used to model the TDP.

In addition, programs have been written specifically for the purpose of this research. These include routines to generate three-dimensional co-ordinates, which define the geometry of the propellers and ducts under consideration, and a program to estimate boundary layer growth over a body, based on the results from the panel code. These programs are designed to run in conjunction with the panel code. In addition to simplifying the geometry definition process, these programs can also be utilised for future design optimisation studies, when a large number of different geometries need to be rapidly created and their solution calculated.

2.3.1 Modelling a Tip-Driven Propeller

Due to the complex nature of modelling rotating propeller geometries within a duct a non-viscous panel method was used. The theoretical hydrodynamic performance of a ducted propeller and the waterjet impeller was investigated using the Department of Ship Science's parallel lifting surface panel code, Palisupan [2.11]. Palisupan had been used successfully to model propellers in the past [2.12], and it offered an inexpensive method for modelling the TDP, without having to use a commercial code.

Surface panel methods are used widely as a flow analysis tool capable of predicting flow around complex three-dimensional objects including impellers and inlets [1.2]. Based on a boundary element approach, potential-flow is solved around arbitrary three-dimensional bodies by mapping quadrilateral panels over the body surfaces. Numerical differentiation of the surface potential allows the surface pressure distribution and hence total body force to be determined.

The surface panel code, Palisupan [2.11], was originally developed to solve the problem of rudder-propeller interaction [2.12], and follows the work of Morino [2.13], Newman [2.14] and Lee [2.15]. It involves a straightforward application of this method to model the interaction between a rotating propeller and surrounding duct, or impeller and waterjet inlet. The approach used is that of the Interaction Velocity Field (IVF) method. The duct and propeller are solved independently and their relative influences are accounted for by imposing an inflow velocity at each panel centroid on a body, which is the spatial circumferential average at that location due to the other body. An iterative process is used where the flow is solved around the propeller or impeller first followed by the duct or

inlet with the imposed velocity due to the impeller. The process is repeated until the body forces do not alter by more than a given amount, chosen at say 0.5%. Typically this takes between 3 and 5 complete cycles.

Results from Palisupan are output in the form of non-dimensional body force coefficients (*Fx, Fy, Fz*) and moment coefficients (*Mx, My, Mz*), based on the geometry axis system. Therefore if the propeller is defined such that its centre axis is in the *X*-direction, it is possible to calculate a value for propeller thrust using *Fx*, and torque using *Mx*.

The implementation of the program uses two input files, a **.cmd* command file and a **.pan* geometry file. The command file prescribes the overall control of the flow solution. Convergence parameters, input geometry files, output data files and variations of the geometry orientation are specified within the command file. The panel code incorporates a powerful surface geometry definition process, which allows considerable flexibility and provides a rapid method of defining geometries for investigation. The body geometry is defined as a separate input file. Within this file a number of sections which make up the body shape are defined using three-dimensional co-ordinates. The wake strip from the lifting body is also defined in a similar manner. In addition, the file contains most of the information necessary for the panel code to model the problem. For instance, the number of panels used, distribution of the panels, details of any reflection planes and definition of the free stream flow are all declared. Additionally a spatially varying inflow velocity field can be defined in either cartesian or cylindrical co-ordinates. For the case of a propeller duct, points defining the cross-section outline at several angles around the circumference of the duct were listed. This enabled Palisupan to create a continuous surface using cubic splines and divide the geometry up into the specified number of panels. Examples of typical command and geometry files are given in Appendix E, however, a more detailed description is given by the panel code user guide [2.11].

Used correctly, surface panel methods are powerful analysis tools [2.11]. However, by its nature, the assumption of potential-flow neglects the influence of viscous flow and separation effects on the flow around bodies. At high Reynolds numbers the influence of fluid viscosity is confined to a thin boundary layer next to the body surface and a region of shed vorticity (wake) behind the body. These regions can have an important effect on the

pressure distribution around a body, and hence total force acting. If sufficiently severe, an adverse pressure gradient can induce flow separation and fundamentally alter the flow regime. It is essential that these possible discrepancies can be identified and their effects on the potential solution accounted for. Further details of the panel code theory are provided in Appendix E.

2.3.2 Propeller and Duct Geometry Definition

Fortran programs were developed to provide a rapid method of generating the three-dimensional co-ordinates necessary to define the nozzle, propeller blade and hub geometries. In addition to simplifying the process of generating panel files for the bodies in question, these programs also provide the basis behind future optimisation studies, when rapid geometry definition is beneficial for studying many variations of geometric parameters.

The propeller definition program read three input files, one which defined the general blade section sizes and two which outlined front and back offsets for each section. In addition, user inputs specified the number of blades, propeller diameter and blade area ratio. Details of the individual input files are provided in Appendix E. The program defined each section on a two-dimensional plane, rotated it about the relevant pitch angle and then mapped it onto a circular arc at the desired radii. The calculation of the hub co-ordinates used the data from the blade input files, particularly the section offsets and radius at the blade root, and an input length. The diameter and length of the hub were set as 60mm, which was the size used for the prototype thruster, however, this could easily be changed to model different propellers. The co-ordinates for just one propeller blade, located at Top Dead Centre (TDC), and only the portion of the hub between two blades are output from this program. Images of these geometries are declared in the panel code, which solves the flow for the correct number of blades and the entire hub.

The duct definition program used one input file, listing the section offsets, and duct characteristics such as length, thickness and diameter, which were input by the user. The program scaled the section size, according to the user inputs, and calculated section co-ordinates at twelve locations around the duct. An alternative version incorporated subroutines to define the bearing casings, either side of the propeller, and the

hydrodynamic stators supporting the bearings in the duct (these components are described in more detail in Chapter 3). This program used two input files, which listed the section shapes for the duct and the stators, and the twist angle on the various stator sections. Further information, provided by the user, included axial position of the stator root, i.e. distance from the propeller plane, and the angle of stator rake. This information was used to calculate three-dimensional co-ordinates of body sections, and the positions of the duct-stator and stator-bearing intersections. With this version of the stator definition program, only a constant section shape could be used along the length of the stator, and for reasons of simplifying the computations, it was assumed that each stator possessed the same section shape and twist properties. For more detailed information on the input parameters used to define these geometries, the input file formats, and the structure of the programs involved, the reader should refer to Appendix E.

The final output formats from the geometry definition programs were in the form of lists of three-dimensional section co-ordinates, which were used as panel code input files. Examples of the panel definitions for the representative geometries are shown in Appendix E.

2.3.3 Boundary Layer Approximation (*blayer.f*)

Although the panel code produces good indicative results, more accurate solutions can be obtained if the boundary layer and flow separation are taken into account. From the potential-flow point of view, the boundary condition of zero normal velocity can be moved from the body wall to a distance δ^*, the boundary layer displacement thickness. This displaced streamline effectively defines a modified geometry, due to the presence of the boundary layer [1.2]. The three steps necessary to include the boundary layer growth in the flow solution are:

1. Solve the potential-flow over the body and obtain the surface pressure distribution.
2. Using the pressure distribution, calculate boundary layer characteristics.
3. Modify the surface boundary conditions for the potential-flow, and solve for the next iteration.

Two approaches exist for modifying the potential-flow boundary conditions. The first is to alter the location of the body surface to take account of the displacement thickness. The second method does not change the geometry, but simulates the displacement by imposing

a velocity normal to the body surface. This velocity is calculated from information provided by the boundary layer solution. In this case the latter method is used because it was more straightforward to implement.

The exact solution of the boundary layer equations are, in most cases, full of mathematical complications and the numerical methods require an amount of work which is not acceptable in practice. These problems have led to the development of several approximate methods which have the limited objective of predicting overall characteristics of the boundary layer, for example momentum thickness, displacement thickness and skin friction, rather than details of the actual flow. For the purpose of improving the panel code solution, such methods are all that are needed to modify the potential-flow. Similar approaches have been demonstrated by Katz and Plotkin [1.2].

A program, *blayer.f*, written in Fortran, has been developed with the specific aim to estimate boundary layer growth and point of separation over bodies, which are modelled by the panel code. *Blayer.f* was designed to act as part of the overall code framework when solving problems using Palisupan. The basic concept for the program followed that used by Holt [2.16], who wrote a boundary layer prediction program specifically to model the flow over a submarine body. However, the program was quite unstable, and was only suitable for bodies that had been panelled in a similar manner to the submarine. It was decided to write a similar program, which was more stable and could be applied to a greater number of flow problems.

The program is essentially split into three components; prediction of the laminar boundary layer growth, turbulent boundary layer growth and an estimation of where the flow will separate. All the equations used within each algorithm are based around the Momentum Integral Equation [2.17]

$$\frac{1}{2}C_f = \frac{\theta}{u_e}.\frac{du_e}{dx}(H+2)+\frac{d\theta}{dx} \qquad (2.5)$$

where $H = \delta^*/\theta$

θ = Boundary layer momentum thickness
δ^* = Boundary layer displacement thickness

along with additional empirical formulae which have been derived over the years. The following sections briefly describe the theories used. Further details are given in Appendix F.

Thwaites' Laminar Boundary Layer Approximation

For the purposes of modifying the panel-code surface conditions, calculation of the boundary layer thicknesses was all that was necessary. It was not necessary to introduce explicit assumptions concerning detailed velocity profiles, as some methods do [2.18]. It has been suggested [2.18] that provided errors of up to 5% in θ, and 10% in δ^* are acceptable, then Thwaites' method should be used. These errors were considered acceptable for this estimation and so the laminar boundary layer prediction used the method derived by Thwaites [2.18]. In addition, this method had previously been proven to give reasonable results when used with Palisupan [2.16]. Thwaites provided correlations between overall boundary layer characteristics [H, l, F] and the shape parameter λ, which can easily be obtained as a function of x by numerical integration of

$$\frac{d}{dx}\left(\frac{\lambda}{u'}\right)=\frac{F(\lambda)}{u} \tag{2.6}$$

after which θ follows from;

$$\lambda=\frac{\theta^2}{\upsilon}.u' \tag{2.7}$$

and then δ^* and τ_ω from the empirical relationships

$$l(\lambda)=\frac{\tau_\omega\theta}{\mu.u} \quad , \quad H(\lambda)=\frac{\delta^*}{\theta} \tag{2.8}$$

Blayer.f uses output data from Palisupan in the form of local panel co-ordinates, pressures and velocities, interpolates the data over the body surface and calculates an approximation for the laminar boundary layer displacement thickness, momentum thickness and skin friction.

Head's Turbulent Boundary Layer Approximation

Most of the more refined methods for calculating turbulent boundary layers are based on the solution of partial differential equations, and produce detailed numerical solutions of the flow within the boundary layer [2.17]. Using a similar argument to that for the laminar boundary layer prediction, many of these calculations are unnecessary for the purpose of this program. Simpler integral methods have been proposed, which approximate the general characteristics of the boundary layer. A successful method of this kind [2.17] was that developed by Head [2.19]. Head derived a procedure for simultaneously calculating the development of the momentum thickness θ, and a quantity referred to as mass flow thickness;

$$\Delta = \int_0^{\delta} \frac{u}{u_e} dy = \delta - \delta^* \tag{2.9}$$

The momentum integral equation is integrated simultaneously with an auxiliary equation, which accounts for the rate at which the boundary layer entrains fluid from the free stream. Head obtained an empirical relation between the non-dimensional entrainment parameter F, and a shape factor parameter $H_1 = \Delta/\theta$. A skin friction relation completes the system of equations needed for the calculation.

The method relies on similar inputs as Thwaites, however, because the turbulent region of a boundary layer cannot start from zero thickness, an initial set of values is required. In this case the initial values are taken as the final set of values obtained from the laminar boundary layer prediction. For this reason, and in order to simplify the computation, a transition *point* was assumed between the laminar and turbulent boundary layers rather than a transition *region*. The effect of this was to create a small discontinuity between the laminar and turbulent boundary layer thickness. However, a simple averaging scheme was employed to smooth out the transition, Figure 2.11. This used end values from the laminar layer and initial values from the turbulent layer. Although this solution was not ideal, the transition discontinuity made negligible difference to the overall force predictions.

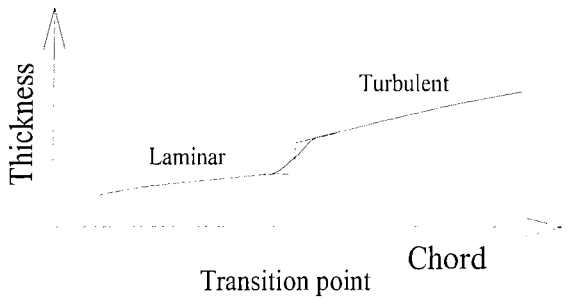

Figure 2.11 - Smoothing the transition point discontinuity.

Prediction of Separation

The final section of the program estimates the likely point of flow separation on the body surface. The method can use either the shape factor, H, or the skin friction coefficient, C_f, as the criterion for separation. Head used the C_f law given by Ludwieg and Tillmann [2.20];

$$C_f = 0.246 \times 10^{-0.678H} R_\theta^{-0.268} \qquad (2.10)$$

which predicts $C_f=0$ as H tends to infinity. An exact value of H corresponding to separation cannot be specified, but a range between 1.8 and 2.4 has been quoted [2.17]. For a NACA 0020 [2.21] section foil at 20° angle of attack, *blayer.f* predictions of the chordwise point of separation, using this range of H values, are given in Table 2.2.

Table 2.2: Point of flow separation on NACA0020 at 20° angle of attack.

H	1.8	1.9	2.0	2.1	2.2	2.3	2.4
% Chord	57.3	64.8	72.1	76.6	79.5	82.5	82.5

As can be seen from Table 2.2, the predicted position varied substantially, between 57% and 83% chord for the range of H values. Without knowing the precise point of flow separation, the more reliable means is to use the C_f values. In this case, $C_f \rightarrow 0$ occurred at 0.817C, which lies within the quoted range of H.

Use of *blayer.f*

The boundary layer approximation program, *blayer.f*, was developed to run in an iterative loop alongside the panel code, Palisupan. The loop was achieved through the use of a script file, which initiated each program in the required order. Flow charts describing the

program structure of Blayer.f, and the interaction with the panel code are presented in Appendix F. Initially Palisupan was used to model the potential-flow problem and an output file, called *foil.0BLI*, was produced. This output file contained co-ordinates of the panel centres, the associated velocity components and pressure coefficients for each body modelled. *Blayer.f* read this output file and sorted the panels into an order which represented individual two-dimensional sections around each body. For a foil-type body, each section was divided into an upper surface and a lower surface, from the leading edge stagnation to the trailing edge. The stagnation point was taken as the centre of the panel with the highest pressure coefficient.

To obtain a more accurate prediction, each surface was split into a large number of *stations* for which the flow characteristics are calculated using a spline subroutine, from the panel data. Typically, 200 stations along a surface were used. Trials had indicated that this number of stations produced a smooth definition of the source strengths, which represented the boundary layer over a surface. The station data was then used by the various boundary layer approximation subroutines and source strengths at each panel centre, representing the velocity normals and hence the boundary layer growth, were output in a file called *foil.00*. This data was then looped back into Palisupan to obtain a more realistic solution. The iterative loop was terminated when the forces on the duct reached a convergence value. Typical results indicated force convergence to within 10% after 4 iterations and 1% after 9 iterations.

Validation

The program *Blayer.f* was used as a means of modifying the panel code predictions, using approximations of viscous effects, to produce results which were closer to reality, but not necessarily exact solutions. In the case of an aerofoil section, for example, the predicted lift should decrease and drag increase once the boundary layer is taken into account. Therefore, all that was required for validation purposes was to show that the inclusion of the boundary layer prediction made the correct changes. Some experimental results for the turbulent boundary layer over a standard aerofoil, carried out by Newman, are presented in Cebeci and Bradshaw [2.17]. The boundary conditions of the flow are also published and these were input into the turbulent boundary subroutine of *Blayer.f*. Figure A2.12 illustrates the comparison, the points show the experimental data whilst the lines indicate

the boundary layer program results. It can be seen that the two sets of results agree well; the shape parameter, H, is predicted very closely, and the skin friction shows good concurrence, as does the momentum thickness. However, calculated θ tends to drop off towards the end of the data, the reason for this is not clear. Nevertheless, this comparison has provided some confidence with the ability of the program to estimate turbulent boundary layer characteristics. A further method of validating the effect of the code is to study how its interaction with the panel code affects the resultant lift and drag of an aerofoil.

Blayer.f was tested with the panel code by modelling a NACA 0020 [2.21] aerofoil, which had originally been tested as a ship's rudder [2.22]. The section shape is illustrated in Figure A2.13. Most published data for aerofoil sections is in the form of two-dimensional results, which do not include the presence of induced drag. Foils are usually tested with their tips bounded by the wind tunnel walls, which behave as reflection planes, and effectively result in an infinite foil with no induced drag. It was not possible to model an infinite foil using Palisupan, as only one reflection plane can be modelled. For this reason it was decided to source some validation data for a finite span foil. Wind tunnel tests on a ship's rudder [2.22] provided the necessary lift and drag characteristics and detailed pressure measurements.

Figure A2.14 plots the lift coefficients obtained, both experimentally and computationally, for NACA 0020 at various angles of attack, the experimental data has been taken from wind tunnel tests [2.22]. It is evident that, as expected, the lift predicted by the panel code alone is larger than the measured data, although only by a small percentage. Once the boundary layer estimation is included in the prediction, the lift coefficients decrease slightly, closer to the experimental data. A similar effect was also seen by Katz and Plotkin [1.2] who coupled a boundary layer prediction code to a potential-flow panel code.

Figure A2.15 plots the drag coefficients for the same aerofoil section at different angles of attack. Similarly, the results from the panel code alone, and from the coupling of the panel code and *Blayer.f* are presented. At lower angles of attack, the panel code predicts the drag of the foil well, and the inclusion of the boundary layer prediction tends to over

estimate the drag. However, at the higher angles of attack, the viscous drag predicted by the panel code is underestimated, and leads to low total drag coefficients. The viscous drag calculated by the boundary layer code is greater, and the coefficients therefore increase, nearer to the experimental data. It can therefore be assumed that the interaction of boundary layer prediction produces a more accurate result than the potential-flow panel code alone.

Figure 2.16 illustrates the effect of using *Blayer.f* on the predicted pressure distribution over the rudder section at 0.07 span. Plotted are pressure coefficients obtained from the panel code alone, from the interaction of the panel code and *Blayer.f*, and from measurements taken during wind tunnel tests of this rudder section [2.22]. The increase in C_p due to the presence of the boundary layer can clearly be seen over the upper surface of the foil, the pressure coefficients have changed by 4-5% in this region. A small change can also be seen along the lower surface of the foil, but the difference is not as pronounced. The pressures along the lower surface exhibit similar values to those without the presence of the boundary layer.

Figure A2.17 plots the pressure coefficients over the upper and lower surfaces of the NACA 0020 foil at 10^{o} angle of attack, for different span locations. The root of the rudder was located at 0.0 span, and the CFD geometry used 80 panels around the chordwise direction and 25 panels along the span of the foil. The panel code values, with the influence of the boundary layer, are compared against test data, which was obtained from wind tunnel tests [2.22]. It is evident that the pressure distributions were predicted accurately by the panel code, the experimental and calculated results agree very closely along both the upper and lower surfaces. There are some slight discrepancies at the span locations closer to the root, where the panel code tended to predict lower pressures towards the leading edge of the upper surface. However, it is possible that the presence of a boundary layer along the floor of the wind tunnel resulted in lower velocities at these low span values. The span locations further away from the root show negligible difference between the two sets of data, however, there is some difference along the back of the foil at 0.97 span, due to tip vortex effects.

As a matter of interest, Table 2.3 lists the predicted point of separation, as a percentage of chord, for the NACA 0020 rudder at different angles of attack. It is evident that the separation occurs at a shorter chord length as the angle of attack increases.

Table 2.3: Point of flow separation on NACA0020 at various angles of attack.

Angle of attack	0	4	10	15	20	25
% Chord	---	---	96.7	94.5	81.7	62.5

Limitations

This version of *Blayer.f* can only be used with confidence for bodies at zero angle of yaw, i.e. when the individual panel sections defining the body experience a straight-ahead flow, with no cross-flow between adjacent sections. This is because the input data for the code is taken from the panel centres which, in the case of foil type bodies, define the body sections parallel to the free-stream velocity. However, a proposed future development for the boundary layer prediction is to use streamline tracing, which will allow yaw angles and cross-flows to be taken into account. The method would involve following the likely route of a streamline from one panel centre to the next, based on surrounding panel characteristics such as surface gradient and local velocities. The boundary layer prediction would then follow the panels that the streamline crossed over, rather than the panels defining the two-dimensional section, as was assumed during this study.

2.3.4 Modelling a Waterjet Inlet Duct

Compared to a propeller in a nozzle the waterjet inlet duct, with no rotating bodies, is a reasonably simple geometry to define. In addition, because separation can readily occur in the region of the inlet lip, and because viscous effects through the duct play an important role in determining the velocity field at the impeller plane, it was chosen to model the inlet duct using a viscous RANS code. The code available was a commercial flow solver, CFX4.1-F3D.

CFX4.1-F3D [2.10] is a suite of programs intended for the prediction of laminar and turbulent flow and heat transfer processes. It is a RANS flow solver, which uses multi-block structured grids of hexahedral cells for modelling three-dimensional geometries. CFX consists of a number of modules for the definition of the problem, the solution, and

the output of results. Appendix H describes the governing equations, which the flow solver is based on. This CFD code was used to model the waterjet inlet duct, the modules used were:

a) **CFX-Meshbuild** - an interactive pre-processor that creates structured multi-block meshes of hexahedral cells for use by a flow solver. Blocks are defined by their vertices and edges and, providing the adjacent blocks share the same face definition, they are joined automatically. Meshbuild also provides a means of defining boundary condition 'patches' from the choice of; inlets, walls, mass-flow-boundaries, pressure boundaries and symmetry planes.
b) **CFX-Setup** - a command file generator. Command programs can either be written from scratch or existing programs can be modified to suit the problem being considered. The command language is a set of commands, sub-commands and associated keywords defining the nature of the flow.
c) **Frontend Module of CFX4.1-F3D** - this takes the input specification of the problem, converts it from a form convenient for the user into a form designed for efficient execution, and performs a detailed error checking before passing the data to the solver.
d) **Solution Module of CFX4.1-F3D** - a multi-block flow solver. Once the geometry file and command program have been produced they are run through this flow solver. The generated flow characteristics are written to an output file and a dump file, which can be used for post-processing.
e) **CFX-View** - a post-processor. Using data from the dump file CFX-View produces graphical outputs for screen display. In addition, files can be produced which can be used with a flow visualisation package.

Definition of the Duct Geometry

The numerical model was based on the dimensions and shape of the wind tunnel model. The waterjet duct shape was initially defined using Wolfson Unit Shipshape [2.23]. Shipshape is a series of programs designed to assist the naval architect in defining, fairing and drawing a set of ship lines [2.23]. Three-dimensional curves are drawn by constructing cubic splines through specified sets of points, and defined as either sections or longitudinals. Shipshape allowed all useful information, such as offsets, point co-ordinates and slopes, to be transferred into a data file and used elsewhere.

A data file from Shipshape was created which contained point co-ordinates defining vertical sections along the duct (Appendix G). These points were input into the interactive multi-block grid generator, CFX-Meshbuild, and used to create duct sections, which were joined to make blocks. These blocks were subsequently sub-divided into hexahedral cells to generate a mesh of the geometry under investigation. Initially, in order to accurately recreate the experimental set-up a wind tunnel working section was also modelled. This was to be used for validation purposes, comparing the results with experimental data gathered. For this reason air was used as the standard fluid in the CFD model. The inflow plane into the working section was modelled as an 'inlet', its outflow plane as a 'pressure boundary' and the duct exit plane as a 'mass-flow boundary.' The conditions defined for the model runs are detailed in Chapter 7.

Difficulties with the generation of the mesh occurred around the regions where the waterjet duct joined the working section, especially at the sharp lip on the bottom centreline of the duct. In this area, and at the upstream end of the inlet where the top centreline rises away from the working section, the grid is an awkward shape. For this reason several individual blocks had to be created and even then the subsequent cells were non-orthogonal in places. The waterjet duct was constructed of 24 blocks and the cells were concentrated towards areas of rapidly changing geometries, such as in the region of the inlet lip and ramp. The numerical model was run using up to 79600 hexahedral cells. The block structure is illustrated in Figure A2.18 and the shape can be compared to the experimental set-up shown in Figure A2.9.

Further details of the analysis methods and the boundary conditions used in each case are described in the subsequent chapters.

2.4 SUMMARY

Both experimental and computational analysis methods are used to investigate the tip-driven ducted propeller, waterjet inlet duct and impeller. Experimentally, the most appropriate means were to use towing tank facilities to study the performance of the ducted propeller, and wind tunnel methods to study the flow through a waterjet inlet duct.

Computationally, a panel code and commercial RANS flow solver are used to model the TDP and waterjet inlet respectively.

As an aid to the computational investigations, several programs have been created to facilitate the geometry definition of the tip-driven thruster. These programs may also be used for future optimisation studies as they provide rapid geometry definition, based on a small number of parameters. In addition, in order to obtain a more realistic solution from the potential-flow panel code, a program has been written to estimate the growth of the boundary layer over bodies, which are modelled by the panel code. Using a script file, this program is run in an interactive loop with the panel code. This chapter has described the analysis methods, however, details of the actual trials are presented in subsequent chapters.

3. DESIGN OF AN ELECTROMAGNETIC TDP

3.1 AIMS

The aim of this chapter is to present the design and construction of the prototype electromagnetic tip-driven propeller. The prototype was designed purely as an experimental unit to obtain a comprehensive set of performance data for TDPs, to prove the concept, and to gain an insight into any design difficulties which presented themselves.

3.2 BACKGROUND

The idea of driving a propeller via its blade tips is not new, but only a limited amount of work has been published on such units. The work, which has been covered, mainly discusses mechanical drives rather than electrical, which offer additional sealing and gearing problems. It is probably due to these limitations that the idea has not been used in practical applications. Radojcic [1.11], however, proposed some mechanical drives, some even with contra-rotating propellers, and explained that latest developments in material technology and motor design now mean that such drive methods are viable alternatives, particularly in specialised applications such as underwater vehicles. The thrusters on an underwater vehicle are required to provide a flexible means of manoeuvring, and should be capable of a good response to inputs from the controller. It is also of benefit if the propulsors provide equal thrust in both forward and reverse directions. This illustrates a further area where a tip-driven propeller would be advantageous.

The use of an electromagnetic drive aims to overcome some of the limitations associated with mechanical drives. With the absence of any physical contact between the drive system and the propulsor, the need for extra sealing mechanisms is eliminated. Such units have been proposed for smaller applications such as Tethered Unmanned Underwater Vehicles (TUUVs) and ROVs, however due to inefficient motors and high production costs many designs have not passed the prototype stage.

Flower et al [1.8] described the design, construction and preliminary motor performance of a prototype integrated switched reluctance unit. It used a sector motor configuration in which the stator did not entirely surround the rotor and propeller ring, it was manufactured as a small arc which sat at top dead centre (TDC) over the rotor. A standard Kaplan K4-55 series propeller with a diameter of 290mm was used, but the unit was not encased within any form of duct or nozzle. It was tested at bollard pull conditions but a full set of results were not achieved because of excessive levels of turbulence in the test tank at motor speeds above 750rpm. The thrust developed at 750rpm was *160N*. From the test data, the expected thrust for the prototype at its maximum speed of 1200rpm was predicted as being *350N*. This gives a thrust coefficient $K_T=0.12$, which was considerably lower than $K_T=0.38$ for the standard K4-55 propeller in open water at zero advance speed. It was thought the decrease in thrust was due to the flow set up in the tank, which gave the propeller an effective advance speed. It was concluded that further work was necessary on the hydrodynamic features of the unit.

Westinghouse Electric Corporation [1.9] published a brief summary of their work on Electromagnetic Tip-Driven Propellers (ETDPs) in 1993. An ETDP was illustrated and it was claimed that conceptual designs for power outputs of up to 50000hp have been developed. Their design was based around a canned induction motor which was hermetically sealed within the duct walls. The rotor was attached to the propeller blade tips, and the propeller was mounted using water lubricated bearings, thus eliminating the need for shaft seals, which cause extra frictional losses. Being an all contained drive unit the benefits of location and mounting, over conventional drive systems, were illustrated. However, comparative sizes and weights for equivalent performance requirements were not given. Westinghouse claimed a militarised version is in production but a commercial product line has not been instigated [3.1].

In comment to the Radojcic paper [1.11], the author suggested the major gains are not likely to be due to a smaller boss, but due to eliminating shafts, shaft brackets and associated appendages drag. The author further suggested there could be a better case for an electrical drive system and believed there was scope for an experimental test programme to determine the relative merits and limitations.

In addition, some further work which has been undertaken on TDPs was highlighted by Allison [1.11]; An electrical tip-driven pump has been under development at the Annapolis Branch of the David Taylor Model Basin, which was suitable for further development and application to a large waterjet propulsor. However, no further data on this was available.

The Harbor Branch Oceanographic Institution (HBOI) [1.10] demonstrated a permanent magnet integrated thruster in which the propeller hub, bearings and spider supports were eliminated. The propeller was attached only to the external ring and there was a small open space where the hub would normally be situated. One unique characteristic of this unit was that it was virtually impossible for a rope to become entangled in the propeller blades. Instead, it would pass harmlessly through the centre. To overcome the sealing friction losses, HBOI experimented with replaceable plastic races using glass balls rather than steel. However, the effectiveness of these bearings was not discussed. The bearings were replaced after an underwater mission at low cost. Holt [3.2] presented some brief test results on this thruster, which showed for a given amount of thrust, the electric TDP required less power than an equivalent electric ducted propeller. In addition, a counter-rotating unit was proposed, which was essentially made from two TDPs placed in series within a single duct.

In response to Radojcic's paper [1.11], two US Patents, regarding tip-driven propellers, were also listed; Wardell [3.3] filed a US Patent in 1980 for a retractable lateral thruster which was located in the hull of a vessel. The thruster was positively driven via the blade tips using a set of gearwheels connected to a reversible DC motor. However, the proposal did not cover any detail on bearing or sealing arrangements.

A second patent [3.4] proposed a drive system for small boats in the form of a propeller enclosed in, and attached to an open ended tube. This tube was driven by the engine through a ring gear rack on the outside of the tube. A stationary housing, attached to the boat hull contained the tube. Bearings and seals between the housing and the tube allowed the space around the tube, and hence all the drive-gear, to be filled with lubricating oil. It was essentially an elongated tip-driven ducted ring-propeller.

An important aspect which has arisen from these past papers is that there have been many design proposals, some of which have been built and tested, however, there has been very little published data on the performance, efficiencies and practicalities of building and using such units. This chapter aims to address these problems. Firstly some of the difficulties involved with the design and construction of an underwater ETDP are high lighted. Overall schematic plans of the possible general arrangements are presented, their pros and cons discussed, and the choice explained. The main section of the chapter is split into various sub-headings which cover the design of individual components for the thruster unit.

3.3 DESIGN BRIEF

The main aims behind the design and construction of this prototype were to develop a tip-driven thruster in order to assess its capabilities, benefits, and practicality for use as a propulsion unit. To this end a list of requirements was drawn up;

a) The unit had to be bi-directional, i.e. be capable of producing equal thrust in both directions - enhancing its use as a manoeuvring/control device. As such, both the propeller blade sections and the sectional shape of the duct had to be symmetrical.
b) The electric motor was to be encased within the walls of the duct.
c) The propeller pitch ratio, P/D = 1.0
d) The propeller Blade Area Ratio = 0.7
e) It was to be driven using a 2kW Permanent Magnet (PM) motor.
f) The propeller diameter, D = 250mm.

Requirements c) and d) were specified because the electric motor had initially been designed using data from existing Kaplan performance charts for a propeller with these characteristics. The final three requirements were included so the thruster could be compared alongside the performance of an existing ducted propeller of similar dimensions.

Due to the fact that the thruster was an experimental prototype which was to be used to obtain a series of results, further requirements were imposed in order to make the unit as flexible as possible. These extra requirements included;

h) The ability to alter the duct section shape.
i) The ability for the unit to be tested wet or dry.
j) The ability to alter the angle of attack of the hydrodynamic stators.

3.4 DESIGN CONSIDERATIONS

The obvious consideration is that the thruster was to be used in deep water. This dictated that all the electrical components and connections had to be sealed for immersion (up to 1000m), any oil lubricated bearings had to be sealed and air cavities minimised. Corrosion resistant and non-water absorbing materials were also necessary. However, the materials used in the vicinity of the stator or permanent magnet rotor had to be of the type which would not disrupt the performance of the motor.

The unit required enough mechanical strength to transmit the developed thrust through the duct to a support and dynamometer framework. Enough strength was also needed to support the rotor accurately in line and at a fixed distance from the stator. In addition, there must also be an adequate joint between the rotor and the propeller blade tips.

It was advantageous to minimise frictional resistance in the bearings and associated seals. The use of seals could be overcome by using water lubricated bearings, however, the bearings themselves offer more frictional resistance than ball-race bearings, due to the increased surface areas, and dry testing would be limited. From practical experience, TUUV manufacturers [2.2,3.5] have found sealed ball-race bearings to be more desirable. The greater wear resistance of ball bearings also had the advantage of ensuring an accurate rotor alignment.

It was preferable for the prototype to be built in modular form, which would ease construction and allow any necessary adjustments to be made relatively easily. The duct itself had to be split into at least two pieces to allow the motor to be located within it.

Studying several existing designs, and design proposals, it was decided that there were four main arrangements that could be considered for the thruster. These were largely focused around the position of the bearings. Figure A3.1 illustrates the proposals. Each diagram represents a schematic view of a section through the centre of the thruster.

Three options were available for the location of the bearings. They could either be mounted around the periphery of the propeller as shown in Figure A3.1a; within the propeller hub (Figure A3.1b); or offset from the propeller and located at the centre of a set of support struts (Figure A3.1d). Locating the bearings at the periphery (Figure A3.1a) would result in a very tidy design without the need for any propeller supports. However, the bearing diameter would be relatively large and problems would arise when attempting to seal the bearings from the ingress of water. Harbor Branch Oceanographic Institution [1.10] used a design similar to this although their bearings were unsealed, replaceable plastic races.

A more conventional arrangement is to locate the bearings along the propeller centreline (Figures A3.1b, c, d) which would result in a cheaper and easier design for this prototype. The smaller shaft seals required would also offer less frictional resistance than larger ring seals located at the periphery of the propeller. A shaft needed to be supported using struts connected to the duct, however, it was possible that these struts could be used as hydrodynamic stators to aid the flow. The support struts could be located either at one side (Figure A3.1c), or both sides of the propeller (Figures A3.1b, d). In practice TUUV ducted thrusters tend only to have one set of supports offset to one side, allowing easy access to the propeller. However in this case, in order to minimise the danger of propeller vibration causing the rotor to come into contact with the duct walls, it was decided to mount the propeller using support struts at each end. The bearings along the propeller shaft could be located either within the propeller hub (Figure A3.1b), for which the propeller would rotate about the shaft, or at the support strut centres (Figure A3.1d), for which both the propeller and the shaft would turn. Again, for reasons of simplicity, it was decided to locate the bearings at the support struts.

3.5 DESIGN LAYOUT [3.6]

After several design iterations it was decided that the overall layout would take the form as shown in Figure A3.1d. The detailed design is illustrated in Figure A3.2, which represents a cross section through the thruster. Various components are labelled on the diagram.

To satisfy the problem of mechanical strength an outer shroud was machined in aluminium alloy into which the stator was shrink fitted. This shroud acted as the 'backbone' for the entire thruster, with all the thrust ultimately transmitted through it. It also provided an ideal heat sink for the stator. Aluminium was chosen because of its characteristic properties; low density, good heat conductivity, non-magnetic and relatively resistant to corrosion.

The propeller was attached to the rotor via its blade tips and the rotor was situated within the confines of the inner duct walls so as not to interfere with the flow through the duct. A shaft passes through the propeller hub and was mounted in sealed bearing units at each end. The bearing casings were located at the ends of three support struts each side of the propeller. These struts passed through the duct profile pieces and secured into the outer aluminium shroud. The supports were also contoured with the hope that they would also act as hydrodynamic stators. The propeller was held in position, axially, on the shaft using a number of pins, which screwed through the propeller hub and located in the shaft.

The following sections give some further detail about the individual components.

3.5.1 Electromagnetic Motor

The overall design of the thruster focused largely around the size of the permanent magnet motor [3.7]. The initial stages of motor optimisation were based on existing performance data for similar sized ducted propellers, the Kaplan K4-70 series. The design was undertaken by the Department of Electrical Engineering at the University of Southampton [3.8] and the motor was optimised to meet specific requirements, in terms of power, torque and speed.

The stator core was manufactured from layers of pre-coated Scotsil 330 steel, each laser cut to a thickness of 0.35mm. These were welded together at several positions around the outer diameter using tig welding, and the outer surface was then skimmed to an accurate diameter. Being unable to secure the stator into the shroud using screws or bolts, the stator was shrink fitted which guaranteed an accurate, close fit.

The rotor consisted of a layer of 34KC-1 grade Neodymium-Iron-Boron (NdFeB) magnets attached to a steel rotor yoke, which was 7mm thick. A 6mm gap existed between the outer diameter of the rotor and the inner diameter of the stator. This spacing is relatively large for permanent magnet motors, but was chosen to allow a 2mm protective coating to be applied to both the stator and the rotor. To provide added security, a porous glass fibre tape was wrapped around the outer diameter of the magnets prior to the rotor being sealed.

Once assembled, the motor was tested and hall-effect devices were accurately positioned within the stator endwindings. The stator cavity was subsequently filled with epoxy, using a centrifugal method, to a depth of 2mm around the inner diameter, which formed a tough, void free, impermeable protective packaging.

3.5.2 Propeller

The main consideration for the propeller was that it had to be attached to the back of the permanent magnet rotor at its tips, requiring a reasonable tip thickness. In addition, the shaft-way through the propeller hub could not be tapered, as in usual propeller applications, so it had to be held axially on the shaft using some locking screws through the hub. The bi-directional requirement was achieved by using a propeller that had the same blade section profiles on the front face as on the back face. This resulted in a one-off propeller being ordered from the manufacturers. Bi-directional propeller blade sections will result in a lower thrust than standard asymmetric sections; however, this compromise was accepted for this prototype manoeuvring/control unit.

A number of options were available for manufacturing the propeller, which to a certain extent also dictated the means of joining it to the rotor. If the propeller was cast in aluminium it could be joined to the rotor steel core using small, machined brackets either side of the blade tips. These would be screwed into the rotor core and riveted through the

blade. The tip to ring joint would then be smoothed using the sealant around the rotor. A second possibility would be to use some thin metal discs located in notches at the blade tips. The disc would be screwed into the rotor and the propeller would then be secured with as little flow interference as possible.

A further possibility existed if the propeller blades were made using a composite moulding, and were mounted on a small metal boss. A thin ring could be moulded, surrounding the blade tips, in the same lay-up. This would provide a good bond between the blades and the ring, and the ring could easily be attached to the rotor core through the use of a number of screws. Not only would this method provide a more substantial propeller to rotor joint, but it would also ease the sealing of the steel ring and rotor magnets. The propeller could also be moulded to required dimensions or section patterns. However, the main drawbacks with this method were the cost and time involved. For this reason it was decided to purchase an aluminium propeller from a local manufacturer.

The final propeller was a four bladed Kaplan type propeller with symmetrical blade profiles. A Kaplan propeller was chosen because the characteristic wide blade tips were beneficial to attaching the rotor to it, and tests have shown Kaplan propellers to be beneficial in ducts [1.5]. The profiles were based on the existing Kaplan K4-70 series ducted propeller [2.1] with a blade area ratio of 0.7. Stainless steel discs, 1.5mm thick and diameter 24mm, were manufactured to join the propeller to the rotor. Three holes were drilled in the discs and two notches were bored into the blade tips, Figure A3.3, the remaining spigot between the notches located into the centre hole of the disc. Having located the discs on the blade tips the propeller was positioned in the rotor and secured using screws through the discs into the rotor core. Once the propeller was mounted in the ring the rotor was potted in epoxy using a centrifugal method. A mould was made to sit around the outside of the ring, both the ring and the mould were spun together on a lathe and epoxy was poured in. The rotor was sealed in epoxy to a depth of 2mm, thus ensuring that the propeller-ring joint (1.5mm thick discs) was sealed and that it would not impose into the flow past the blade tip.

3.5.3 Bearings

As mentioned in Section 3.4, the thruster used standard single row angular contact, metal ball-race bearings. These were located within a bearing casing on each side of the propeller. Each casing was supported in the centre of the thruster using three support struts. To prevent the ingress of water the bearings were sealed using a conventional approach as shown schematically in Figure A3.4.

Essentially the walls of the bearing casing provided a cylindrical chamber, which was sealed on both sides of the bearing and filled with oil. At one end of the chamber a rubber diaphragm was mounted which sealed the oil on one side, and was open to the external water pressure on the other side. A shaft seal was located at the other end of the chamber. The method assumes the oil chamber is kept under a positive pressure by the diaphragm, and if there is any leakage beneath the shaft seal, it will be the oil escaping, not water entering.

Three support struts rather than four were used for each bearing casing in order to minimise any possible pulsating effects which may occur between them and the four bladed propeller. A metal dowel and circular flange were machined on the end of each support, these dowels located into a hole in the casing and the flange onto a machined flat on the casing side. The supports were accurately machined to fit precisely between the bearing casing and the external aluminium shroud of the thruster. Therefore the casing, bearing and hence propeller shaft were accurately held on the duct centreline, to a tolerance of 0.01mm.

It is known [3.9,3.10] that the use of pre or post swirl stators can improve propulsive efficiency by recovering some of the rotational energy loss, increase thrust and reduce unbalanced propeller torque, which can create undesirable directional stability problems. The support struts for this prototype were primarily designed for mechanical strength and accurate alignment of the propeller bearings and shaft. However, they have been machined with an elliptic profile and the use of a dowel to locate them in the bearing casing provided a means of altering their angle of attack by up to 30° from the centreline. So the possibility of using them as a performance improvement, or energy saving, device could be studied. Figure A3.5 provides some detail of the support strut design.

3.5.4 Duct Profiles

The motor, rotor and shroud had to be as hydrodynamically efficient as possible, and duct profiling pieces were attached to each end of the thruster. The possible duct shapes were constrained by the size of the motor and associated aluminium shroud. Because the profile pieces were not structural the only limitation on the choice of material was that it was either impermeable, or could be adequately sealed against water penetration. A material often used on small ducted propeller units for underwater vehicles is a Nylon based synthetic material, which is relatively light, water resistant, hard wearing and offers enough strength for the motor to be supported from it. The thrusters are also often attached to the main body of the vehicle through the duct. However the fact that the profile pieces for this prototype were not structural members meant such material was an unnecessary cost.

With the thought that the prototype would not be spending long periods immersed, the most cost-effective solution was to use sealed wooden ducts. Wood offers a cheap and easily machined material, and if sealed adequately it is relatively stable in water. The duct profiles were therefore manufactured from staggered sections of mahogany joined together in a brick type pattern providing even greater stability. The ducts were milled on a lathe and the finished rings sealed using epoxy. This method has been used successfully to seal previous experimental wooden foils against water penetration. To allow access for the bearing support struts, the ducts were split and therefore two rings were machined for each end of the thruster. The rings were secured using stainless steel screws, which located into the aluminium shroud.

For the purposes of investigating the influence of duct section shape, three pairs of different duct profiles were manufactured. The half sections are illustrated in Figure A3.6. Using this design, the duct profiles could be swapped between either ends of the thruster so different combinations of profiles could be investigated. The inner surface of each duct, at the location of the propeller, remained constant as an axially cylindrical form. Duct s2037 was derived from the original Marin Duct 37 [2.1], which was a relatively thick section needing little alteration to accommodate the electric motor. S2637 was a stretched version of s2037, having a slightly smaller nose radius, and f2637 was the same length as s2637, but possessed a flatter inner surface (hence the prefix, f) and a nose

radius closer to the baseline. The combinations of ducts that were tested in the towing tank are described in Chapter 4.

3.6 ASSEMBLY JIG

There was a small clearance gap between the stator and the rotor within which strong magnetic forces existed. It was therefore essential to be able to control the positioning of the rotor, supported at its centre by the propeller shaft, and the stator during assembly of the thruster. An assembly jig was therefore designed and built.

The easiest arrangement was to lie the motor in its shroud on one end and lower the propeller and rotor into position. Not only was the lateral positioning of the motor and rotor important, to achieve a uniform gap, but also the rate of descent of the rotor into the motor had to be controlled. If not, the magnetic forces could have the tendency to 'snatch' the rotor down onto the motor, causing possible damage.

The motor and shroud were aligned in position on a base plate using three guides located around the periphery of the shroud. One of the bearing casings was also located on the base plate. The descent was controlled by attaching the propeller and rotor to an M16 screw thread and lowering it slowly through a winding handle and bearing, supported on a cross beam above the jig. Aluminium plate was used for the jig base and the guides; standard channel section was used for the crossbeam and supports over the motor. Figure A3.7 illustrates the general layout of the assembly jig. The components used in the prototype TDP are illustrated in Figure A3.8, and the finished unit is shown in Figure A3.9.

3.7 SUMMARY

The concept of an electromagnetic tip-driven ducted propeller has been taken from the initial conceptual ideas, through the design process to manufacturing drawings for a prototype. From these drawings, a prototype thruster has been successfully built for the specific purpose of experimental testing. A 2kW permanent magnet motor, encased within the duct walls, drives the propeller via a ring of magnets attached to the blade tips using a

series of small metal discs. The novel design allows testing, in either air or water, to be carried out in both forward and reverse directions with several different duct section shapes, different hydrodynamic stator angles of attack, and various angles of yaw. For this reason several components, which were designed to aid testing, would ultimately be of simpler construction. Similarly the materials, from which components have been machined, are subject to change with future developments. Appendix I illustrates some of the design drawings from which the tip-driven propeller was manufactured.

Some difficulties were encountered during the design and manufacture of the prototype, which have been successfully overcome. Possibly the most challenging stage of construction was attaching the propeller to the rotor ring, however, a final production version may be free of such difficulties if different methods and materials were used, as discussed in Section 3.5.2. A further challenge was sealing the rotor with epoxy, for which a special mould was made and spun on a lathe with the rotor. In addition, because some components were designed to be tested at different angles of attack, they proved to be difficult to manufacture. However, most of the problems encountered were largely due to the fact that this was a prototype. If such a unit was to go into production, several stages of the construction could be simplified.

A major advantage of the tip-driven system is that the supporting bearings need not be located along the centreline of the thruster. There is the possibility of locating them around the periphery of the rotor [1.10,3.2], which results in clear flow into the propeller. However in this instance, mechanical integrity was more important. Once the drive mechanism has been successfully proven, design modifications and improvements can then be made. The commissioning tests for the prototype are described in the next chapter, and these are followed by detailed experimental tests at different operating conditions, including various propeller speeds, advance speeds and duct profiles.

4. EXPERIMENTAL TESTS OF AN ELECTROMAGNETIC TDP

4.1 AIMS

This chapter describes the experimental tests, which were carried out, on the prototype ETDP in the towing tanks. There were several aims to the tests. To assess how well the drive mechanism worked in practice and to measure the performance of the unit in order to fully understand its characteristics. In addition, to obtain a reliable and accurate set of data which will be available in the public domain, and for use when validating the CFD model of the ducted propeller in Chapter 5. Before using CFD codes to predict any future developments it is necessary to obtain an indication of the accuracy of the predicted results. By modelling the ETDP both physically and computationally (Chapter 5), an assessment of the CFD code can be made.

4.2 TEST PROGRAMME

It was necessary to conduct some initial commissioning tests on the prototype TDP, and its relevant apparatus, prior to carrying an extensive test programme. The commissioning tests were carried out in order to verify that the thruster and the data acquisition systems worked as they were intended. Because the time reserved for testing in the larger tank at Southampton Institute was limited, the commissioning tests and additional bollard pull, or zero advance speed, tests were performed in the towing tank at the University of Southampton. The tests carried out in this tank consisted of bollard pull studies using two thrust measurement systems. One method was the dynamometer arrangement, which was described in Chapter 2, and the other was a simple load cell system, used by a local TUUV manufacturer [2.2]. The load cell method was used to verify results obtained from the more complex dynamometer system. The load cell was a far more straightforward mechanism, which provided a direct thrust measurement without the complexities of interaction effects and calibration calculations. However, it measured force only in the thrust direction, and it was not possible to connect it to a data acquisition system. Results from the load cell system were therefore used as a basis to verify the dynamometer predictions, calculated using calibration relationships, which had been defined during earlier calibration tests (Appendix C). The prototype was tested at different propeller

speeds, with different duct shapes and stator angles of attack. Table 4.1 illustrates the range of combinations that were studied.

Table 4.1: Commissioning and bollard pull tests on the prototype TDP.

Duct Profile	Thrusting Direction	Propeller rpm	Stator angle	Force Measurement
s2037	Forward	$0 \rightarrow 1200$	0^o	Dynamometer
	Reverse	$0 \rightarrow 1200$	0^o	Dynamometer
s2637	Forward	$0 \rightarrow 1200$	0^o	Dynamometer
	Reverse	$0 \rightarrow 1200$	0^o	Dynamometer
a2637	Forward	$0 \rightarrow 1200$	0^o	Dynamometer
	Reverse	$0 \rightarrow 1200$	0^o	Dynamometer
s2037	Forward	$0 \rightarrow 1200$	$\pm 5^o$	Dynamometer
	Reverse	$0 \rightarrow 1200$	$\pm 5^o$	Dynamometer
s2037	Forward	$0 \rightarrow 1200$	$\pm 10^o$	Dynamometer
	Reverse	$0 \rightarrow 1200$	$\pm 10^o$	Dynamometer
s2037	Forward	$0 \rightarrow 1200$	$\pm 20^o$	Dynamometer
	Reverse	$0 \rightarrow 1200$	$\pm 20^o$	Dynamometer
s2037	Forward	$0 \rightarrow 1200$	0^o	Load Cell
	Reverse	$0 \rightarrow 1200$	0^o	Load Cell

Figure 4.1 illustrates the duct section shapes, and their representative names, which were tested in the towing tanks. The profiles are based on the half-sections, illustrated in Figure A3.6.

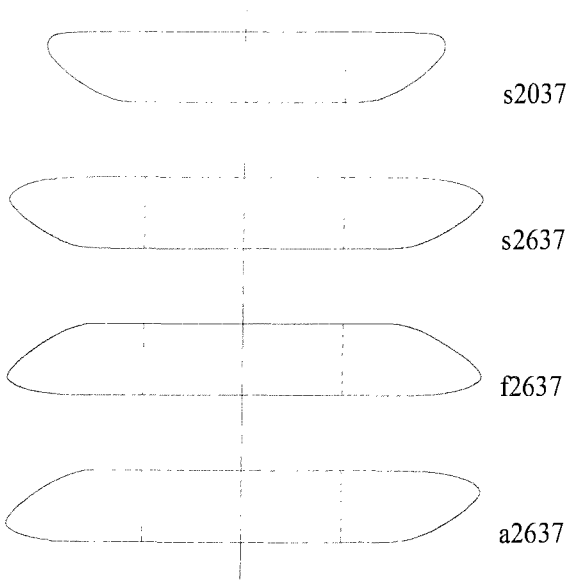

Figure 4.1 – Duct section shapes tested in the towing tank.

The dashed lines through the duct sections in Figure 4.1 represent the position from which the leading or trailing edge profiles could be removed. The mid-body of each duct consisted of a 150mm long parallel section, which housed the electric motor.

Dynamic tests on the thruster were carried out in the towing tank at Southampton Institute. The large towing carriage allowed the thruster to be suspended from it, and the data acquisition equipment to be positioned on it. The aim of these tests was to study the performance of the TDP over a range of advance coefficients. A similar test programme to that for the commissioning and bollard pull tests was used, however, the additional variable in this case was the speed of advance. Table 4.2 lists the combinations of variables that were tested. Intervals of 0.5m/s were used through the range of advance speeds.

Table 4.2: Dynamic tests on the prototype TDP.

Duct Profile	Thrusting Direction	Propeller rpm	Advance speed (m/s)	Stator angle
s2037	Forward	$0 \rightarrow 1200$	$0.5 \rightarrow 2.5$	0^o
s2637	Forward	$0 \rightarrow 1200$	$0.5 \rightarrow 2.5$	0^o
	Reverse	$0 \rightarrow 1200$	$0.5 \rightarrow 2.5$	0^o
f2637	Forward	$0 \rightarrow 1200$	$0.5 \rightarrow 2.5$	0^o
a2637	Forward	$0 \rightarrow 1200$	$0.5 \rightarrow 2.5$	0^o
	Reverse	$0 \rightarrow 1200$	$0.5 \rightarrow 2.5$	0^o

It was not possible to run the towing carriage in the reverse direction, so turning the thruster through 180^o on the dynamometer allowed tests to be performed with the thruster in the reverse direction. The load cell force measurement system was used for these dynamic tests because it provided an instantaneous measurement of the thrust. A calibration test had been carried out on this load cell and it was found to be reliable and accurate. A maximum error of 3.5% in the force measurement was recorded, and the cell tended to under read the applied force. The use of the dynamometer system, with its slow channel sampling rate, would have limited the tests to a practical advance speed of just 0.5m/s. Further studies for the thruster at angles of yaw have been carried out using the dynamometer apparatus, but connected to a more rapid data acquisition system. However, the results have not been presented as part of this work because, for the purposes of this investigation, the more important results were considered to be the straight-ahead thrust

results. It is only the straight-ahead performance that is required for studying a tip-driven impeller in a waterjet duct.

Because it was not possible to measure the torque of the propeller using the load cell apparatus, a theoretical torque was calculated, based on the propeller delivered power and speed, $Q=P/\omega$. The delivered power was measured using a Universal Power Analyser, with an accuracy of ±0.1W at the lower propeller speeds (typically < 850rpm) and ±1.0W at the higher propeller speeds. This change was due to the automatic scale change on the digital display once the power increased above 1kW. Tests showed that the propeller speed could be set to within ±10rpm, corresponding to $\omega=\pm 1.05 rads/s$, which along with the power error margins gives an accuracy for the torque absorbed as ±0.1Nm at powers below 1kW, or ±1.0Nm at higher powers.

4.3 PRESENTATION OF RESULTS

Results from the commissioning and bollard pull tests are presented as plots of absolute thrust or torque against either propeller speed or propeller delivered power, for different duct profiles and stator angles of attack. Figures A4.4 to A4.13 present the results for these tests. In addition, the efficiencies of both the PM motor and inverter were calculated, and the results plotted against power in Figure A4.6. The effect on thrust of altering the stator angle of attack was also investigated, and the results for a propeller speed of 1100rpm are given in Figure A4.12.

Results from the dynamic tests on the prototype TDP are presented as thrust and torque coefficients against advance coefficient, in a similar manner to conventional propeller performance charts, Figures A4.14 to A4.18. Results are given for the thruster running in both the forward and reverse direction, although fewer tests were carried out in the reverse direction due to time limitations.

4.4 DISCUSSION OF RESULTS

4.4.1 Commissioning Tests

The water depth in the University Lamont tank was 1.22m, and initially the thruster was suspended to a depth of 350mm. The depth of the thruster was dictated by the position of suitable mounting beams from which to hang the dynamometer. However, at this shallow depth the unit was prone to ventilation, i.e. drawing air into the propeller from the water surface. This phenomenon initiated at relatively low propeller speeds, and it was seen to reduce the measured thrust substantially. Ventilation was prevented, to a certain extent, by floating a thin sheet of plywood on the water surface just forward of the thruster, however, at higher propeller speeds ventilation initiated again over a period of time. Due to these problems, the supporting framework was subsequently re-located and the thruster mounted at a greater depth of 755mm. This small increase in depth overcame the majority of ventilation problems, however, some examples of ventilation were occasionally witnessed, thought to have been triggered by debris in the water.

The resultant trends from the dynamometer agreed well with theoretical relationships for speed and thrust, and the response between force and moment was linear. The results were also repeatable to within 5%, which considering the unsteady flows in the tank, and the fact that the motor speed differed slightly between tests, is thought to be reasonable. The motor speed was set using a variable voltage supply, and when attempting to conduct repeat tests it proved difficult to set exact propeller rpm values. Generally the propeller speed never varied more than ±10rpm between repeat tests. It was evident, however, that the absolute values of thrust were over-predicted by the dynamometer calibration. Because of these high values, the thrust results were scaled according to subsequent results obtained from the Seaeye load cell. Although not ideal, this solution offered the best scaling method in the time available. Because the scaling factor was reasonably constant across the range of propeller speeds, Figure A4.2, and the results were repeatable to within 5%, the scaled results were thought to be acceptable.

The University tank was relatively small and concerns were expressed towards the problem of re-circulating flow, caused by the thruster, providing an effective advance speed and hence reduction in measured thrust. This phenomenon was previously

highlighted by Flower et al [1.8], and also by TUUV manufacturers [2.2]. Figure A4.3 illustrates a general decrease in measured thrust as time increases for a range of propeller speeds. The time in this case was measured from the instant when the desired rpm had been reached. Although the overall trend shows a decrease in thrusts, the measurements tend to fluctuate. This is thought to be due to the unsteady flow, which was set up in the tank once the thruster had been turned on. The thrust decrease was thought to be due to the initiation of flow re-circulation, providing an effective advance speed. Trend-lines have been drawn through the data series in Figure A4.3, and the higher propeller speeds exhibit greater thrust decreases, which is likely to be caused by greater flow re-circulation speeds. In order to minimise the effect of this in the force measurements, the propeller speed was ramped up quickly and thrust measurements recorded immediately after the required speed had been reached. The data acquisition system averaged a set of force measurements over a period of fifteen seconds. The time dependent studies (Figure A4.3) illustrated this to be a suitable period, as only a marginal drop in thrust was seen within this initial period. Some bollard pull conditions were also repeated in the larger Institute tank.

4.4.2 Bollard Pull Tests

Thrust versus Power

Figure A4.4 plots the forward thrust achieved using different duct shapes for a given inverter input power. The graph indicates that at the bollard pull condition, there is little variation in thrust between duct shapes, for a given inverter power. The thrust tends to be proportional to power$^{0.72}$.

The thrust achieved for a given propeller delivered power is plotted for one set of ducts on Figure A4.5. Forward thrust is proportional to delivered $P_D^{0.69}$, which is slightly greater than the theoretical $P_D^{0.66}$. This difference is likely to be a result of the increased power loss in the gap between the rotor and the stator. In addition, the effect of different Reynolds numbers between similar tests, altering the flow regime through the propeller and duct, will mean an exact theoretical relationship cannot be achieved. It is evident that slightly more power was required in the reverse direction to obtain a particular thrust. This

suggests either the flow conditions were different for both directions (see below), or an asymmetry existed in the thruster construction.

Efficiencies

The motor and inverter efficiencies are shown on Figure A4.6. The inverter possesses a relatively constant high efficiency across the range of input powers. Although there is some scatter with the data points, all the values lie above 95% efficiency, and the average value is 97%. The motor also appears to be very efficient, values of 90% are achieved for input powers over 500W. However, the motor efficiency drops substantially at powers lower than 100W.

Torque

Torque characteristics (based on propeller power and speed) for the thruster with duct s2037, are presented in Figure A4.7. The trend illustrated shows torque approximately proportional to n^2, as expected. The maximum calculated torque was 13.8Nm at just over 1000rpm. Predictions indicate a torque of approximately 19Nm at a propeller speed of 1200rpm. Figure A4.7 also illustrates that torque was 5-7% greater when the thruster was running in the forward direction. A possible explanation for this is due to re-circulating flow effects in the tank. These are discussed in more detail below.

Different Duct Shapes

To investigate duct shape influence several duct combinations were tested in both the forward and reverse directions. Symmetrical (fwd/aft) profiles and one asymmetrical duct section were tested. The inner surface of each duct, at the location of the propeller, remained constant as an axially cylindrical form. The first duct was the symmetrical duct s2037, derived from the original Marin Duct 37, having a length of 0.20m. The second duct was a stretched version of the first, s2637, having a slightly smaller nose radius and an overall length of 0.26m. The third duct, a2637, was also 0.26m long but had an asymmetrical section. The leading edge was that from the s2637 duct, but the trailing edge had a relatively flat inner surface from the centreline to a low nose radius. In all cases, the duct thickness was 38.5mm.

The resultant forward and reverse thrust measurements are plotted in Figures A4.8 and A4.9. The variation of thrust between the ducts was small but measurable, both symmetrical ducts remained very similar, but the asymmetrical section produced slightly more thrust, at the higher propeller speeds, in the forward direction, and slightly lower thrust in the reverse direction.

The measured thrust is seen to be proportional to n^2. However, it is also evident that a greater thrust was obtained in the forward direction than in the reverse direction. Such a result is to be expected for the asymmetrical duct, which showed a maximum decrease of 20%. However, forward and reverse thrust differences were also evident for the symmetrical ducts. At 1000rpm, the difference was of the order of 10% for duct s2037. There were several possible explanations for this; Firstly, a voltage offset might have existed in the dynamometer system due to electrical interference from other pieces of equipment. This offset would be of the same magnitude and sign, regardless of thruster direction, hence producing a difference in the measured forces. This was tested by running the thruster out of water and detached from the dynamometers. No dynamometer voltage offset was recorded and this theory was shown not to be the case. Secondly, there might have been some misalignment of the thruster in the fwd/aft direction. This theory was tested by turning the unit through small angles of yaw to find an angle where $T_{fwd} \approx T_{aft}$. However, no significant angle offsets were observed using this method.

The third possible reason for differences in the forward and reverse thrust values was due to flow re-circulation. For ease of assembly and for suitable location of electrical equipment, the thruster was mounted closer to one end of the tank than the other. When thrusting forward the downstream tank length was 20m, in reverse it was 5m. Once running, flow re-circulation could be seen and a clearly defined 're-circulation length' was evident on the water surface. At 1000rpm, the re-circulation length was approximately 7m, which was larger than the available tank length when the thruster was running in reverse, Figure 4.10. It was therefore assumed that the shorter downstream tank length resulted in a quicker re-circulation response, reducing the available thrust. To clarify this, the unit was turned through 180° on the dynamometers and thrust measurements taken again. The results showed an increase of 4.5-5.0% thrust in the reverse direction and a decrease of 3.0-4.0% in the forward direction at 1000rpm. Therefore a large percentage of

the directional thrust differences was attributed to the phenomenon of re-circulating flow within the confines of the tank. These problems were also highlighted by Flower et al [1.8]. They experienced far greater losses (up to 60%) with a similar propeller in a small test tank, however, the dimensions of their tank are unknown so a direct comparison cannot be made. Further reasons for the differences could be due to slight asymmetries in the construction of the thruster, although this was difficult to quantify.

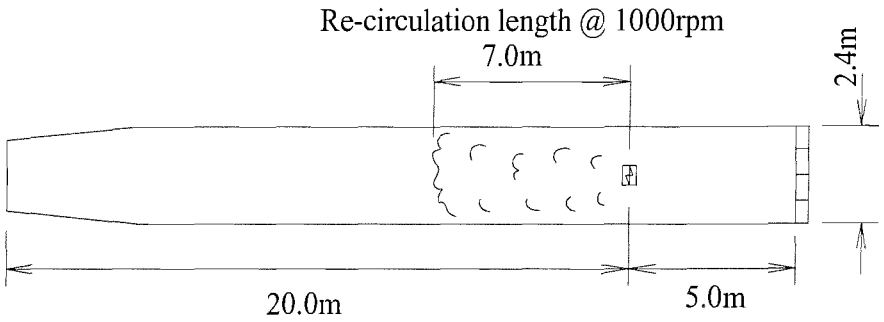

Figure 4.10 - Position of thruster in the University Lamont tank.

There was also evidence of varying lateral forces when running in reverse. Similarly, this was attributed to the greater re-circulation and tank velocities, which induced significant forces on the power cables leading into the side of the thruster.

Stator Angles

The prototype was designed and built to allow small changes in the hydrodynamic stator angles to be investigated. Results from the panel code (Chapter 5) indicated that a stator angle of 10^{o} increased the thrust by 2-3%, and -10^{o} reduced the thrust by a similar amount, however, these results were obtained by modelling the thruster at an advance speed. Figure A4.11 indicates the sign convention used for the stator angles of attack. In this instance, the angle of the aft stators was always the same as the forward stators.

Similar changes in stator angles were investigated in the Lamont tank. Figure A4.12 plots the relative forward and reverse thrust changes due to different stator angles. The propeller speed was 1100rpm. In both cases, unlike the CFD predictions, the optimum thrust was achieved with the stators at 0^{o}. A stator angle of 10^{o} tended to decrease forward thrust by approximately 6% and decrease reverse thrust by approximately 5%. As

expected, a stator angle of 20° decreased both forward and reverse thrust even further. The lowest thrusts were obtained when the stator angles were negative (-10° or -20°) which agrees with panel code predictions (Chapter 5). However, it remains to be seen whether the stators at a positive angle of attack are of benefit or not when the thruster is at an advance speed.

Effect of the Support Cylinder

The thruster was supported using a cylinder of OD=100mm from the dynamometer system. During the tests it had been noted that the re-circulation velocity could impose a drag on the cylinder in the particular direction which would cause an augment in measured thrust. In order to quantify the effect of this cylinder, a plastic cylinder of similar dimensions was bolted around the Seaeye load cell support arm.

Having carried out the tests with the cylinder in place, an increase in thrust was seen to be the case for both forward and reverse directions. An increase of approximately 3%, up to a maximum of 10N at the higher propeller speeds, was measured. However, it must be noted that the re-circulation appeared to be unsteady, and as such the drag of the cylinder would vary with time.

Assuming a drag coefficient of 1.1 for the cylinder [4.1], it was calculated that the flow speed necessary to cause 10N of drag was in the order of 0.5m/s, which illustrates a large re-circulation velocity. In addition, if the effective advance speed of the thruster was 0.5m/s, at 1000rpm this would produce an advance coefficient of $J=0.12$, which in turn would decrease the thrust at bollard pull by 15%.

4.4.3 Advance Speed Tests

Tests on the thruster at different advance speeds were carried out in the towing tank at Southampton Institute. This facility enabled the TDP and associated framework to be supported off the back of the towing carriage, and the necessary acquisition systems to be secured on the carriage. The thruster was towed along the tank at various speeds, and the 60m length of the tank allowed enough time for measurements to be made.

Some repeat bollard pull tests were carried out in this tank, prior to the advance speed tests, in order to test the repeatability of the thrust measurements. Figure A4.13 illustrates the comparison between bollard pull results for duct s2037 in the Lamont tank and in the Institute tank. There was a very good agreement between the two test results for both the forward and reverse thrusts, however, the reverse thrusts measured in the Institute tank were marginally greater than those in the Lamont tank. It was thought that the larger Institute tank dimensions did not confine the re-circulation as much as the smaller Lamont tank (Section 4.4.2). These results provided confidence to continue with the advance speed tests using the same measurement apparatus.

To take account of the wave and viscous drag on the support cylinder, force measurements were taken for the cylinder alone at the various advance speeds, with no thruster attached, the drag results are plotted in Figure A4.14. The subsequent thrust measurements for the TDP were suitably modified using the resultant cylinder drag forces, and the results presented have taken this into account. It was assumed that any interaction effects between the cylinder and the thruster were negligible.

Figure A4.15 plots the thrust coefficients, K_T, against advance coefficient, J, for different duct combinations on the prototype thruster. The coefficients are defined in the usual manner as;

$$J = \frac{v}{nD} \quad , \quad K_T = \frac{T}{\rho n^2 D^4} \tag{4.14}$$

Where v is the advance speed (m/s), n the propeller revolutions per second, D the propeller diameter (m), T the thrust (N) and ρ the water density (kg/m^3). Also shown are the K_T characteristics for the standard Kaplan K4-70 propeller in Marin duct 37. For all duct shapes, the forward thrust coefficient at zero advance speed was approximately K_T=*0.4*, giving 625N at 1200rpm. K_T decreases as J increases and the drag of the thruster was seen to outweigh the thrust at approximately J=*0.55*, where the values cross K_T=*0.0*. This J value is particularly low compared to the standard ducted K4-70 propeller, which crosses the axis at J=*0.8*. However, the initial thrust of the prototype is lower than the standard ducted K4-70, and its drag is likely to be greater due to the thicker duct, needed

to house the motor, and the presence of stators and bearings. The effective pitch of the propeller due to the presence of the duct may also have a detrimental contribution. The effect of the extra drag is expected to decrease with a larger ETDP unit as the thickness of the motor, and hence the duct, would not alter significantly.

Furthermore, it can be assumed that changes in the local flow velocity, caused by the presence of the duct, alter the local flow pitch angle and hence the effective pitch at which the propeller is operating at. This in turn could reduce the performance of the propeller. Data for the standard Kaplan K4-70 propeller, in Marin duct 37 [2.1], suggests 20% of thrust is lost when the propeller pitch ratio is reduced from 1.0 to approximately 0.9. If it is assumed that the prototype propeller responds in a similar manner to the standard K4-70, this highlights another potential source of thrust reduction, which requires further investigation.

Results for the thruster running in reverse are shown in Figure A4.16. A very similar trend is seen to that in Figure A4.15, however, the values for each duct are all slightly lower than the forward K_T results, an average decrease of 7% was seen. The asymmetrical duct exhibits the greatest difference between forward and reverse thrust of 12%, which was to be expected, and these results are consistent with those seen from the bollard pull tests in the Lamont tank. In the reverse direction, the maximum K_T value was approximately *0.38*, giving 412N at 1000rpm, and 594N at 1200rpm.

The drop in thrust from the standard Kaplan K4-70 propeller in Marin duct 37 was likely to be due to the propeller having symmetrical blade sections. Results from the panel code indicated a decrease of approximately 20% in K_T when compared to the standard Kaplan unit. 20% would decrease K_T=*0.55* to K_T=*0.44*. Further losses could also be attributed to the symmetrical duct, gap friction, and drag on the stators and bearing casings.

K_T Difference Between Ducts

As with the bollard pull tests, the influence of using different duct shapes was small but measurable. The results from the advance speed tests can be seen on Figures A4.15 and A4.16. The thrust produced by the symmetrical s2037 and s2637 ducts were very similar, however, both f2637 and asymmetrical ducts produced higher values of K_T. F2637

produced the greatest thrust and this result agrees with panel code predictions (Chapter 5). The panel code suggested that duct f2637 produced the lowest J value at the propeller, which results in a higher thrust.

K_Q Difference Between Ducts

Because torque was not measured during the tank tests, a theoretical torque was assumed based on calculated propeller power and the motor, hence propeller, speed; $Q=P/\omega$. This yielded the torque coefficient, K_Q, results plotted in Figure A4.17.

$$K_Q = \frac{Q}{\rho n^2 D^5} \tag{4.15}$$

where Q = torque (Nm).

Also plotted on Figure A4.17 are the torque characteristics for the standard K4-70 propeller in Marin duct 37. Comparing the test results to the standard data, it is evident that the trend-line was followed closely, exhibiting an increasing drop in K_Q with advance coefficient. However, whereas the standard $K_Q=0.044$ at $J=0$ (for $P/D=1.0$), the experimental data produced values of K_Q from 0.046 to 0.052, depending on duct profile, and the values remain consistently higher across the range of advance coefficients. Unlike the K_T results, these are larger than the standard results.

Figure A4.18 plots similar results for the thruster running in reverse. In a similar manner to the K_T results, the torque coefficients are lower in the reverse direction. The maximum K_Q is in the range between 0.044 and 0.048, equating to a torque of 19Nm at 1200rpm. Another observation was that duct f2637 tended to produce higher K_Q results than the symmetrical profiles. This is possibly another influence of the slower flow into the propeller.

4.5 SUMMARY

The prototype electromagnetic tip-driven propeller unit was successfully tested and the concept of driving the propeller via the blade tips using an efficient motor has been proven to work. Comprehensive bollard and dynamic tests were carried out on the prototype thruster to evaluate its performance, and a detailed database of results has been obtained. These tests included a full range of advance speeds, propeller revolutions, duct geometries and limited variation of stator angles. The thruster produced about 600N of thrust for a propeller power input of 2kW. Within the power range of 0.5-2.2kW the motor demonstrated an efficiency of 90%.

At bollard conditions, the thrust output was about 20% lower than the standard Kaplan K4-70 propeller in Marin duct 37. It was possible to identify three likely contributions to this loss of performance:

a) As expected the use of a symmetrical propeller will reduce performance. CFD results have indicated up to 20% reduction in output thrust when symmetrical propeller section shapes are used, compared to the original Kaplan asymmetric profile (see next Chapter).
b) The design pitch does not account for the actual ahead speed within the duct, which is controlled by the duct profile. This varies and was shown to give rise to changes in performance (thrust and torque) of the order of 5%.
c) There was also an amount of friction loss present in the gap between the rotor and stator.

The thrust coefficient, K_T, reduced more rapidly compared to the standard Kaplan ducted propeller performance, as the advance speed increased. This was due to the essential increase in thickness of the duct to enclose the electric motor and the use of a symmetrical duct. This effect is expected to decrease with a larger ETDP unit as the thickness of the motor, and hence the duct, would not alter significantly.

Different duct profiles have been tested. The differences in performance were measurable and in the range of up to 5%. Best performance was obtained with the duct that minimised the change in advance speed. The effect of different stator angles was also investigated.

The results indicated that for the current design, zero angles produced best thrust output at bollard pull conditions. All other angles reduced the thrust, which was believed to be due to increased drag on the stators.

The data obtained from the experimental tests on the TDP can be used to validate a CFD model of the thruster. Once validated, a computational model can be used as a tool for gaining an understanding of the complex flow regimes involved, for investigating the effect of further design modifications, and as a means of optimising characteristics such as duct and propeller geometries. Work on a CFD model of the prototype is presented in Chapter 5.

5. COMPUTATIONAL ANALYSIS OF A TIP-DRIVEN DUCTED PROPELLER

The experimental TDP has provided good data for one propeller-motor combination in a series of duct profiles. However, it would not make economic sense to make physical models of all the propellers and duct sections, which may need investigation. It is more advantageous to create a computational model of the unit, which will provide a means of being able to predict, to a reasonable degree of accuracy, the performance expected for various propeller and duct geometry combinations. Computational modelling offers a quick turn-around between tests for a great number of different duct shapes and thickness. It also offers a fairly comprehensive solution to the flow in relatively short time periods.

5.1 AIMS

The main aim of this chapter is to provide a theoretical prediction of the flow behaviour and performance expected for the representative tip-driven propeller. Further aims include the development of a computational model, which will provide a means of predicting the likely performance of similar units, and to investigate the possible benefits of TDPs for use in applications such as waterjets. To this end it was decided to use the lifting surface panel code, Palisupan [2.11]. Palisupan offers a far simpler method of defining the duct and propeller geometries than CFX4.1. It possesses the ability to model a rotating body relatively easily, and because it is a potential, non-viscous solver, it should reach a solution in a fraction of the time that CFX4.1 could achieve. However, account needs to be taken of the limitations of the panel code predictions.

5.2 TESTS

Before modelling the prototype tip-driven propeller, the panel code was used to model a standard ducted propeller unit - the Kaplan K4-70 propeller in a Marin 37 duct [2.1]. This was done in order to obtain a comparison between the computational predictions and reliable experimental data to assess the capabilities of the code. Having found good agreement between the two sets of data, the code was further used to predict the

performance of the prototype TDP. These predictions are subsequently validated using results obtained from towing tank tests on the unit in Chapter 4.

5.2.1 Kaplan K4-70 in Marin Duct 37

Oosterveld [2.1] published a comprehensive set of data for several ducted propeller combinations, one of which was the Kaplan K4-70 propeller in the Marin 37 duct for which a design chart was presented. This chart provided an excellent source of initial validation data for the panel code. The standard four bladed propeller was modelled with a hub diameter of *0.2R* and helical wake sheets were modelled which flowed from the trailing edge of each blade. The duct and blade section shapes were defined using offset data presented by Oosterveld [2.1]. The means by which the geometries were defined are described in Chapter 2, with further detail provided in Appendix E. Figure 5.1 illustrates the panel definition of the Kaplan K4-70 propeller.

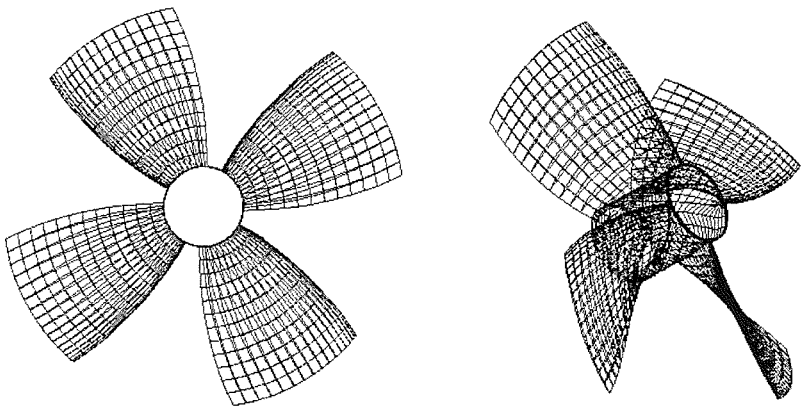

Figure 5.1 – Panel definition of the Kaplan K4-70 propeller.

Wake Sheet

Three-dimensional lifting problems require a wake to be modelled, since the bounded vorticity needs to be continued beyond the wing [1.2]. The correct modelling of the freely convected propeller wake is essential to the accurate prediction of propeller performance. However, the evolution of the wake shape is fraught with numerical difficulties especially close to the propeller tip. The Kutta condition states that the flow leaves a sharp trailing edge smoothly and the velocity there is finite [1.2]. For most aerofoils, this suggests that the flow leaves the foil along the bisector line of the trailing edge. The adaptation of a propeller wake to follow the stream surface, which produces zero pressure loadings across

the wake, is very difficult [5.1]. Previous experience [5.1] has indicated that a reasonable approximation to the wake can be achieved by using a fixed wake.

Vortex elements shed by a rotating propeller are convected by the resultant relative velocity composed of the free-stream velocity, U, an angular velocity component, $r\omega$, plus the axial, radial and tangential components induced at the shed element by all members of the vortex array [5.2]. Therefore the trajectory of the shed vortices is not a true helix as the induced velocities vary with distance from the propeller. However, further downstream from the propeller, say two or three diameters, as the axial inductions reach an asymptotic value and the radial component vanishes, a true helical pattern is achieved [5.2]. The pitch of these helices will be a function of the hydrodynamic pitch angle [5.2].

The usual approach is to approximate the wake sheet by a pure helical surface with a prescribed pitch obtained from either the undisturbed inflow pitch angle, or the hydrodynamic pitch angle, calculated from lifting line theory [5.3]. More elaborate methods have also been developed [5.3], which take into consideration the roll-up of the vortex sheet and contraction of the slipstream. However, some parameters defining these wakes had to be specified by the user, based on experimental observations. Relatively simple methods have been demonstrated to be reasonably successful [5.3,5.4]. These methods used an initial wake represented by a helical surface, whose pitch was the geometric pitch of the propeller blade, followed by a fixed pitch helical wake further downstream.

The length of the fixed wake sheet was defined as a multiple of the propeller diameter. Figure A5.2 illustrates the effects of wake length on the resultant propeller thrusts. The propeller modelled was a K4-70 series, with diameter 0.25m, and pitch ratio $P/D=1.0$, and the number of panels along the wake remained constant at 100. The predicted thrusts initially decreased as wake length was increased, but soon settled to a reasonably constant value at wake lengths of $2.5D$ or more. A similar trend was seen with the torque predictions. Therefore, subsequent propeller tests used wake lengths of three diameters. Similar tests were carried out by Maitre [5.4], who found a wake length of 8 radii to be acceptable.

Kerwin and Lee [5.3] carried out a sensitivity study on the effect of slipstream contraction on thrust coefficient, K_T, for three assumed values of wake pitch. Findings suggested that contraction of the slipstream increased predicted thrust. However, the sensitivity to contraction was less than that of wake pitch, which was found to be the most critical parameter. As a matter of note, having carried out water tunnel measurements, Kerwin [5.3] stated that the slipstream contraction ratio, r_w/R, was very close to *0.83* for a wide variety of propeller types over a reasonable range of advance coefficients in the neighbourhood of their design point. The exceptions were highly skewed propellers, whose slipstreams tended to contract less, $r_w/R=0.92$ for a propeller with a 72° skew. For reasons of simplicity, no downstream radial contraction was applied to the wake, although this will limit the accuracy at lower advance ratios.

In addition to its length, the number of panels through the wake was studied using the same propeller model and a constant wake length of *3.0D*. The wake was modelled using 25 to 300 panels. The effect on propeller thrust and torque exhibited a similar trend to varying the wake length, although the changes in thrust were less pronounced. Table 5.1 lists the results.

Table 5.1: Effect of number of wake panels on predicted propeller thrust and torque.

No.of panels	25	50	75	100	150	200	250	300
Thrust (N)	423.9	420.9	420.4	420.0	419.8	419.8	419.8	419.7
Torque (Nm)	14.21	14.12	14.10	14.09	14.09	14.09	14.09	14.09

The predicted thrust, in Table 5.1, begins to stabilise for wakes with 100 panels or more. For this reason, it was assumed that 150 wake panels provided a suitable model.

The default average wake pitch used by the geometry definition program (Section 2.3.2) was equal to the average blade section pitch, however, the user had the option of changing this. The pitch of the helical wake sheet is defined in the same manner as the blade section pitch. It has been suggested [5.1] that the specification of the wake pitch can be based on blade-element momentum (BEM) results for axial and circumferential velocity at the propeller plane. The initial wake shape is defined in the direction of the section pitch, followed by a uniform pitch for all sections, which is the average of all the pitches estimated using BEM theory. Varying this value of average wake pitch alters the total

thrust of the propeller. However, rather than produce another model of the propeller an empirical approach was used to determine a suitable average wake pitch.

In order to study the effect of varying the average wake, the Kaplan K4-70 propeller in Marin duct 37 was modelled using a range of wake pitch values, both above and below the default value, at various advance coefficients. The two areas of interest were the effect the average wake pitch had on solution convergence and resultant thrust values. However, before studying the wake pitch, firstly consider the convergence parameters.

An indication of convergence was given by the maximum trailing edge pressure differences, dC_Pmax, which was output by the panel code after each iteration. The value of dC_Pmax for convergence was stated by the user in the command file, it is usually set at *0.01* [2.11]. Tests indicated that reducing the value of dC_Pmax for convergence from 0.5 to 0.01, for a panel model of the Kaplan propeller at $J=0.5$, resulted in a thrust increase of 1N. At $J=0.255$, the maximum change in predicted thrust between convergence parameters $dC_Pmax=0.5$ and $dC_Pmax=0.005$ was 0.25N. Because the effects on the overall thrust were minimal, the value of dC_Pmax set as the convergence parameter for the propeller was 0.5. For convergence to occur within a reasonable time scale, an acceptable limit for the initial dC_Pmax was set as 250.

Now returning to the effect of wake pitch. Figure A5.3 plots the initial dC_Pmax values, obtained after the first iteration for the ducted K4-70 propeller at different advance coefficients, J, using different average wake pitches. The default average blade section pitch in this case was *0.24m*. It is interesting to see that a large discontinuity occurs in the dC_Pmax values. For average wake pitches below *0.20m* the initial pressure differences are very large, the minimum being approximately *1000*, at the highest advance coefficient. Although these solutions did begin to converge, the time necessary to reach the convergence limit of $dC_Pmax=0.01$ would have been far too long to be practical.

With the exception of this discontinuity, the effect of changing the average wake pitch made little difference to the initial dC_Pmax values, and hence time to convergence. However, a larger advance coefficient reduced the dC_Pmax values and resulted in quicker solution times across the range of wake pitches.

Figures A5.4 to A5.7 illustrate the effect of wake pitch on the resultant thrusts and torque coefficients, predicted by the panel code. The propeller thrust (Figure A5.4) tends to increase with increasing wake pitch, however, the rate of increase falls as the advance coefficient, J, rises. At $J=0.8$ the thrust remains fairly constant along the range of wake pitches.

Figure A5.5 shows the thrust developed by the duct, made non-dimensional in the same manner as the propeller thrust, i.e. with respect to the propeller diameter and speed. Although the duct thrust is not directly affected by the propeller wake, some effects are noticed due to the interaction velocity field. In contrast to the propeller thrust, the duct thrust tends to decrease as wake pitch rises. But again, the effects diminish with higher advance coefficients. The effect on the total thrust predicted for the ducted propeller is shown in Figure A5.6. There remains a slight increase in total thrust as wake pitch increases, but the rates of increase are lower than the propeller alone due to the addition of the duct thrusts, which exhibited negative gradients.

The effect of average wake pitch on the predicted torque (Figure A5.7) is not so clear-cut as the thrust results. Yet again, the results at the highest advance coefficient, $J=0.8$, show very little response to the different pitch values. For an increasing wake pitch, the predicted torque values at $J=0.6$ and $J=0.4$ increase slightly, whereas at $J=0.2$ and $J=0.1$ the torque values decrease, although there is a slight rise between wake pitches of $0.22m$ and $0.24m$.

It was concluded that when modelling the ducted propeller at advance coefficients of $J=0.6$ or above, it is safe to assume that whichever average wake pitch is used, the results will remain fairly constant. For this reason, the default wake pitch was used at the higher advance coefficients. For the lower advance coefficients, the wake pitch used was that which resulted in the predicted thrust being as near to the published data [2.1] as possible. The wake pitches used are given in Table 5.2, and Figure 5.8 illustrates a typical wake sheet defined using the panel code, from one propeller blade, which would be located on the right hand side of the diagram.

Table 5.2: Average wake pitch used at each advance coefficient for K4-70.

Adv.Coeff. J	0.1	0.2	0.3	0.4	0.5	0.6	0.7	0.8
Wake pitch (m)	0.20	0.20	0.20	0.20	0.22	0.24	0.24	0.24

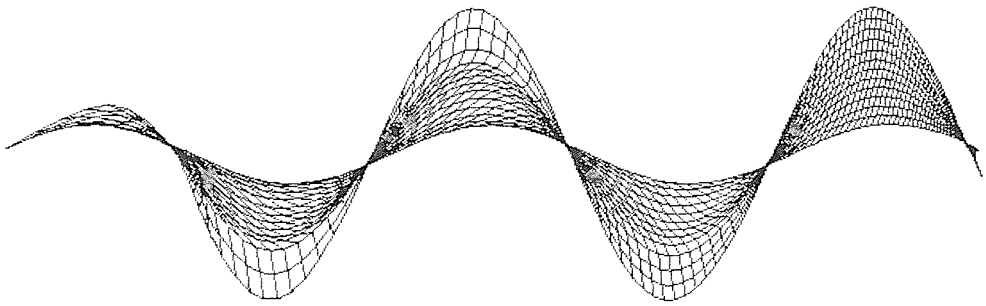

Figure 5.8 - Typical panel code defined wake sheet from one propeller blade.

Grid Dependency

A CFD model is only ever as good as the numerical mesh or grid, which is used to define the geometry. A grid that is too coarse may produce inaccurate results, and a finer grid will provide greater accuracy. However, if the number of cells or panels is too high, the program may struggle with memory requirements, and the time required for a solution could be greatly increased. A compromise often has to be made, and the grid is chosen so that relatively good results can be achieved in reasonable time scales.

A straightforward method to assess the grid dependency is firstly to run the model using an assumed grid size, which is believed to define the geometry reasonably well, to obtain an initial set of results. Secondly, to run the same model using finer grids, with more panels. Once the difference between results from subsequent tests begins to minimise, it can be assumed that the solution is relatively independent of the grid size. The grids used to define the propeller and the duct were both examined in this manner.

There are two directions in which the grid size can be altered. In the case of the propeller blade, the number of panels can be altered in the chordwise (N_c) and spanwise (N_s) directions. For an aerofoil section, the more important panel distribution is in the chordwise direction, over which the pressure distribution, and hence lift are calculated. A three-stage process is recommended to optimise these combinations [2.11]:

1. For a constant value of N_c, study the effect of altering N_s. Plot the force results against the total number of panels used.
2. For a constant value of N_s, study the effect of changing N_c. Plot the force results against the total number of panels used.
3. From the two variation studies it should be possible to identify an optimum ratio of N_c to N_s. Maintaining this ratio, the total number of panels should be varied.

Figure A5.9 illustrates the effect of altering N_c and N_s on the predicted propeller axial thrust coefficient, K_T. The value of N_c indicates the number of panels used around both the front and back faces of the section, the panels were clustered towards the leading edge. For a constant panel number in the chordwise direction, $N_c=74$, it was seen that an increase in N_s tended to decrease the value of K_T. However, the change in K_T was small, 5% between $N_s=18$ and $N_s=28$. Because this change was small, and because a greater number of panels resulted in greater times to convergence, it was decided to use $N_s=18$ for the blade model.

For a constant $N_s=18$, an increase of N_c resulted in an increase of K_T. The variation in K_T was greater than when N_s was altered, a trend expected when changing the more dominant chordwise distribution. However, the trend line begins to level off towards the higher values, $N_c>70$. In this case, grids with N_c of 60 or above tended to take longer times to converge, and so the final value of N_c, used to define the propeller blade was 54. This resulted in K_T values only 2% lower than when $N_c=74$, which was regarded to be a suitable compromise.

A ratio of $N_c/N_s=3.0$ was therefore chosen to be an adequate representation for the blade. Figure A5.10 plots K_T against the total number of panels, for various combinations of N_c and N_s, which gave a ratio of approximately 3.0. The K_T values remain very similar within the range of panels, the slight variations are in accordance with slight changes in N_c/N_s. Because the total number of panels had a negligible effect on the result, it was decided to model the blade using $N_c=54$ and $N_s=18$. It was thought that this combination defined the blade in enough detail and provided a solution in a reasonable time scale, i.e. in a matter of tens of minutes, rather than hours.

Similar studies were carried out for the duct in a free-stream flow. It was seen that for a constant N_s of 30, defining the circumference of the duct, the drag results began to converge after N_c=*41*. Increasing N_s values resulted in an increase of drag forces, but by a slower rate of change than when varying N_c. The value of N_s was chosen to provide a solution in a reasonable amount of time. The resultant N_c and N_s values were *50* and *45* respectively.

The panel code was used to model the Marin duct 37 shrouding the four bladed Kaplan propeller. The geometry was run at advance speeds up to 2.5m/s, the propeller diameter was 246mm and the internal diameter of the duct was 250mm. The resultant gap between the propeller blade tip and internal surface of the duct ensured that no blade panel interacted with a duct panel, which was a possibility as the cylindrical duct surface was defined using a series of flat surfaces, Figure 5.11.

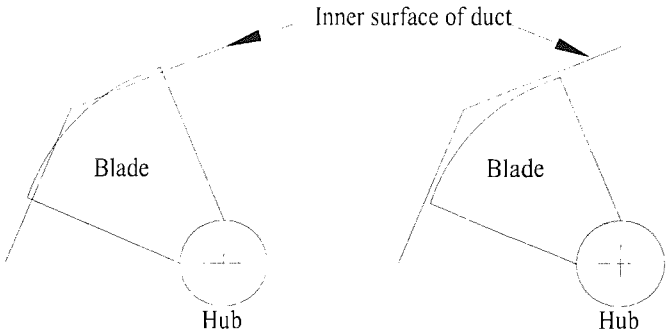

Figure 5.11 - Exaggerated view of gap between panel models of propeller blade and duct.
a) Incorrect propeller radius, with panel interference at the tip.
b) Corrected propeller radius, no panel interference.

Only the definitions of one propeller blade and the portion of the hub between two adjacent blades were required to model the propeller. Images of these geometries were declared in the panel code, which solved the flow for the correct number of blades and the entire hub. The propeller blade was modelled using 972 panels, the portion of the hub was defined using 170 panels, and the duct using 2250 panels. This was found to give a reasonable level of convergence for an acceptable amount of computational time.

The boundary layer prediction program was not run in conjunction with the propeller geometry because, due to the presence of cross-flows between each blade section, the boundary layer growth would have been modelled incorrectly. The program could have been incorporated if a streamline tracing method was used to follow the boundary layer growth. However, this process was not included in the program due to time limitations, and doing so would have greatly increased the computational time to convergence. A test was carried out using the boundary layer code with a panel model of the K4-70 propeller, and a 5% decrease in propeller thrust was found. However, the boundary layer prediction cannot be assumed to be accurate for the propeller blade, and for this reason it was not used with subsequent propeller geometries, although it has been used with the duct geometries.

Results

Because a rotating propeller exists within the duct, the forces on individual duct panels will vary with time, due to the passage of the propeller blade. However, as the geometry and its associated flow are axisymmetrical, and only the straight-ahead cases (0^o yaw) were studied, these variations should cancel out. It was therefore assumed that obtaining a solution for an instant of time, rather than an average over a period of time should provide a valid result. However, this assumption cannot be justified for the pressure results around individual duct sections. For this reason, the pressure distributions have been consistently taken around the duct section at TDC, where a blade exists if the propeller is present in the model. Both total forces and pressure coefficients over the surfaces were obtained from the panel code and the results have been analysed accordingly.

Figure A5.12 illustrates the pressure coefficient, *Cp*, distribution along the inner and outer surfaces of the standard Marin duct 37 alone in a free-stream. The duct leading edge is located at *X=0.1* The pressure coefficient is a non-dimensional representation of the local pressures with respect to the free-stream dynamic pressure. Essentially,

$$Cp = \frac{P_0 - P}{\frac{1}{2}\rho U_o^2} \tag{5.1}$$

Where *Cp*=1.0 indicates local stagnation,

Cp=0.0 indicates the local velocity being equal to the free-stream velocity,

Cp<0.0 indicates the local velocity being greater than the free-stream velocity.

It is therefore possible to obtain an understanding of the flow's behaviour from the Cp distributions over the duct surfaces.

The pressure coefficients along the inner surface of the Marin duct 37 in free-stream (Figure A5.12) exhibit a decrease in pressures from the leading edge stagnation to Cp=*-1.5* at X=*0.04* as the flow accelerates into the duct. This is followed by an increase in pressures towards the trailing edge (X=*-0.1*), present because it is potential-flow. It is clear from this plot how symmetrical the inner surface of the standard duct is. However, the leading edge gradients are slightly lower suggesting a slightly larger radius. The outer surface exhibits a quicker drop in pressure near the leading edge, around a sharper radius than that along the inner surface. This is followed by a deceleration to near free-stream velocity along the back of the section, before reaching the trailing edge at X=*-0.1*.

Figure A5.13 illustrates a similar Cp distribution along the inner and outer surfaces for the standard Marin duct 37 with the presence of the standard Kaplan K4-70 propeller. The propeller plane is located at X=*0.0*. The pressures on the inner duct surface decrease further in the presence of the propeller, a Cp as low as *-3.0* is present. However, the outer surface exhibits less pressure drop around the nose radius, followed by a similar deceleration to the back of the section. Lower pressures are clearly seen toward the leading edge half of the section, thus indicating a component of forward thrust.

In addition to pressure coefficients, velocity fields can also be obtained from Palisupan by supplying the code with an input file, which lists the cartesian co-ordinates of the points at which the data is required. In this instance, the file listed points defining several radii through the propeller plane. Such data would be of use during the optimisation of blade section shape, when it is necessary to know the typical flow field the propeller or impeller is operating in. The pressure coefficient plots only provide an indication of the relative pressures and hence velocities over the surface of the duct walls. Figure A5.14 plots the radially averaged velocity profiles, across the propeller plane, for the duct in free-stream conditions. The axial velocity is shown as a ratio of free-stream velocity, Uo. The centre of the duct is located at r/R=*0.0*, and the inner surface of the duct wall at r/R=*1.0*. It can

be seen how much the flow near the Marin 37 duct wall has been accelerated, values of *u/Uo* are as high as *1.36*. This acceleration was also evident on the *Cp* plot along the duct surface (Figure A5.12). The velocities tend to decrease with smaller radii, i.e. greater distance from the duct wall, however, the flow near the centre of the duct was still quicker than free-stream.

The velocity profile for the standard Marin 37 duct, with the presence of the Kaplan K4-70 propeller, is illustrated in Figure A5.15. The minimum radius plotted in this case is *0.04m* (*r/R=0.32*) as the propeller hub itself occupied a radius of *0.03m*. In a similar manner to the Marin duct 37 alone (Figure A5.14), there is an increase in relative velocities nearer to the duct wall, however, the presence of the propeller blades is evident by the increased values of *u/Uo*. All the velocities are greater than any obtained within the duct alone, thus indicating greater accelerations which were also evident in the plots of pressure coefficients (Figures A5.12 & A5.13).

Figures A5.16 and A5.17 plot thrust and torque coefficients, K_T and K_Q, for given advance coefficients, J, for both the computational and published data at propeller pitch ratios of *0.8*, *1.0* and *1.2*. J, K_T and K_Q are defined in the usual manner as;

$$J = \frac{v}{nD} \quad , \quad K_T = \frac{T}{\rho n^2 D^4} \quad , \quad K_Q = \frac{Q}{\rho n^2 D^5} \qquad (5.2)$$

For all pitch ratios the trends were predicted well by the panel code. For pitch ratios of 0.8 and 1.0, K_T values have been accurately predicted at advance coefficients of *0.4* or higher. For values of J lower than $J=0.4$, the panel code tends to overestimate K_T values, however, the relative values between the different pitch ratios remain similar to the experimental data. At the higher pitch ratio of 1.2, the CFD results have again over predicted the K_T values at the lower advance coefficients, but have also under estimated K_T at the higher J values. A constant wake pitch was used over the range of advance coefficients for each *P/D*, and it is thought that if a larger wake pitch was to be used for $P/D=1.2$, the predicted K_T values above $J=0.4$ would lie closer to the experimental data.

Figure A5.17 illustrates the torque results for the same ducted propeller model. The trends were again predicted well, i.e. K_Q decreasing at a greater rate as J was increased, however, the absolute values are offset from the published data. The predicted torque was lower than the experimental data, across the range of advance coefficients, for $P/D=1.2$. Similarly, it was also lower for $P/D=1.0$, but by a smaller percentage (approximately 5% compared to 12% at $J=0.1$), and at this pitch ratio the torque was predicted well at values of $J\leq 0.4$. At the lower propeller pitch ratio of $P/D=0.8$, the K_Q results at $J<0.3$ were over-predicted, but only by a small amount, and at lower J values there was a good correlation between the panel results and the published data. At the higher advance coefficients all the pitch ratios exhibit the similar tendency of a more rapid decrease in the CFD K_Q values than the published data. The predicted values of K_Q would be expected to increase if viscous effects were taken into account over the blade surfaces.

Using this method of validation an indication of the accuracy and reliability of the code was obtained which provided increased confidence to further use the code to model the prototype thruster. Although the results at the lower advance speeds are high, the relative differences between the models are reasonably accurate.

5.2.2 Prototype Tip-Driven Propeller

In a similar manner as described above, the panel code was used to model the tip-driven ducted propeller. The propeller blades and duct were modelled using the same diameters and panel distributions as the standard Kaplan unit. In addition, because the tip-driven propeller was based on the K4-70 propeller, the wake pitches also remained the same. The bearing casings used 296 panels, and each stator was made up of 162 panels. Due to geometrical difficulties, it was not possible to model the rotor, attached to the propeller blade tips, or the gap between the rotor and stator.

The model was run for the similar advance coefficients to those experienced during the towing tank tests. The propeller speed remained constant at 1200rpm throughout the panel models, only the advance speed was altered to achieve the desired advance coefficient. Tests had indicated that at similar advance coefficients, but using different propeller speeds, the panel code predicted the same thrust and torque coefficients to within 1%. Sets of duct profiles were used during the experimental tests and the different section

shapes were also modelled using the panel code. Figure A3.6 illustrates the duct sections studied. Profile s2037 was based on the Marin duct 37 [2.1], duct s2637 was largely a stretched Marin 37 with a smaller nose radius, and f2637 was essentially designed as a trailing edge, having a relatively flat inner surface and low nose radius.

Figure A5.18 illustrates the geometry of the panel code model next to a photograph of the actual prototype. There is only one propeller blade shown in the panel model, the single blade geometry was reflected three extra times around the centre axis of the hub in order to model the four bladed propeller.

Results

The results have been presented in a similar manner to those in the Section 5.2.1, the study of the standard Kaplan propeller and Marin 37 duct. In this section the term 'symmetrical duct' refers to bi-directional ducts for which both the leading and trailing edge of the duct sections possess the same geometry, i.e. the symmetry plane is the propeller plane. This is illustrated in Figure A5.19.

Figure A5.20 plots the pressure coefficient distribution over the surface of the symmetrical s2037 duct section with the presence of a symmetrical Kaplan type propeller. The propeller plane is located at $X=0.0$. The pressure distribution is very similar to the standard Marin duct 37 and Kaplan propeller (Figure A5.13), although the coefficients along the inner surface are slightly lower. The flow along the outer surface is again similar to free-stream, but the drop in pressures around both the leading edge and trailing edge is less severe. This will be due to the straightening of the section outer wall, parallel to the centreline, which results in a smaller surface gradient change around the leading and trailing edge radii.

Figure A5.21 illustrates similar results for the symmetrical s2637 duct with the same propeller located at $X=0.0$. Clearly there is a less severe drop in pressure from the stagnation point around the outer surface of the duct, perhaps due to the smoother transition from the leading edge nose radius to the back surface of the section. Once on the back face, the flow follows the free-stream velocity much more closely than the shorter duct. The inner duct surface exhibits the familiar trend of accelerated flow into the

duct, lower pressures towards the forward half of the section, a slight drop in pressures past the propeller plane, and deceleration back to the trailing edge. A greater rise in pressure coefficients, before the propeller plane, compared to the shorter s2037 duct (Figure A5.20) is evident due to the increased distance from the inlet curvature to the centre plane.

The pressures along duct f2637 show quite different results (Figure A5.22). There is a rapid drop in pressures as the flow enters the duct around the small leading edge nose radius, however, due to the subsequent lack of curvature on the duct section, the pressures quickly recover. There is a slight acceleration past the propeller plane, but otherwise, the pressure rises until the potential-flow rounds the trailing edge to the aft stagnation point. For this section shape, the outer surface now indicates a similar trend to the inner surface of the previous ducts, although the pressure changes are less severe.

Figure A5.14 illustrates the axial velocity distribution over a number of radii in the centre of three symmetrical ducts with no propeller present. For ducts s2037 and s2637, the results are similar to those obtained for the standard Marin Duct 37. All velocities are greater than free-stream, and with increasing radii the relative velocities increase, although the increase in the longer duct, s2637, is less pronounced. The trends for duct f2637 look similar, however, an important difference is that the velocities are all less than free-stream, the maximum value of u/Uo being 0.82. In the centre of this duct, u/Uo is closer to 0.74. Thus f2637 is predicted to be acting as a decelerating duct in a free-stream.

Figure A5.15 shows the velocity profiles for the same ducts as above, but with the presence of a symmetrical propeller. Again, the trend of increasing velocity away from the centre is illustrated, and all the u/Uo values are larger than the free-stream condition. The average velocities through f2637 are now greater than free-stream.

Figure A5.23 plots the panel code results in the form of total thrust coefficients, K_{TT}, based on the total thrust of both the duct and the propeller, and the duct thrust coefficient, K_{TD}, based on the duct thrust alone. It is interesting to note that the more significant variations between the use of different duct profiles occur towards the higher advance coefficients. The ducted propeller with duct section s2637 produced approximately 10%

more thrust than duct s2037. At lower advance coefficients the total thrust from duct f2637 was similar to s2037, however f2637 produced greater K_{TT} values at higher advance speeds. At advance coefficients greater than $J=0.4$, f2637 developed more thrust than both s2037 and s2637 ducts. However, the proportion of the total thrust produced by duct f2637 was far lower than the other two ducts, thus indicating a greater propeller thrust. This is likely to be due to the decrease in the amount of acceleration the onset flow experienced, meaning the propeller was effectively operating at a lower advance coefficient, than in the other two ducts, therefore producing a greater thrust. In addition, a smaller amount of velocity distortion will mean fewer changes in the local flow pitch and hence the effective propeller pitch (Section 4.4.3). The propeller is therefore more likely to be working closer to its design pitch, thus offering improved performance.

The predicted thrust values towards the bollard pull condition (J=0.0) do not vary considerably between duct shape. This is largely due to the fact that a greater proportion of the thrust is developed by the propeller at this condition. Although the duct itself does tend to produce more thrust with decreasing advance coefficients, the duct thrust as a fraction of the overall thrust decreases. Further work is necessary on the wake model to gain better accuracy at these conditions.

A study into the likely effects of altering the hydrodynamic stator angle of attack was carried out for the thruster with duct s2637. A series of advance speeds was run with the stators at 0^o, 10^o, and -10^o angle of attack, the results are plotted in Figure A5.24. The results indicated that a stator angle of 10^o increased thrust by 2-3%, and -10^o reduced the thrust by a similar amount across the range of advance coefficients.

Similar studies were carried out on the prototype thruster in the test tank (Chapter 4), but only for zero advance speed conditions. In contrast to the CFD results, it was seen that at bollard pull both stator angles of 10^o and -10^o decreased the overall thrust; 10^o angle of attack by approximately 6%, and -10^o by 12%.

5.2.3 Comparison with Experiments

The experiments detailed in Chapter 4 were used to provide validation data for the panel model of the prototype thruster. Experimental and panel code results of thrust and torque are plotted in Figures A5.25 and A5.26.

The results from the experimental tests produced lower thrust coefficients than those predicted by the panel code, Figure A5.25. However, it must be noted that the panel code is a non-viscous flow solver, and as such better performance figures would be expected.

In a similar manner to the standard Kaplan trials, the over-prediction is greater at the lower advance speeds. Although the absolute values are greater, the CFD results do predict similar curve gradients to the test data, which are relatively steep for ducted propellers. It is thought that this rapid drop in thrust is a consequence of the extra drag from the thicker duct sections, necessary to house the electric motor. In addition, for similar propeller pitch ratios, a predicted decrease in thrust of approximately 20% was evident when modelling the symmetrical propeller and duct, rather than the standard Kaplan K4-70 in Marin duct 37. This lower initial thrust could also be a reason for the steep curves.

The experimental results showed small changes in thrust coefficients due to the use of different duct shapes. All ducts developed similar thrust values at the lower advance coefficients, but duct f2637 produced slightly higher thrusts as advance coefficient increased. The results from ducts s2037 and s2637 remained similar across most of the J values, although s2637 did produce a higher K_T at $J=0.475$. In contrast, the CFD predictions show s2637 produced more thrust across all J values, however, the trend between ducts s2037 and f2637 was better predicted by the panel code, with f2637 being increasingly beneficial towards the higher advance speeds.

Although zero advance speeds, or bollard pull conditions, could not be modelled successfully, a bollard condition was estimated by extrapolating the results obtained for several advance speeds. For the panel model of the thruster, a thrust coefficient of $K_T=0.544$ was estimated for $J=0.0$. At 1000rpm, this would mean a thrust of 590N. If it is

assumed that 15% is lost due to re-circulation (Section 4.2.6), the new thrust is 502N. For similar speeds, the tank tests produced a thrust of 433N.

It has been shown that the panel code produced higher absolute K_T values than the experimental tests, however, the relative differences between ducts were similar, especially between s2037 and f2637. Table 5.3 lists the percentage increase in thrust from s2037 to f2637 for several advance coefficients. Although the advance coefficients do not agree exactly, the relative differences are very similar. It is also noted that the slightly higher panel code differences are likely to be due to the slightly greater advance coefficients used.

Table 5.3: Relative increase in K_T between duct s2036 and f2637.

Experiment		Panel Code	
J	% increase of K_T from s2037 to f2637	J	% increase of K_T from s2037 to f2637
0.230	3.0	0.255	3.5
0.311	10.0	0.341	11.0
0.475	79.0	0.508	85.0

Results for the predicted torque of the thruster are presented in Figure A5.26. Unlike the thrust coefficients, the K_Q values have been under-predicted by the panel code, and in a similar manner to the standard Kaplan K4-70 trials (Section 5.2.1), the slopes of the CFD trend-lines are steeper than the experimental data. An additional torque was present in the experimental tests, from the gap friction between the rotor and stator, which was not possible to model using the panel code. However, the gap power loss was estimated to be 100W at 1200rpm [3.8], which would produce an increase in K_Q of only 0.0022. Another reason for the lower torque results might be due to the use of a fixed propeller wake sheet. The relative effects on K_Q due to different duct shapes were predicted reasonably well. Duct s2637 produced slightly more torque than s2037, but a greater overall torque was evident for f2637.

5.3 SUMMARY

A computational lifting surface panel model has been developed to investigate the likely performance of ducted propellers and similar applications. The model has been validated against existing experimental data for a standard ducted propeller unit. Given the assumptions of a fixed propeller wake model, and the lack of propeller viscous effects, the results showed good correlation with the published experimental data. Along with the geometry definition programs, which have been written (Chapter 2), this means any propeller-duct combination, within reason, can be adequately modelled using this method.

The panel code has been used to predict the performance of the prototype tip-driven ducted propeller. The results have been compared to experimental tests carried out on the prototype unit and, although the absolute thrust values were larger than the test results, and the predicted torque values were lower, the general trends and relative differences between ducts were adequately reproduced.

The results have provided increased confidence with the code and it is expected that this method of analysis can be used as an aid to optimising the hydrodynamic characteristics of future ducted propeller units. However, there still exists scope for future work into the modelling of the propeller wake sheet, and the boundary layer prediction over the propeller blades, using streamline tracing techniques.

6. WIND TUNNEL TESTS OF A WATERJET INLET DUCT

The aim of this study was to investigate the possible implications of using a tip-driven impeller in a waterjet system. In order to assess the performance implications, without the use of a suitable experimental facility, a computational model of the waterjet system will ultimately be developed. Computational fluid dynamics offers the ability to carry out a range of parametric tests without the need to re-use expensive test facilities. However, the complex shape of the waterjet duct and its surrounding hull can present difficulties to current CFD codes. Further problems occur when necessary extra details such as the drive shaft, inlet grills and lip shapes are included in the model geometry. Before these details can be considered, it was required to have confidence in the validity of the three-dimensional flow solution obtained through the basic duct alone. For this to be done, it was necessary to obtain detailed and accurate experimental data of the flow for comparison purposes.

6.1 AIMS

The main aim for conducting wind tunnel tests on the waterjet duct was to create a reliable database of accurate measurements for use when validating CFD predictions. In addition, it was intended to gain an understanding of the flow characteristics of the duct. Various papers have been published regarding experimental testing of waterjet ducts, these are discussed in the following section. The majority have used towing tanks, cavitation tunnels or actual open water trials. The use of a wind tunnel allows a more effective testing environment than either towing tank or cavitation tunnel facilities. The duct and all the necessary apparatus remained fixed in one position whilst the fluid was drawn past the duct, and each run could take as long as necessary. The apparatus required, and its set-up, to test in air is less complicated, and as long as the air speed is kept at $M<0.3$, the flow can be considered to be incompressible.

The duct was investigated using surface pressure tappings around the duct walls, leading to pressure coefficient (Cp) distributions, and traverse probing of the flow using pitot probes in order to obtain velocity profiles. The apparatus set-up was described in Chapter 2.

6.2 BACKGROUND

Several methods for investigating waterjets have been tried and tested. Experiments range from the use of small models to full scale jet units in boats and on test rigs, the fluid used has also varied between water and air. Waterjet testing is not as straightforward as conventional propellers, a propeller can easily be placed in a cavitation tunnel, but a waterjet model has to be mounted on top of the tunnel. This creates the problem that the expelled water has to be collected and somehow returned to the tunnel at the same rate as it was discharged. In addition to cavitation tunnels, tests have also been carried out using towing tanks and wind tunnels. However, in order to measure the flow rate from a waterjet outlet nozzle in a towing tank, the discharged water has to be collected in a tank suspended behind the model, thus adding complications to the apparatus set-up.

KaMeWa [6.1], a waterjet manufacturer supplying units worldwide has a unique test facility in the form of two cavitation tunnels, one is a free surface tunnel and the other is of a conventional closed section type. Tests with complete waterjet units have been conducted at corresponding full-scale ship speeds of well above 70 knots. Their tests are divided into three major components;

a) a complete waterjet unit test in the free surface tunnel;
b) an inlet test in the conventional tunnel;
c) a pump unit test.

The complete waterjet unit test is undertaken to verify performance predictions and to study certain properties in order to improve the system. These properties being the onset of inlet and pump cavitation, waterjet unit efficiency, static and dynamic load on impeller blades, total vertical forces acting on the ship hull, pressure pulses, noise characteristics and forces generated by the steering and reversing gear. The objective of the inlet test is to optimise the inlet concerning cavitation, efficiency and velocity distribution in front of the pump unit. The pump unit test determines the flow, head, efficiency and cavitation properties of the pump.

Hoshino and Baba [6.2] experimented using both a towing tank and a cavitation tunnel. In order to determine the propulsive performance they expressed the overall efficiency as a system of components of efficiency. To obtain the hull efficiency, a self-propelled model

in a towing tank was used. Three hull types were investigated; a semi-displacement craft; a superconducting magneto-hydrodynamic (MHD) propulsion ship model and a hydrofoil catamaran model with a pod inlet. A pod inlet was also tested alone in a cavitation tunnel and a Laser Doppler Velocimeter used to measure the velocity distributions just before the waterjet pump. Having gathered the experimental results a power prediction method was suggested and subsequently compared with measured values from a test boat. Agreement between the two was generally good. Also mentioned in the paper was an arrangement of a stand test for a hydrofoil (pod) waterjet pump in full scale, this was conducted to obtain pump characteristics. Thus, if the head difference was measured in a sea trial, the pump head and flow rate could be calculated.

A pod type inlet was also tested by Minsaas [6.3] using a free surface tunnel. The model was equiped with static pressure holes spread internally along the duct wall as well as a rake with Pitot-static tubes at the pump inlet. The model had exchangeable inlet lip rings and by means of a controllable pump the flow rate entering the inlet could be varied. Internal static and total pressure surveys were carried out as a function of inlet velocity ratio and cavitation number, from these data inlet loss coefficients could be derived. An example of the results of total pressure measurements across the pump inlet plane was shown and indicated two phenomena; a pronounced drive shaft shadow at the upper centre of the inlet plane, and two symmetrical zones of low energy below the shaft, which became more pronounced as the flow rate increased.

An experimental approach to obtain the pressure distribution on the inner surface of a flush type waterjet intake duct in self-propulsion conditions was described by Okamoto et al [2.8]. The tests were carried out in a towing tank using a model ship equipped with a waterjet intake duct. The pressure distributions were measured at ninety eight pressure tappings under various loadings of the pump at a constant ship speed of 4.083m/s. Mass flow rates through the duct were measured using the velocity distribution at the nozzle aft end, and a relationship between the impeller revolution and mass flow rate was obtained for the one ship speed.

Results of the pressure distributions were illustrated as pressure coefficients plotted around each section and along the bottom, top and side centrelines of the duct. An attempt

was also made to calculate the three orthogonal components of the forces acting on each area around each pressure hole, and longitudinal distributions of each component (forward, vertical and lateral) of the non-dimensional forces were shown. The results of their analysis indicated the additional thrust generation of an intake duct and the portion of thrust generation. However, they stressed that the complete evaluation of the force acting on the intake duct requires the consideration of the shear stress and the introduction of a CFD code.

Interaction effects occur between waterjets and the surrounding hull, which produce discrepancies between the resistance of the bare hull and the thrust required to propel the vessel in practice. While the effects are normally accounted for by such factors as the Thrust Deduction Fraction, it is still not clear what the effects are, or how they should be calculated. Terwisga [6.4] discussed the physical phenomena accounting for the interaction effects on the waterjet-hull system and derived efficiency terms for which an indication of the magnitudes were given. In addition, methods for the determination of these effects and a short description of some self-propulsion tests were given. Due to the complicated nature of the interaction mechanisms, and a lack of complete and systematic data, Terwisga [6.4] advised that if a reliable powering prediction was required, it is necessary to conduct self-propulsion tests.

Alexander and Terwisga [6.5] divided the interaction effects into changes in the hull resistance by the presence of the waterjet and changes in waterjet thrust due to the presence of the hull. Tests in the form of towing tank, wind tunnel, full scale and CFD calculations were proposed to attempt to clarify and properly account for these interaction effects.

Coop and Bowen [6.6] proposed and discussed possible mechanisms of hull-waterjet interaction having amalgamated information from existing performance prediction theory, computational fluid dynamics and wind tunnel investigations. The mechanisms included hull after-body pressure changes due to the presence of the waterjet which influence the centre of pressure and the dynamic lift, and jet system force components, in particular lift and momentum forces. It was seen that the most significant effects were expected to be due to the momentum change through the waterjet system which produces lift and

momentum effects on the hull. It was also possible that the presence of the protruding stream tube under the hull caused an extra down-load. Full-scale experiments involving the use of a test boat were proposed, the data from which could be used to refine the understanding of the interaction mechanisms and enhance the performance prediction techniques. Free body diagrams were used to analyse the forces impinging on both the bare hull and waterjet propelled hull, and the concept of an interaction vector was proposed. A method for incorporating this with existing theory was discussed and some preliminary results presented.

The Department of Ship Science has carried out a programme of work on waterjet hydrodynamics over the last few years. The major component has been the development and testing of a wind tunnel scale model of a representative waterjet inlet duct. Moss [2.6] built a model of a waterjet intake duct, based upon the geometry of the unit used by Okamoto et al [2.8], which could be bolted onto the side of a wind tunnel. Pressure tappings were fitted to the wall of the jet unit at several radial sections, and there was also the capability of mounting traverse mechanisms for Pitot probes along the top edge of the duct. The aim was to assess the feasibility of modelling waterjet intake units using air rather than water and to investigate the pressure distribution within the duct. The model was shown to produce reasonable results and these were presented in the form of pressure coefficients around radial sections and along the bottom, mid and top centreline of the duct.

SSPA has carried out numerous towing tank tests on vessels fitted with waterjet propulsion and Dyne and Lindell [6.7] reviewed some of the more important projects. The paper largely focused on the full-scale powering and resistance predictions, based on the tank tests, and a method which SSPA has developed was presented and explained.

At a similar time to when the author was carrying out the wind tunnel tests described in this thesis, similar tests were being undertaken at the University of Tasmania. Roberts and Walker [6.8] presented a brief summary of the work that Roberts had carried out for his PhD thesis [1.3]. Their experimental set up was similar to the author's work, although a closed circuit wind tunnel was used with artificial boundary layer thickening, and the duct was also smaller having a diameter of 150mm. The duct was constructed in acrylic to

allow for flow visualisation. The work focused on the effect of hull boundary layer thickness on duct flow, and a comprehensive set of measurements were taken for a thin boundary layer and a thick boundary layer. It was concluded that the intake loss coefficient remained approximately constant and was little influenced by the hull boundary layer. However, increased boundary layer produced slightly larger regions of inlet flow separation, but resulted in a lower level of flow distortion at the pump inlet.

A recent development at MIT [6.9] has been a large water tunnel for the purpose of testing waterjet pump units. The units are mounted in a straight duct within the tunnel working section and the flow rate is controlled by a valve downstream of the test pump. Initial tests have shown the facility to produce a comprehensive set of results including pump characteristics such as flow rate, torque, rpm, static pressure rise, inlet and outlet velocity fields.

It has been seen that over the last few years several experimental methods have been used for the testing of waterjets, all of which have been successful. These experiments, although reliable and accurate, are still expensive and time consuming. It is for this reason that more research is being carried out with the use of CFD, and as the computer technology advances, the results are becoming more reliable. However, the experimental results are still required in order to validate the predictions obtained from the computers. For the purposes of validation the precise knowledge of the geometry and flow conditions, coupled to reliable pressure and velocity measurements were required. This was most easily achieved using the existing apparatus available in the Department of Ship Science.

6.3 TEST PROGRAMME

Experiments were carried out at a combination of wind tunnel speeds and impeller speeds corresponding to three distinct operating regimes. These settings were based on visualisation of flow through the waterjet. Figure A6.1 illustrates a representation of the wool tuft patterns at the three operating regimes. The wind speed was set using the wind tunnel manometer whilst the waterjet impeller remained turned off. The impeller was then started and run up to the required speed. Upon doing this, the indicated wind tunnel speed increased. Conditions of each test case are shown in Table 6.1. The Inlet Velocity Ratio,

IVR, is defined as the ratio of mean flow speed at the duct exit to the indicated wind tunnel speed (equivalent ship speed).

Table 6.1: Wind Tunnel Test Case Conditions.

Test Case Number	1	2	3
Indicated Tunnel Speed (Impeller off)	15m/s	10m/s	10m/s
Impeller rpm	950	875	1051
Indicated Tunnel Speed (Impeller on)	21.1m/s	14.8m/s	15.2m/s
Inlet Velocity Ratio, IVR	0.883	1.173	1.406

Under the conditions for Case 1 the wool tufts showed separation occurring on the upper duct wall and attached flow on the lower wall. For Case 2 it was seen that separation was beginning to form on the lower wall, and Case 3 indicated a definite separation on the lower duct wall. The flow along the upper wall was fairly well attached for both Cases 2 and 3.

The Reynolds number of the flow through the duct based on the exit diameter and exit speed was in the range of 0.32×10^6 to 0.37×10^6 which is at least 3 to 4 orders of magnitude lower than full-scale but double that achieved in the towing tank by Okamoto [2.8]. The Mach number, based on the highest air speed measured, had a maximum value of 0.032, thus incompressibility was guaranteed.

6.4 PRESENTATION OF RESULTS

Pressure coefficient distributions along the upper and lower centrelines are shown in Figures A6.2 and A6.3. It should be noted that the *Cp* values indicate the pressure relative to that at the impeller (exit) plane for each individual test case. Repeat tests confirmed that the *Cp* results were reliable, generally to an accuracy of within $Cp \pm 0.06$. Sometimes slightly larger differences were evident in the regions of large surface gradients, such as near the lip or the ramp at the inlet plane. The maximum *Cp* difference was recorded as $+0.12$. Occasionally, the results illustrated large spikes in the pressure measurements, but these were explained by the scanivalve failing to reset correctly at the end of a test. In such instances, these results were ignored and the test repeated again.

In addition, velocity profiles were obtained through several sections along the duct using pitot probes in a traverse mechanism, which measured the position of the probe from the top wall to an accuracy of *0.5mm*. In each case a Betz manometer was used to obtain a measure of the velocity, which was defined relative to the local top wall static pressure measurement. The pressure difference, measured as a height of water using the Betz manometer, was recorded to the nearest *0.05mm*, and it was also seen that the measurements were repeatable to *±0.05mm* during a test. This equates to the velocity measurement having a maximum error of *±0.9m/s*. Results are given in Figures A6.4, A6.5 and A6.6 as graphs of velocity ratio against distance into the duct from the upper surface. The relative measurement positions are indicated in Figure A2.10.

6.5 DISCUSSION OF RESULTS

6.5.1 Pressure Distributions

The top centreline *Cp* variations, shown in Figure A6.2, show a definite increase in *Cp* towards the inlet for increasing IVR. This indicates that, as expected, the greater the velocity ratio the greater the acceleration of the flow through the duct. For Case 1 the flow is decelerated from the free-stream value. Once the velocity ratio has been increased, in Case 2, the *Cp* values are generally greater than zero, with the exception of the acceleration around the ramp at the inlet. The highest velocity ratio, Case 3, shows another increase in the *Cp* values. In case 3 all positions exhibit a slower flow than at the exit. Also shown are two results from Okamoto [2.8], for IVRs of *0.92* and *1.056*, which lie reasonably well within the wind tunnel data. Similar trends are seen between the two sets of results, however, the sharp drop in *Cp* towards the beginning of the ramp was not evident in Okamoto's results. The discrepancy may be due to small differences between the geometry of the models at this point due to manufacturing constraints.

One noticeable feature on the bottom centreline *Cp* variations, Figure A6.3, is that the *Cp* values are generally lower for test case 1, suggesting higher relative velocities. This agrees strongly with the fact that the flow was attached along the bottom wall during this case. The relative velocities fell slightly for Cases 2 and 3, during which some separation occurred along the bottom wall, producing higher *Cp* values. Another point to highlight in Figure A6.3 is that for each test case the relative pressures decrease towards the lip of the

duct. In this region the *Cp* values are close to zero. It was not possible to obtain a measurement at the lip due to the physical construction of the model.

Similar results from Okamoto [2.8], at IVRs of *0.92* and *1.056*, have also been plotted on Figure A6.3. Although similar pressure patterns exist for the two sources of data, it is clear that Okamoto's *Cp* values are higher towards the inlet lip. This, again, is probably due to geometrical differences; the wind tunnel model had a much sharper lip than the duct tested by Okamoto [2.8]. Further downstream, however, the pressure coefficients exhibit similar magnitudes.

6.5.2 Velocity Profiles

The velocity profile results from test Case 1 are shown in Figure A6.4. Clearly indicated on the graph is the separation region towards the top wall of the duct. This area can be seen to increase from about *50mm* to *130mm* deep at sections A and EA. Section EA possesses a slight separation towards the lower wall of the duct. This decrease in effective flow area caused by the additional area of separation may explain the velocity increase from section A.

Figure A6.5 illustrates the velocity profiles for Case 2. It is clear that a zone of separation exists at the lower duct wall, and this separation appears to grow towards the impeller plane EA. The relative velocities are higher than Case 1 and, with the exception of section D, the profiles show the expected trend of increasing velocities along the duct from C to EA. The velocity profiles for Case 3 are shown in Figure A6.6. As for test Case 2, the separation region occurs towards the lower duct wall, although for this case it is much more pronounced. The velocity ratio in Case 3 is *1.4* and the indicated velocities are the highest of all three cases. Again, the trend is of increasing velocities along the duct, although section D shows relatively higher velocities than expected. This is thought to be due to a reduction in the effective cross-sectional area at this position.

6.6 SUMMARY

The wind tunnel experiments proved to be an effective technique for the study of flow through this waterjet duct. Pressure and velocity distributions along and through the duct were obtained together with a visualisation of the flow characteristics. The resulting trends were expected and the measured velocity profiles generally agreed with what had been shown by the wool tufts. The results illustrated the development of flow separation, on the lower surface of the duct, at higher inlet velocity ratios.

A comprehensive set of reliable data was obtained for the flow through the inlet duct, which provided a detailed indication to the behaviour of the flow. The data can also be used to validate future theoretical models of the duct. In addition, the geometry and flow measurement data for this waterjet duct was supplied to DERA [6.10], in order to be used for comparison purposes during CFD parametric studies [1.4].

Much time and planning was required in order to achieve results such as these. Ideally, there are many more measurements and combinations of tests which could have been carried out, but this was not practical with the speeds attainable in the tunnel or with the time available. However, a CFD model of the waterjet duct can be developed and, once validated using this data, can be used to study further operating conditions. The following chapter discusses the development of such a model.

7. COMPUTATIONAL ANALYSIS OF A WATERJET INLET DUCT

7.1 AIMS

The aims of the work presented in this chapter were to produce, using the commercially available CFX4.1-F3D [2.10] flow solver, a three-dimensional computational model of the representative waterjet duct to be validated using the data gathered from the wind tunnel tests. Once validated the model can be used to obtain flow patterns through the duct, under different operating conditions. These flow patterns, or velocity fields, can subsequently be imposed on a panel model of a waterjet impeller, and the performance can be studied (Chapter 8).

The results obtained and the validity of the results are described. The CFD geometry was then further expanded into a model which included the aft half of a hull surrounding the duct. Stages along the way include investigations into the effects of trim and drift on the flow through, and the forces acting on the duct. Interaction effects are discussed briefly before a summary of the work is given.

7.2 BACKGROUND

With the introduction of more powerful and faster computers the use of CFD as a research tool is becoming increasingly popular. There are now several commercially available CFD codes on the market that are able to cope with the complex geometry of the waterjet and produce reliable results.

One of the earliest CFD representations of a waterjet intake was presented by Forde et al [7.1] using Euler codes on non-viscous flows. The definition of the correct geometry within the grid generator was found to be very difficult with a lack of interfaces between CAD systems and advanced CFD calculations. To get around this problem they developed a surface line and surface generator especially for waterjet intake applications. The geometrical design procedure was based on three control lines. One curve described the contour line on top of the duct and a second line described the lower contour line. These lines were also symmetry lines for the duct. A third line described the side contour

of the intake duct. Finally, two surfaces were generated between curve one and three, and between three and two. The lines and surfaces were generated using Bezier curves and surfaces.

Three different design cases were calculated using the CFD techniques. Two being flush type intakes with different cross sectional area distributions, and the third a pod type intake. The same ship speeds and power setting conditions were applied to all cases, and the results were given as losses and velocity factors. The losses were obtained from the total pressure drop from upstream conditions to the waterjet pump flange. The CFD calculations showed the complexity of the flow, where the losses were generated and how it had influence on the waterjet impeller and total efficiency. Areas exposed to cavitation problems were also highlighted. However, it was concluded that CFD analysis requires advanced measurements for verification of the calculations.

The use of CFD as a cost effective and practical design tool for the design and analysis of waterjet propulsion systems was discussed by Seil et al [7.2]. In order to do this a three-dimensional flush-type waterjet unit was simulated using a RANS based code with turbulence modelling. The computational simulation was performed using the commercially available CFD software, Fluent^{TM}. Modelling issues addressed in the paper included mesh generation, boundary conditions, turbulence modelling and impeller simulation.

The meshes used in the simulation were body-fitted co-ordinate, single block structured meshes, produced by Fluent's pre-processor. The inclusion of the impeller shaft housing was deemed too difficult and it was decided to model the intake duct alone. Free stream velocity conditions were imposed on all the boundaries of the domain external to the waterjet except the downstream boundary, which was set as a boundary of constant pressure. The effect of the impeller was treated as a pressure rise associated with a predetermined pump characteristic.

The results were used to calculate a value for duct efficiency, although the accuracy of these values varies due to the simple duct geometry with no appendages. Cavitation was

evident but no flow separation was observed. Overall the simulation produced good results and the initial hypothesis about a practical design tool was validated.

In a later paper Seil et al [7.3] developed this model to study the optimisation of waterjet inlets using the mathematical approach of minimising an objective function. A single block, body-fitted co-ordinate structured mesh, created using a program written by themselves, was used to model one half of the duct. Three duct geometries with different ramp angles and lip radii were examined for an inlet velocity ratio of 0.6. No drive shaft or surrounding hull structure was modelled. Few results were published, but it was concluded that a larger lip radius or duct angle was beneficial for lip cavitation, and resulted in a larger vertical force acting on the duct. However, for each case tested, cavitation was likely to occur on the underside of the lip.

A more detailed approach was later developed [7.4], whereby a customised mesh generator was used to automate the examination of a large number of geometries. Using a similar scheme, the objective was to optimise a generic inlet duct to eliminate the cavitation on the underside of the lip. The optimised ramp angle was steeper, and the cavitation performance was found to improve by using a smaller lip radius, which is in contrast to the previous findings [7.3]. However, concerns were expressed by the author about increased flow separation around the sharper lip when operating at off-design cases.

Szantyr and Bugalski [7.5] presented a numerical method for modelling the waterjet intake, channel and outlet by a discrete distribution of sources. The impeller, guide vanes and other lifting elements were represented by lifting surfaces comprising of a discrete distribution of vortices, sources and sinks. The method was intended for the prediction of flow streamlines and velocity distribution, pressure distribution, hydrodynamic forces and presence of cavitation.

The internal surface of the waterjet was modelled by a number of flat quadrangle panels. All lifting elements were modelled by lifting surface theory which is based on simulating hydrodynamic loading on the foils with the appropriate distribution of vorticity, and simulating the foil thickness with the appropriate distribution of sources and sinks. The

block diagram of the computer program was illustrated to describe the interaction between all elements of the waterjet within the simulation. As a validation for the numerical model, Szantyr and Bugalski [7.5] had carried out some experiments using a waterjet propulsor mounted on top of a cavitation tunnel and a description of the set-up was included. Results of the calculated velocity profiles concurred generally quite well with those from the experiments, and the analytical method seemed to reproduce the overall tendencies of impeller thrust and torque reasonably well.

English [7.6] also investigated whether it was possible to model a waterjet computationally using a lifting surface panel method. The waterjet was defined using a Shipshape lines definition package and was transferred through data files into a lifting surface program originally developed to model the interaction between ship propeller and rudder. To produce a realistic flow an alteration was made to model the impeller. A source was imposed which effectively sucked flow through the jet. The method did not take into account that the flow at a waterjet impeller varies spatially and temporally. The lifting surface formulation was also irrotational and inviscid and consequently ignored viscous action. There was therefore a lack of boundary layer and subsequent areas of cavitation and separation had to be estimated. The investigation was successful, however there were doubts as to how the weaknesses in the modelling effected the results.

The local flow around a flush-type waterjet installed in a mathematical hull, of which the waterplane was parabola and constant throughout the draught was simulated by Yang et al [7.7]. The primary concern was to examine the flow performance in terms of pressure distribution. The model of the waterjet duct was a truncated version of that used by Okamoto et al [2.8], and the ship speed and flow rate through the impeller section were taken to reflect a set of experimental conditions.

The flow field around the ship including the waterjet was computed first using a potential code with higher-order boundary elements. The velocity field obtained from the potential code was then imposed as an inlet boundary condition for a 3-D viscous code. Limited results were given in the form of pressure distributions along the ramp and lip centrelines, and at several cross sections throughout the duct. Some numerical results showed a qualitative agreement with experiments, however the mathematical hull was

not representative of the hull used during the experiments. It was concluded that the pressure distribution along the ramp was critical to cavitation inception, and that along the lip was responsible for appendage drag. Changes in thrust deduction factor were also noted as the vessel trimmed, explained by the changes in inlet pressure distributions, but no data was published.

Latorre [7.8] investigated the surface pressure distribution in a waterjet intake. A two-dimensional Navier-Stokes model of a basic hull with and without the waterjet system was used. Trim was also imposed on the hull and its effects on the pressure distribution within two different inlet shapes were presented. The results were compared to published experimental data of a model boat and waterjet in a towing tank and wind tunnel tests. Although limited results were presented for the two-dimensional model, it was concluded that trim has a significant influence on the waterjet inlet pressure distribution and its efficiency - something which was also postulated earlier by Hoshino & Baba [7.9].

Two-dimensional diffuser and lip section shape were investigated by Pylkkanen [7.10], and later Pylkkanen [7.11] carried out investigations as to whether a two-dimensional flow model was adequate at the initial design stage. Two sets of wind tunnel measurements were used as the test cases for the CFD code, and the capability of the code to predict waterjet inlet flow was discussed. The FLOW3D Release 3.1 (1991) code was used for the analysis of the waterjet flow. The two-dimensional grid represented the centreline plane of the inlet duct and calculations were carried out for several sizes of grid. The calculation domain was divided into four blocks for grid generation and the impeller diameter was 0.4m.

The calculations were made for two ship speeds, one being near to and the other above the design speed. The mass flow through the pump was taken from wind tunnel measurements and the exit mass below the bottom of the ship was obtained from continuity. The results from the CFD code agreed reasonably well with those from the experiments however, there were some discrepancies due to the fact that there was a fixed floor at a shorter distance below the bottom of the craft in the wind tunnel test. The tunnel tests also incorporated a drive shaft in the intake duct.

Dai et al [7.12] briefly mentioned the limitation of CFD with two-dimensional models and, referring to Pylkkanen [7.10], claimed that two-dimensional methods, whilst providing rapid turnaround in design iterations, are oversimplified for complex three-dimensional inlet flows. This argument was also strengthened by Hu and Zangeneh [7.13] who showed that three-dimensional effects have important implications on the flow, especially on the lower duct wall near the lip, and on the upper wall at the duct exit. Dai et al [7.12] further discussed the three-dimensional model proposed by Forde et al [7.1], and considered the geometric modelling technique was limited because it applies Beizer curves or surfaces only according to area distributions. No local fine-tuning was available. To overcome these limitations, Dai et al proposed a method for designing a flush inlet by systematically specifying inlet geometric parameters, and automatically generating a panel model to be analysed by a panel code.

Gustafsson and Widmark [7.14] detailed the modelling of a waterjet duct within a hull by coupling two codes together. The first flow solver was used to model the hull with an active inlet present, the inlet being modelled by a uniform distribution of sinks. The results were used as inputs to the second solver, which modelled the intake duct and a small part of the surrounding hull. The pump was represented as a uniform volume force and the drive shaft was modelled as being non-rotational with non-slip surfaces (i.e. the surface velocity set to zero). The overall results were compared to towing tank data and the predicted outlet losses were seen to be slightly higher than the tank tests. Results for the inlet losses were of opposite trends to the tank tests and were questionable. A lifting vertical force was observed at low Froude numbers (F_n), but a downward vertical force at higher F_n, the action of the force moving towards the intake with higher IVRs.

Hu and Zangeneh [7.13] also modelled a drive shaft during an analysis of the flow through a three-dimensional waterjet duct. The commercial code, Fluent^{TM}, was used to model an inlet duct with a drive shaft, and surrounded by a flat plate, which represented the hull of a vessel. Conditions were studied modelling the shaft as both a non-rotational and a rotational body, and the effect on the flow at the duct exit plane was studied. Although there was a lack of detailed experimental validation, it was shown that the presence of a drive shaft had an important effect on the flow field in the duct, near to lip region and at the duct exit. The rotation of the shaft also had an effect on the impeller

inflow velocity field, but this was only significant at low Reynolds numbers ($\approx 1.2\times10^5$, based on inlet diameter). The importance of trim on the flow through the duct was also highlighted, however, the effect of a 4° trim angle was only studied briefly.

Hu and Zangeneh [7.15] presented an automatic optimisation method with the aim to minimise stagnation pressure loss through the intake duct. An 'in-house' RANS code was firstly used to optimise the two-dimensional shape of the duct centreplane, the ramp wall being optimised first and then fixed as the lip shape was optimised. A commercial RANS code (Fluent^{TM}) was subsequently used to model a three-dimensional duct, including shaft, which was designed around the optimised centreplane section. It was claimed that two existing ducts had been optimised with 20% reduction in losses, more uniform flow at the impeller face and suppressed separation at the lip wall. However, the only validation data given was a comparison between the two CFD codes, using the v component of velocity. No experimental data was used.

A paper focusing on flow uniformity in front of the impeller was published by Verbeek and Bulten [7.16], who utilised both wind tunnel tests and CFD models. The CFD model was of a similar arrangement to this author's, but only consisted of 46,500 cells, which is relatively coarse. However, a reasonable agreement with the wind tunnel jet exit velocity field was obtained for a low IVR. Further studies concluded a longer hull produced greater non-uniformity due to more boundary layer, but this is in contrast to the findings of Roberts and Walker [6.8], who found increasing hull boundary layer thickness resulted in a lower level of flow distortion at the pump inlet. It was also concluded that the more turbulent the flow, the more uniform the velocity field was.

Bulten [7.17] later investigated the influence on boundary layer ingestion even further using a similar CFD model, this time validated by comparing ramp pressure coefficients with wind tunnel data. It was concluded that a thicker boundary layer resulted in higher net thrust and higher efficiency, but at the cost of a lower total pressure at the impeller face, which could worsen any cavitation problems. A similar result to that of Roberts and Walker [6.8].

Watson [1.4] presented a detailed discussion on the problems of geometry definition, grid generation and the physical modelling of the flow through a waterjet inlet duct. An intake duct, based on the duct geometry from this work, was meshed using a mixed-grid of 408,000 tetrahedra in the inlet duct and 587,000 prisms below the ground plane. Watson [1.4] claimed that as a minimum multi-block grids should be in excess of one million cells to ensure grids with acceptable levels of skewness for even the simplest of duct geometries.

The majority of the CFD reviews have compared their results with existing test data. On the whole, the comparisons have been good, however, some discrepancies have also come to light. One significant reason for these disagreements is that the geometries of the CFD models were different from the physical models or the full-scale units upon which they were based. This is because of the limitations of the computational codes. The most difficult objects to model through a waterjet are its internal appendages, the intake grill, drive shaft and impeller, especially if the later two rotate. Due to the complexity of these problems they have often been excluded from the waterjet geometry, which has remained a relatively simple intake duct. In order to obtain a suitable validation of a CFD model the geometry is required to be of the same shape and size as the experimental geometry.

Another observation is that most of the computational models have been running flat with a free-stream flow (equivalent ship speed) parallel to the duct inlet plane. With the exception of Latorre [7.8] and Hu and Zangeneh [7.13], no models have been examined whilst operating in off-design flows. With the introduction of more advanced CFD codes this will become easier to do and would be worth investigating.

7.3 WORKING SECTION - WATERJET MODEL

7.3.1 Aims

This model was constructed in order to simulate the test conditions experienced during the wind tunnel analysis of the waterjet duct. Doing this allowed a direct comparison between the two analyses to be obtained, which could be used as a validation process for the RANS code.

7.3.2 CFX Flow Solver

A command program was created for this geometry using CFX4-Setup. The command file variables were chosen to recreate as closely as possible the experimental conditions; incompressible, steady, turbulent flow. The influence of using different turbulence models was not part of the aims of this study, investigations such as this have been carried out by other authors [7.13,6.8,1.4]. For this reason the default k-ε turbulence model was used, which had been found to give reasonable results by Hu and Zangeneh [7.13]. The speed of flow into the working section was set to that used in the wind tunnel tests. The mass flow through the duct exit was based on the product of speed at the exit midpoint and the cross-sectional area. The flow through the exit plane of the working section was obtained by the use of mass continuity. A waterjet impeller operating at a constant rate of revolution does not necessarily experience a constant mass flow rate through the duct, hence the thrust and inlet velocity ratio vary. However, for simplicity a constant mass flow rate through the duct exit was defined for all the CFD models. Table 7.1 lists the conditions defined for each case, which were obtained from the experimental tests.

Table 7.1: Conditions Set For Each CFD Test Case.

Test Case Number	1	2	3
Working Section Inflow Speed	21.1m/s	14.8m/s	15.2m/s
Duct Exit Speed	18.6m/s	17.4m/s	21.3m/s
Duct Exit Mass Flow	1.123kg/s	1.051kg/s	1.286kg/s
Inlet Velocity Ratio (IVR)	0.88	1.17	1.42

Some modifications to the solution strategy had to be made before a reasonable level of convergence was obtained for the solution. A more accurate, higher order than the default, discretization method was used for the k and epsilon equations. These two variables were also iterated three times within each global iteration and under-relaxation was employed for the turbulent and velocity variables. One of the most common causes of lack of convergence within CFX is due to the cross-derivative diffusion terms in the k and ε equations on non-orthogonal grids [2.10]. There was a facility for under-relaxing these terms during the course of a calculation and, as the grid was non-orthogonal in some areas, this was done for the first 250 iterations. These strategies and a copy of a

typical command file, listing the parameters used for the CFX waterjet duct models, are described in more detail in Appendix H.

The solution was seen to converge to an acceptable level (residuals of $1x10^{-3}$) after 700 iteration cycles. The code was run on a multi-user Sun Sparc 1000 with eight 60mhz processors. Output data such as pressure, velocities and local forces throughout the geometry were readily obtainable from the solution.

7.3.3 Comparison with Experiments

The results of the CFD model were validated by comparing them to the results obtained from the wind tunnel tests on a model of the same waterjet duct geometry. This initial CFD model of the full inlet duct, having a total cell number of 89650, 20100 being within the duct, was run for the same three conditions as tested in the laboratory. Pressures were obtained along similar centrelines and made non-dimensional in the same manner as those in the experimental tests.

Figure A7.1 presents both the experimental and CFD pressure distributions along the top centreline of the waterjet duct for three inlet velocity ratios, IVR, where IVR is the ratio of the duct exit velocity to the wind tunnel flow speed (ship speed). It can be seen that the comparison with the experimental results is good. However, it is evident in all three cases that the CFD result is offset slightly from the experimental points. The CFD results indicating higher *Cp* values. This was thought to be due mainly to the method used to calculate the experimental mass flow rate. This was based on the velocity at the mid-point of the exit plane calculated relative to the top centreline pressure P_A. The experimental tests and CFD results indicated a static pressure gradient across the exit plane at Section A. Based on a linear variation, this would imply the mass flow rate used for the CFD calculation resulted in an IVR which was between 3% and 5% higher than the actual IVR tested in the wind tunnel.

The comparison of pressure coefficients along the bottom centreline is shown in Figure A7.2. The general trends agree very well and the offset is less pronounced than along the top centreline. However, an unexpected result is the decrease in *Cp* towards the lip. In this area a pressure increase is more likely to be experienced as a stagnation point tends

to be located in the vicinity of the lip. The reason for the low *Cp* was thought to be due to poor grid quality, or skewed cells, in the region of the lip, which had proven to be very difficult to model.

7.3.4 Summary

Although the absolute values of the predicted pressure coefficients are offset and do not agree exactly with those obtained during the experimental tests, the overall trends are closely followed and the relative changes appear to be of the correct order. These results provided increased confidence in the ability of the code to produce reliable results and, as such, it was used for further studies.

7.4 EFFECT OF TRIM AND DRIFT

A sideways motion of a vessel, for example at low speeds, impairs the performance of the intake and affects the manoeuvring thrust available [7.18]. Using this CFD code, there exists the ability to study the effects of running the inlet duct for off-design cases.

7.4.1 Alterations to the Model

The CFD model was further used to investigate various inlet conditions including trim and drift. A further two meshes were created in which the working section was lengthened, widened and three of its walls were defined as pressure boundaries, thus providing a flat plate structure around the waterjet inlet, Figure A7.3. In addition, the waterjet block structure was redefined in order to produce a more orthogonal cell structure. One model was of half the waterjet and flat plate with a symmetry plane defined along the centreline. This model consisted of 23 blocks with up to 55720 cells, 13120 within the duct, corresponding to a full waterjet duct model of 111440 cells, and was used to solve the flow for various angles of trim. Another geometry modelled the full waterjet duct and consisted of 27 blocks with up to 56000 cells, 18080 being within the duct. This was used to study the flow for various angles of drift. In each model the waterjet duct consisted of 15 blocks and the remainder made up the flow domain beneath the flat plate. Each block was sub-divided into smaller cells and where required, the cells were concentrated towards areas of greater interest. These geometries were run at the mid inlet velocity ratio of *1.17*.

The mass flow rate was based on the product of the measured velocity at the exit plane and the outflow area. This value of mass flow rate was held constant for all the conditions of drift and trim, which were solved for an IVR of *1.17*. The increased duct losses for drift and trim would result in a change in mass flow rate for a constant impeller rate of revolution. This makes direct matching of the condition of steady forward speed difficult and for this reason a constant mass flow rate condition was used.

The resultant trends obtained agreed reasonably well with the experimental data for the straight-ahead condition although only a relatively coarse grid was used. The relative results for the effect of drift and trim agreed with that expected and for the purposes of investigating the influence on an impeller were deemed acceptable.

The influence of the number of cells on the results was investigated for the new mesh [7.19]. Half-duct cell numbers were varied from 6200 to 13120, corresponding to a total cell number variation of 20200 to 55720. It was found that the resultant pressure coefficients remained at very similar values, the maximum change being only *±0.02*. The predicted forces acting on the duct, however, altered by up to 30% in some areas due to differing cell numbers. It was thought that large distortion of cells in these regions affecting the iteration of the pressure was responsible for these differences. A significant difference between the predictions by this new mesh and the initial grid was a rise in pressure towards the lip along the bottom centreline, which was more likely to be expected, and a lower *Cp* value further along the bottom centreline, possibly due to flow acceleration from around the area of lower velocities at the lip. The reason why the initial geometry predicted a decrease in *Cp* was put down to poor grid quality.

In addition, a significant result of increasing the number of cells was to increase the computational time and hence the real time taken for the solver to finish. This was the deciding factor as to how many iterations and cells to use for the investigations into trim and drift. These were chosen as 9040 duct cells and a subsequent total cell number of 27240 for the half-duct model, and double these values for the full jet model. The maximum number of iterations was set as 800 [7.19].

7.4.2 Presentation of Results

The results obtained were plotted as pressure coefficients along the top and bottom centrelines of the duct (Figures A7.4, A7.5, A7.6, A7.7). It is important to note that pressure is defined relative to the top centreline point at the exit plane for each case. In addition, Figures A7.8 to A7.13 present the effects of trim and drift on the axial, radial and angular velocities of the flow across the impeller face plane at *0.7* radius. Three angles of trim were investigated, $+7^o$, -7^o and $+15^o$, and 5^o and 10^o angles of drift were studied. Positive trim was representative of a vessel trimming bow up.

7.4.3 Discussion of Results

Trim:

Figures A7.4 and A7.5 illustrate the pressure coefficient distributions. Along the top centreline it is seen that an increase in trim produces a decrease in the relative pressures towards the inlet. This is expected with positive trim because the inflow is at an angle closer to that of the ramp of the duct.

The rise in *Cp* values towards the lip, along the bottom centreline, for zero trim can be seen on Figure A7.5. It is also predicted that the relative pressures increase towards the inlet lip due to increasing trim. The pressures also appear to stabilise towards the duct exit with the exception of negative trim, which produces a slightly lower relative pressure at the exit.

Drift:

Figures A7.6 and A7.7 show results for the influence of drift. It is seen that drift affects the pressure distribution along the whole length of the duct. The top centreline distribution undergoes a pressure drop along its length with the exception of a slight rise past the exit. The bottom centreline also sees a relative pressure drop along its length except for a point at $X=-0.1$. The influence of drift along the entire top and bottom centrelines is to be expected as the fluid enters the duct at an oblique angle and will be concentrated towards one side of the duct. However, the graphs show that the predicted pressure coefficients along the top and bottom centrelines are nearly identical for both 5^o and 10^o drift. These results were double-checked using a mesh with 63520 cells rather than the original 54480 cells, and the same results were predicted. Further investigations

at more angles of drift and some experimental data are required to have confidence in these results.

Impeller Plane Velocity Distributions:

It is inevitable that the presence of trim or drift on the system will also effect the pressure, and hence velocity, distribution across the exit plane of the duct. Figures A7.8, A7.9 and A7.10 present the variations of axial, radial and angular velocities at *0.7* radius due to the effects of trim. The angle from Top Dead Centre (TDC) is only taken up to 180^{o} as the CFD geometry only modelled half the duct. It can be assumed that the flow was symmetrical about the centreline. The effects of drift are illustrated in Figures A7.11, A7.12 and A7.13.

Trim:

An immediate observation is that for the three velocities negative trim has the opposite effect to positive trim. In general, greater axial velocities exist towards the upper half of the duct, as do positive radial velocities. The prediction that radial velocities are positive towards the top half but negative towards the lower half, coupled with the angular velocities, could indicate the presence of vortices within the duct, which might have arisen due to the curved sides around the inlet lip. Positive trim increases axial velocity towards the upper half, but negative trim decreases it. However, the angular velocities are increased around the entire radius due to negative trim.

Drift:

Drift produces quite different results. A major effect is the lack of symmetry around the radius. Both radial and angular velocities exhibit greater speeds offset to one side of the duct centreline. This is expected with an oblique inflow. The axial velocity is decreased towards the top half of the duct and increased in the lower half. This is also the case for the radial velocities. Angular speeds, as with negative trim, are increased around the entire radius again.

Table 7.2 lists the total forces, acting on the duct, calculated by the flow solver for the *X*, *Y* and *Z* co-ordinates. *X* being along the jet (aft to for'd.), *Y* is the vertical component and *Z* the lateral co-ordinate. Note the fluid modelled was air.

UNIVERSITY OF SOUTHAMPTON LIBRARY

Table 7.2: Total Duct Forces (N) Predicted By CFX4.1-F3D.

Trim	Drift	*X*	*Y*	*Z*
-7°	0°	-0.894	-0.989	0.000
0°	0°	-0.766	0.786	0.000
15°	0°	-0.995	4.699	0.000
0°	5°	-1.519	2.871	-1.246

It is indicated that when the waterjet duct is subject to trim or drift the resistance of the unit increases, especially when drift is imposed - in this case 5^o drift almost doubled the resistance of the zero degrees case and, as expected, some lateral forces are produced. However, the duct tends to produce more lift (*Y* forces) with drift, and certainly with positive trim.

7.4.4 Summary

The influence of trim and drift produces a change in the pressure distributions, hence velocity and force distributions along the duct and across the outflow plane. In reality this would impose a non-uniform flow at the face of the impeller reducing the performance. In addition, there would also be a change in mass flow rate through the duct affecting the overall thrust of the unit. However, some effects, such as the extra lift produced, may be of benefit to the overall system. For this to be observed, the whole system, including the duct and surrounding hull, as a single unit needs to be considered.

7.5 HULL-WATERJET MODEL

7.5.1 Aims

In order to produce a more realistic model of an operational waterjet duct it was necessary to model a hull shape around the inlet rather than a flat plate. To reduce computational time only the aft half of a hull was modelled. This assumed that the upstream influence of the waterjet was negligible over the forward part of the hull, and this was subsequently seen to be the case.

7.5.2 The Representative Hull Definition

The hull was based on a Series 64 hull [7.20] as similar jet-hull configurations are in operation and data on this hull was readily available. Point co-ordinates defining sections along the hull were input into CFX-Meshbuild. Splines were created between the points to define sections, and blocks were created externally of these sections to define the flow domain beneath the hull. The structure is shown in Figure A7.14. At present, the hull shape has not been optimised to accept the waterjet inlet, it is defined up to the waterline and no free surface effects have been taken into account. It was assumed that the influence of the waterjet on the hull bottom would not strongly influence wavemaking resistance.

7.5.3 Presentation of Results

Pressures along the duct and forces on the waterjet and hull were obtained for an inlet velocity ratio of *1.17*. In addition, the bare hull alone was run at the same flow conditions in order to directly compare the frictional and pressure forces acting on the hull with and without a waterjet.

7.5.4 Discussion of Results

Figure A7.15 shows the predicted top centreline pressure coefficient distribution for the flow through the duct in the presence of the hull. It is seen that the top centreline relative pressures rise towards the inlet of the duct but soon settle to very near the original values without the hull. This rise might be due to the possible growth of a boundary layer along the hull or the slight change in angle between the hull and the ramp. This angle was greater for the flat plate case. The hull influence on the bottom centreline pressure distribution is illustrated in Figure A7.16. The predicted results indicate a decrease in relative pressures, from the flat plate case, at the lip, but a general increase through the duct is evident. The resistance forces acting on the duct unit did not alter significantly due to the presence of the hull, however, it was predicted that the duct would produce more lift.

Table 7.3 lists the total forces in the X, Y and Z co-ordinates calculated by the flow solver for two IVRs. Note that the fluid used in this case was air and only the aft half of the hull is considered.

Table 7.3: Forces Predicted By CFX4.1-F3D.

Total Forces (N) IVR=1.17	*X*	*Y*	*Z*
Hull Alone (no duct)	-2.5	-2.9	0.0003
Hull Forces + Duct Inlet [a]	-2.8	-3.0	0.0004
Hull Forces + Duct Forces [b]	-3.6	-1.3	-0.0069
Total Forces (N) IVR=1.25	*X*	*Y*	*Z*
Hull Alone (no duct)	-2.5	-2.9	0.0003
Hull Forces + Duct Inlet [a]	-2.8	-2.9	0.0006
Hull Forces + Duct Forces [b]	-3.5	-1.0	-0.0028

Superscript 'a' denotes the hull with the waterjet inlet, but without the duct forces being taken into account. Superscript 'b' denotes the hull with the duct, including the forces in the duct.

From these results it is possible to see how the presence of a waterjet duct affects the overall forces in the system. The resistance of the system is increased and the force in the Y direction also increased suggesting the duct provides some lift. The equivalent total forces for a higher inlet velocity ratio are also presented. Again, the presence of the duct affects the forces in the same manner. The values do not alter significantly for the higher IVR, however, the resistance of the hull and duct is slightly lower at the higher IVR, possibly suggesting better flow through the duct, and the duct also appears to produce more lift.

These hull effects suggest that if a waterjet duct is to be designed for a specific application, not only does the flow through the duct have to be studied, but the additional influence of the surrounding hull must also be taken into consideration.

7.5.5 Thrust Deduction

The flow over the hull in the vicinity of the waterjet intake is disturbed due to the suction. The boundary layer ahead of the lip is likely to be absorbed by the jet and a new boundary layer will develop on the hull behind the stagnation point on the intake lip. Vortices are also likely to occur at the corners where the duct joins the hull. Consequently there will be a difference between the bare hull resistance and the resistance of the hull with the waterjet present. This resistance augment is commonly expressed as a Thrust Deduction Fraction, t;

$$T(1-t)=R_T \tag{7.1}$$

where $$T=\dot{m}(V_e - V_i) \tag{7.2}$$

and T = Thrust,

R_T = Total hull resistance with no waterjet present,

$\dot{m}$ = Mass flow rate through the waterjet,

V_i = Inflow velocity,

V_e = Exit velocity.

Before proceeding it must be noted that this section has been presented purely for interest, in order to demonstrate how the presence of a waterjet duct has an influence on overall vessel resistance, and that CFD codes possess the ability to be used for such calculations. The results obtained have been calculated using air as the working fluid in order to obtain a direct comparison with the previous waterjet models. For this reason the aim is to illustrate the relative changes rather than absolute results. Several methods for determining the thrust deduction factors of waterjet driven craft have been published, but no single method has yet been accepted as the standard. Manufacturers tend to rely on their existing empirical databases, largely based on resistance tests, to account for the interaction effects [7.21]. The analysis presented here is based on a resistance method using some broad assumptions.

Assumptions:

Consider the following schematic model of the Series 64 hull form with a waterjet duct.

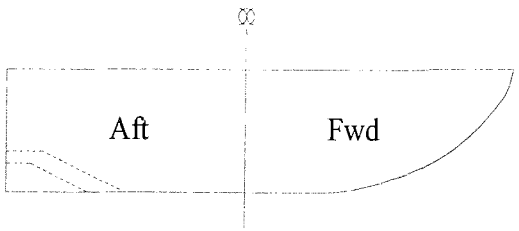

For this hull it is assumed that

$$R_T = R_V + R_R \tag{7.3}$$

where R_T = Total hull resistance with no waterjet present,

R_V = Viscous resistance,

R_R = Residuary resistance.

It is also assumed that the viscous resistance, or skin friction, can be split into forward and aft components. So Equation 7.3 can be written as,

$$R_T = R_{V_{aft}} + R_{V_{fwd}} + R_R \tag{7.4}$$

Using the Series 64 data [7.20] the total hull resistance, R_T, in air was calculated as *5.7N*, and from the CFD analysis of the aft hull alone, $R_{V_{aft}}$ was *2.48N*. So using,

$$R_T - R_{V_{aft}} = R_{V_{fwd}} + R_R \tag{7.5}$$

a value for the forward hull and total residuary resistance was found as *3.22N*. Because no further data was available on these two components of resistance ($R_{V_{fwd}} + R_R$), it was assumed that their value remained constant for the hull with or without the presence of the waterjet duct.

Now, if R_{CFD} is the resistance of the aft hull with the presence of the waterjet duct, calculated by the CFD code, a new hull total resistance is assumed as,

$$R_{T2} = R_{CFD} + (R_{V_{fwd}} + R_R) \tag{7.6}$$

Finally, assuming the thrust produced by the waterjet pump delivered the correct amount for the self-propulsion condition, i.e. the total resistance, R_{T2}, equated to the thrust, T, a thrust deduction factor, t, was calculated using Equation 7.1. Table 7.4 lists the results.

There are two thrust deduction fractions presented for each IVR, the first neglecting the duct resistance, the second including the duct resistance. Based on the assumptions listed above, the results indicate that an increase of up to 15% in resistance occurred due to interaction effects at the given IVRs for this hull and waterjet combination.

Table 7.4: Resistance Calculations.

IVR	$(R_{V_{inlet}} + R_R)$ (N)	$R_{CFD}{}^a$ (N)	$R_{CFD}{}^b$ (N)	$R_{T2}{}^a$ (N)	$R_{T2}{}^b$ (N)	t^a	t^b
1.17	3.22	2.78	3.56	6.00	6.78	0.05	0.15
1.25	3.22	2.79	3.52	6.01	6.74	0.05	0.15

Superscript 'a' denotes the hull with the waterjet inlet, but without the duct forces being taken into account. Superscript 'b' denotes the hull with the duct, including the forces in the duct.

7.5.6 Summary

As stated at the beginning of Section 7.5.5, this method was a study of the interaction effects, based on some broad assumptions, in an attempt to obtain an indication of the effects on the vessel resistance. There is still some disagreement as to how thrust deduction should be calculated for waterjet propelled craft [7.21] and little data has been published on it. Past measurements and predictions of interaction effects have, in some cases, suggested they increase hull resistance whilst, in other cases, decrease resistance. Van Terwisga [6.4] indicated a thrust deduction factor ranging from +20% to +0.5% for one hull form, but for another hull, a range of +5% to -4%, varying with ship speed. Coop and Bowen [6.6] illustrated similar findings, and Hoshino and Baba [7.9] found small positive values for one model and small negative values for a second model. It appears that interaction effects can be significant and thrust deduction factors can be either positive or negative depending on hull form, waterjet geometry and ship speed. This emphasises the importance of modelling the hull form around the duct. It has been suggested [7.21] that future optimised hull forms may feature afterbody lines that are quite different from the adapted propeller-driven hull forms of today.

This chapter has presented the development of a computational model of the representative waterjet duct, using a commercial viscous flow solver. Results from the model have been compared to data from the wind tunnel tests, and it has been shown that the calculations produce reliable solutions for the flow. Chapter 5 presented the development of a computational model of a ducted propeller, which was also shown to

produce reliable results. Now that the two models have been successfully proven individually, the following chapter couples them together in order to assess the performance of an axial-flow impeller in a waterjet inlet duct.

8. COUPLING OF THE TDP AND INLET DUCT MODELS

8.1 AIMS

Both the computational models of the waterjet inlet duct and ducted TDP have been shown and proven individually. The next stage of the work couples the viscous waterjet duct model to the potential-flow propeller model in an attempt to study the performance of an impeller under various waterjet inlet duct conditions. The duct conditions are derived from the trim and drift conditions, which were modelled in Chapter 7. In addition, a non-rotating drive shaft has been included in the CFX intake duct geometry, to study its effects on the impeller performance, and to assess the benefits of using a tip-driven impeller.

The panel code assumption of potential-flow neglects the influence of viscous flow and separation effects on the flow around bodies. These regions can have an important effect on the pressure distribution and hence total force acting on the body and it is essential that they are identified and their effects accounted for [2.11]. These effects are important, especially for off-design cases, on waterjet inlets where the presence of large separation zones can significantly change the nature of the flow arriving at the impeller. For this reason, the flow through the waterjet intake duct was not investigated using Palisupan. As described in Chapter 7, this was achieved through the use of a fully viscous RANS flow solver. Inflow velocity fields into the impeller were derived from the CFX4.1 results under various conditions of trim and drift, these were imposed into the panel model of the impeller. Because the imposed flow was obtained from a fully viscous solver, it was considered to have adequately taken into account the effects of phenomena such as boundary layers and separation.

Allison et al [1.18] provided a brief history on the design of impellers for waterjets and a good summary of the principal design methods in use. Allison et al [1.18] also described a means of coupling a lifting-surface (vortex-lattice) code to a viscous flow solver for use as a tool towards impeller design. The RANS calculation included the impeller hub and casing surfaces, and body forces distributed over the swept volume of each blade row represented the blade rows. The forces were derived from the blade forces calculated by

the lifting-surface calculation. Thus an iterative loop was initiated whereby the effective flow from the RANS code was imposed back into the vortex-lattice code, and so forth.

The interaction of the two codes was used by Taylor et al [8.1] for the purpose of the design and analysis of a waterjet pump. The vortex-lattice model addressed the blade-to-blade interactions whilst the RANS solver captured the through-flow based upon the hub and casing geometries. The entire inlet duct was not modelled. Some brief thrust and torque coefficient results for the rotor under a certain operating condition were given, but convergence problems were also highlighted. The convergence problems were encountered due to the blade forces resulting in a 'front' of change of flow quantities, which convected downstream in the initial iterations. The outlet boundary condition of constant static pressure was also incompatible with residual swirl components from the pump.

A further update on this lifting-surface and RANS coupling [6.9] compared some revised CFD predictions with water tunnel experimental results for a mixed-flow waterjet rotor, stator and housing unit operating at 1200rpm. Velocities upstream and downstream of the pump agreed well, as did the pump pressure rise and torque.

8.2 REPRESENTATIVE MODELS

8.2.1 Waterjet Intake Duct

Using the RANS flow solver, surface pressure distributions and velocity profiles through the duct and at the duct exit under various conditions of trim and drift were obtained in Section 7.4. These velocity profiles were used as the input profiles for the waterjet impeller model. In addition, the geometry of the waterjet duct from Chapter 7 has been modified to include a representative horizontal drive shaft. The new block structure of this geometry is illustrated in Figure A8.1, the shaft diameter was 40mm, which was based on an existing waterjet system with a similar duct diameter. In order to include the drive shaft the block structure and hence cell structure of the geometry had to be altered, which meant the validation of the code, carried out in Chapter 7, was not strictly justified in this case. Indeed there was no available experimental data to compare this model against. In light of this the grid dependency of this geometry was investigated.

The initial mesh used for the waterjet duct and drive shaft model consisted of 128550 cells in total, 34500 of which defined the actual half-duct model. The remainder defined the flow domain beneath the duct inlet. To study the effect of cell density, a second model was created which had a total number of 279000 cells, 90000 which defined the half-duct. The predicted pressure coefficients, *Cp*, along the top and bottom centrelines of the duct, obtained from each model were compared. Figures A8.2 and A8.3 illustrate the results, plotted in a similar manner to the pressure results in Chapter 7.

The pressure results along the top centreline (Figure A8.2) compared well between the two geometries. There is negligible difference in *Cp* values through the duct, however, the denser mesh predicted a marginally lower pressure at the ramp inlet, where the flow enters the intake. The results are also similar along the bottom centreline (Figure A8.3), although there was slightly more variation between the absolute values. The denser mesh had a tendency to produce higher pressures along this wall, with the exception of the lip location (*X=0.2*) where a lower pressure was predicted. The maximum change in pressure coefficients was seen to be approximately *±0.05*.

The trendlines shown on Figures A8.2 and A8.3 are similar to those found during the previous CFX tests in Chapter 7 (Figures A7.4 and A7.5), although the presence of the drive shaft has produced an overall increase in pressures along the top centreline. In addition, the pressures towards the lip region, along the bottom centreline at *X=0.0* and *X=0.1*, have also increased. However, there is a decrease in Cp at the inlet lip, reminiscent of the original CFX duct geometry (Figure A7.3), which was attributed to poor grid quality in that region (Section 7.3.3). Hu and Zangeneh [7.13] also saw similar changes in pressure coefficients near the lip. The drive shaft is located at approximately *X=0.2* on Figure A8.2, however, due to the lack of measuring positions, defined within the CFX command file, detail of the pressures close to the shaft has not been shown. Hu and Zangeneh [7.13] presented such measurements, which showed a decrease in *Cp* on the upstream side of the shaft, and an increase in *Cp* on the downstream side.

Using the above results it was assumed that the relative differences in the flow solution, between various test cases were adequately represented using this new CFX duct and drive shaft geometry model.

8.2.2 Representative Waterjet Impeller

The performance of the Kaplan K4-70 series propeller was modelled in Chapter 5 and it was shown that the panel code produced good predictions. Because no performance data or geometry definitions of specific waterjet impellers were readily available, generic characteristics of an axial-flow impeller were discussed with a local waterjet manufacturer [8.2]. The impeller geometry was defined using these characteristics and the blade sections were largely based on those of the standard K4-70 propeller, for which Palisupan had modelled well. It was assumed that this model was adequate enough to provide a representation of a typical axial-flow impeller [8.2], Figure 8.4.

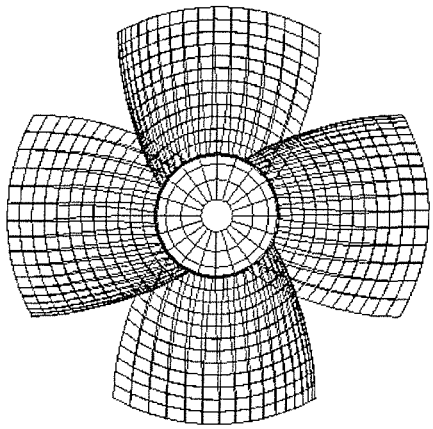

Figure 8.4 – Panel definition of the representative axial-flow impeller.

The diameter of the impeller was *248mm*, the blade area ratio (BAR) was *1.0* and it had a hub diameter of *0.3D*. The impeller was positioned in the centre of a circular cylinder, having a length of 0.1m and a similar internal diameter to the waterjet duct exit plane. Table 8.1 lists the section pitch angles.

Table 8.1: Impeller section pitch angles.

r/R	0.3	0.4	0.5	0.6	0.7	0.8	0.9	1.0
Pitch Angle	55°	60°	65°	65°	65°	65°	65°	65°

In order to aid convergence, the resultant wake pitch followed the blade section geometric pitch for a distance of *D/8* downstream of the blade, an average pitch was then imposed for the remainder of the wake. Because no experimental data was available for validation and because the impeller was based on the K4-70 propeller, the same factors for the fixed

wake pitch were used (Section 5.2.1). Although the detailed load distribution on the individual blades will be altered using this approach, the overall thrust was reproduced reasonably well (Section 5.2.1), and hence the likely upstream influence and the magnitude of the changes in total blade thrust due to the influence of the inlet could be investigated. Each impeller blade was modelled using 972 panels, which were clustered towards the leading edge of the blade. The hub was defined using 680 panels and these were distributed in order to align with the blade panels.

The impeller was run at a constant advance air speed of *17.4m/s* and three advance coefficients (*J=0.2, 0.3, 0.6*) were considered. Table 8.2 lists the conditions for which the impeller was tested.

Table 8.2: Impeller test cases.

Advance Coef^{n}, J	0.2	0.3	0.6
Wake Average Pitch (m)	0.18	0.18	0.17
Velocity field flow conditions	0^{o} Trim 7^{o} Trim -7^{o} Trim 5^{o} Drift -5^{o} Drift 0^{o} + Shaft	0^{o} Trim 7^{o} Trim -7^{o} Trim 5^{o} Drift -5^{o} Drift 0^{o} + Shaft	0^{o} Trim 7^{o} Trim -7^{o} Trim 5^{o} Drift -5^{o} Drift 0^{o} + Shaft

For all cases: Impeller advance speed = 17.4m/s. Impeller diameter = 248mm.

The impeller advance speed was defined as the average velocity based on the waterjet duct exit area and the mass flow rate obtained from the experimental results. This mass flow rate had been subsequently used as a boundary condition for the RANS flow solver.

8.3 PERFORMANCE OF THE IMPELLER

8.3.1 Impeller inflow velocity profiles

The input velocity fields for the impeller were obtained from the previous work carried out using the RANS flow solver, described in Chapter 7. The results from this code provided the three cartesian components of velocity (u, v, w) at several nodes over the impeller face plane of the waterjet duct. In addition, the velocity components in the presence of the shaft were obtained from the modified geometry, described in Section

8.2.1. These were used to define the inflow velocity field for a panel model of the impeller, Figure A8.5. The degrees of trim and drift represent the angle at which the waterjet inlet duct was rotated through relative to the oncoming free stream flow. A positive value of trim is representative of a vessel trimming bow up (Figure A8.6).

The nodal velocity values across the impeller plane were found using nearest neighbour interpolation to provide an averaged velocity at varying radii, in addition to a regular cartesian velocity distribution across the plane. These inflow velocity fields were defined within the panel code geometry file. Figures A8.7 and A8.8 plot the average axial and angular velocities across the radius of the plane for each case of trim and drift. As indicated in Figure A8.7, the only significant variations in the average axial velocities occur at radii less than *0.4R*, where both trim and drift tend to decrease the velocity. However, this region is largely occupied by the impeller hub and was unlikely to bear much influence on the blades. The axial velocities over the radii of the blade did not vary significantly due to trim, however, there was a slight increase when the duct was at an angle of drift.

Also plotted in Figure A8.7 are the average axial velocities when a drive shaft was modelled in the duct. Because of the shaft presence, the velocities are only plotted at radii greater than *0.15R*, however, the average velocities rise from the shaft radius to higher values than the other flow conditions. This was thought to be due to the smaller effective cross-sectional area at the duct exit, due to the drive shaft presence, which produced larger velocities for the constant mass flow rate. In a similar manner to the other trim conditions, the velocities decrease towards the duct wall.

The average angular velocities in Figure A8.8 illustrate how much more swirl is induced through the duct when it is at an angle of drift. Although there is some variation shown due to trim, it is a small amount and is again confined to the smaller radii where the hub would be located. External of *0.45R*, the swirl under trimmed conditions remains fairly constant, however, under conditions of drift it changes rapidly and switches direction towards the duct wall at *1.0R*. Interestingly, the average angular velocities with the drive shaft model remained relatively low, however, in a similar manner to the drift conditions,

a rapid increase in the negative direction occurs towards the duct wall. The reason for this is uncertain, but it might be an effect of a flow shadow [6.3] behind the drive shaft.

Table 8.3 provides a summary of the maximum and minimum values and the standard deviation of a typical set of velocities, which were used to calculate an averaged radial velocity value.

Table 8.3: Summary of velocity distribution at 0.7R (m/s).

		Axial	Radial	Angular
0 Degrees Trim	Maximum	18.79	1.34	1.72
	Minimum	17.27	0.13	0.00
	SD	0.46	0.62	0.93
7 Degrees Trim	Maximum	18.91	0.98	1.34
	Minimum	17.45	0.19	0.00
	SD	0.47	0.55	0.38
-7 Degrees Trim	Maximum	19.16	1.59	2.38
	Minimum	17.63	0.10	0.00
	SD	0.93	0.67	0.77
5 Degrees Drift	Maximum	21.45	1.21	4.48
	Minimum	15.80	0.01	0.00
	SD	2.03	0.58	2.51
0 Degs + Shaft	Maximum	21.73	1.91	0.80
	Minimum	15.41	0.01	0.00
	SD	1.50	0.90	0.43

Table 8.3 indicates an increase in the maximum axial velocity, as the flow becomes more localised under conditions of trim and drift. The greatest velocity existing when the drive shaft was present. In addition, the standard deviation suggests greater variations of axial velocity under trim and drift, 5^o drift exhibiting the largest deviation. Little change is evident for the radial velocities, but the drive shaft model possessed the highest value and the greatest standard deviation. However, this was not the case for the angular velocities. As expected, the angular velocities were more pronounced at 5^o drift when, increasing swirl was induced into the flow. These results present an indication to the types of flow present at the duct exit plane, under various operating conditions. However, it must be noted that a different geometry mesh was used for the drive shaft model, and Table 8.3 represents the results at only one radius.

Figures A8.9 and A8.10 illustrate the CFX predicted axial velocity profiles at the waterjet half-duct exit plane for zero degrees trim with and without the presence of the drive shaft. Figure A8.9 shows a marked increase in velocity towards the upper half of the plane, and a decrease in velocities towards the bottom dead centre (BDC) position. A similar reduction of velocities at this location was also seen by Watson [1.4]. When the drive shaft was included in the model, Figure A8.10, the flow towards the lower half of the plane exhibited similar patterns, however, there was also a small area of lower velocities above the shaft at TDC. It is also noted that the velocities have increased slightly from Figure A8.9 to A8.10.

8.3.2 Impeller Thrust

A panel code model of the impeller was run for each case of trim and drift outlined above at the three advance coefficients listed in Table 8.2. The output from the code provided relevant components of total force on the body which were converted, in the usual manner, into thrust coefficients, K_T. Using rotational symmetry only one blade of the impeller and a quarter of its hub were defined in the geometry file for the panel code. The results provided a time averaged propeller performance.

Figure A8.11 presents the results for the impeller on a standard K_T, J chart. The variation in thrust between angles of trim was predicted to be minimal, ±1% K_T. Likewise, similar results were obtained between drift angles of $\pm 5^o$. However, the change in overall thrust between the duct at an angle of trim and an angle of drift is larger. Thus indicating that the impeller in this inlet is much more sensitive to conditions of drift rather than trim. This is likely to be due to the sharp edge on the sides of the entrance to the duct, present in the CFX model of the duct.

The small change in thrust under conditions of trim can be explained due to the fact that the input velocity profiles remained fairly constant for each angle of trim considered. This was apparent in Figure A8.7 where most variation in the average velocity was seen in the hub region. The flow regime under conditions of drift is less uniform and as such a slightly lower thrust is obtained. Although the inlet duct geometry was symmetrical about its centreline, a difference in K_T values between the two cases of drift is to be expected as

the flow will exhibit an angular velocity, or swirl, which will either be of benefit or detriment to the impeller performance.

The impeller thrust obtained from the duct velocity field with the presence of the drive shaft is also plotted in Figure A8.11. There is clearly a marked offset between this condition and the previous trim conditions with no shaft. The drive shaft has the effect of decreasing the predicted thrust by approximately 28% across the range of advance coefficients. The reason for this is thought to be partly due to the increase in axial velocities (Figure A8.7) experienced because of the smaller effective cross sectional area and the constant mass flow rate used. This would have the effect of altering the effective advance coefficient of the impeller, thus reducing the thrust output. However, further experimental analysis is required to fully verify these calculations.

Although the changes in mean thrust between conditions of duct trim and drift are as expected, the actual magnitudes involved are small. This is thought to be due to the use of a constant mass flow rate at the duct exit plane in the original CFX models. Thus the difference in thrust can be attributed effectively to a change in relative rotative efficiency of the impeller.

8.3.3 Impeller Blade Loadings

It is essential to minimise dynamic blade loads and pressure fluctuations, not only to minimise losses, but also fatigue failure [8.3]. To study the likely variation in cyclical force acting on a blade of the rotating impeller, the entire four blades and the hub were defined in the panel code geometry file, creating a model of 4508 panels. The code was then run to solve the impeller as it rotated through quasi-steady intervals of 10^o within the cylinder using a regular cartesian grid of inflow velocities derived from the RANS calculations. The model was run for the same flow conditions as above, but only for the advance coefficient of *0.3*.

Figures A8.12 to A8.17 plot the resultant axial, radial and circumferential loads, made non-dimensional in the same manner as thrust coefficient K_T, acting on a single blade as it completes one revolution under the various inflow conditions. In all cases the angular forces are relatively small and tend to sum to zero over the revolution. The radial

components show fluctuating negative values throughout the cycle and indicate a mean K_T of *-0.02* for each case.

Figure A8.12 plots the result for the impeller in an ideal uniform inflow field, of similar average velocity to the conditions obtained from the RANS model. As expected, the axial thrust loading on the blade remains constant, at $K_T=0.12$, throughout the revolution. Figures A8.13 to A8.15 illustrate the results when the impeller is subjected to the trim and drift inflow fields derived from the CFX models. The axial thrust component is predicted as having two peaks of thrust at 80^o and 270^o for all cases, with the thrust dropping quite rapidly to a fairly constant level through the lower half of the section. The results for 0^o, 7^o and -7^o trim are very similar, although there exists a single higher peak of thrust at TDC at 7^o trim (Figure A8.14). A similar overall trend is followed for the axial values at 5^o drift (Figure A8.16), however the values are marginally lower on one side of the duct.

Similar results are plotted, in Figure A8.17, for the case when the drive shaft is included. A noticeable effect is the lower axial K_T values throughout the revolution. The average thrust coefficient is approximately $K_T=0.10$, rather than $K_T=0.12$ for the previous conditions. This reduction in thrust loading is similar to that seen in Figure A8.11. Also evident are marginally lower peak values in the radial and angular force components. Although the thrust is reduced because of the presence of the drive shaft, Figure A8.17 indicates less severe fluctuations in the blade loadings, which would result in lower vibrations, and better fatigue properties. Whether this phenomenon is true for all cases involving a drive shaft, or whether it is localised to this particular test requires further study.

Figures A8.18 and A8.19 illustrate the predicted axial velocities at several vertical sections through the half-duct for zero degrees trim, with and without the presence of the drive shaft. Similar flow patterns can be seen near the duct inlet, at the right hand side of the figures, but the presence of the drive shaft, Figure A8.19, protruding through the ramp wall results in a shadow of low velocities above the shaft. Further downstream the duct these lower velocities slowly make way for higher velocities, which spread from around the side of the shaft. The final velocity fields at the duct exit plane are as described in Section 8.3.1. Interestingly, Figures A8.18 and A8.19 also indicated low velocity regions

along the lower wall of the duct, which agrees with the wind tunnel flow visualisation in Chapter 6.

Table 8.4 lists the values of the maximum, minimum and standard deviation of the total integrated forces on a single blade under the different inflow conditions tested.

Table 8.4: Summary of resultant non-dimensional loads on a single impeller blade.

		Axial	Radial	Angular
0 Degrees Trim	Maximum	0.141	0.002	0.031
	Minimum	0.114	-0.034	-0.031
	SD	0.008	0.012	0.022
7 Degrees Trim	Maximum	0.141	0.002	0.031
	Minimum	0.114	-0.033	-0.031
	SD	0.009	0.011	0.021
-7 Degrees Trim	Maximum	0.142	0.002	0.031
	Minimum	0.113	-0.034	-0.031
	SD	0.010	0.012	0.022
5 Degrees Drift	Maximum	0.141	0.002	0.031
	Minimum	0.102	-0.033	-0.031
	SD	0.012	0.012	0.022
0 Degs + Shaft	Maximum	0.1048	0.002	0.022
	Minimum	0.0840	-0.022	-0.022
	SD	0.004	0.008	0.005

Table 8.4 indicates little change between the maximum and minimum load values for each flow condition with the exception of the drive shaft model, which resulted in lower axial blade loadings. The standard deviation shows a greater variation in axial force on the blade when the impeller is under conditions of trim and drift. The greatest variation was evident at 5^{o} drift for which the inflow velocities were least uniform. This further illustrates the sensitivity of the unit to changes in drift under which detrimental, non-uniform impeller inflow fields are produced. Values for the radial and angular forces show little difference between the cases, however, the standard deviation is lower with the presence of the drive shaft.

8.4 INTERACTION OF WATERJET IMPELLER AND INLET

It is relatively straightforward to impose velocity results obtained from CFX into the panel model of the impeller. However, the reverse is full of complications. As a result of this, in order to study interaction effects between the inlet duct and impeller, the inlet duct was also modelled using Palisupan.

The surface panel model of the inlet is shown in Figure A8.20, with a single blade of the impeller and hub in place. This inlet duct was defined using 2000 panels distributed over a plane representing the hull surface and the internal ducting. The sections used for the inlet duct geometry definition were the same as those used for both the experimental model and CFX model.

For the purpose of investigating the upstream influence of the impeller on the performance of the waterjet two approaches were adopted. Firstly, the flow through the impeller and duct was solved using the IVF method (Section 2.3.1) for the zero trim condition. However, this neglected the effects that boundary layer development has on limiting the mass flow rate. So a second approach was adopted which assumed that the viscous flow effects were accounted for in the onset velocity field into the impeller. For this approach rather than including the geometry of the impeller, the impeller velocity wakefield, obtained from the previous studies (Section 8.3.2), was imposed at the duct exit plane. Although, the absolute duct forces (viscous dominated) were not calculated, relative changes in force levels due to the impeller could still be estimated for alterations of trim and drift.

The full interaction problem was run for the impeller and inlet at 0^o drift and 0^o trim. The calculation required significant computer resources. At each cycle, for every duct panel, between 10 and 35 velocities were calculated and then averaged. Convergence of propeller thrust and duct forces occurred after 12 complete cycles. The lack of the correct viscous resistance was manifest in the reduction in impeller thrust from $32N$ within the cylinder to $17.6N$ with the duct, reflecting a larger induced velocity at the impeller plane (higher J) and thus reduction in thrust. As a matter of note the calculated duct axial force (X direction) was $2.3N$ which was much higher than the CFX predicted value of $0.766N$

(Section 7.4.3). The high value reflecting the large duct speeds and lower pressures on the duct lip.

The effect of drift and trim on the duct forces using the second approach, where the impeller wakefield in the presence of the RANS predicted nominal wake was imposed at the duct exit, was obtained much more rapidly. Each run modelling the duct with an imposed, impeller generated, velocity field took 15 minutes on a workstation. Table 8.5 presents the percentage change in duct forces (X along the duct axis and Y in the vertical direction), relative to that component of force acting on the duct without the impeller present, for the trim and drift conditions.

Table 8.5: Change in Duct Force Due to Impeller.

Test condition	%Change in X	%Change in Y
Straight ahead, 0 Degrees Trim and Drift	34.2	53.0
5 Degrees Drift	33.4	52.4
7 Degrees Trim	7.5	7.5
-7 Degrees Trim	-3.4	3.4

Table 8.5 indicates that the presence of the impeller causes the greatest change in forces at the zero trim, and 5^o drift condition. However, it must be noted that the poor grid resolution at the inlet lip resulted in a large discrepancy in the absolute pressure force between the positive and negative trim conditions with those for drift and straight-ahead conditions. However, these values were not strongly influenced by the impeller force and hence it was expected that the relative change was representative of the local change in flow conditions due to the presence of the impeller.

8.5 SUMMARY

A fully viscous CFD RANS solution of the flow through a waterjet intake duct has been coupled to a potential-flow panel code, which modelled a rotating axial-flow impeller. Velocity results for the waterjet intake duct, operating at various trim angles and with the presence of a drive shaft, have been imposed into the panel code model of a typical impeller. The resultant impeller thrust and blade loadings have been studied under these various inflow conditions. Initial results suggest that when the intake duct is operating at

off-design flows, i.e. at angles of trim or drift, there is a small, but measurable, decrease in impeller thrust, especially due to an angle of drift. The presence of a drive shaft was seen to reduce the thrust coefficient by up to $K_T=0.11$ across the range of advance coefficients, however, the resultant blade loadings were less severe. This would result in lower vibrations, and better fatigue properties, but whether this phenomenon is true for all cases involving a drive shaft, or whether it was localised to this particular test case requires further study.

The possibility of being able to investigate the interaction between a waterjet intake duct and its impeller has been illustrated. Although limited with the assumption of a constant mass flow boundary at the duct exit during the initial CFD investigations, and the subsequent average impeller advance speed based on this mass flow rate, the methods have yielded reasonable, and potentially useful results. With future refinement to the models, it should be possible to predict what effects a change in the duct geometry has on the overall performance of the impeller and the waterjet unit as a whole.

The results obtained have not been validated due to the lack of experimental data. They have been accepted on the grounds that they follow trends that might be expected for such flows. All CFD codes provide the engineer with a prediction of how the flow might behave under specific, often limited, conditions. They are expectations which might, or might not, live up to reality. These results must therefore be taken as an estimate of the flow behaviour. However, it is expected that the developed method could be used as the basis for developing the preliminary design of a large-scale model duct and impeller for testing in a wind tunnel. Likewise, it has the potential for use as part of the waterjet design process, for investigations of cavitation inception, noise and induced vibration and impeller shape optimisation.

Having seen the potential benefit of increased waterjet impeller performance due to the removal of the drive shaft, Chapter 9 will discuss the likely implications of using a tip-driven impeller system.

9. WATERJET TDI - IMPLICATIONS

9.1 AIMS

The work presented so far has included a study of both a waterjet inlet duct and a tip-driven ducted propeller. The CFD model used to study the TDP has been coupled to the model of the inlet duct in an attempt to model an axial-flow waterjet impeller. Further development from this study considered the possibility of using tip-driven impellers in waterjets, and the effects of the presence of the drive shaft, through the inlet duct, were investigated in Chapter 8. It was predicted that eliminating the drive shaft resulted in a performance gain for the axial-flow impeller.

This chapter aims to assess the implications, both beneficial and detrimental, of using a tip-driven system for a waterjet impeller. The discussion concentrates on an electromagnetic drive system because this has been studied throughout the previous chapters, however, some of the aspects could also apply to a mechanical driven system. The possible benefits and limitations are considered from both a performance and practical point of view. Finally a brief case study is described.

9.2 BENEFITS OF A TIP-DRIVEN IMPELLER

The most obvious hydrodynamic benefit is the elimination of the drive shaft and bearing, which protrude through the top wall of the duct. It was shown in Chapter 8 that the removal of the drive shaft results in an increase of impeller thrust. In addition, it eliminates difficulties with shaft alignment and duct manufacture. It is generally the case that larger waterjet units are supplied to the shipyard without an inlet duct. This component has to be constructed by the shipyard [9.1], in addition, the forward bearing, mounted on top of the inlet or set into the aft bulkhead, and stern seal also have to be fitted by the shipyard. The resultant tolerances for shaft line-up therefore tend to be quite onerous [9.1]. Figure A9.1 illustrates a schematic installation of a typical shaft-driven axial-flow waterjet pump. Figure A9.2 is a representation of the same duct with an ETDI installation, note the unobstructed inlet duct. A further possibility of using this type of

drive is the potential of installing more than one impeller in series, thus producing a multi-stage pump. However, the implications of this would require further research.

In addition to reducing shaft alignment problems, the lack of drive shaft should also mean manufacture of the inlet duct is more straightforward, and less time consuming. A lighter structure might also be able to be used, having no need for a shaft support, reducing the weight of the jet system.

As a waterjet constitutes lost buoyancy, or added weight, it is beneficial to keep the unit as short as possible, however this means an increase in the ramp angle [7.18]. The ramp angle, also dictated by the height of the pump axis and engines above the base, must remain as small as possible for minimal disturbance. Use of a tip-driven impeller would disassociate the ramp angle from the position of the engines. However, the height of the inlet would still be constrained by the diameter of the impeller, and hence the drive system, at the transom.

There is a trade off between a sufficiently large transom and large impeller diameter for better efficiency, and a sufficiently modest transom to keep hull resistance low [9.2]. The impeller diameter also prescribes the overall weight of the jet system. In addition, the tunnel as part of the vessel will produce suction and pressure areas, which increase or reduce drag in different operating conditions [1.17]. It is therefore evident that a final inlet design is a compromise, between several variables, which meets the specified requirements as best as possible. Ducts are usually designed for the cruise condition under which the vessel will spend most of its time. However, a tip-driven impeller results in greater flexibility of the tunnel dimensions, allowing for possible enhanced optimisation.

If the TDI was designed and built in a similar manner to that of the TDP by the Harbor Branch Oceanographic Centre [1.10], i.e. possessing the ability to allow debris to pass through the centre of the propeller, it could eliminate the necessity of an intake grill, which is another source of loss. But this is only possible if the thrust bearings are situated at the periphery of the impeller, which for the high thrust loads in question, could pose a significant design challenge.

The intake grill on the inlet of a waterjet duct has not been modelled during any of the CFD analysis found in the published literature. The reason is due to the fact that the geometry of the grill adds far too many complications to the geometric model of the flow domain. However, evidence has shown that the presence of a grill can have a noticeable effect on vessel performance, 2 knots off vessel top speed has been quoted [9.1]. For larger jets (diameter ≥ 650mm), opinion becomes divided as to whether an intake grill is necessary or desirable. If grills are used, not only will they disrupt the flow through the duct even further, especially at angles of drift, but they themselves are also subject to high frequency oscillatory forces and have to be designed to withstand these loads, in addition to minimising losses.

Should an electric drive be used, the only connection between the motor and the engines, or generators, is a power cable. This provides great flexibility for the location of the power plant in the vessel. It also means that waterjet units can be used in narrow hulled vessels in which engine size might have previously been a constraining parameter. There also exist possible implications for podded waterjet designs, which at present rely upon a relatively long duct to draw water up to the shaft driven impeller. A TDI means the impeller could be situated at a lower height, reducing the ducting length and hence the losses associated with it.

9.3 LIMITATIONS OF A TIP-DRIVEN IMPELLER

Locating the driving mechanism at the transom results in increased weight towards the stern of the vessel, effecting the trim and resistance of the vessel. However, the extra weight would only be a fraction of the total machinery mass and positioning the power plant further forward could reduce the extra trimming moment. This flexibility is available with an electric drive.

It is essential to be able to transmit the waterjet thrust forces reliably to the vessel. The significant part of the propelling force is carried by the impeller blades, whilst the remainder arises from the rearward facing surfaces in the duct [7.18]. The impeller forces must be transmitted to an interface, usually a flange connection between the inlet duct and jet at the transom, before being absorbed by the ship. In the case of a tip-driven unit, all

the thrust developed by the blades would have to be transmitted through the transom, possibly requiring additional thrust bearings. Svensson [1.19] claimed a better position for the thrust bearings, rather than along the shaft, is in the impeller hub, transmitting the load to the transom. This arrangement would be essential for the TDI. However, contrary to Svensson [1.19], Warren et al [9.1] claimed the transom area, so far as waterjet loads are concerned is redundant, the duct itself is so much stiffer. However, Warren et al [9.1] may have employed a different bearing installation from the arrangement which Svensson [1.19] discussed.

Concern is expressed over the ease of installation of an electromagnetic drive. However, if the TDI is manufactured as a modular unit, the construction of the drive system on the transom should not be too onerous. Components may include the stator, the impeller and rotor mounted in a bearing and the pump outer casing. Figure A9.2 illustrates schematic diagrams of these components. For the layout shown, the stator would first be attached to the transom, at the duct exit. Having been assembled beforehand, the impeller and rotor, mounted in the hub bearings supported by the hydrodynamic stator vanes, can then be brought into position and fixed. Finally, the remaining nozzle shell and reversing mechanism can be attached. The delicate stage of construction would be positioning the impeller and rotor within the stator ring. As with the prototype TDP, strong magnetic forces exist between the two components, however, the impeller could be eased into position using guide bolts. It has been suggested [9.3] that this motor arrangement would not be practical at high powers in the region of 1MW. The magnetic forces in this case would be too strong, and the threading of the rotor into the stator could not be controlled safely. 500kW was suggested as the practical maximum power. This does not nullify the concept, it merely limits the drive mechanism to smaller waterjet units.

A potential problem with the smaller TDP thruster units in contaminated waters is the accumulation of debris in the gap between the stator and rotor, leading to erosion of protective coatings. Whether this would be such a problem in a waterjet system is difficult to say. However, the short-term solution to this would be to use a brush-type seal around the periphery of the gap to keep larger pieces of debris out without too much friction loss. A more permanent solution might be to provide some type of flushing mechanism, which clears any trapped particles away.

The major deciding factor of whether to use a new propulsion device or not is the cost. Will it be cheaper to buy, run or maintain than existing machinery? At this stage of the study it is difficult to assess. There are numerous factors to be taken into account, from the initial cost of manufacturing the individual components, to the efficiency of the engines, or generators in producing the necessary power. One cost which is anticipated to reduce, is the cost of installing the jet unit. As described above, the installation only requires components to be attached to the transom, no problems exist with shaft alignment. However, one cost which is likely to rise is the price of the impeller with the rotor ring attached to the blade tips. The electric motors themselves need not be expensive if built in sufficient quantities, the expensive process is joining the rotor to the impeller blades. If manufactured in large enough quantities, there is no reason why it should be any more expensive than existing jet units. However, it is difficult to assess the running costs at this stage (generator efficiencies, longevity of impeller/rotors, etc...), without further operating experience.

9.3.1 Size of the Electric Motor

The electric motor used in the prototype TDP can deliver 5.5kW, at an efficiency of 88%, at its thermal limit [9.3], although the nominal rating of the propeller was 2kW. At 2kW, the motor has a higher efficiency of approximately 92% (Figure 4.6), which was one of the reasons for down-rating the motor. The other reason was mechanical strength constraints: the motor could not be made smaller than it is. The typical power range for waterjets is much greater than this. Power ratings of between 30kW and 260kW have been quoted for a jet with a similar impeller diameter to the ETDP [9.4,9.5]. An important question therefore arises; how does the size of the motor change with power requirements?

The power, P, of an electric motor can be related to its basic dimensions and electric and magnetic loadings by [9.6]:

$$P = kBA\left(\frac{\pi D^2}{4} L\right)\omega \qquad (9.1)$$

where B is the magnetic flux density, or magnetic loading, in Tesla, A is the electric loading in amps/m, ω is the angular speed of the motor in rads/s, D is the diameter of the stator bore, L is the active length of the rotor and k is a constant that depends on the type of motor and the particulars of its windings. In the case of the brushless Permanent Magnet (PM) motor used for the prototype TDP, k is approximately equal to 2. The expression between the brackets $(\pi D^2 L/4)$ is the volume of the motor, V_m.

The magnet and electric loadings, B and A, are also largely dependent upon the type of motor. In this case, B=0.4T, which is lower than usual because of the relatively large gap between rotor and stator. A typical value for PM motors is B=0.8T. The electric loading is defined as the total rms ampere conductors in stator slots per rotor peripheral length,

$$A = \frac{N_c I}{\pi D} \tag{9.2}$$

where N_c is the number of conductors around the stator diameter, and I is the current in amps. It can therefore be assumed that the value of kBA remains fairly constant for a particular motor type. So it can now be written:

$$P = k_2 V_m \omega \tag{9.3}$$

where $k_2 = kBA$.

and since torque, $Q = P/\omega$, it can be assumed

$$Q = P/\omega \propto V_m \propto motor\ mass. \tag{9.4}$$

For a propeller producing constant thrust, $I \propto Q$, and hence

$$I^2R \text{ loss} \propto Q^2 \tag{9.5}$$

So initially, using Equations 9.3 and 9.5, in order to keep the motor volume as small as possible for a given power, or to increase the efficiency for a given motor volume, it looks beneficial to run the motor at a high speed, low torque condition. From the electric motor point of view this appears to be a reasonable compromise, since the power requirement

does not vary significantly between the high speed and the optimum power condition, δP. Figure 9.3 illustrates the typical relationship between power, torque and propeller pitch ratio, for a constant thrust [9.7].

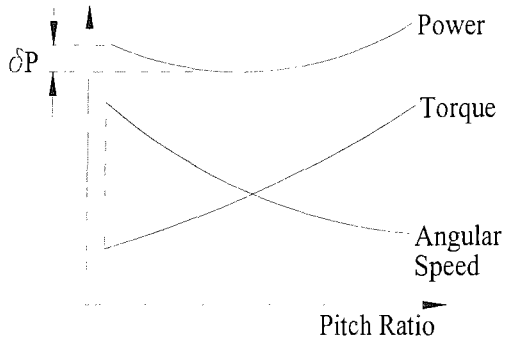

Figure 9.3 - Typical plot of motor power and torque versus pitch ratio for a propeller delivering constant thrust.

However, for the application considered in this study there is an additional source of loss in the form of friction loss, within the gap between the rotor and stator. This gap loss, P_G, is proportional to ω^3 [9.8], and is therefore minimised if a low motor speed is used, which contradicts the previous requirements. The friction loss in the prototype thruster was estimated to be 100W at 1200rpm [9.9]. Previous studies have shown that the optimum design speed occurs when the power friction loss is approximately equal to the I^2R loss [9.8]. It is possible to reduce the speed of the motor, for a given thrust output, if the propeller pitch is increased. However, increasing the pitch also increases the torque requirement which, assuming a fixed motor dimension, increases the predominant ohmic loss in the motor [9.10]. However, the ohmic losses can be minimised by using a longer rotor active length, L, and with careful selection of motor length and propeller pitch, the thrust efficiency can be maximised [9.10].

Stator Thickness

The motor volume in Equation 9.1 only takes account of the length and internal diameter of the stator. A further consideration is the thickness of the stator core, which determines the overall diameter of the motor. The core length, L_c, or stator thickness, is proportional to the magnetic flux, ϕ, carried through it, and

$$\phi = BA_p \tag{9.6}$$

where A_p is the pole area.

Hence for a given magnetic flux density, B, as the number of poles is increased, the stator core thickness can decrease, Figure 9.4 illustrates this with schematic diagrams of basic 2 and 4 pole motors.

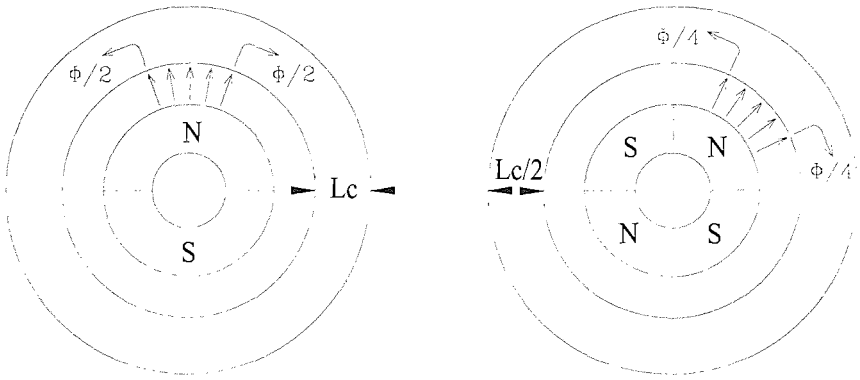

Figure 9.4 - Schematic diagram of 2 and 4 pole PM motors.

However, it is not always practical to increase the number of poles in order to reduce the size of the stator. In the case of the prototype motor there are three stator teeth for every pole, around which the windings are wound, which have to be wide enough to carry the magnetic flux without saturating. If a greater number of poles are used there will come a point when the teeth are too thin and too difficult to manufacture. Furthermore, with a greater number of poles, a larger proportion of magnetic flux is lost between adjacent poles. The prototype TDP uses 24 poles, which is adequate for diameters of between 200-300mm [9.3]. However, as the stator diameter increases, the core thickness, as a proportion of the diameter, decreases.

9.4 CASE STUDY FOR AN ELECTROMAGNETIC TDI

Consider a waterjet system with a similar impeller diameter to the diameter of the ETDP, i.e. 250mm. Using manufacturer's data [9.5], for a typical operating condition, consider

the delivered thrust at bollard pull conditions, zero vessel speed, to be about 6.5kN. This can be achieved with approximately 90kW, and the shaft speed range for this power lies between 2125 to 3500rpm, depending on impeller. A summary of this condition is given in Table 9.1.

Table 9.1: Typical characteristics of a waterjet unit with impeller diameter ~ 250mm.

Bollard Thrust (kN)	6.5
Power (kW)	90
Shaft speed range (rpm)	2125 to 3500
Angular velocity (rads/s)	223 to 367
Torque (Nm)	418 to 254

Assuming that the characteristics of the electromagnetic motor are similar to those for the prototype TDP, and these basis values are designated by suffix 1, i.e. P_1=2kW, D_1=0.25m, L_1=0.028m, and ω_1=125.67rads/s. We know,

$$\frac{P_2}{P_1} = \frac{\omega_2}{\omega_1} \qquad \text{for a given motor volume, } Vm \qquad (9.7)$$

$$\frac{P_2}{P_1} = \frac{Vm_2}{Vm_1} \qquad \text{for a given motor speed, } \omega \qquad (9.8)$$

and

$$\frac{P_{G2}}{P_{G1}} = \left(\frac{\omega_2}{\omega_1}\right)^3 \qquad (9.9)$$

where suffix 2 denotes the values for the modified impeller motor.

To keep the gap friction losses as low as possible, consider the new motor speed to be at the lower range of the quoted values, say 2200rpm. From Equation 9.7, this would result in a power increase to P_2=3.7kW, which is still within the thermal limit of 5.5kW. A secondary result is to increase the gap friction by 6 times. Now for this speed the volume of the motor needs to be increased to obtain the power required. However, because the diameter is fixed at 0.25m only the length can be altered. Using Equation 9.8, the length would need to be increased by 24 times, resulting in L_2=0.69m, which is not practical.

Further possible size and speed combinations are presented in table 9.2. Cases 5 and 6 have been presented in Table 9.2 to demonstrate the effect of substantially reducing the length of the motor by increasing its diameter.

Table 9.2: Possible motor characteristics to absorb 90kW power.

	Power (kW)	rpm	L (m)	D (m)	Unit Gap Loss due to speed (1 unit ≈ 100W)
Basis Motor	2	1200	0.028	0.250	1.0
Case 1	90	2200	0.687	0.250	6.2
Case 2	90	2500	0.605	0.250	9.0
Case 3	90	3000	0.504	0.250	15.6
Case 4	90	3500	0.432	0.250	24.8
Case 5	90	2500	0.300	0.355	9.0
Case 6	90	2500	0.421	0.300	9.0

However, the unit gap friction losses shown in Table 9.2 are not only a function of the motor speed. The gap losses are also proportional to the coefficient of friction, C_f, gap length and R^4 [9.8], where R is the radius of the rotor, Equation 9.10.

$$P_G = \frac{C_f}{4}\pi\rho\omega^3 R^4 L \tag{9.10}$$

where C_f is given by [9.8]

$$C_f = \frac{1}{16}\left[\log\left(\frac{\varepsilon}{3.7}+\frac{5.74}{R_n^{0.9}}\right)\right]^{-2} \tag{9.11}$$

where ε is the relative surface roughness and the Reynolds number, R_n, is based on the diameter and peripheral speed of the rotor. Taking the size of the gap into account increases the gap power loss by a considerable amount. Table 9.3 illustrates the total increase in gap losses, as a function of speed, length and diameter.

Table 9.3: Total increase in gap loss, taking into account gap size.

Case	Basis	1	2	3	4	5	6
Total Unit Gap Loss	1.0	133.7	166.5	231.7	306.2	356.1	248.4
% of design power	5.0	14.9	18.5	25.7	34.0	39.6	27.6

Comparing cases 5 and 6 in the above tables it can be seen that, in terms of the gap loss, it is more beneficial to increase the length of the motor than the diameter. This case study considered the power of the basis motor to be increased to 3.7kW, however, it has been suggested that 5.5kW can be achieved before its thermal limit is reached. This increase in the basis power would result in smaller dimensions than those listed in Tables 9.2 and 9.3.

9.5 SUMMARY

Benefits and limitations of a tip-driven waterjet impeller have been outlined, and the possibility of using this drive mechanism in a waterjet installation has been discussed. Studying the drive system from the view of replacing the shaft driven impeller with a unit similar to the prototype TDP has shown that unless a fundamental property of the motor can change, it seems that there is little use for this type of electromagnetic drive. The motor simply cannot deliver the required powers in a small enough package. The only uses would be confined to small work-boat type vessels with small waterjets and low power requirements. There is little use in converting these small vessels to electric drive. Much greater powers than 90kW are achievable using larger motor diameters, however, the powers do not match the requirements of the waterjet units with similar dimensions.

This is not to say the concept of tip-driven waterjet impellers should be rejected. For a full analysis, the overall view of the propulsion system has to be taken into account, including the implications of changes to the power plant, and possible changes to the intake duct design. In addition, there still exists the possibility of using mechanical drives. With only a gear mechanism at the transom, a mechanical TDI results in less physical volume and lower weight towards the stern of the vessel. It offers similar benefits such as easier assembly and integration into the hull, and potential performance improvements, from the hydrodynamic point of view. However, there exists the problem of sealing the drive around the periphery of the impeller without creating excessive friction loss, and the location of the power plant is constrained through the use of a drive shaft. It is believed that a mechanical drive, able to cope with higher powers, would offer a better compromise for larger waterjets, however, there exists the question of whether the extra mechanical losses curtail the hydrodynamic performance gains. Further investigations into this area are required.

The fact that only an axial-flow impeller has been considered during this study does not mean the proposed drive system is unsuitable for mixed or centrifugal pump systems. The drive would still work for these pumps, although, changes would be necessary for the blade tip to rotor fastening.

Computational methods have been developed to study the performance of waterjet intake duct and impeller performance. This chapter has discussed the implications of using a tip-driven impeller in a waterjet propulsion system, based on findings from the previous chapters. Chapter 10 will discuss the conclusions of the work, including observations that have been noted during the study and areas which would benefit from further research.

10. CONCLUSIONS

The use of a tip-driven impeller in a waterjet propulsion system has been proposed and the implications assessed. It has been seen that the concept offers potential benefits in the form of hydrodynamic performance improvements, easier assembly and integration into the hull, and greater flexibility in machinery location.

Although there are several benefits to using a tip-driven impeller, the use of an electromagnetic drive is limited by the physical size of the motor required. Based on the motor characteristics of the prototype TDP, an ETDI would only be applicable to the smaller range of waterjet systems, and the lower power requirements. A mechanical TDI, however, would require less physical volume than the equivalent electric motor, for a given power, but the position of a drive shaft and necessary machinery would be constrained. There is also the problem of sealing the drive without creating excessive friction loss. It is believed a mechanical drive offers a better compromise for the larger waterjets, however, there exists the question of whether the extra mechanical losses curtail the hydrodynamic performance gains.

If either the electrical or mechanical losses can be minimised by future developments, a tip-driven impeller does offer the potential to increase performance of a waterjet system, with the added benefits listed above.

10.1 SECONDARY OBSERVATIONS

Further to the main conclusion, several stages during the study have yielded their own observations and conclusions. The findings have been broken down into five different sections:

10.1.1 Prototype TDP Design and Manufacture

A prototype, 250mm diameter, Electromagnetic Tip-Driven Propeller (ETDP) unit has been successfully designed and built. The ETDP used a 2kW permanent magnet motor to drive the propeller at speeds of up to 1200rpm, and it was designed to be symmetrical about the propeller plane, in order to develop equal thrust in both forward and reverse

directions. A dynamometer and support framework has been constructed for the unit, and the thruster can be tested in the towing tanks at the University of Southampton and at Southampton Institute. The thruster can be tested at various advance speeds in both forward and reverse directions with different duct section shapes, and different hydrodynamic stator angles of attack. As a prototype, the thruster was designed specifically for experimental testing, however, tests have shown that the thruster design has the potential to be used as a practical manoeuvring and control device on underwater vehicles.

During the design and manufacture of the prototype some difficulties were highlighted. Possibly the most challenging stage of construction was attaching the propeller to the rotor ring, however, a final production version may be free of such difficulties if different methods and materials are used. A further complexity was sealing the rotor with epoxy, for which a special mould was made and spun on a lathe with the rotor. In addition, because some components were designed to operate at different angles of attack, they proved more difficult to manufacture. However, most of the problems encountered were largely due to the fact that this was a prototype. If such a unit was to go into production, several stages of the construction could be simplified. A major advantage of the tip-driven system is that the supporting bearings need not be located along the centreline of the thruster. There is the possibility of locating them around the periphery of the rotor, which results in a clear flow into the propeller.

10.1.2 Tank Testing of a Tip-Driven Propeller

The prototype ETDP has been successfully tested in two towing tanks and the concept of driving the propeller via the blade tips using an efficient motor has been proven to work. Comprehensive bollard pull and dynamic tests were carried out on the prototype thruster to evaluate its performance, and a detailed database of results has been obtained. These tests included a full range of advance speeds, propeller revolutions, duct geometries and variation of stator angles. The thruster produced about 600N of thrust for a propeller power input of 2kW. Within the power range of 0.5-2.2kW the motor demonstrated an efficiency of 90%.

At bollard pull conditions, the thrust output was about 20% lower than the standard Kaplan K4-70 propeller in Marin duct 37. It was possible to identify three likely contributions to this loss of performance:

a) The use of a symmetrical propeller will reduce performance. CFD results have indicated up to 20% reduction in output thrust when symmetrical propeller section shapes are used, compared to the original Kaplan asymmetric profile.
b) The design pitch did not account for the actual ahead speed within the duct, which is controlled by the duct profile. This varies and has been shown to give rise to changes in performance (thrust and torque) of the order of 5%.
c) There was also an amount of friction loss present in the gap between the rotor and stator.

The thrust coefficient, K_T, reduced more rapidly compared to the standard Kaplan ducted propeller performance, as the advance speed increased. This was due to the essential increase in thickness of the duct to enclose the electric motor and the use of a symmetrical duct. This effect is expected to decrease with a larger ETDP unit as the proportional thickness of the motor, and hence the duct, would decrease.

Different duct profiles have been tested. The differences in performance were measurable and in the range of up to 5%. Best performance was obtained with the duct that produced minimum advance speed acceleration. The effect of different stator angles was also investigated. The results indicated that for the current design, zero angles produce best thrust output at bollard pull conditions. All other angles reduced the thrust, which was believed to be due to increased drag on the stators, however, further investigation is necessary.

10.1.3 Computational Modelling of Tip-Driven Propellers

A computational lifting surface panel model has been developed to investigate the likely performance of ducted propellers and similar applications. Along with geometry definition programs, which have been created, it is now possible to model many propeller-duct combinations. The model used a fixed propeller wake sheet with no downstream contraction, however, the pitch of the wake could be varied for different propeller operating conditions. At higher advance coefficients, $J=0.6$ or more, it was seen that

using the geometric blade pitch as the wake pitch was acceptable. Tests have shown this to produce reasonable results, however, difficulties were experienced when modelling low advance coefficients. For this reason, bollard pull predictions have been extrapolated from the data calculated for higher J values.

A program to estimate the likely boundary layer growth over bodies has been developed to run in an iterative loop with the panel code. The use of this program has been shown to produce more realistic solutions than the potential-flow code alone, predicted lift is reduced and drag is increased. The boundary layer program is particularly suited to aerofoil type geometries, and in addition to the boundary layer growth a point of flow separation can also be estimated. The code has been validated against wind tunnel data for a finite aerofoil section, and results were seen to be adequate for the purposes of correcting the potential-flow solutions. However, this version of the code can only be used with confidence for bodies at zero angle of yaw, i.e. when the individual panel sections defining the body experience a straight-ahead flow, with no cross-flow between adjacent sections. Hence it was only used with the duct model, and not for the propeller geometry. A proposed future development for the boundary layer prediction is to use streamline tracing, which will allow yaw angles and cross-flows to be taken into account.

The panel code was used to predict the performance of the prototype tip-driven ducted propeller. The model included representative geometries of the propeller, duct, bearing casings, and forward and aft stators. The results were compared to experimental tests carried out on the prototype unit and, although the absolute thrust values were larger than the test results, and the predicted torque values were lower, the general trends and relative differences between ducts were adequately reproduced. It is anticipated that the inclusion of the boundary layer code would reduce the thrust results and raise the torque predictions. Nevertheless, the results provided increased confidence with the code and it is anticipated that this method of analysis can be used as an aid to optimising the hydrodynamic characteristics of future ducted propeller units.

10.1.4 Wind Tunnel Testing of a Waterjet Inlet Duct

The use of a wind tunnel is an effective technique for investigating waterjet duct inlet flows. The experimental facility provided a reliable method for generating accurate data

for numerical validation studies. Generally, pressure coefficients were obtained to an accuracy of $Cp \pm 0.06$, and velocities to $\pm 0.9 m/s$. Pressure and velocity distributions along and through the duct were obtained together with a visualisation of the flow characteristics for three different inlet velocity ratios. Pressure distributions, along the upper and lower walls of the duct, were found to be similar to those obtained by Okamoto et al [2.8], during self-propulsion tests of a similar duct. The resulting trends were as expected and the measured velocity profiles generally agreed with what had been shown by the wool tuft studies. At low inlet velocity ratios, flow separation was seen to occur on the upper duct wall, near the inlet, but at the higher IVRs separation was evident on the lower duct wall, downstream of the inlet lip.

A comprehensive set of reliable data was obtained for the flow through the inlet duct, which provided a detailed indication to the behaviour of the flow. The data can also be used to validate future theoretical models of the duct. However, much time and planning was required in order to achieve results such as these. Ideally, there are many more measurements and combinations of tests which could have been carried out, but this was not practical with the speeds attainable in the tunnel or with the limited time available.

10.1.5 Computational Modelling of Waterjet Inlet Ducts

A computational model of the representative waterjet intake duct has been created using a fully viscous commercial code, CFX4.1-F3D. The model was used to simulate the wind tunnel tests conditions, and the model produced good results, which gave a reasonable correlation with experimental data. There was a slight offset between the results due to differences in mass flow rate. The duct flow was also studied for off-design conditions, i.e. small angles of trim and drift. The influence of trim and drift caused a change in the pressure distributions, hence velocity and force distributions along the duct and across the outflow plane. This imposes a non-uniform flow at the face of the impeller reducing the performance. Although the model calculated reasonable predictions for the influence of trim and drift, further validation work for these cases is necessary.

A study of the interaction effects, based on some broad assumptions, has been carried out in an attempt to obtain an indication of the effects on the vessel resistance. Interaction effects can be significant and thrust deduction factors can be either positive or negative

depending on hull form, waterjet geometry and ship speed. In this instance, a thrust deduction fraction of $t=0.15$ was calculated. The generation of the waterjet duct and hull topology is a time consuming process. However, it has been shown that the influence of the hull must be considered when investigating the performance of a waterjet duct.

A fully viscous CFD RANS solution to the flow through a waterjet intake duct has been coupled to a potential-flow panel code, which modelled a rotating axial-flow impeller. In addition, a representative drive shaft was included in the viscous flow model so the effect of using a tip-driven impeller could be studied. Velocity results at the duct exit plane were input into the panel model of the impeller as inflow velocity fields. It was seen that the impeller thrust decreased when the intake duct was operating at an angle of yaw, but the presence of the drive shaft reduced the performance even further, a 28% decrease in K_T was predicted. However, these results need further validation work.

The possibility of being able to investigate the interaction between a waterjet intake duct and its impeller has been illustrated. Although limited with the assumption of a constant mass flow boundary at the duct exit during the initial CFD investigations, and the subsequent average impeller advance speed based on this mass flow rate, the methods have yielded reasonable, and potentially useful results. With future refinement to the models, it should be possible to predict what effects a change in the duct geometry has on the overall performance of the impeller and the waterjet unit as a whole.

CFD codes provide a comprehensive solution of the flow relatively quickly. There is also a quick turn-around between tests and the influence of different inlet flow conditions can be studied easily. However, there is often a compromise between the accuracy, number of cells and time available for a CFD run. The benefits to the engineer of using such CFD flow solvers during the initial design stages of a waterjet duct have been illustrated. In particular, the ability to obtain detailed surface pressure and viscous force distributions allows a far greater understanding of the resistance and propulsion aspects of using waterjets.

However, as a word of caution, CFD codes provide the engineer with a prediction of how the flow might behave under specific, often limited, conditions. They are expectations

which might, or might not, live up to reality. These results must therefore be taken as an estimate of the flow behaviour. Nevertheless, it is expected that the developed method could be used as the basis for developing the preliminary design of a large-scale model duct and impeller for testing in a wind tunnel. Likewise, it has the potential for use as part of the waterjet design process, for investigations of cavitation inception, noise and induced vibration and impeller shape optimisation.

10.2 CONTRIBUTIONS

In completing the objectives several contributions have been made to this particular field of research:

1. The considerations of designing and building an electromagnetic tip-driven propeller have been highlighted, and a prototype TDP has been successfully built for the specific purpose of experimental testing.
2. Performance results for a tip-driven propeller unit have been published, illustrating the potential uses of such units and helping to understand where future performance gains might be found.
3. The prototype provides a platform from which future propeller–duct–stator combinations can be studied.
4. Programs have been developed which, given a list of section offsets, rapidly define the three-dimensional geometry of propellers and ducts. It is now possible to produce a panel model of many ducted-propeller combinations. In addition, the rapid generation of these CFD geometries should be of benefit to future design optimisation studies, when it is necessary to model a large number of geometries.
5. For additional accuracy, a program to estimate boundary layer development and point of flow separation has been written to run in an iterative loop with the panel code.
6. A RANS code has been used to study the flow through a waterjet inlet duct, and the effect of the duct at angles of trim and drift has been studied in more detail than in previous literature.
7. A method of coupling a potential-flow panel code to a viscous RANS flow solver is demonstrated and provides a means of modelling both a waterjet inlet duct and impeller together. The performance of an axial-flow impeller has been presented for various intake duct flow conditions, including a study with the presence of a drive shaft.

8. The implications of using a tip-driven impeller in a waterjet system have been approached. This could lead to future changes in inlet duct design, and has opened the field for further areas of research and investigation.

10.3 FURTHER WORK

This section outlines areas in which there is scope for further work. Some of the areas have come to light during the course of this study, others from the benefit of hindsight. They are subjects that the author feels will enhance and further this research, but which due to a lack of time, have not been included in this study.

The effect on the flow through the waterjet duct at angles of trim or drift has not been validated due to a lack of experimental data. The design and development of a new wind tunnel model of the waterjet inlet duct would enable a greater number of flow conditions to be tested, and the effect of various appendages to be studied. The requirements for this model would include the ability to be rotated and tested at an angle of trim or drift, although a trim angle would be more difficult to achieve, and the ability to be studied with or without the presence of a representative drive shaft and inlet grill. Furthermore, the phenomenon of lower blade loadings with the presence of the drive shaft, as seen in Chapter 8 albeit for only one flow condition, requires further study.

An enhancement of the method used to couple the RANS waterjet duct model to the panel code impeller model is to impose the upstream influence of the impeller directly into the RANS model, as a modified outlet boundary condition. This could probably be achieved via a matching process on a plane slightly upstream of the impeller.

This work has initiated the investigation into a new drive method for waterjet impellers by studying the theoretical performance characteristics. A general design proposal has been presented but it does not take into account detailed mechanical design of the installation, only schematic arrangements have been proposed. Further work would be necessary on the design of a typical installation. In addition, the possible implications of using more than one tip-driven propeller, or impeller, in series can be studied.

It must be stressed that, although not investigated here, the proposed tip-driven impeller is just as useful, if not more so, in pod inlets. An ETDI installed in a pod inlet could reduce the necessity of extra ducting to raise the water to the pump unit. This in turn would reduce the duct loss and added mass of water in the vessel. Furthermore, the removal of the drive shaft and the subsequent increased ability to locate the impeller at a number of locations along the duct may invoke an ultimate redesign of the waterjet duct itself. Although this issue has not been studied, it is hoped the tools developed would aid such an investigation. Duct redesign is merely noted as a possible area of further research.

Although not studied in much detail during the course of this work, it has been suggested that mechanical TDIs might offer a more practical solution than ETDIs for larger waterjet units. However, this concept requires further investigation. An unknown factor is the means of sealing the drive mechanism and the associated friction loss.

Finally, the work presented has studied the proposal of a tip-driven waterjet impeller system principally from a hydrodynamic point of view. A thorough proposal must consider all the aspects associated with the propulsion system, including required changes to the power plant arrangement, and its implications such as costs, efficiencies, weights and sizes.

REFERENCES

CHAPTER 1

1.1 RAWSON KJ, TUPPER EC - "*Basic Ship Theory.*" Vol.2. 3rd edition. Published by Longman Scientific & Technical.

1.2 KATZ J, PLOTKIN A - "*Low Speed Aerodynamics, From Wing Theory to Panel Methods*" Published by Mcgraw-Hill Inc, 1991.

1.3 ROBERTS JL - "*The Influence of Hull Boundary Layers on Waterjet Performance.*" PhD Thesis. Department of Civil and Mechanical Engineering, University of Tasmania. 1998.

1.4 WATSON SJP - "*The Use of CFD in Sensitivity Studies of Inlet Design.*" RINA International Conference on Waterjet Propulsion, Latest Developments. Amsterdam, Oct.1998. Paper No.8.

1.5 "*Principles of Naval Architecture.*" Edited by EV Lewis. Published by SNAME. 1967.

1.6 HARVALD SA - "*Resistance and Propulsion of Ships.*" Published by John Wiley & Sons, 1983. pp198-218.

1.7 OOSTERVELD MWC - "*Ducted Propeller Systems Suitable for Tugs and Pushboats.*" Journal of International Shipbuilding Progress, Vol.19, 1972.

1.8 FLOWER JO, RICHARDSON KM, POLLOCK C - "*An Experimental Integrated Switched Reluctance Propulsion Unit; Design, Construction and Preliminary Results.*" Read at the Institute of Marine Engineers, 9th Jan 1996.

1.9 Anonymous - "*An Integral Electric Motor Propeller.*" Ship and Boat International. Jan/Feb 1993. Issue 93/1, pp41-43.

1.10 HOLT JK - "*Developing a High Efficiency Ring Thruster for Underwater Vehicles.*" Harbor Branch Oceanographic Institution, Inc. Engineering Division, 1995.

1.11 RADOJCIC D - "*Tip-Driven Propellers and Impellers - A Novel Propulsion Concept.*" SNAME Propellers and Shafting '97 Symposium, Virginia Beach, Sept.1997.

1.12 ALLISON J - "*Marine Waterjet Propulsion*" Trans SNAME, Vol.101, 1993. pp275-335.

1.13 ROY SM - "*The Evolution of the Modern Waterjet Marine Propulsion Unit.*" RINA International Symposium on Waterjet Performance, Latest Developments. London, Dec.1994. Paper No.1.

1.14 Anonymous - "*Jetting Ahead.*" The Motor Ship. Aug.1995.

1.15 SEIL GJ - "*Development of Waterjet Intakes for 100 Knots.*" Fifth International Conference on Fast Sea Transportation, (Fast'99). Seattle, Aug-Sept.1999. pp853-868.

1.16 LAZARKIEWICZ S, TROSKOLANSKI AT - "*Impeller Pumps.*" Published by Pergamon Press Ltd. 1965.

1.17 TORNEMAN G - "*Applications of Complete and Integrated Mixed-Flow Waterjet Propulsion Systems.*" RINA International Conference on Waterjet Propulsion, Latest Developments. Amsterdam, Oct.1998. Paper No.13.

1.18 ALLISON J, STRICKER JG, ATHAVALE MM, KERWIN J, TAYLOR T - "*Modern Tools for Waterjet Pump Design and Recent Advances in the Field.*" RINA International Conference on Waterjet Propulsion, Latest Developments. Amsterdam, Oct.1998. Paper No.2.

1.19 SVENSSON R - "*Waterjet Propulsion - Experience from High Powered Installations.*" RINA International Symposium on Waterjet Propulsion, Latest Developments. London, Dec.1994. Paper No.3.

CHAPTER 2

2.1 OOSTERVELD MWC - "*Ducted Propeller Characteristics.*" RINA Symposium on Ducted Propellers 1973. Paper No.4, pp35-69.

2.2 BLAMIRE I - Personal communication. Seaeye Marine Ltd. Seaeye House, Lower Quay Road, Fareham. Hampshire. PO16 OPQ. June 1998.

2.3 MOLLAND AF, TURNOCK SR - "*Wind Tunnel Investigation of Propeller Loading on Ship Rudder Performance.*" Trans RINA Vol.134, 1992.

2.4 MOLLAND AF - "*The Design, Construction and Calibration of a Five-Component Strain Gauge Wind Tunnel Dynamometer.*" University of Southampton, Ship Science Report No. 1/77. Nov.1976.

2.5 ABU SHARKH S, HUGHES AW, TURNOCK SR, BATTEN W – "*First 2kW Prototype – Test Results.*" Prototype Integrated Electric Thrusters for Work-Class Underwater Vehicles. University of Southampton, School of Engineering Sciences. Technical Note ITM04, Nov.1999.

2.6 MOSS R. "*Wind Tunnel Modelling of a Waterjet Propulsion System.*" M.Sc.Thesis, Jan.1995, The University Of Southampton.

2.7 PEASE MR - "*The Design and Development of a Model Waterjet Impeller.*" University Of Southampton, Department Of Ship Science, M.Sc. Thesis, Oct.1995.

2.8 OKAMOTO Y, SUGIOKA H, KITAMURA Y. "*On the Pressure Distribution of a Waterjet Intake Duct in Self Propulsion Conditions.*" Second International Conference on Fast Sea Transportation. (Fast'93) p.843-853.

2.9 KENNING O, RICHARDS C, NEVILL G, POLLARD E - "*Enhancement of the University 3' by 2' Subsonic Wind Tunnel Incorporating Adaptive Wall Technology.*" University of Southampton, Master of engineering group design project. 1996.

2.10 "*Environment User Guide", "CFDS-Flow3d User Guide*" and "*CFX4.1 User Guide.*" UK AEA TECHNOLOGY, Harwell. 1995.

2.11 TURNOCK SR - "*Technical Manual and User Guide for the Surface Panel Code: Palisupan.*" University of Southampton, Ship Science Report No.100. Oct.1997.

2.12 TURNOCK SR, MOLLAND AF, WELLICOME JF - "*Interaction velocity field method for predicting ship rudder-propeller interaction.*" SNAME Propeller/Shafting Symposium 94, Paper 18.1-14. Virginia Beach USA, Sept. 1994

2.13 MORINO L, KUO C-C - "*Subsonic Potential Aerodynamics for Complex Configurations: A General Theory.*" AIAA Journal, Vol.12, No.2. Feb.1974.

2.14 NEWMAN JN - "*Distribution of Sources and Normal Dipoles over a Quadrilateral Panel.*" Journal of Engineering Mathematics, Vol.20. pp113-126. 1986.

2.15 LEE T-J - " *A Potential Based Method for the Analysis of Marine Propellers in Steady Flow.*" Ph.D. thesis, MIT Dept. of Ocean Engineering. Aug. 1987.

2.16 HOLT NDA – "*An Investigation into Alternative Submarine After Hydroplane Configurations Using Surface Panel Methods.*" University of Southampton, Department of Ship Science, Third Year Project Report. No.SS461, 1997.

2.17 CEBECI T, BRADSHAW P - "*Momentum Transfer in Boundary Layers.*" Published by Mcgraw-Hill.

2.18 CURLE N - "*The Laminar Boundary Layer Equations.*" Oxford University Press, 1962.

2.19 GREEN JE - "*The Prediction of Turbulent Boundary Layer Development in Compressible Flow.*" Journal of Fluid Mechanics Vol.31, part 4, pp753-778.

2.20 LUDWIEG H, TILLMANN W - "*Investigations of the Wall Shearing Stress in Turbulent Boundary Layers.*" NACA Report TM 1285, 1949.

2.21 ABBOTT IH, VON DOENHOFF A- "*Theory of Wing Sections.*" Dover Publications, Inc. New York. Published 1959.

2.22 MOLLAND AF, TURNOCK SR – "*Wind Tunnel Tests on the Influence of Propeller Loading on Ship Rudder Performance: Four Quadrant Operation, Low and Zero Speed Operation.*" University of Southampton, Ship Science Report No.64. Oct.1993.

2.23 "*Shipshape Manual- Version I.*" Wolfson Unit for Marine Technology and Industrial Aerodynamics. 1990.

CHAPTER 3

3.1 SPENCE W - Personal communication. Westinghouse Electric Corporation, Electro-mechanical Division, Cheswick, Pennsylvania. Nov.1998.

3.2 HOLT JK, WHITE DG – "*High Efficiency, Counter-Rotating Ring Thruster for Underwater Vehicles.*" Symposium on Autonomous Underwater Vehicle Technology (AUV), pp337-339 Massachusetts, 19-20 June 1994.

3.3 WARDELL GS - "*Retractable Bow Thruster.*" U.S. Patent No.04294186. Filed 25-1-80. Patent date 13-10-81.

3.4 ROCHESTER WG - "*Marine Steering and Propulsion System.*" U.S. Patent No.04822308. Filed 21-9-87. Patent date 18-4-89.

3.5 HARTLEY D - Personal communication. Slingsby Engineering Ltd. Kirkbymoorside, York. YO62 6EZ. June 1998.

3.6 ABU SHARKH SM, HUGHES AW, EL-HAMI M, BATTEN W - "*Design and Manufacture of the First 2KW Prototype.*" Prototype Integrated Electric Thrusters for Work-Class Underwater Vehicles. University of Southampton, Departments of Electrical Engineering and Ship Science. Technical Note ITM02, May 1998.

3.7 ABU SHARKH SM, HARRIS MR, STOLL RL - "*Design and Performance of an Integrated Thruster Motor.*" IEE International Conference on Electrical Machines and Drives EMD'95. Durham, U.K. Sept.1995. pp395-400.

3.8 ABU SHARKH SM, HUGHES AW, EL-HAMI M, BATTEN W - "*Preliminary Design of the First 2KW Prototype.*" Prototype Integrated Electric Thrusters for Work-Class Underwater Vehicles. University of Southampton, Departments of Electrical Engineering and Ship Science. Technical Note ITM01, Feb.1998.

3.9 GUNER M, GLOVER EJ - "*Propeller/Stator Propulsors for Autonomous Underwater Vehicles.*" Symposium on Autonomous Underwater Vehicle Technology (AUV). Massachusetts, USA. 19-20 June 1994. pp331-336.

3.10 GUNER M, ATLAR M - "*A Rational Approach to the Design of Propeller/Stator Combination.*" International Shipbuilding Progress, Vol.46, No.447. pp241-263.

CHAPTER 4

4.1 SCHLICHTING H - "*Boundary Layer Theory.*" 4th Edition. Published by McGraw-Hill.

CHAPTER 5

5.1 TURNOCK SR - "*Prediction of Ship Rudder-Propeller Interaction Using Parallel Computations and Wind Tunnel Measurements.*" Ph.D. thesis, University of Southampton, Dept. of Ship Science. 1993.

5.2 BRESLIN JP, ANDERSON P – "*Hydrodynamics of Ship Propellers.*" Published by Cambridge University Press, 1994.

5.3 KERWIN JE, LEE CS – "*Prediction of Steady and Unsteady Marine Propeller Performance by Numerical Lifting-Surface Theory.*" SNAME Transactions, Vol.86, pp218-253. 1978.

5.4 MAITRE TA, ROWE AR – "*Modelling of Flow Around a Marine Propeller Using a Potential Based Method." Journal of Ship Research,* Vol.35, No.2, pp114-126, June 1991.

CHAPTER 6

6.1 AREN P, AARTOJARVI R, CRONER P. "*Review of Test Methods Adopted for Waterjets at the KaMeWa Marine Laboratory.*" 21st International Towing Tank Conference, 1996. Supplement to the report of the Waterjets Group.

6.2 HOSHINO T, BABA E. "*Determination of Propulsive Performance of Waterjet in Model and Full Scales.*" 21st International Towing Tank Conference, 1996. Supplement to the report of the Waterjets Group.

6.3 MINSAAS KJ. "*Flow Studies with a Pitot Inlet in a Cavitation Tunnel.*" 21st International Towing Tank Conference, 1996. Supplement to the report of the Waterjets Group.

6.4 van TERWISGA T. "*The Effect of Waterjet-Hull Interaction on Thrust and Propulsive Efficiency.*" First International Conference on Fast Sea Transportation. (Fast'91) pp1149-1167.

6.5 ALEXANDER K, TERWISGA Tv. "*Recent work on waterjet-hull interaction effects.*" 9th International High Speed Surface Craft Conference. Singapore 1993.

6.6 COOP HG, BOWEN AJ. "*Hull-Waterjet Interaction Mechanisms: Theory and Validation.*" Second International Conference on Fast Sea Transportation. (Fast'93) pp.855-866.

6.7 DYNE G, LINDELL P - "*Waterjet Testing in the SSPA Towing Tank.*" RINA International Symposium on Waterjet Propulsion, Latest Developments. London, Dec.1994. Paper No.2.

6.8 ROBERTS JL, WALKER GJ - "*Boundary Layer Ingestion Effects in Flush Waterjet Intakes.*" RINA International Conference on Waterjet Propulsion, Latest Developments. Amsterdam, Oct.1998. Paper No.7.

6.9 TAYLOR TE, KIMBALL RW - "*Experimental Validation of a Coupled Lifting-Surface/RANS Procedure for Waterjet Pump Design and Analysis.*" Fifth International Conference on Fast Sea Transportation, (Fast'99). Seattle, Aug-Sept.1999. pp893-900.

6.10 WATSON SJP - Personal communication. DERA Haslar, Gosport. Hampshire. PO12 2AG. 7th Nov.1997.

CHAPTER 7

7.1 FORDE M, ORBEKK E, KUBBERUD N. "*Computational Fluid Dynamics Applied to High Speed Craft with Special Attention to Water Intake for Water Jets.*" First International Conference on Fast Sea Transportation. (Fast'91) pp69-87.

7.2 SEIL GJ, FLETCHER CAJ, DOCTORS LJ. "*The Application of Computational Fluid Dynamics to Practical Waterjet Propulsion System Design and Analysis.*" Third International Conference on Fast Sea Transportation. (Fast'95) pp1379-1390.

7.3 SEIL GJ, FLETCHER CAJ, DOCTORS LJ. "*Optimisation of Waterjet Inlets Using Computational Fluid Dynamics.*" Fourth International Conference on Fast Sea Transportation, (Fast'97). Vol.1. Sydney, July 1997. pp59-64.

7.4 SEIL GJ - "*Computational Fluid Dynamics Optimisation of Flush-Type Waterjet Inlets.*" RINA Transactions. Issued for written discussion, Jan.2000.

7.5 SZANTYR JA, BUGALSKI T. "*A Numerical Method for Hydrodynamic Analysis of Waterjets.*" Third International Conference on Fast Sea Transportation. (Fast'95) pp1271-1282.

7.6 ENGLISH EG. "*An Investigation into the Computer Modelling of a Waterjet Propulsion Unit.*" B.Eng.Honours Report, 1994/95, The University of Southampton.

7.7 YANG CK, LEE YB, CHOI HS. "*A Numerical Analysis of the Flow Around the Waterjet Inlet.*" Third International Conference on Fast Sea Transportation. (Fast'95) pp1391-1401.

7.8 LATORRE R. "*Numerical Study of Waterjet Inlet Pressure Distribution.*" Naval Engineers Journal. Vol.107, No.5, pp67-78.

7.9 HOSHINO T, BABA E. "*Self Propulsion Tests of a Semi-Displacement Craft Model With a Waterjet Propulsor.*" Journal Society of Naval Architects of Japan. Vol.155, 1984, pp50-57.

7.10 PYLKKANEN JV. "*Design of Waterjet Inlet: Selection of Main Dimensions and Two-dimensional Diffuser and Lip Section Shape.*" VTT Manufacturing Technology, Technical Report VALB-29.

7.11 PYLKKANEN JV. "*A Test Case of the Application of a CFD Code for Predicting Waterjet Inlet Flow.*" 21st International Towing Tank Conference, 1996. Supplement to the report of the Waterjets Group.

7.12 DAI C, KERR C, NGUYEN P, WANG H. "*A Novel Flush Inlet Design Methodology for Waterjet Propulsion.*" Third International Conference on Fast Sea Transportation. (Fast'95) p.1367.

7.13 HU P, ZANGENEH M - "*Analysis of 3D Viscous Flow Through a Water-jet Intake Duct Under Different Operating Conditions.*" Proceedings of FEDSM'98. ASME Fluids Engineering Division Summer Meeting. Washington DC. June 21-25 1998.

7.14 GUSTAFSSON LT, WIDMARK C - "*3-Dimensional CFD Calculation of a Complete Waterjet Unit.*" RINA International Conference on Power, Performance and Operability of Small Craft. Southampton, Sept.1997. Paper No.5.

7.15 HU P, ZANGENEH M - "*A Method for Automatic Optimisation of the Intake Duct Geometry of Marine Waterjets.*" Fifth International Conference on Fast Sea Transportation, (Fast'99). Seattle, Aug-Sept.1999. pp843-851.

7.16 VERBEEK R, BULTEN N - "*Recent Developments in Waterjet Design.*" RINA International Conference on Waterjet Propulsion, Latest Developments. Amsterdam, Oct.1998. Paper No.1.

7.17 BULTEN N - "*Influence of Boundary Layer Ingestion on Waterjet Performance Parameters at High Ship Speeds.*" Fifth International Conference on Fast Sea Transportation, (Fast'99). Seattle, Aug-Sept.1999. pp883-892.

7.18 ENGLISH JW - "*Practical Considerations on Waterjets with Flush Intakes.*" RINA International Symposium on Waterjet Propulsion, Latest Developments. London, Dec.1994. Paper No.11.

7.19 HUGHES AW, TURNOCK SR - "*Computational Fluid Dynamic Investigation of Hull-Waterjet Flow Interaction.*" University of Southampton, Ship Science Report No.102. Sept.1997.

7.20 HUGH YH Yeh - "*Series 64 Resistance Experiments on High-Speed Displacement Forms.*" Marine Technology, July 1965.

7.21 Proceedings of the 22nd International Towing Tank Conference (ITTC), Vol II. pp587-597. Sept.1999.

CHAPTER 8

8.1 TAYLOR TE, KERWIN JE, OTTO SCHERER J - "*Waterjet Pump Design and Analysis Using a Coupled Lifting-Surface and RANS Procedure.*" RINA International Conference on Waterjet Propulsion, Latest Developments. Amsterdam, Oct.1998. Paper No.5.

8.2 PARKER R, HAMPSON S - Personnal communication. Vosper Thornycroft Hydraulic Power Division. Northabour Road, Cosham, Portsmouth.. Hants, PO6 3TL.

8.3 SVENSSON R - "*Waterjet Propulsion - Experience from High Powered Installations.*" RINA International Conference on Waterjet Propulsion, Latest Developments. Amsterdam, Oct.1998. Paper No.3.

CHAPTER 9

9.1 WARREN NF, KECSMAR J, SIMS N - "*Waterjet Propulsion - A Shipbuilder's View.*" RINA International Symposium on Waterjet Propulsion, Latest Developments. London, Dec.1994. Paper No.4.

9.2 Van TERWISGA T - "*A Parametric Propulsion Prediction Method for Waterjet Driven Craft.*" Fourth International Conference on Fast Sea Transportation, Fast'97. Vol.2, pp661-667. Sydney, July 1997.

9.3 ABU SHARKH SM - Personal communication. School of Engineering Sciences, Department of Mechanical Engineering. University of Southampton. Feb 2000.

9.4 "*Jane's High Speed Marine Transportation. 1996-1997.*" Edited by SJ Phillips.

9.5 "*Vospower Waterjets.*" Vosper Thornycroft, Hydraulic Power Division. Northarbour Road, Cosham. Portsmouth. PO6 3TL.

9.6 ABU SHARKH SM - "*Electric Motors for the Thrusters of UUVs.*" Design studies of power electronic drive systems for the thrusters of unmanned underwater vehicles. Technical note UVD04. University of Southampton, Department of Electrical Engineering. July 1994.

9.7 ABU SHARKH SM - "*Propeller Hydrodynamics.*" Design studies of power electronic drive systems for the thrusters of unmanned underwater vehicles. Technical note UVD01. University of Southampton, Department of Electrical Engineering. August 1993.

9.8 ABU SHARKH SM - "*Design and Performance of an Integrated Thruster Motor.*" Design studies of power electronic drive systems for the thrusters of unmanned underwater vehicles. Technical note UVD06. University of Southampton, Department of Electrical Engineering. June 1995.

9.9 ABU SHARKH SM - "*Performance of the First 2kW Prototype - An Update.*" Personal communication. Department of Electrical Engineering, University of Southampton. 15th Dec 1998.

9.10 ABU SHARKH SM, HARRIS MR, CROWDER RM, CHAPPELL PH, STOLL RL, SYKULSKI JK - "*Design Considerations for Electric Drives for the Thrusters of Unmanned Underwater Vehicles.*" Sixth European Conference on Power Electronics and Applications. Seville, Spain. 19-21 Sept.1995.

APPENDIX A: FIGURES

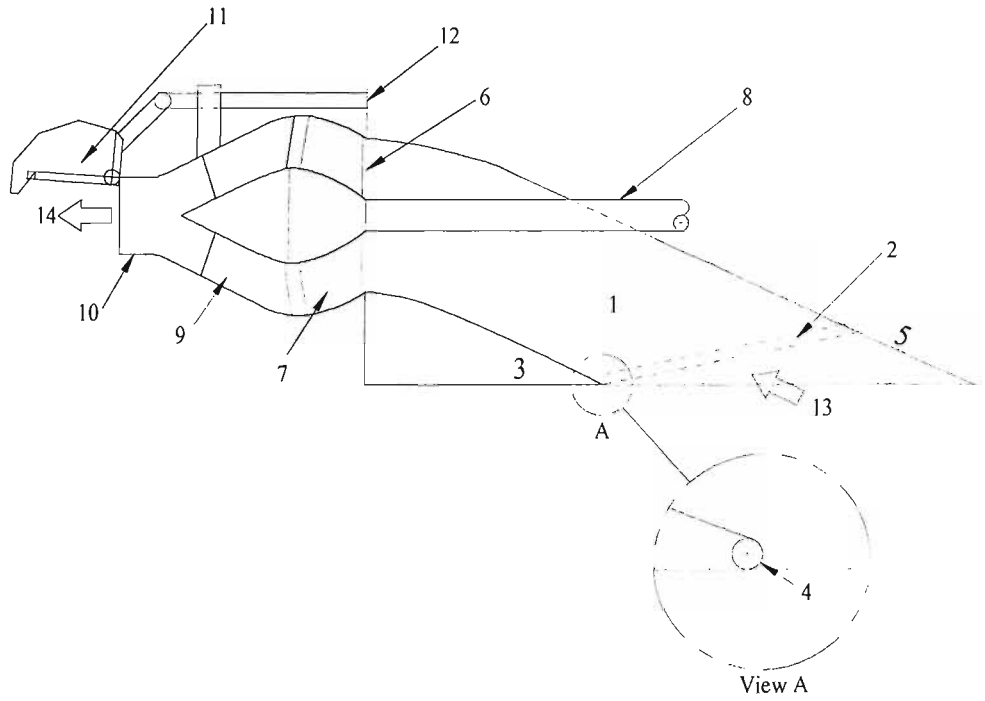

1 = Inlet duct
2 = Inlet grill
3 = Inlet lip
4 = Inlet lip radius
5 = Inlet ramp
6 = Duct exit, or impeller inlet plane
7 = Impeller blade
8 = Drive shaft
9 = Sator, or guide vane
10 = Outlet nozzle
11 = Reversing bucket
12 = Transom
13 = Inflow
14 = Outflow

Figure A1.6 - Schematic diagram of a typical flush waterjet inlet duct.

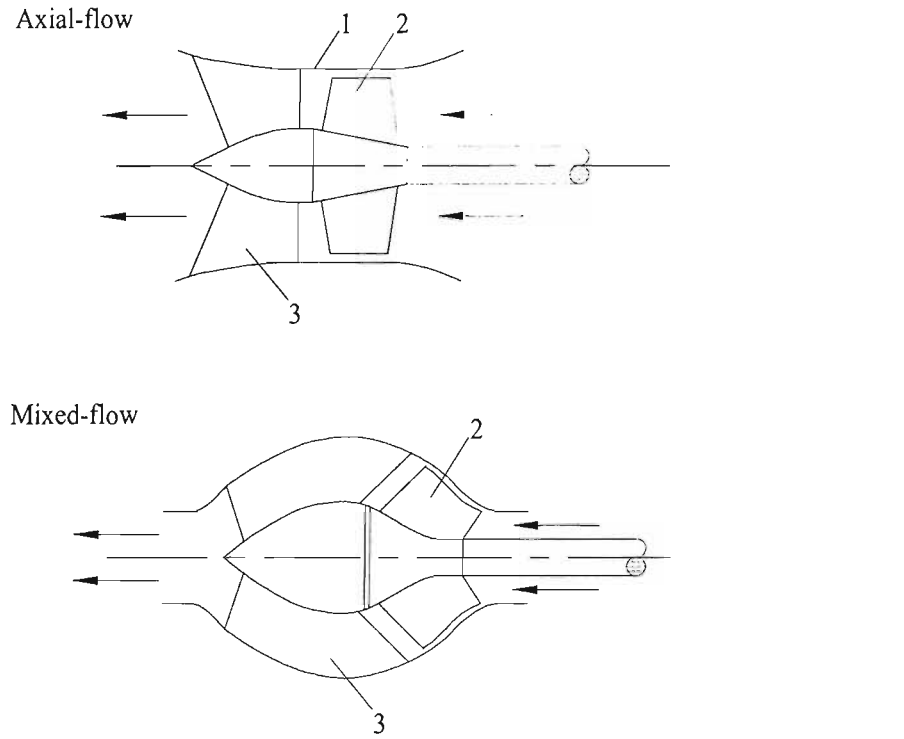

1 = Pump casing 2 = Impeller 3 = Guide vane

Figure A1.8 - Schematic diagram of different impeller flow types.

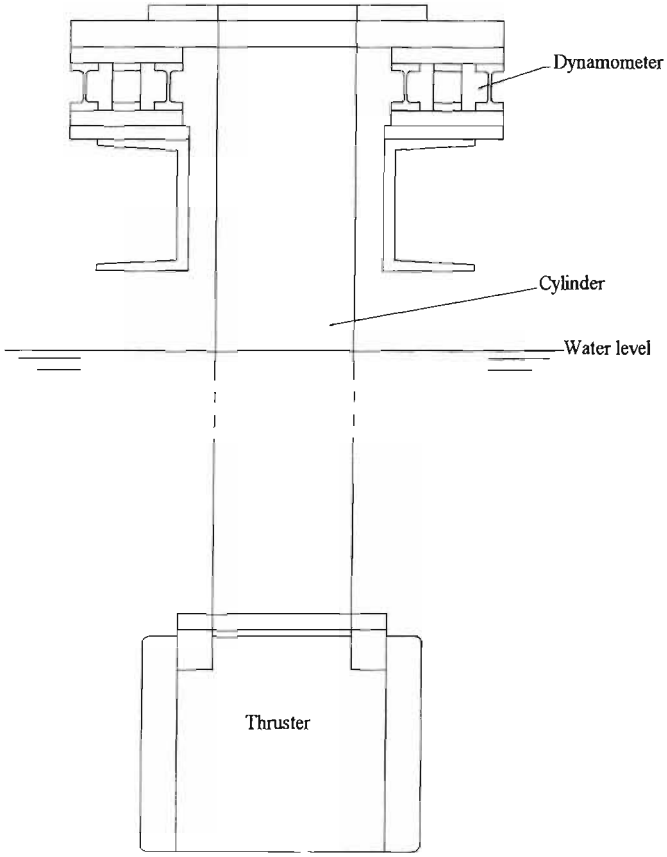

Figure A2.1 - Dynamometer thruster support.

Figure A2.2 – Photograph of the TDP towing tank test set-up.

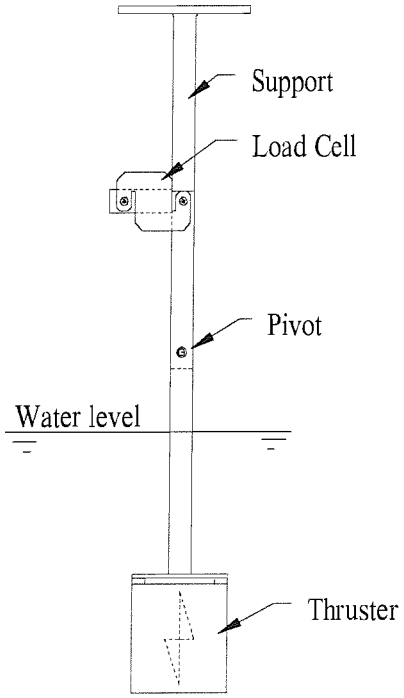

Figure A2.4 - Seaeye Marine load cell support.

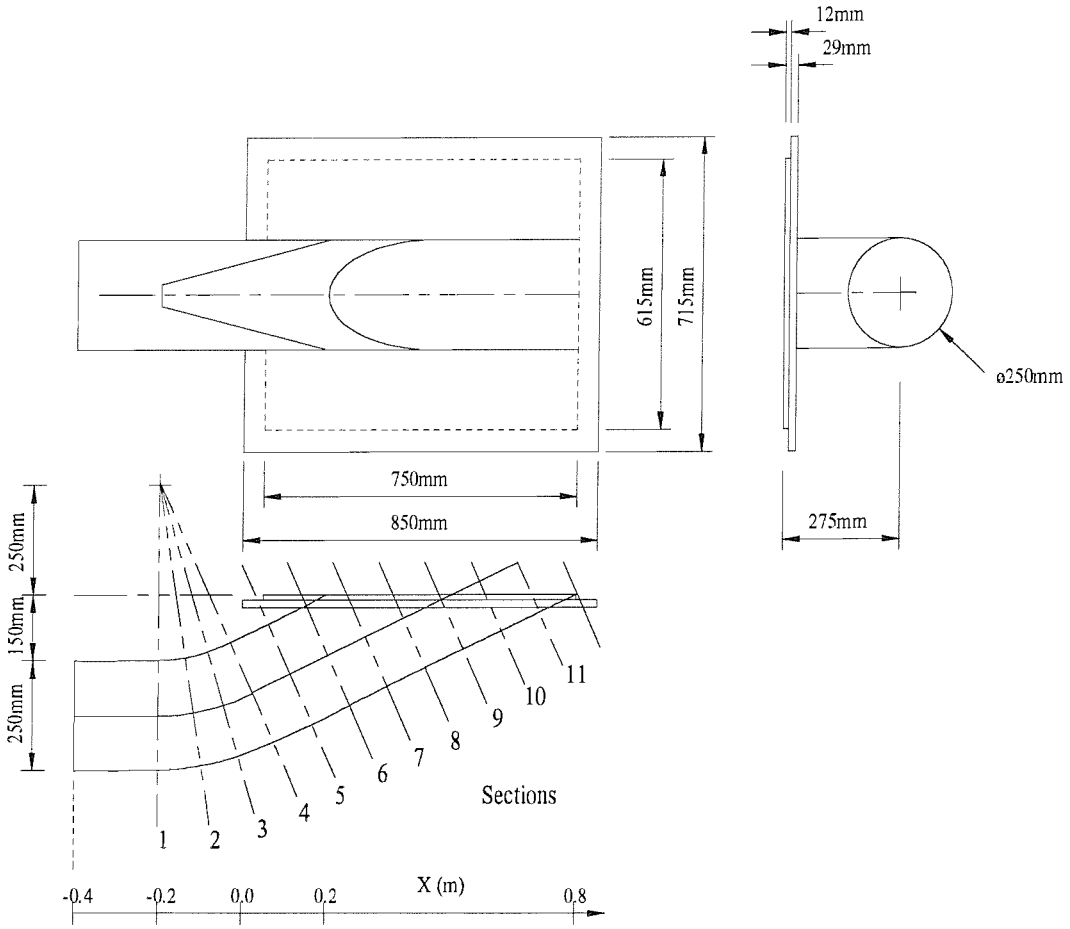

Figure A2.7 - Representative waterjet inlet duct geometry.

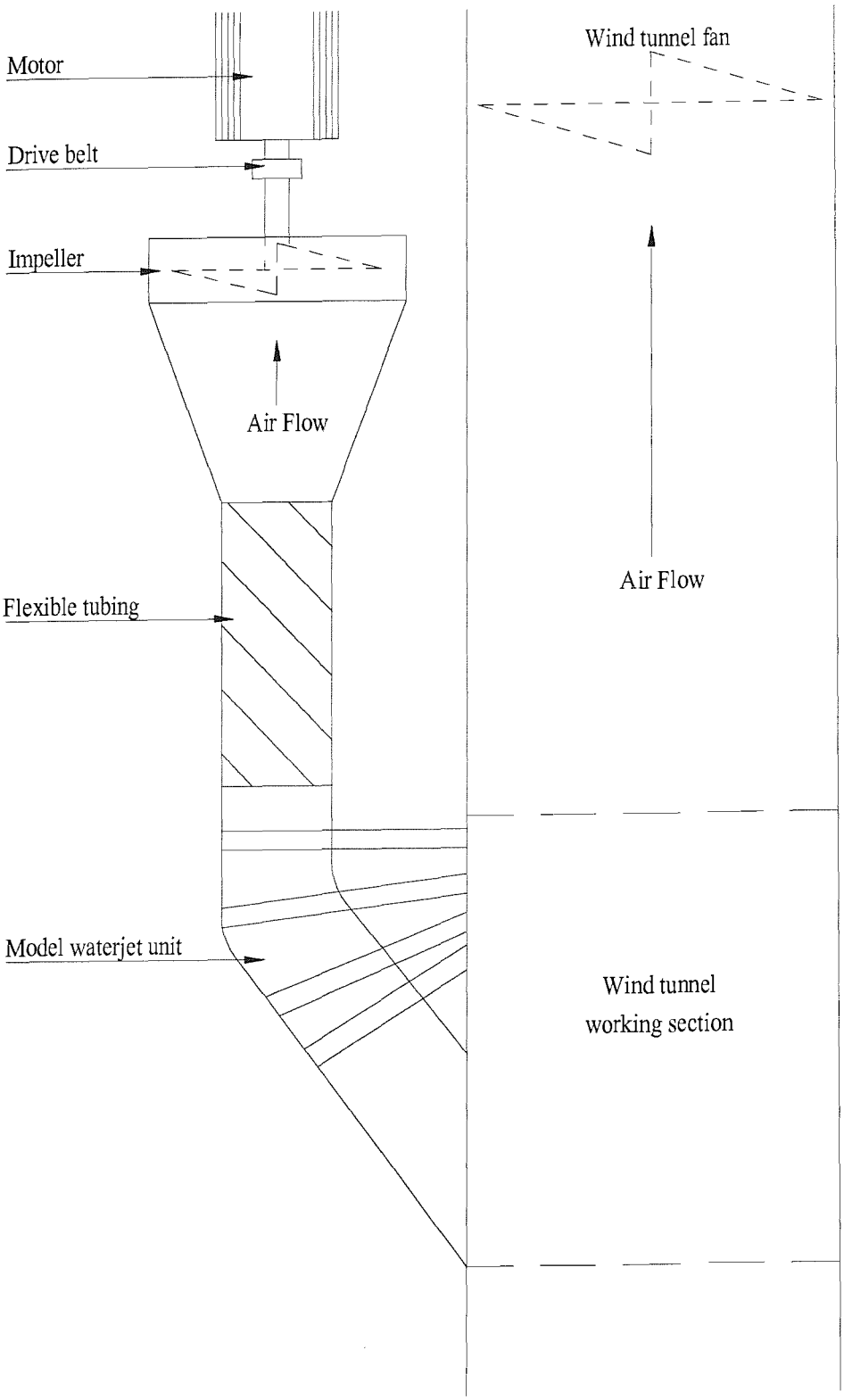

Figure A2.8 - Plan view of wind tunnel test set-up.

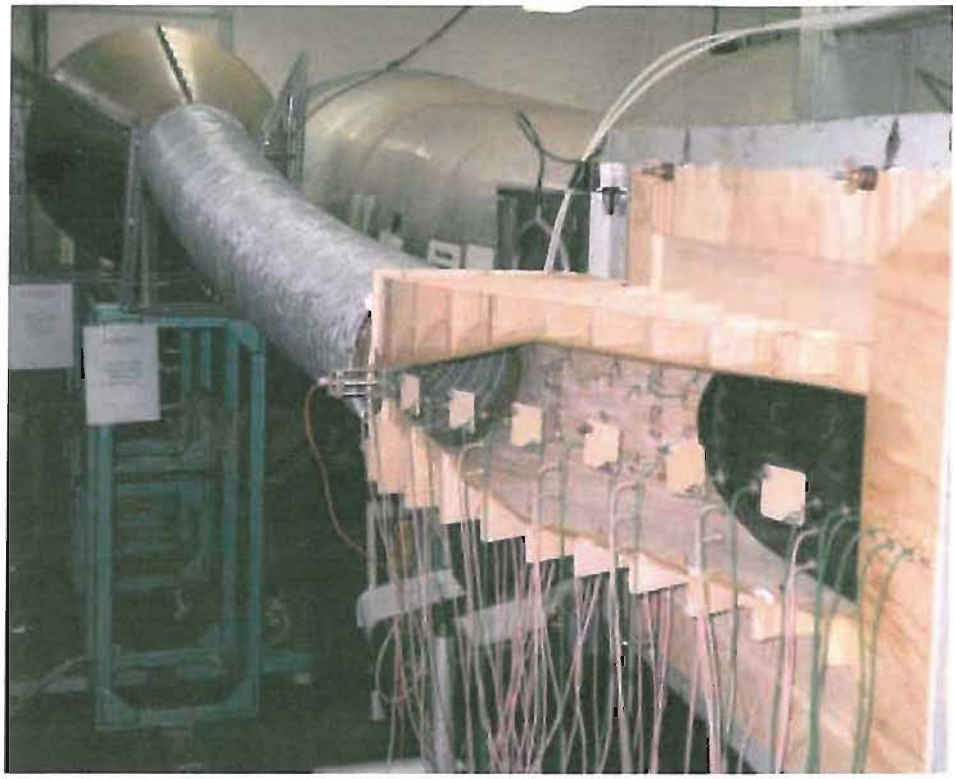

Figure A2.9 - Photograph of the wind tunnel test set-up.

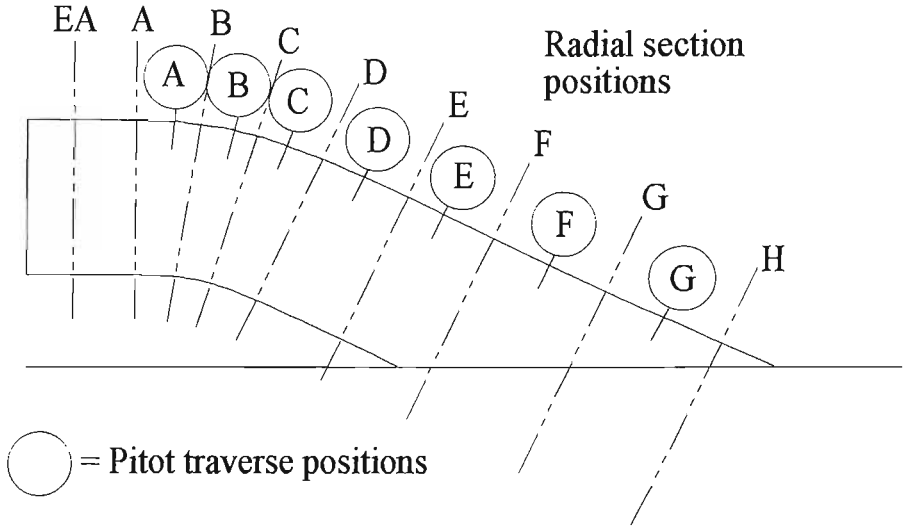

Figure A2.10 - Relative measurement positions along the waterjet inlet duct.

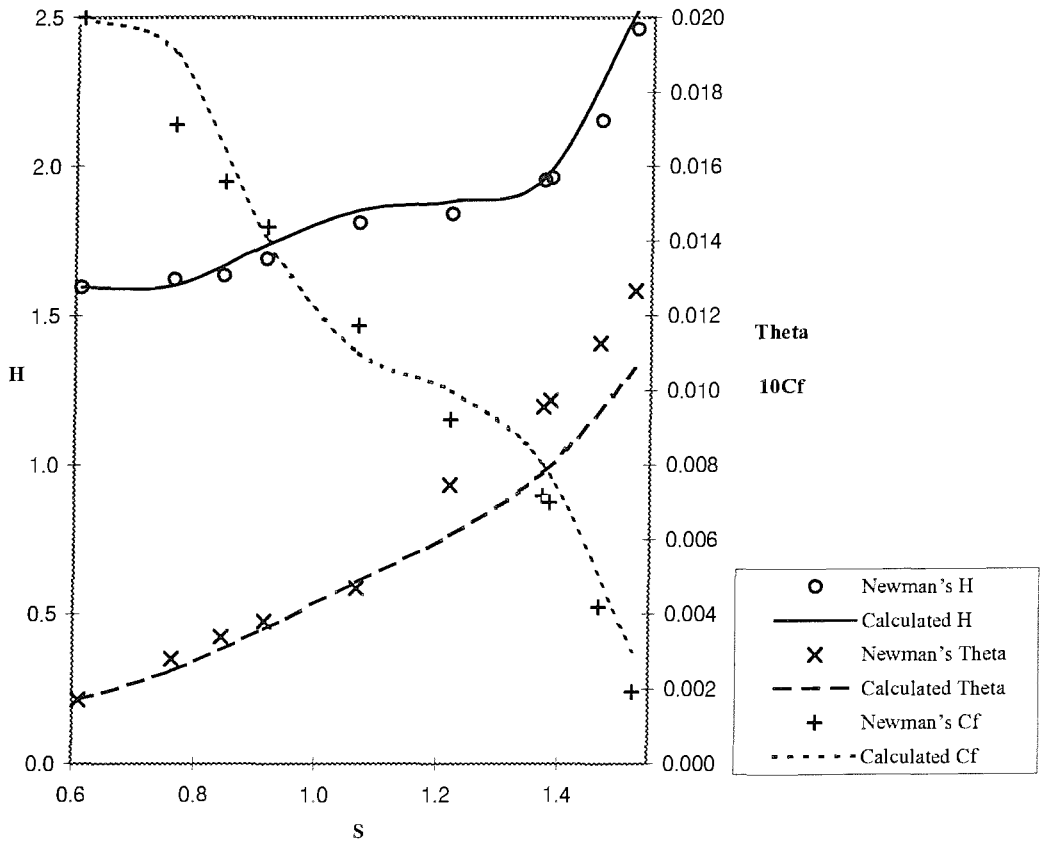

Figure A2.12 - Blayer.f turbulent boundary layer prediction vs Newman's data.

NACA 0020

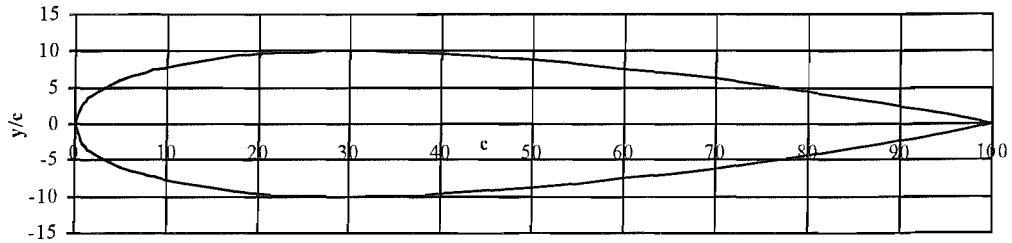

Stations and ordinates given in per cent of aerofoil chord.

Upper Surface		Lower Surface	
Station	Ordinate	Station	Ordinate
0	0	0	0
1.25	3.16	1.25	-3.16
2.5	4.36	2.5	-4.36
5.0	5.93	5.0	-5.93
7.5	7.00	7.5	-7.00
10	7.81	10	-7.81
15	8.91	15	-8.91
20	9.56	20	-9.56
25	9.90	25	-9.90
30	10.00	30	-10.00
40	9.67	40	-9.67
50	8.82	50	-8.82
60	7.61	60	-7.61
70	6.11	70	-6.11
80	4.37	80	-4.37
90	2.41	90	-2.41
95	1.35	95	-1.35
100	(0.21)	100	(-0.21)
100	0	100	0

LE Radius: 4.48 per cent c

Figure A2.13 - Section data for NACA 0020 aerofoil.

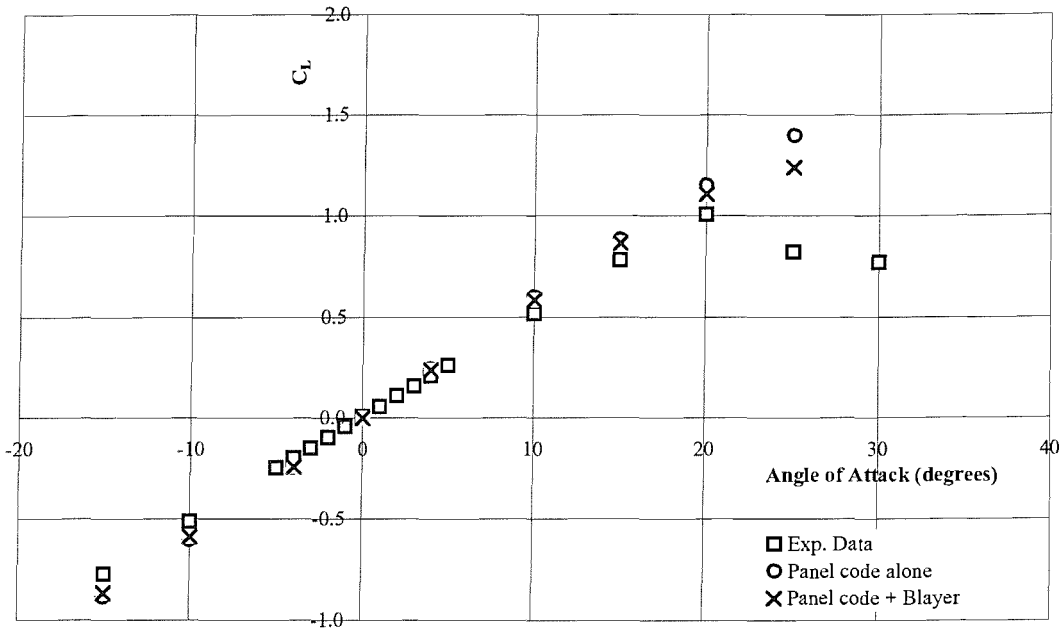

Figure A2.14 - Lift coefficients of NACA 0020 rudder section at various angles of attack.

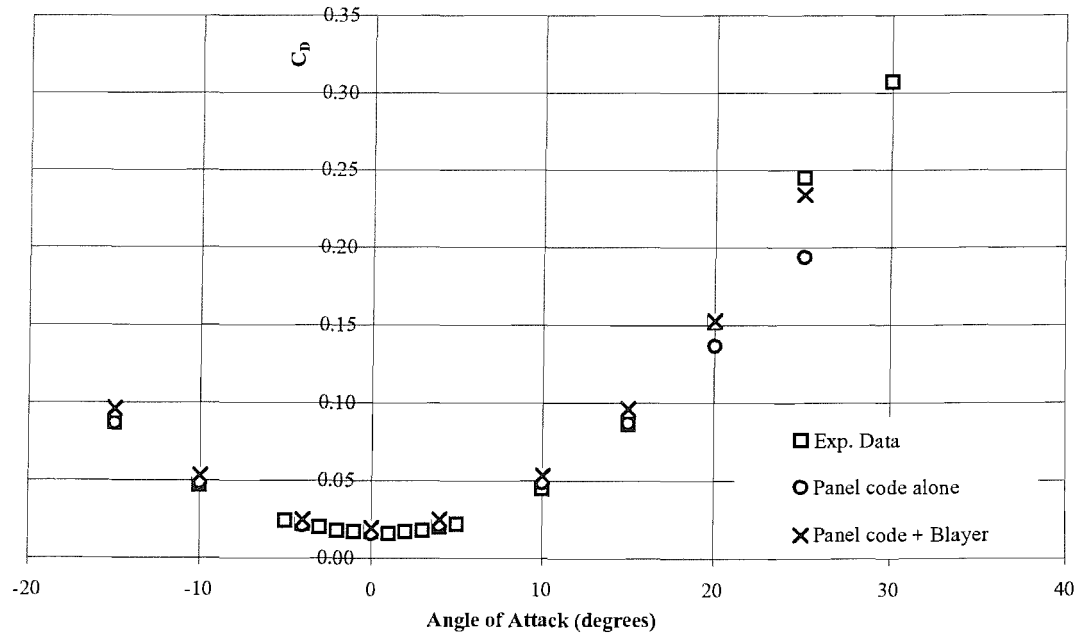

Figure A2.15 - Drag coefficients of NACA 0020 rudder section at various angles of attack.

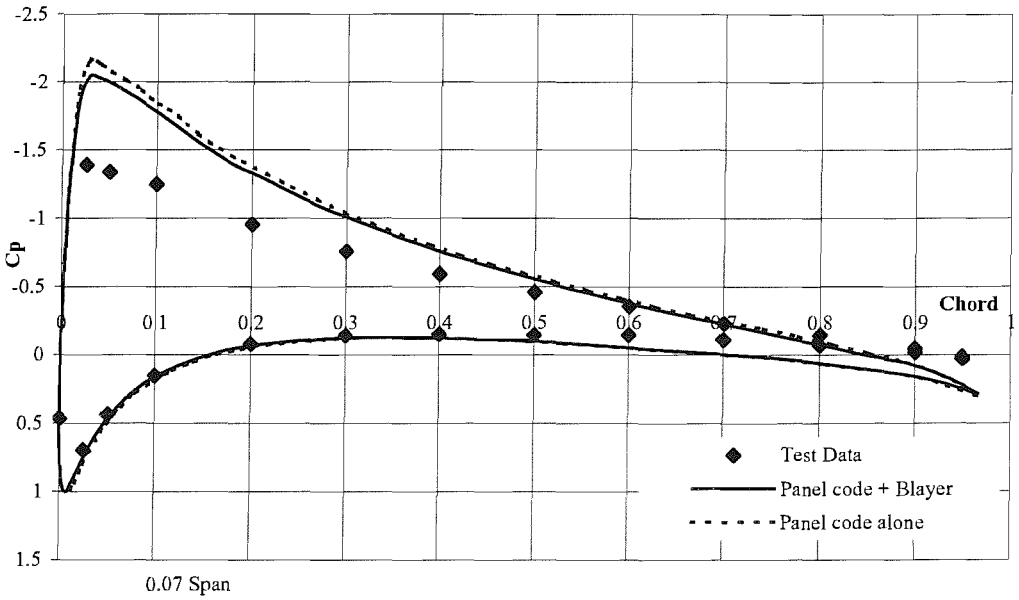

Figure A2.16 - Effect of boundary layer on Cp distribution over rudder section at 0.07 span.

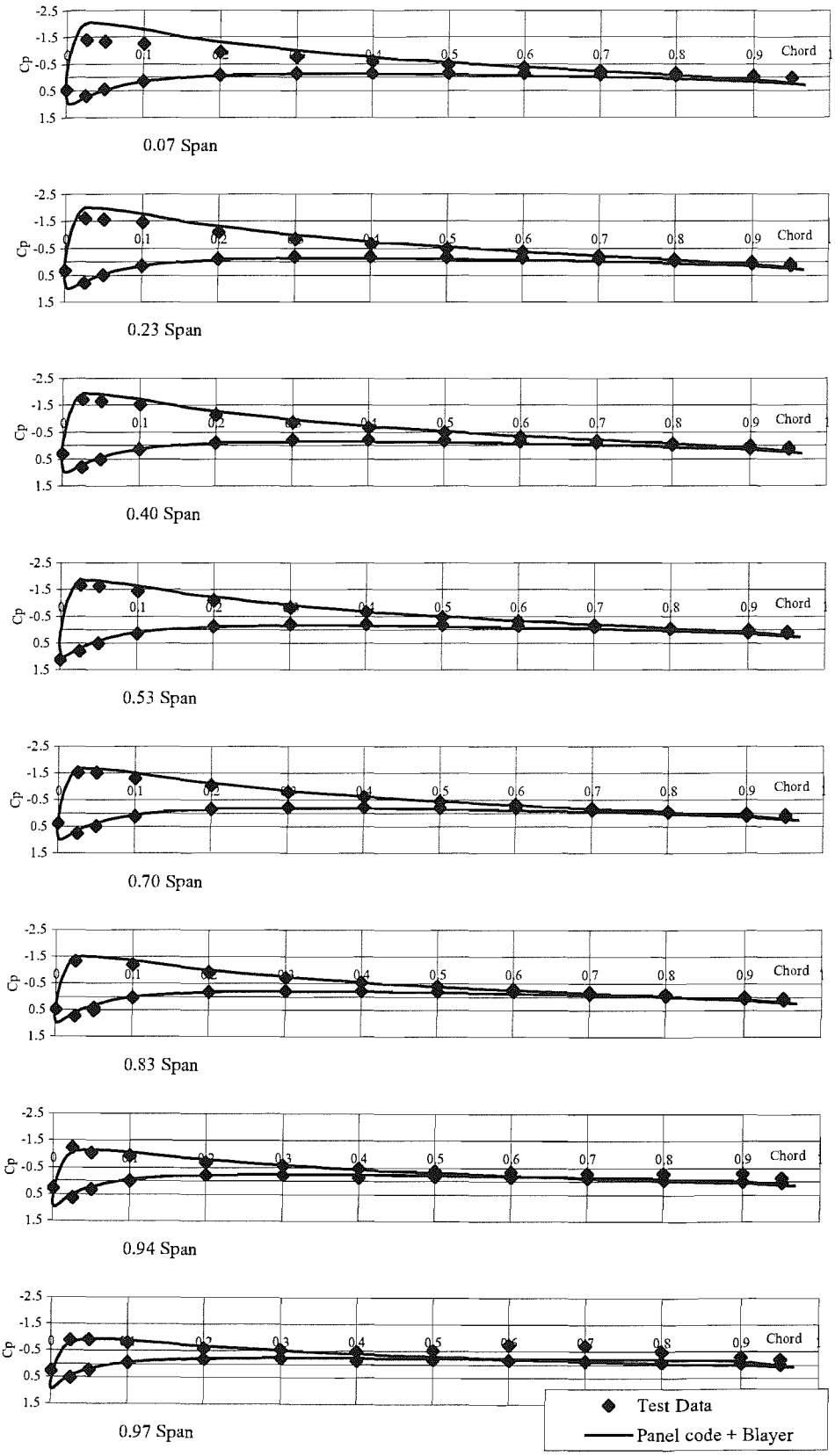

Figure A2.17 - Cp distributions at several span locations along NACA0020 rudder.

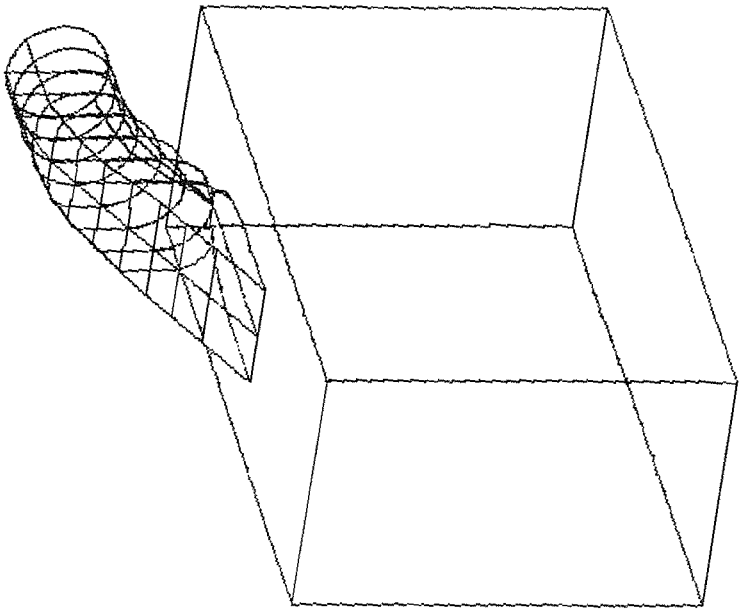

Figure A2.18 - Block structure for CFX waterjet-wind tunnel section model.

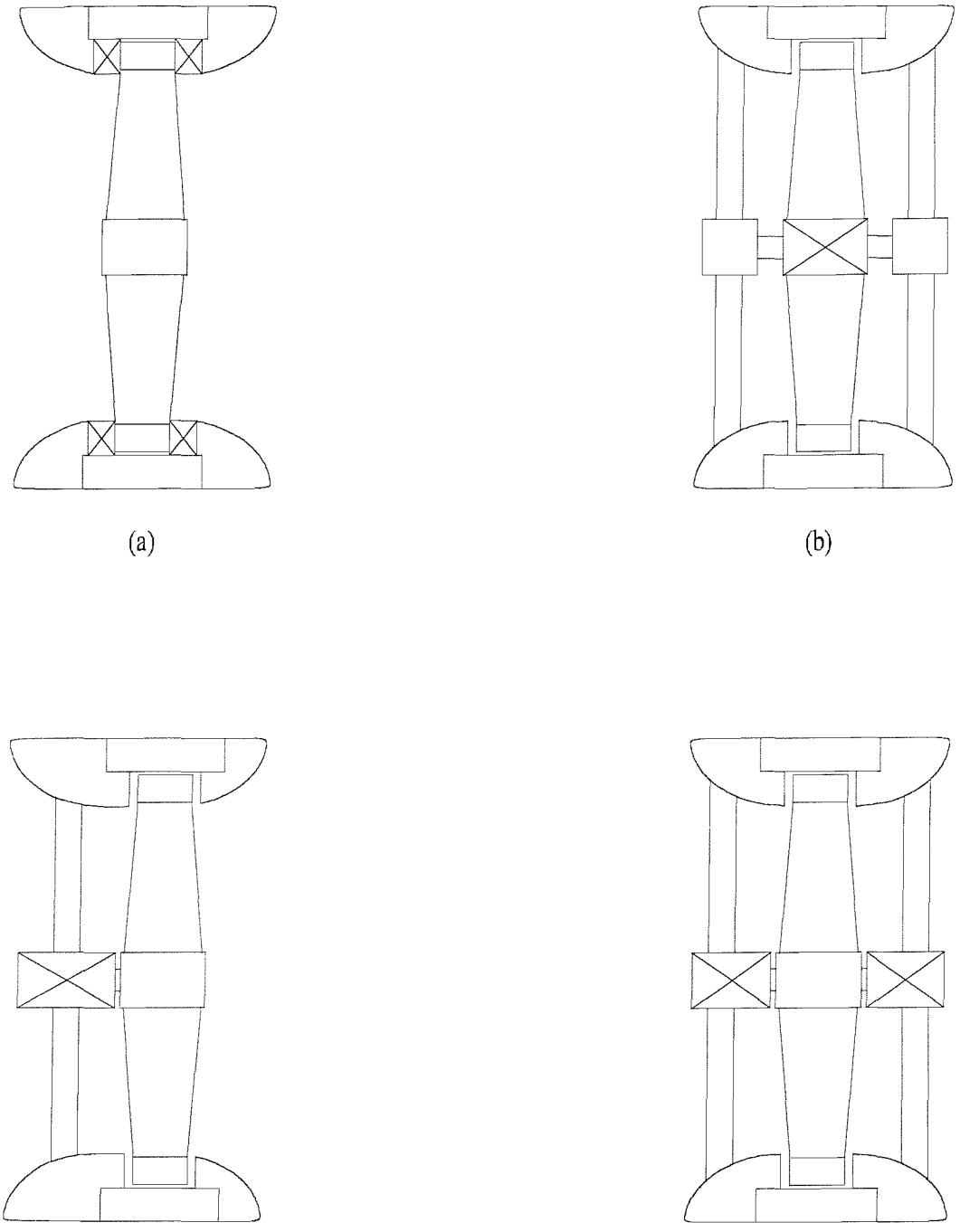

Figure A3.1 - Possible bearing locations for ETDP.

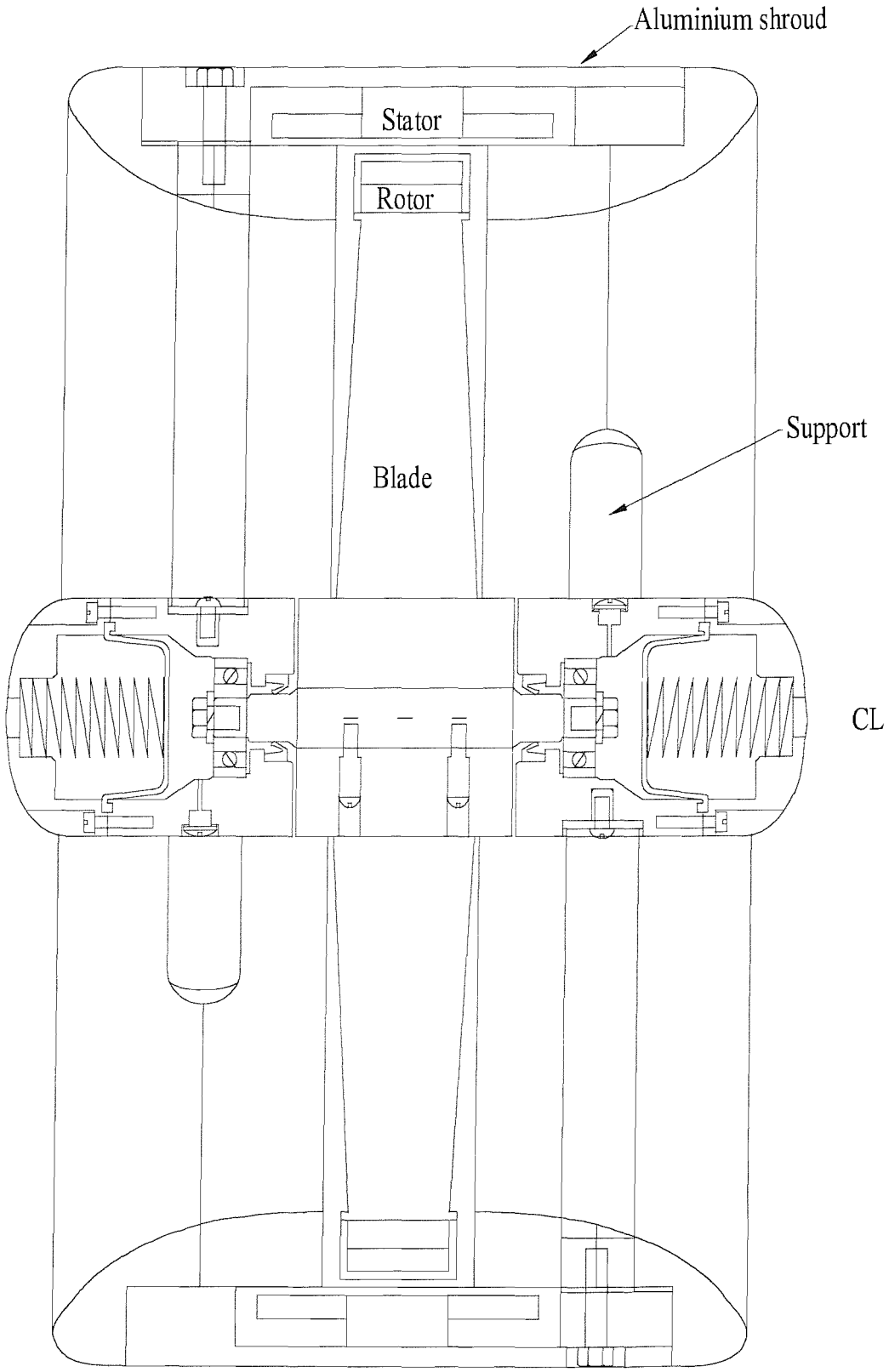

Figure A3.2 - Electromagnetic Tip-Driven Propeller (ETDP) general arrangement.

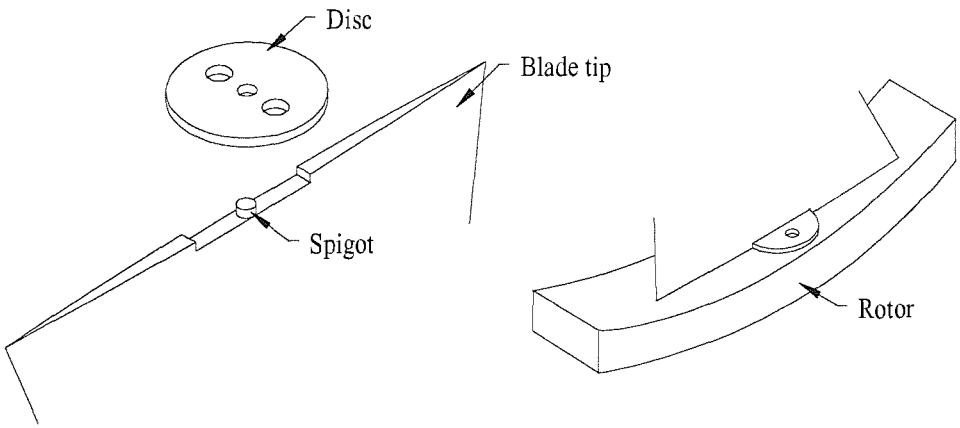

Figure A3.3 - ETDP Propeller to rotor joint (not to scale).

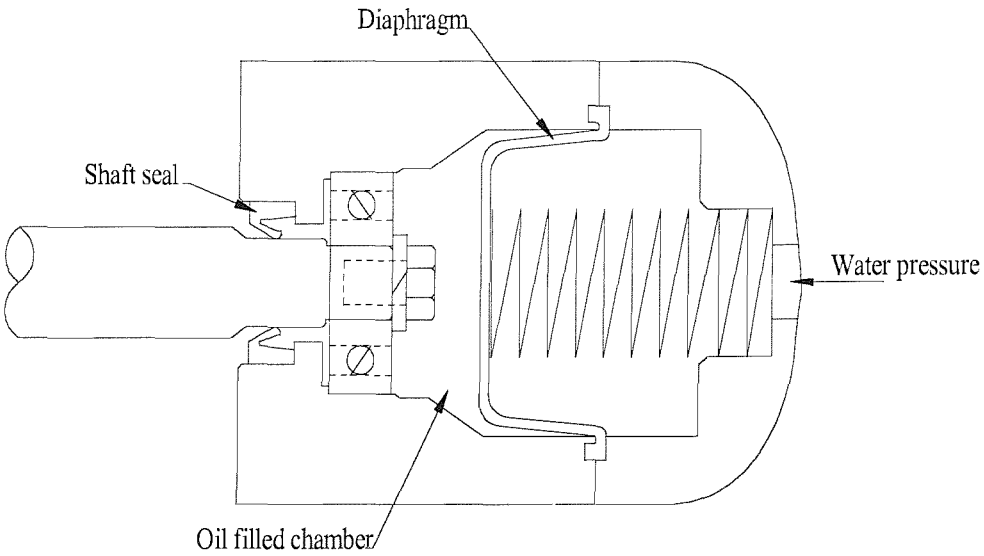

Figure A3.4 - ETDP Bearing seal mechanism (not to scale).

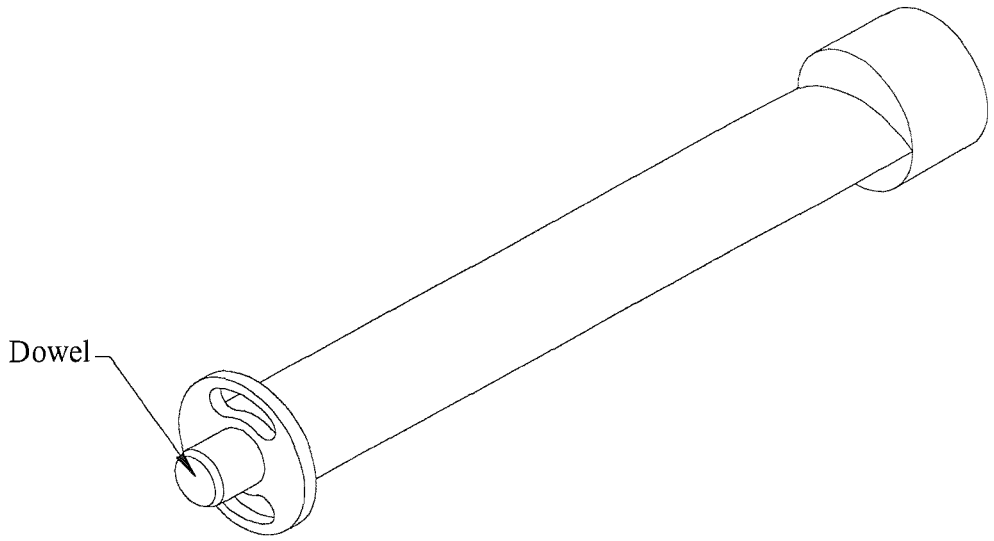

Figure A3.5 - ETDP Bearing support strut (not to scale).

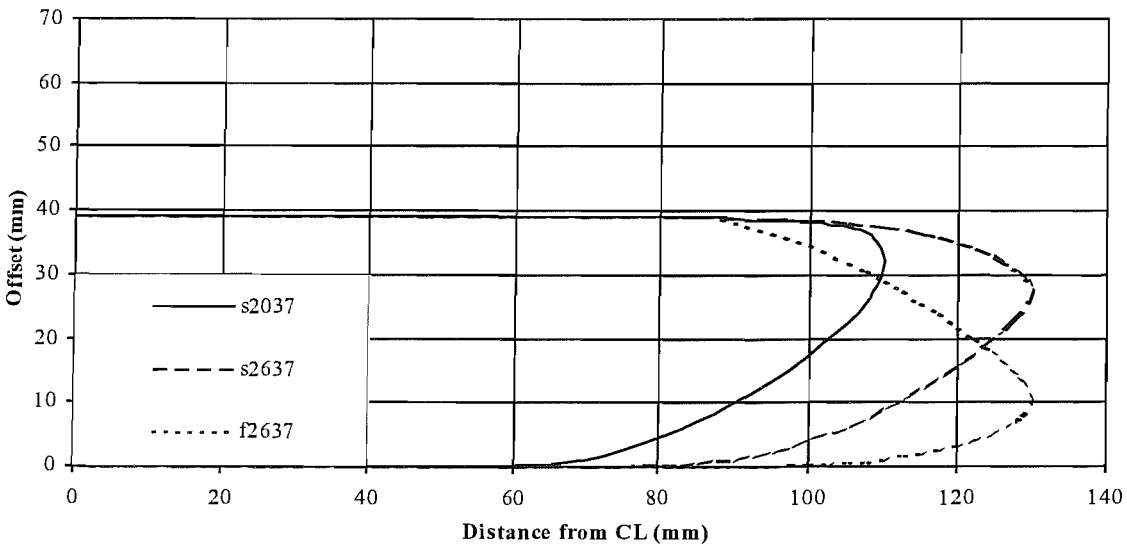

Figure A3.6 - ETDP duct section profiles.

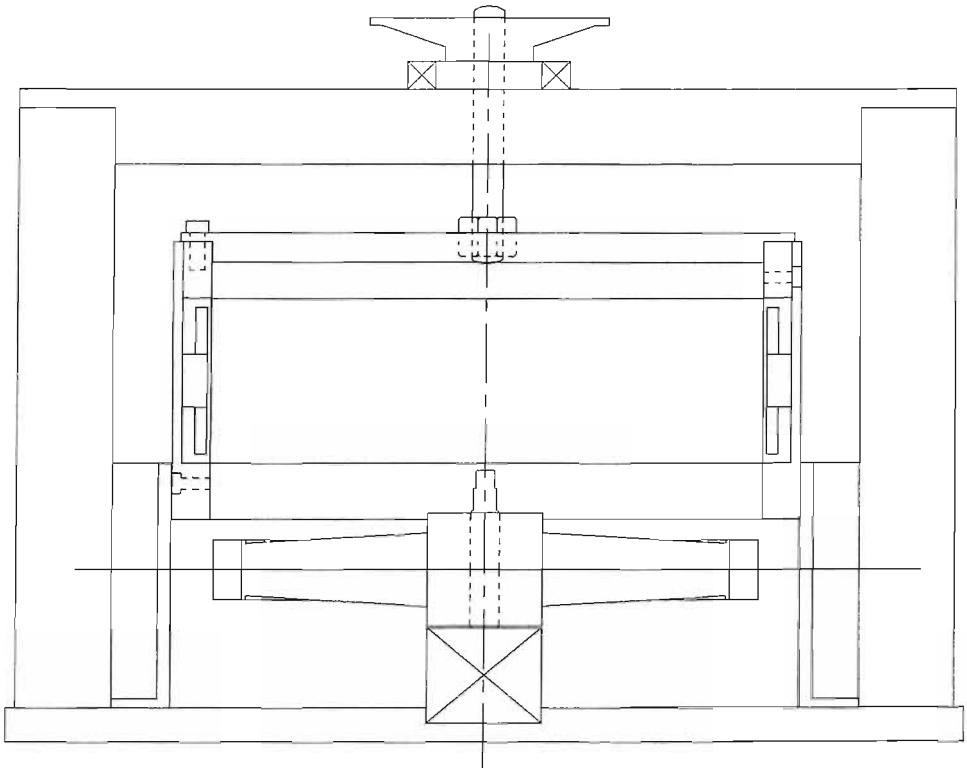

Figure A3.7 - ETDP Assembly jig arrangement.

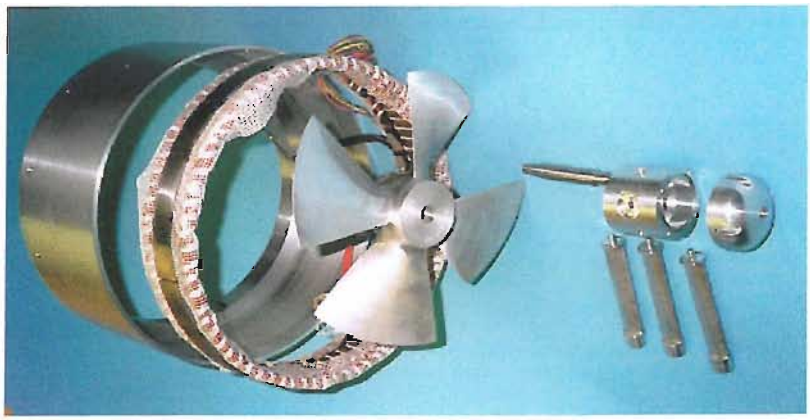

Figure A3.8 – Components used in the prototype TDP. From left to right: Aluminium shroud, stator, propeller, propeller shaft, bearing casing and supports.

Figure A3.9 – The completed prototype TDP.

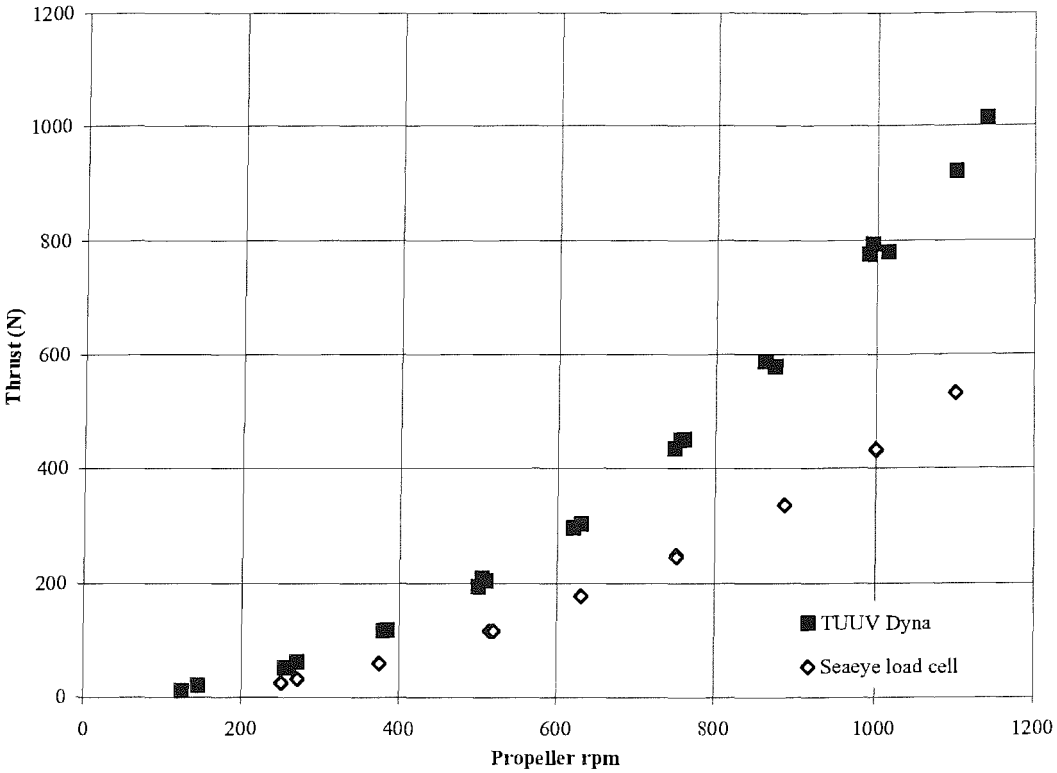

Figure A4.2 - Thrust comparison between the two thrust measurement systems.

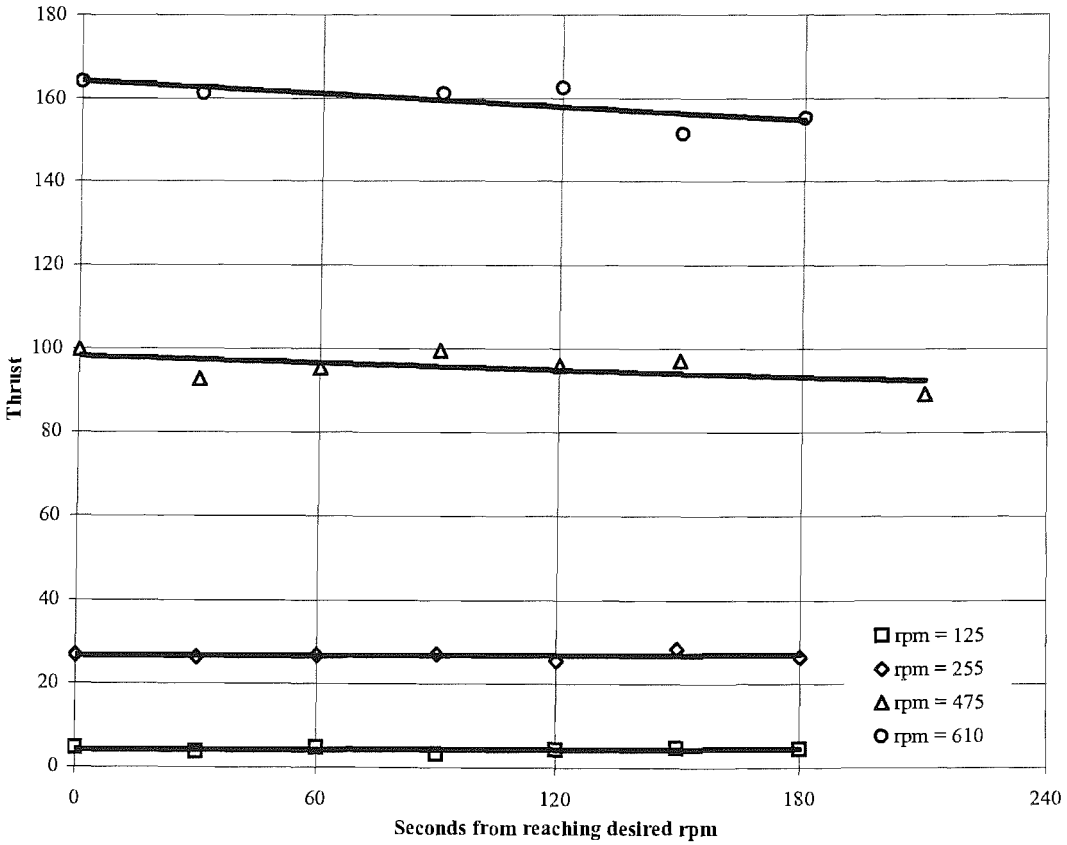

Figure A4.3 - Time history of TDP forward thrust at bollard pull conditions.

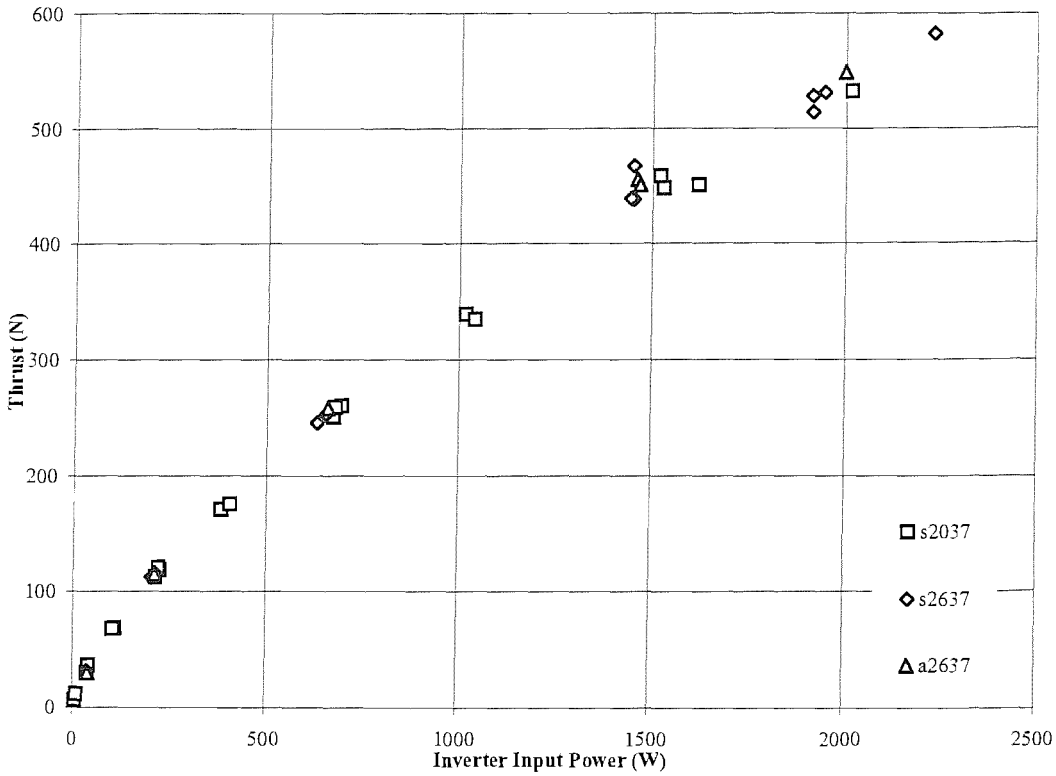

Figure A4.4 - Thrust achieved for a given inverter input power at bollard pull conditions.

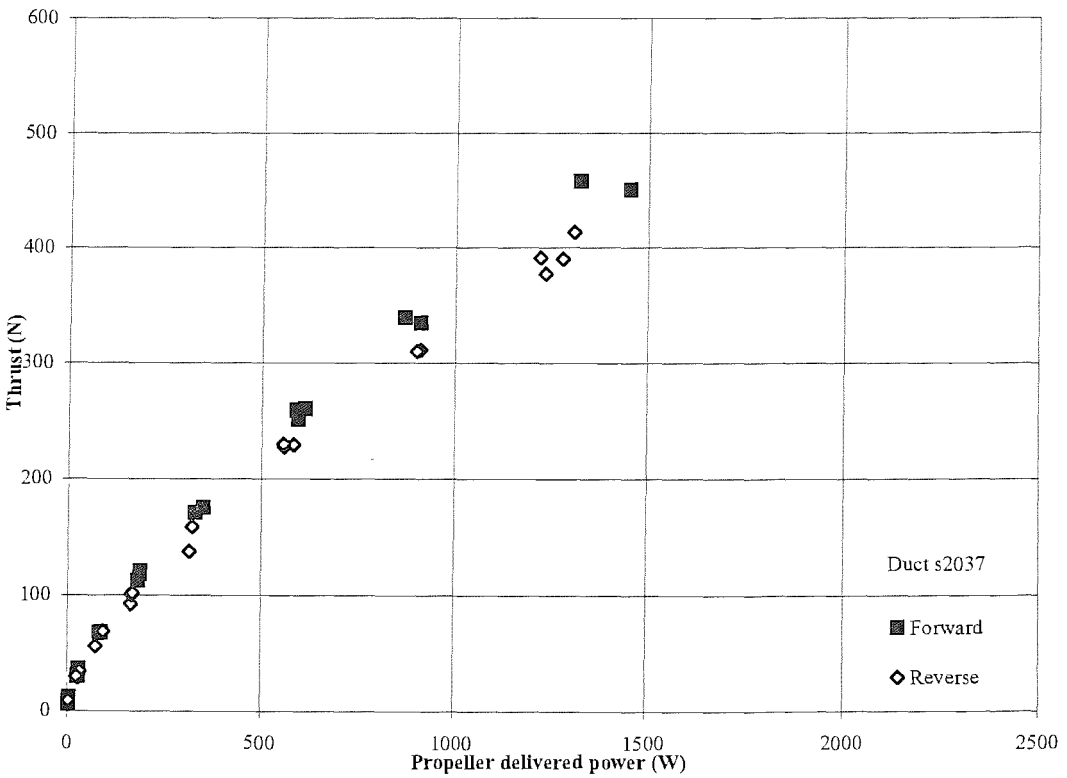

Figure A4.5 - Thrust achieved for a given propeller delivered power at bollard pull conditions.

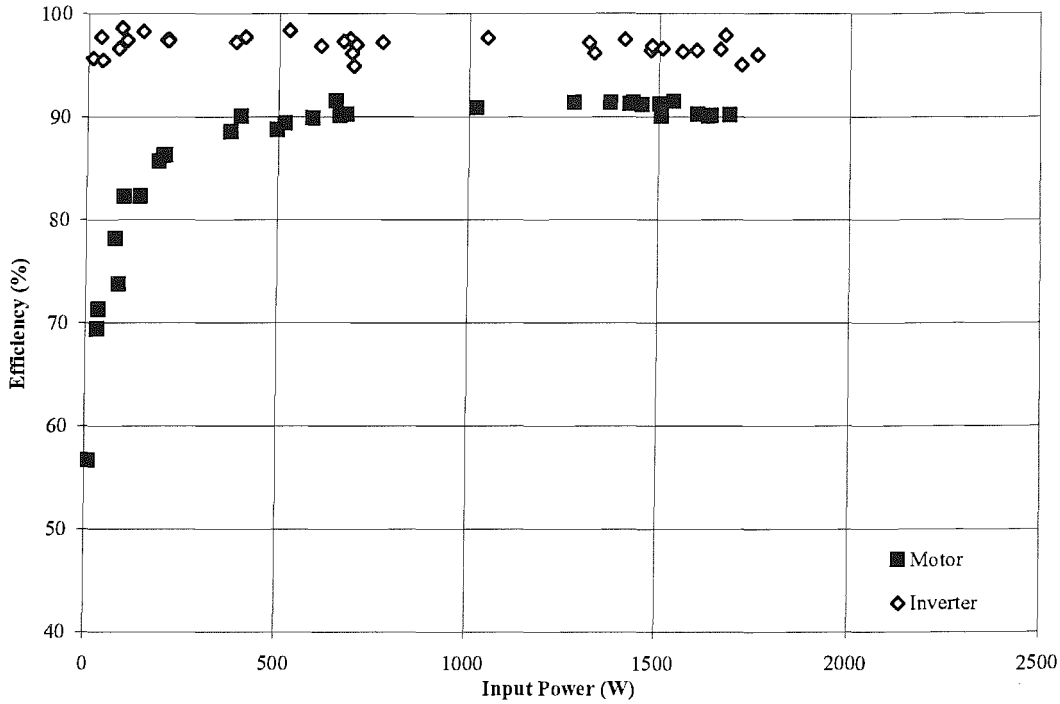

Figure A4.6 - Calculated motor and inverter efficiencies.

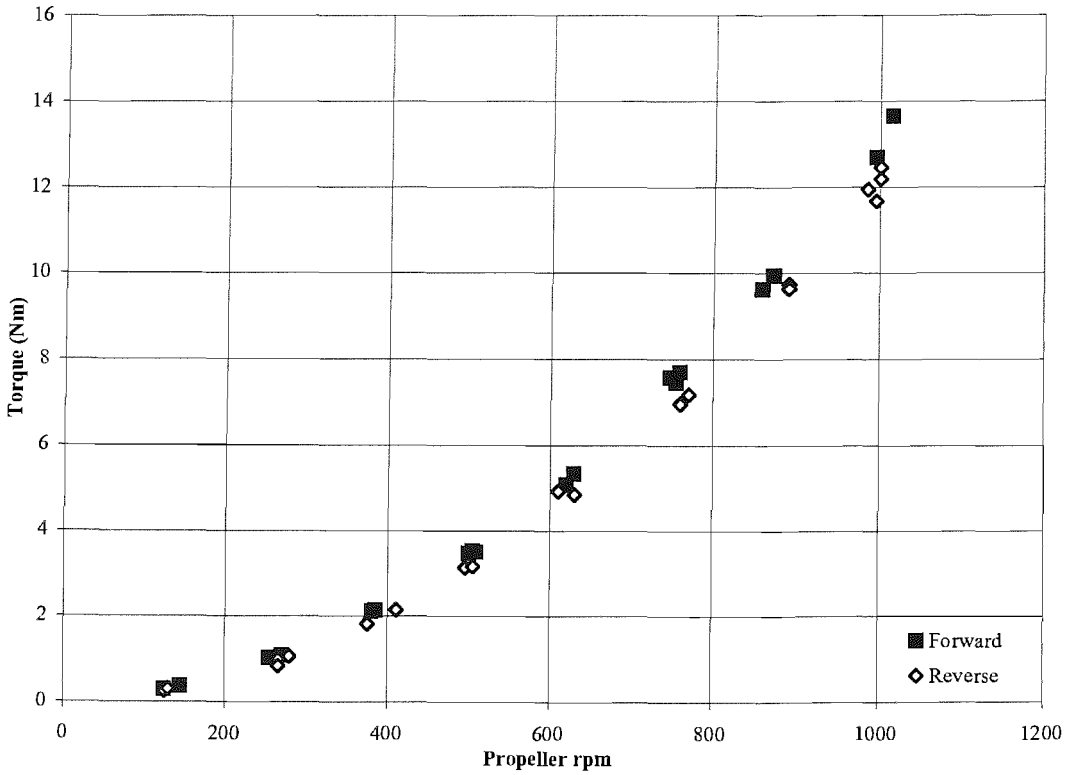

Figure A4.7 - Calculated torque (based on motor power output) for duct s2037, at bollard pull.

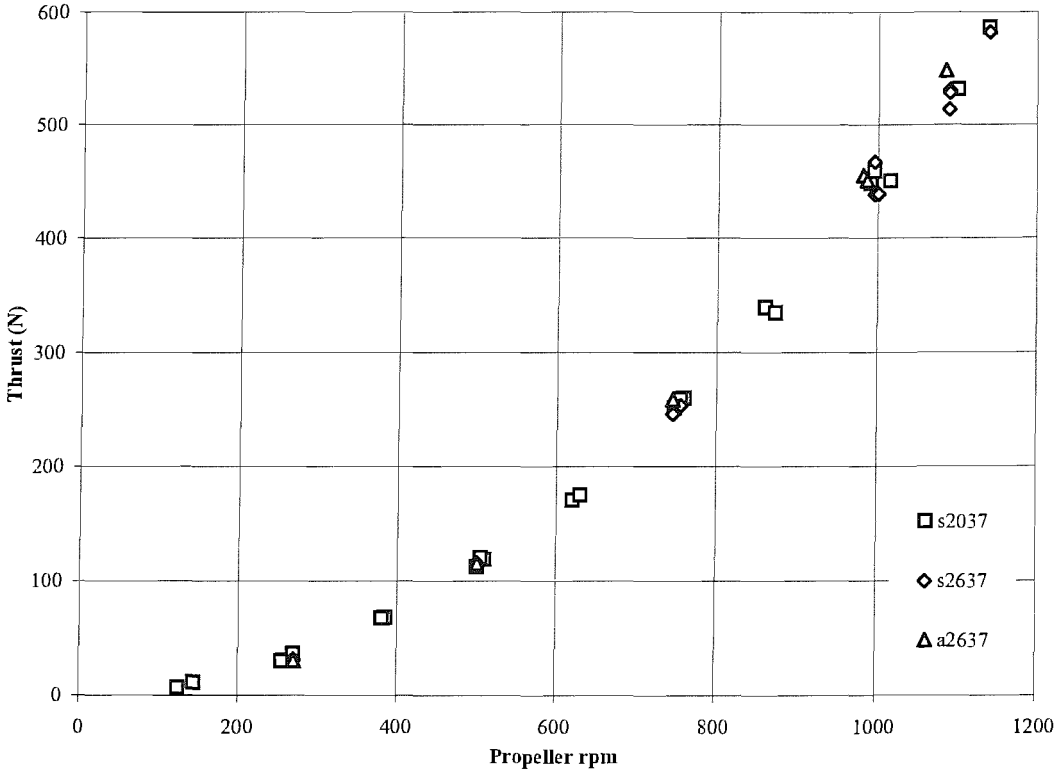

Figure A4.8 - Bollard pull forward thrust for the TDP with three different duct section shapes.

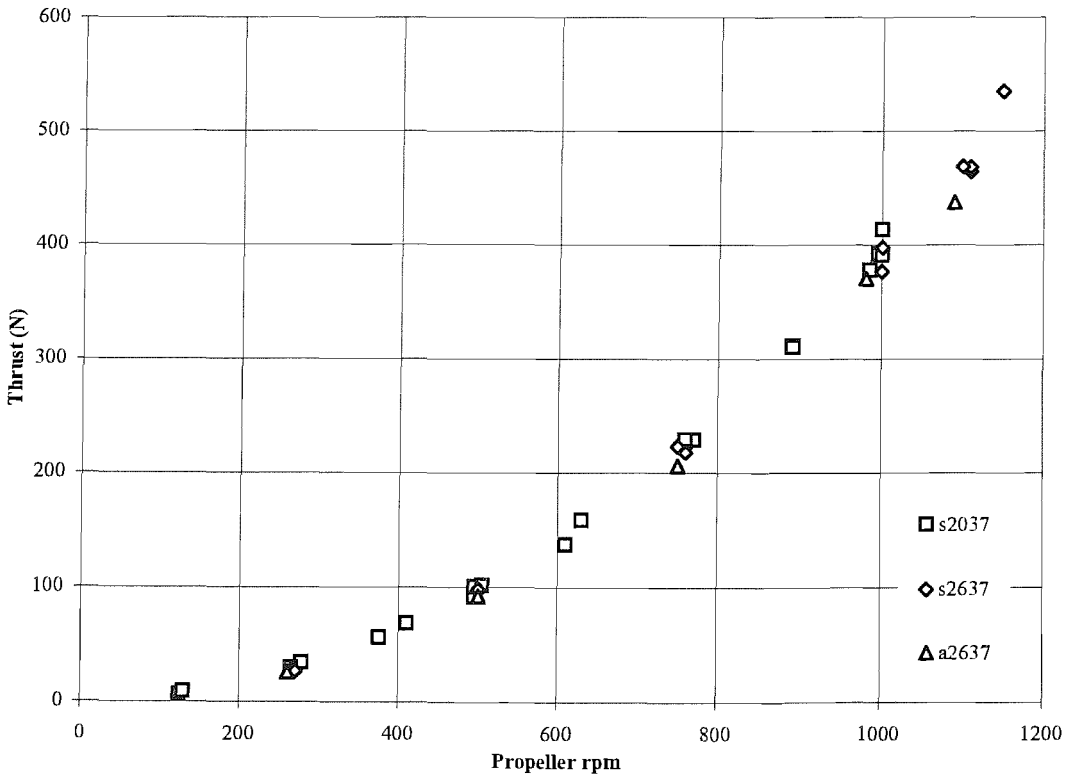

Figure A4.9 - Bollard pull reverse thrust for the TDP with three different duct section shapes.

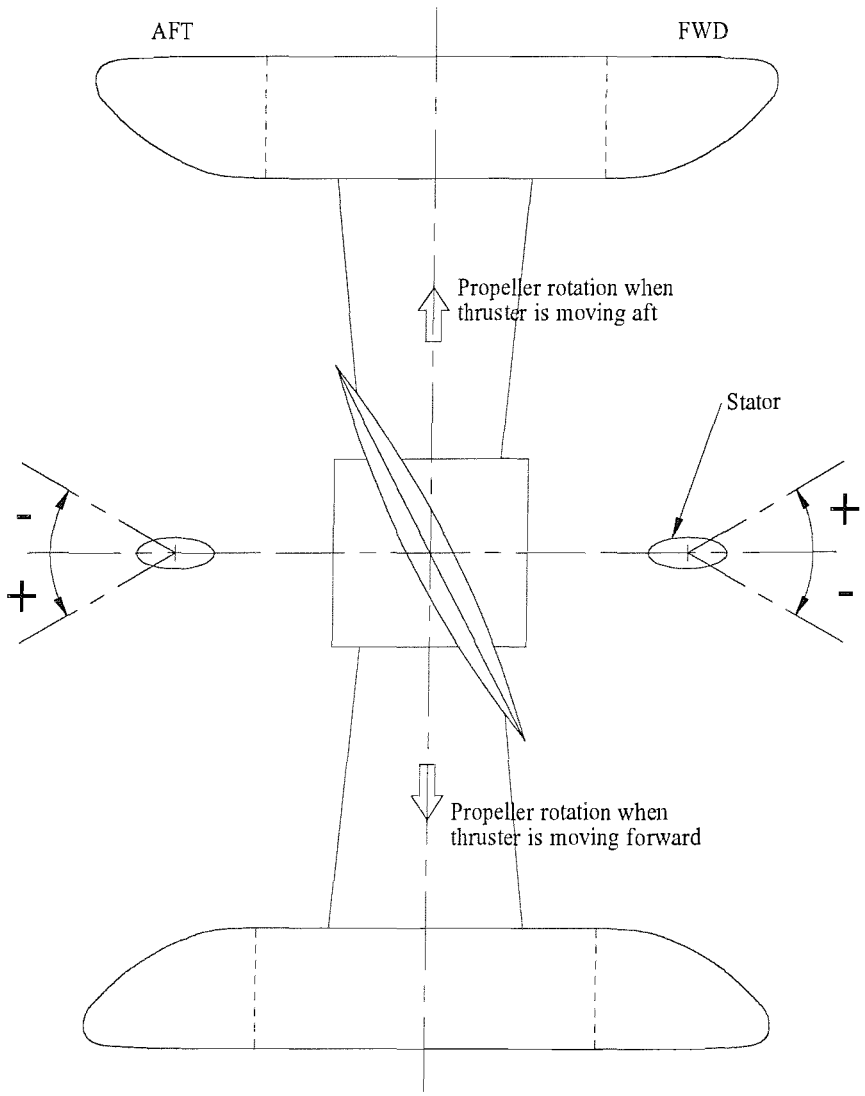

Figure 4.11 - Hydrodynamic stator angles of attack.

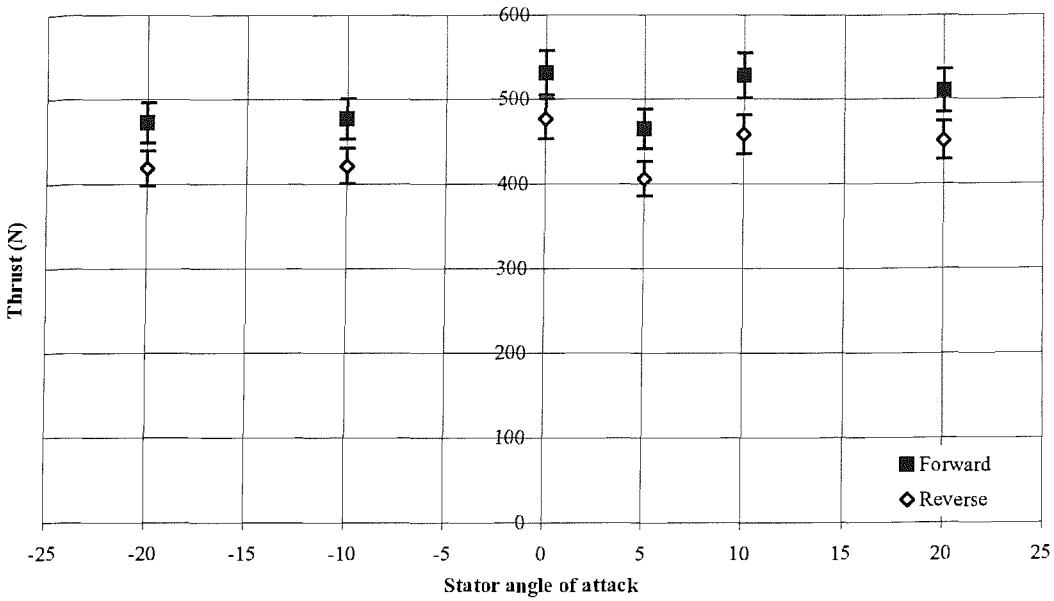

Figure A4.12 - Effect of stator angle with duct s2037, at 1100rpm, at bollard pull.
5% error bars included.

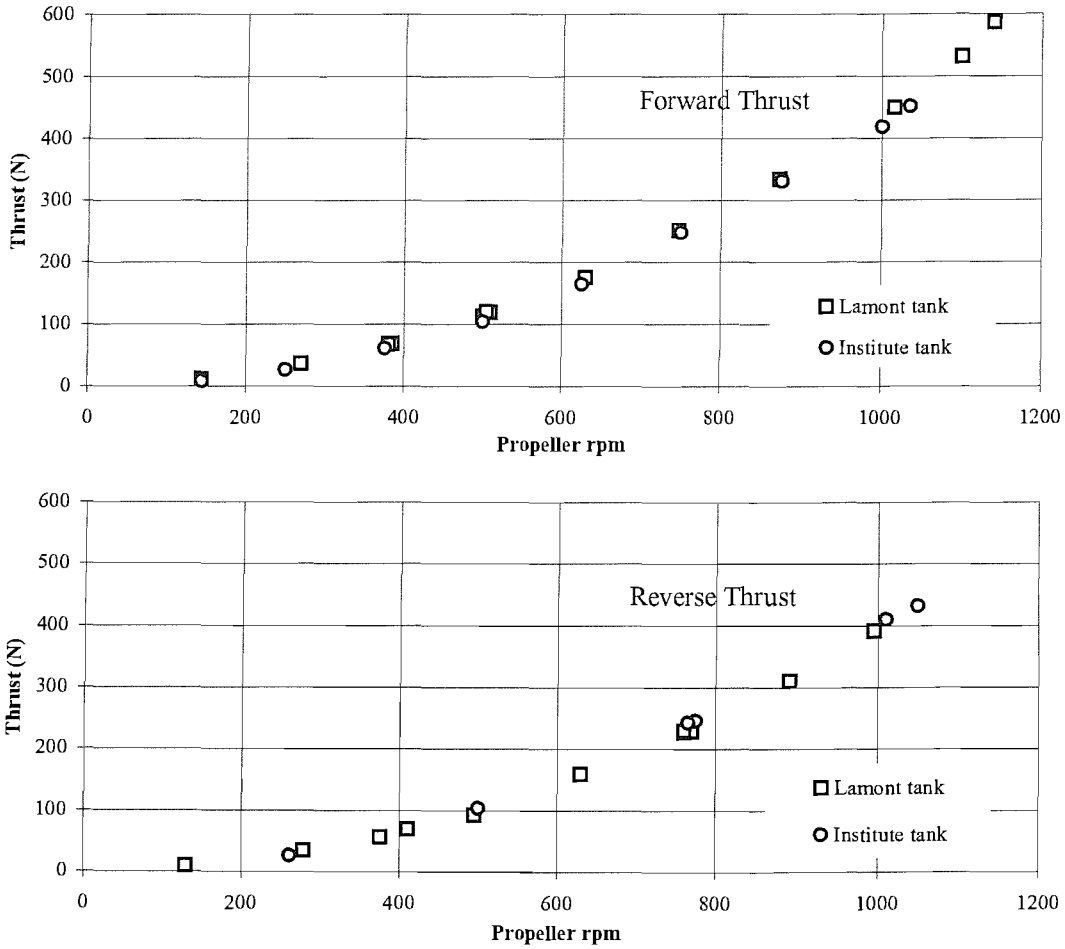

Figure A4.13 - Comparison of s2037 bollard pull tests in two towing tanks.

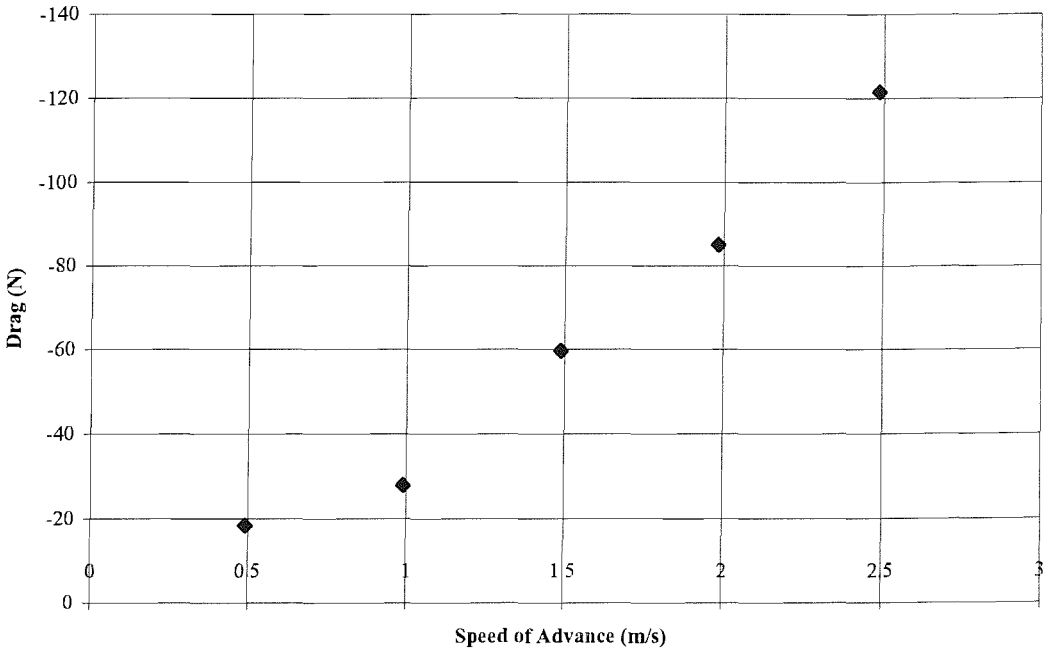

Figure A4.14 - Drag of support cylinder.

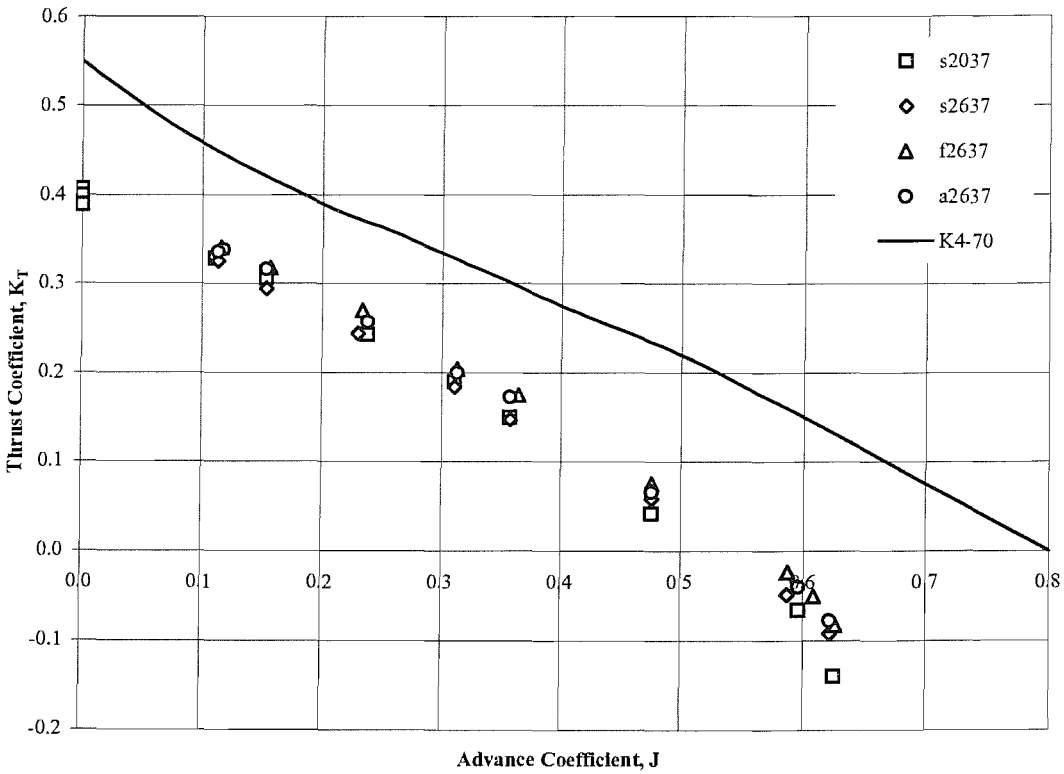

Figure A4.15 - K_T, J chart for the prototype ETDP running in the forward direction.

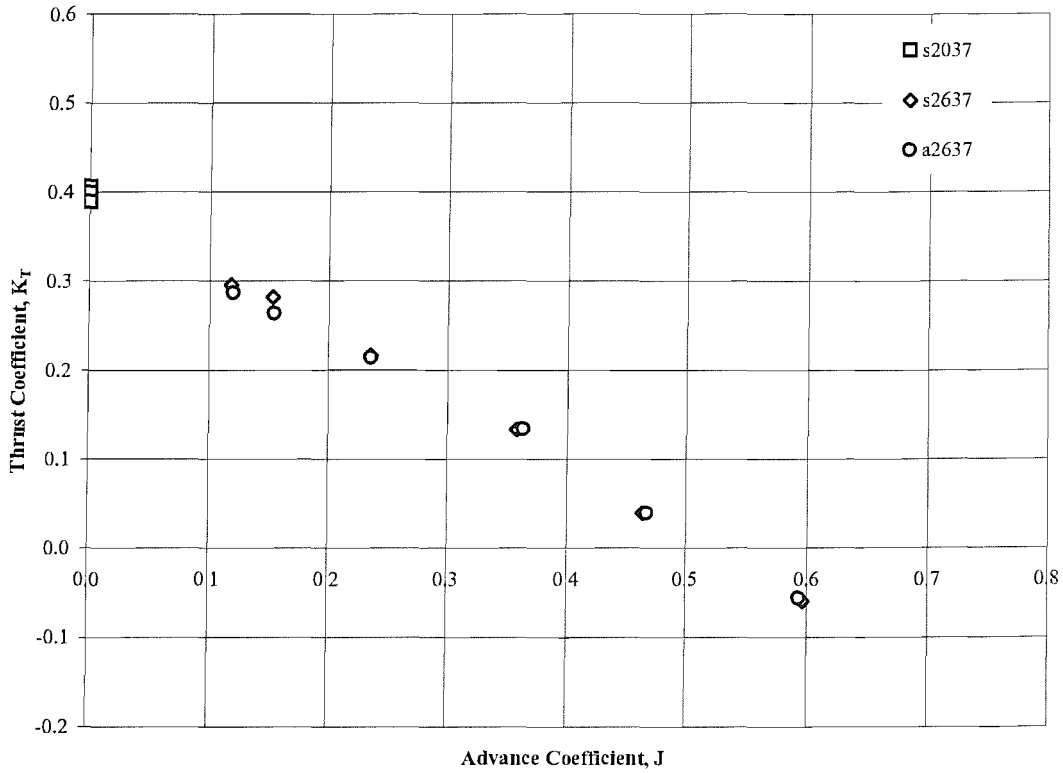

Figure A4.16 - K_T, J chart for the prototype ETDP running in the reverse direction.

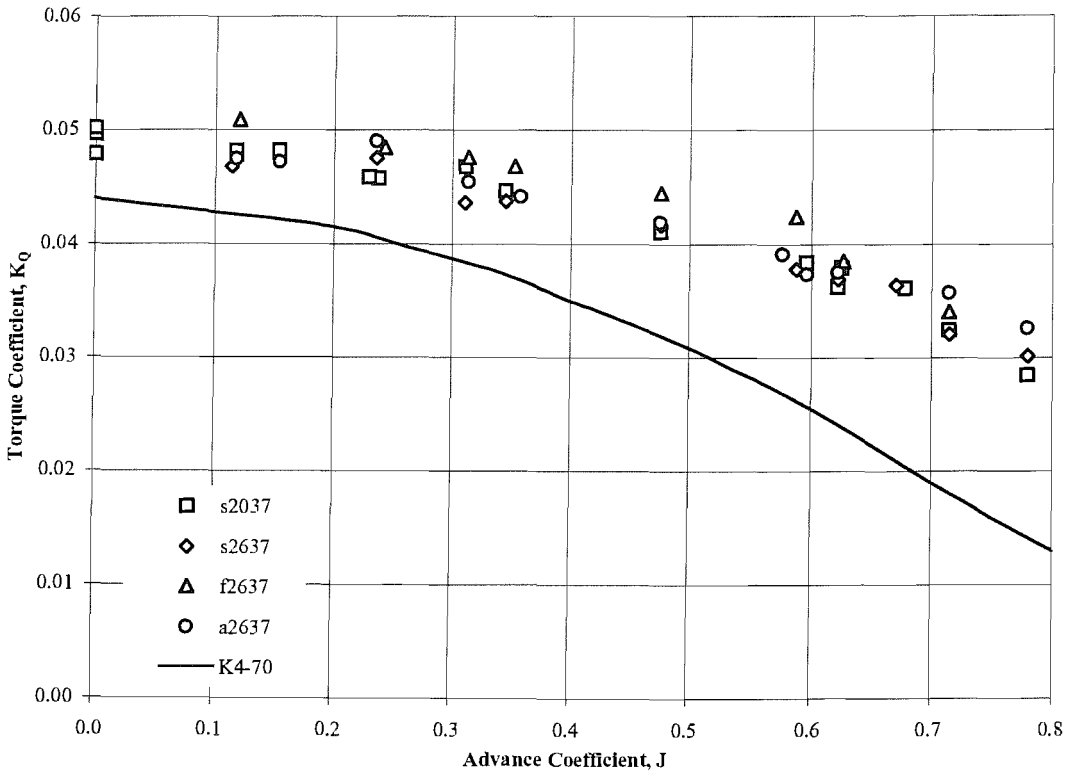

Figure A4.17 - K_Q, J chart for the prototype ETDP running in the forward direction.

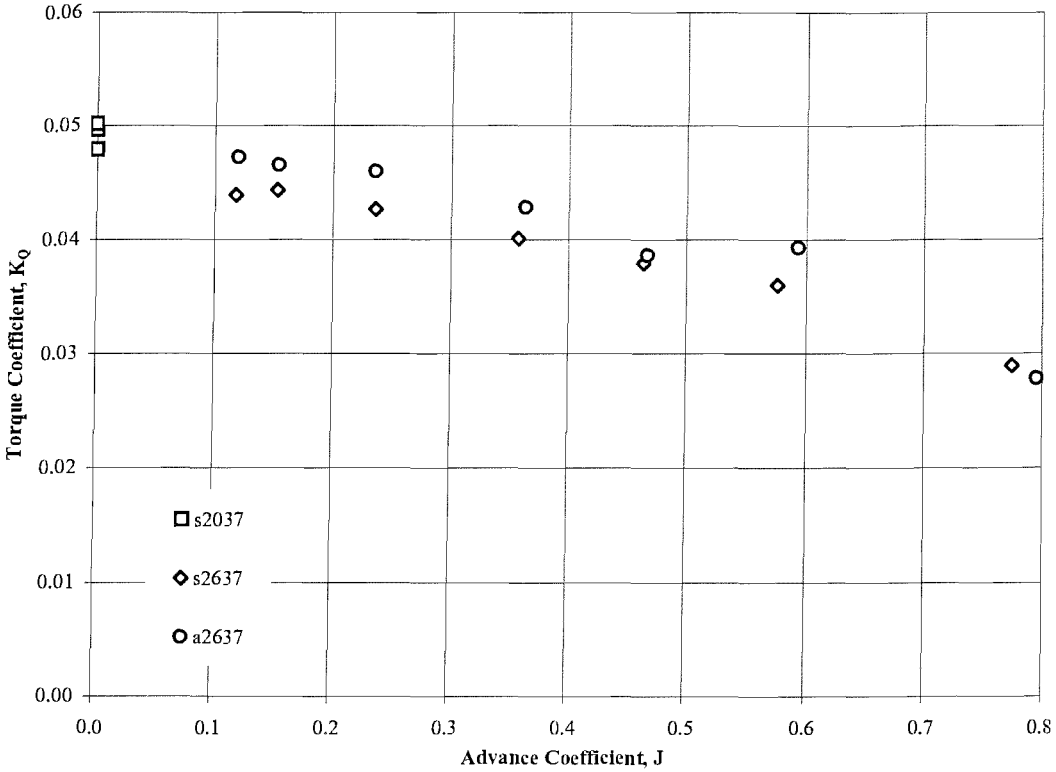

Figure A4.18 - K_Q, J chart for the prototype ETDP running in the reverse direction.

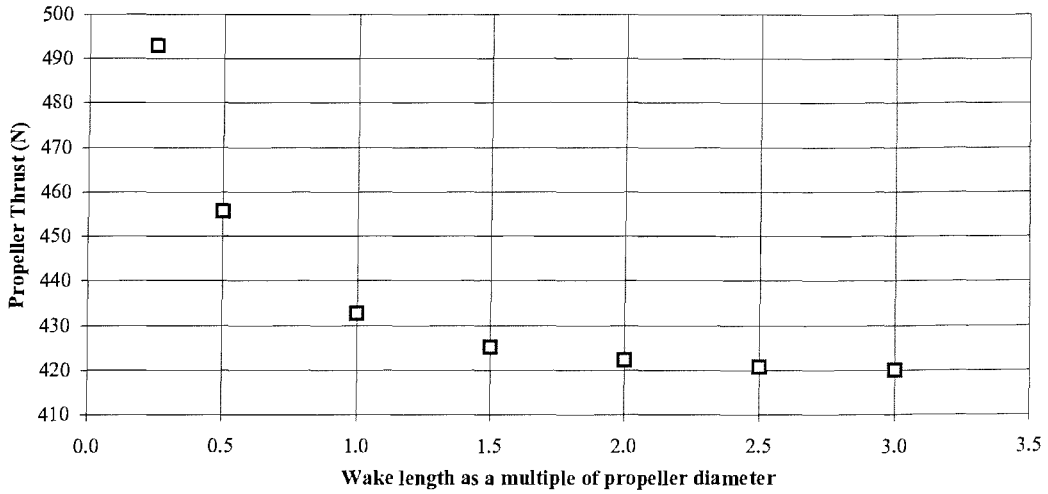

Figure A5.2 - Effect of fixed wake length on propeller thrust (100 wake panels).

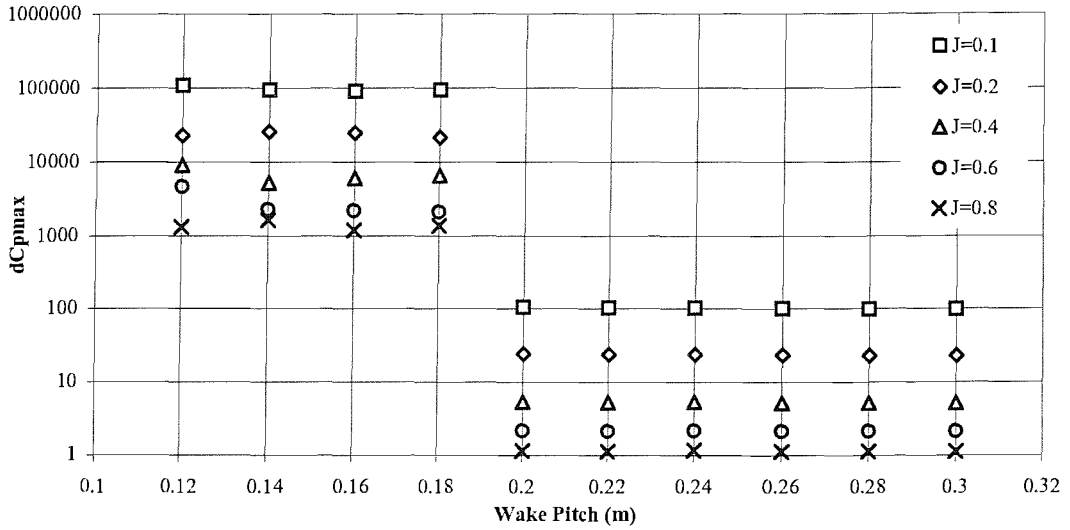

Figure A5.3 - Influence of wake pitch on propeller convergence parameter dCpmax.
Kaplan K4-70, P/D=1.0, 1000rpm

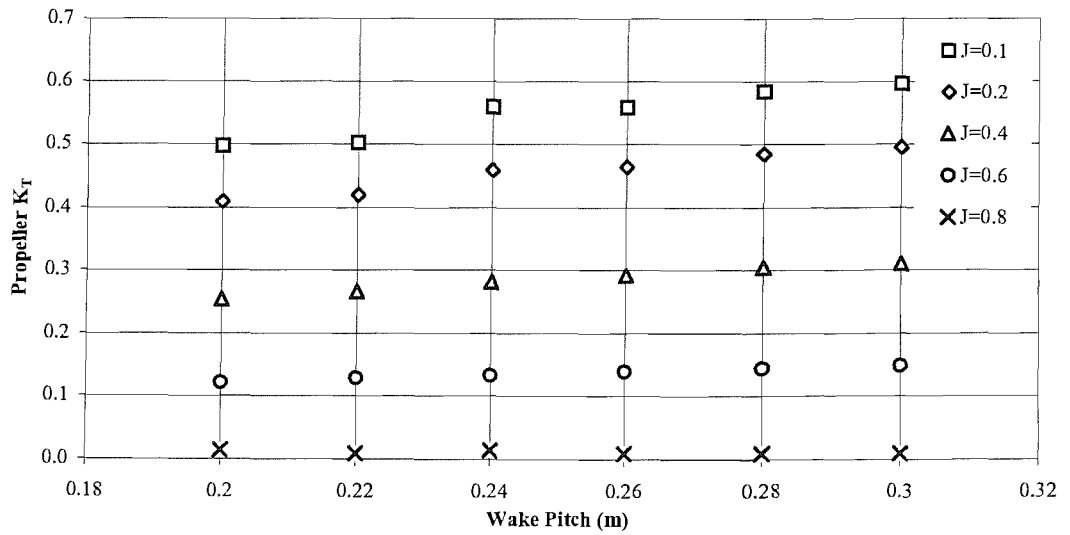

Figure A5.4 - Influence of wake pitch on predicted propeller thrust.

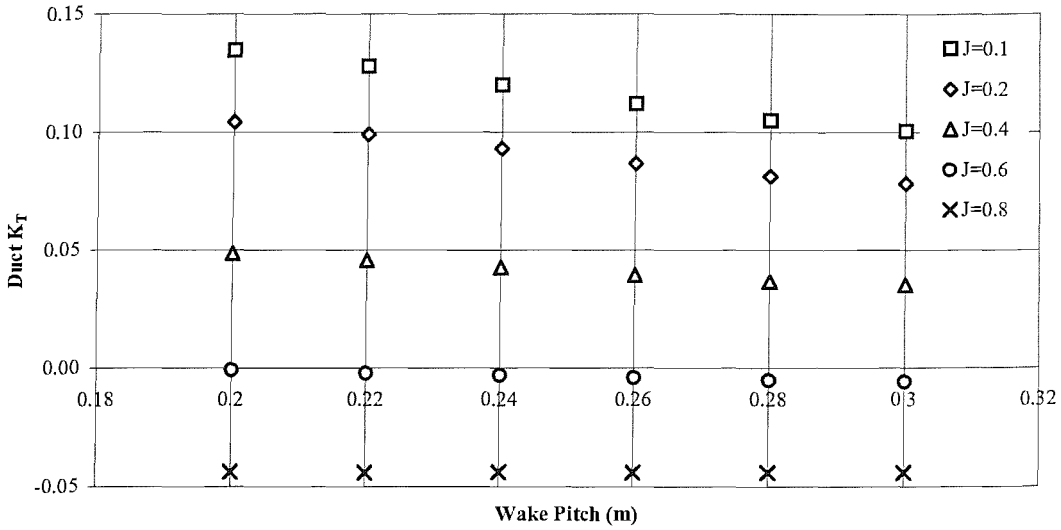

Figure A5.5 - Influence of wake pitch on predicted duct thrust.

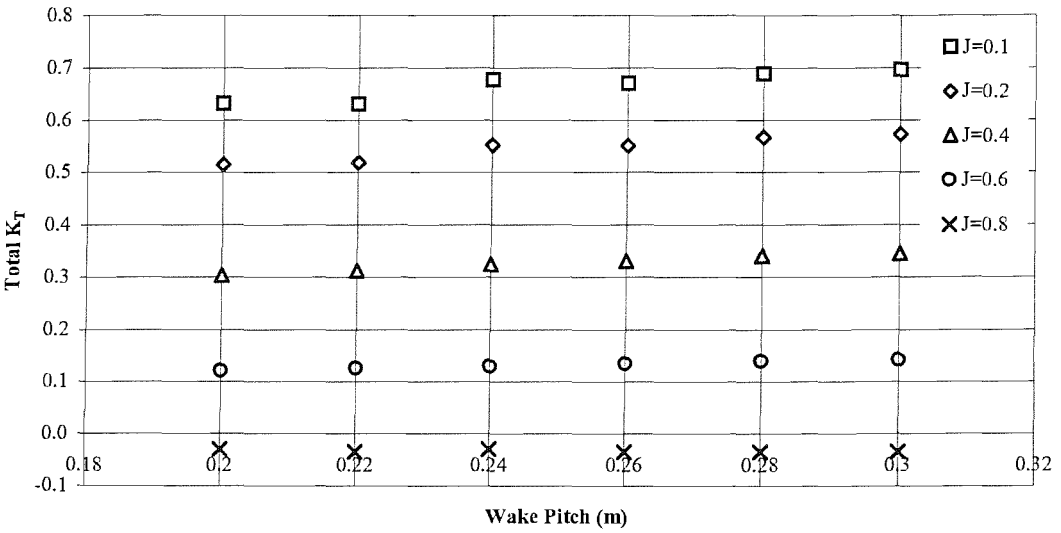

Figure A5.6 - Influence of wake pitch on predicted total thrust.

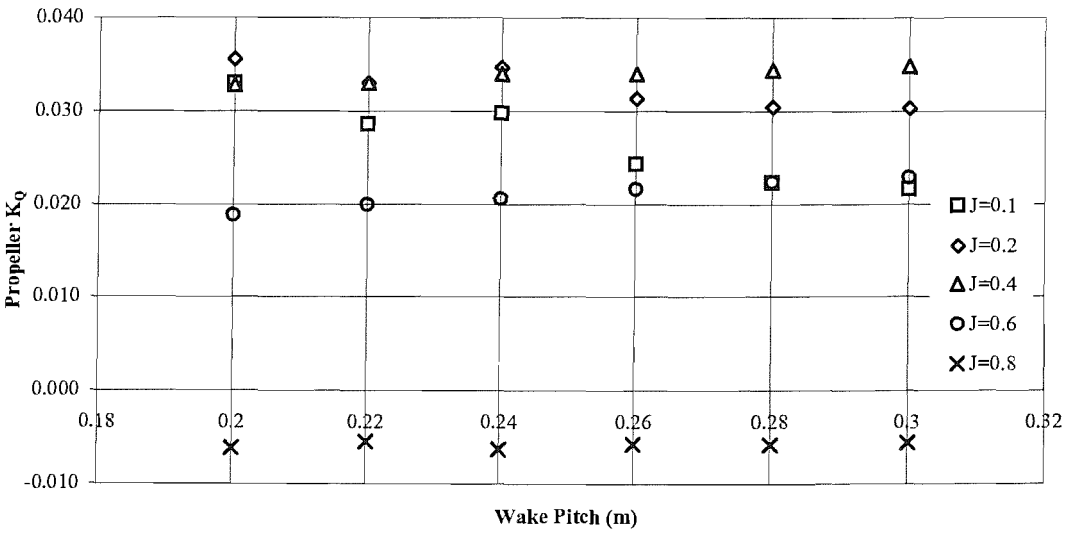

Figure A5.7 - Influence of wake pitch on predicted propeller torque.

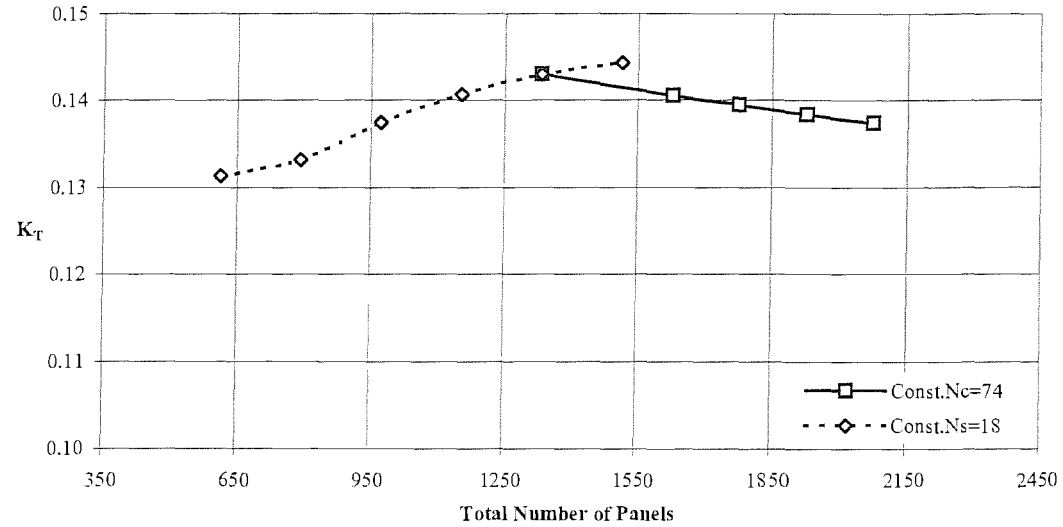

Figure A5.9 - Influence of panel ratio on predicted blade axial force.

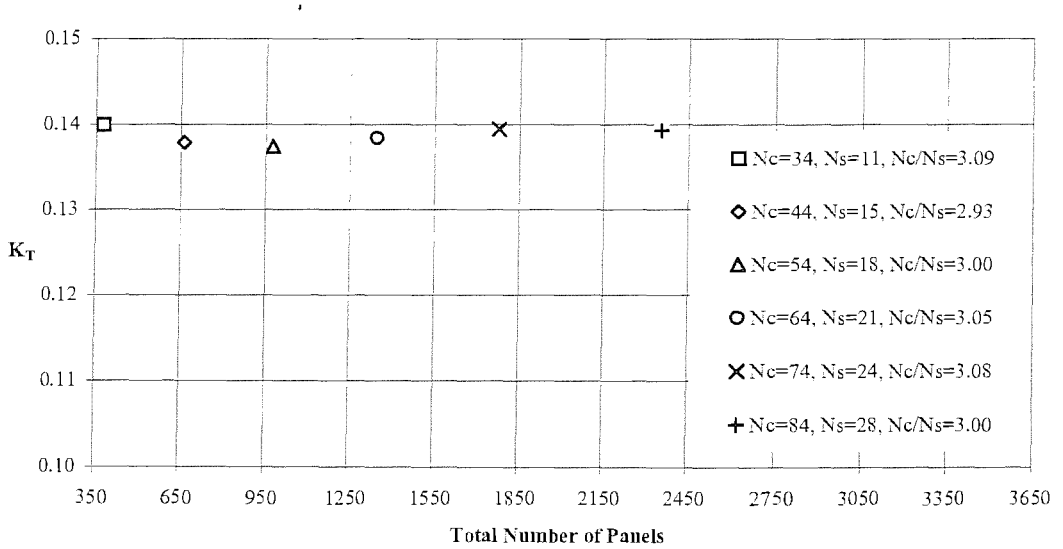

Figure A5.10 - Influence of panel number on predicted blade axial force, Nc/Ns=3.0

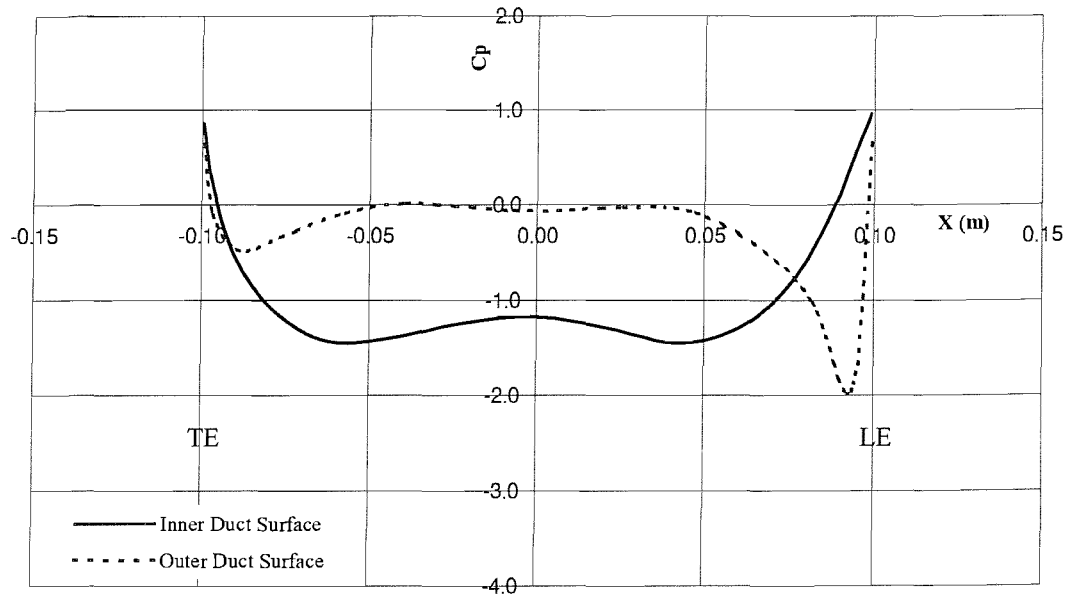

Figure A5.12 - Cp distribution along a Marin duct 37 section.

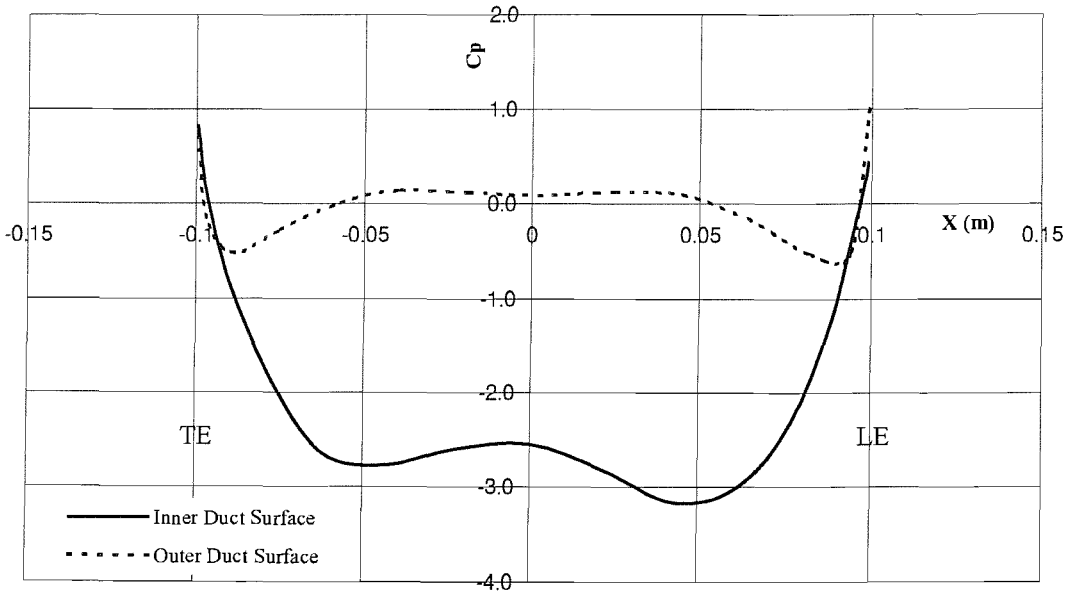

Figure A5.13 - Cp distribution along a Marin duct 37 section with Kaplan K4-70 propeller.

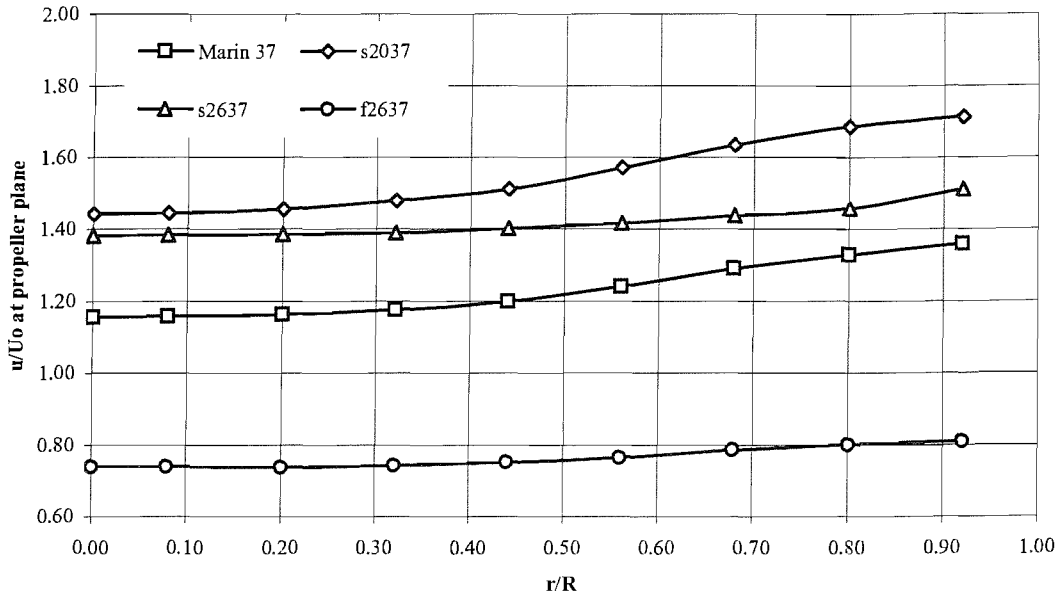

Figure A5.14 - Duct velocity profiles at centre plane, free-stream conditions.

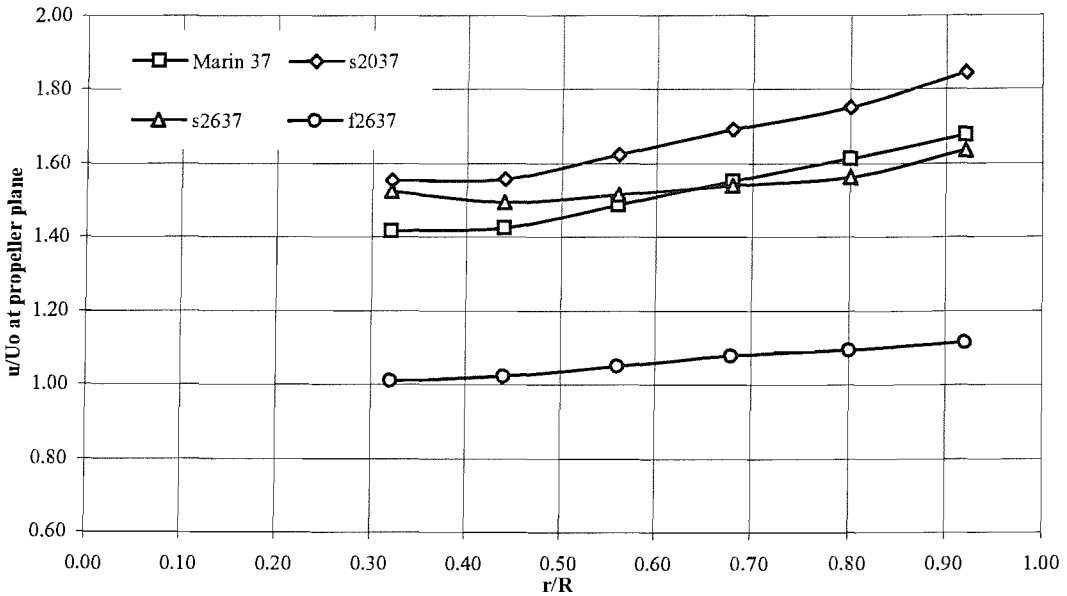

Figure A5.15 - Duct velocity profiles at centre plane with influence of propeller.

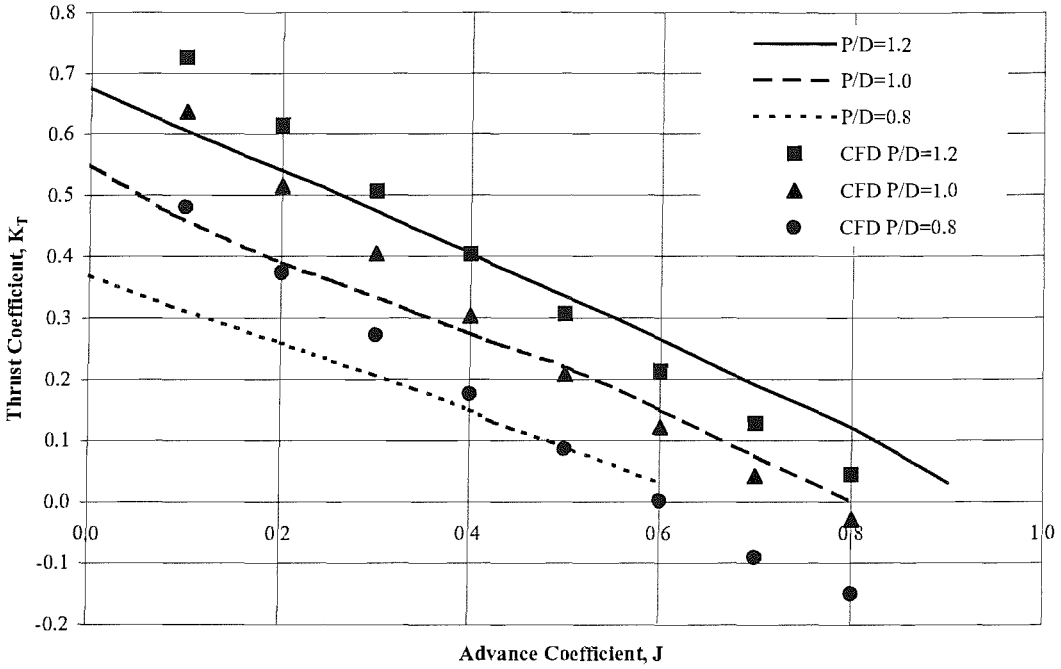

Figure A5.16 - K_T, J chart for K4-70 propeller in Marin duct 37. CFD vs experimental.

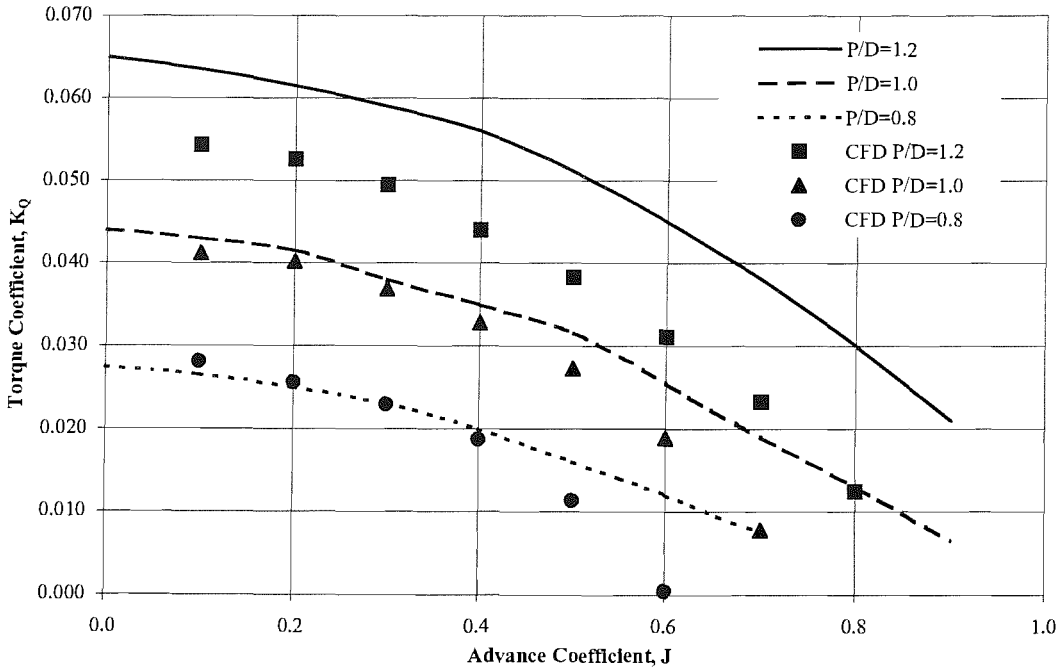

Figure A5.17 - K_Q, J chart for K4-70 propeller in Marin duct 37. CFD vs experimental.

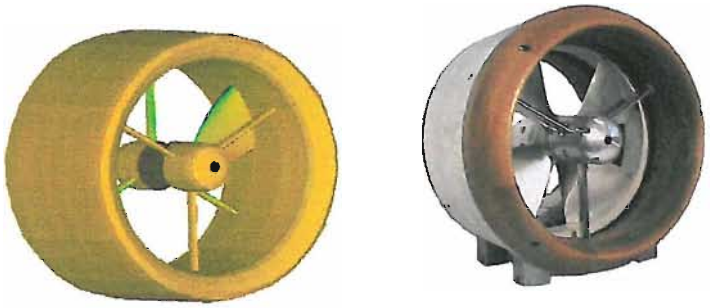

Figure A5.18 - Panel model of TDP next to photograph of the prototype.

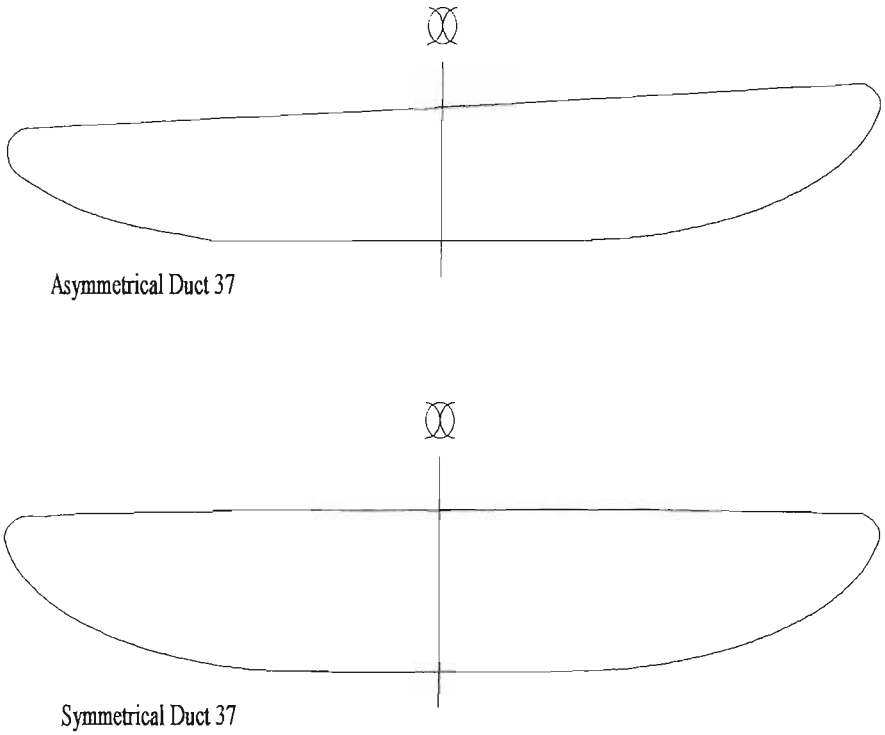

Figure A5.19 – Symmetrical and asymmetrical duct sections.

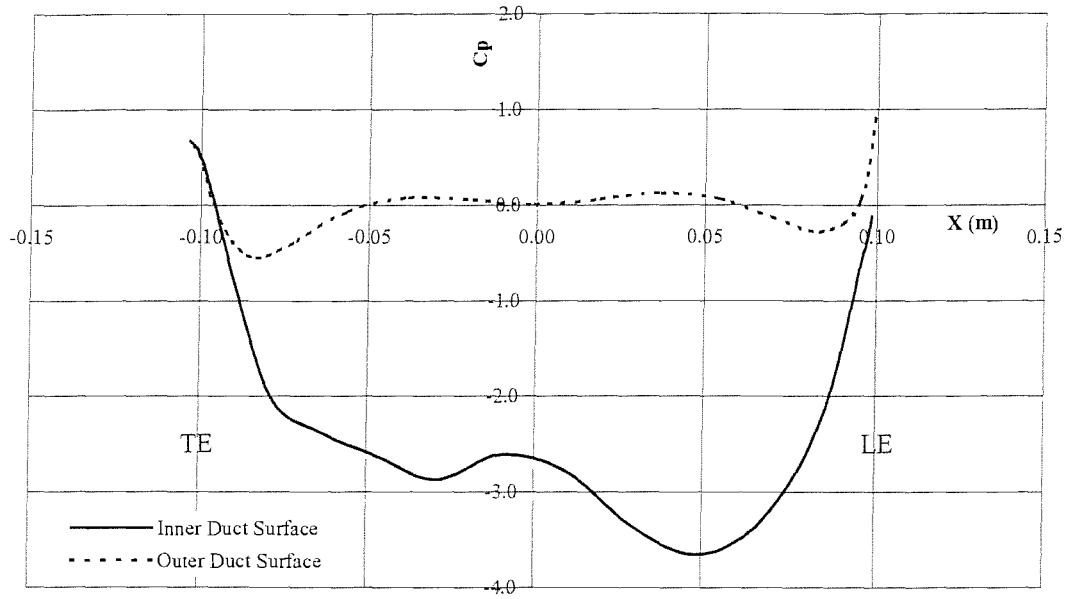

Figure A5.20 - Cp distribution along symmetrical duct s2037 with symmetrical propeller.

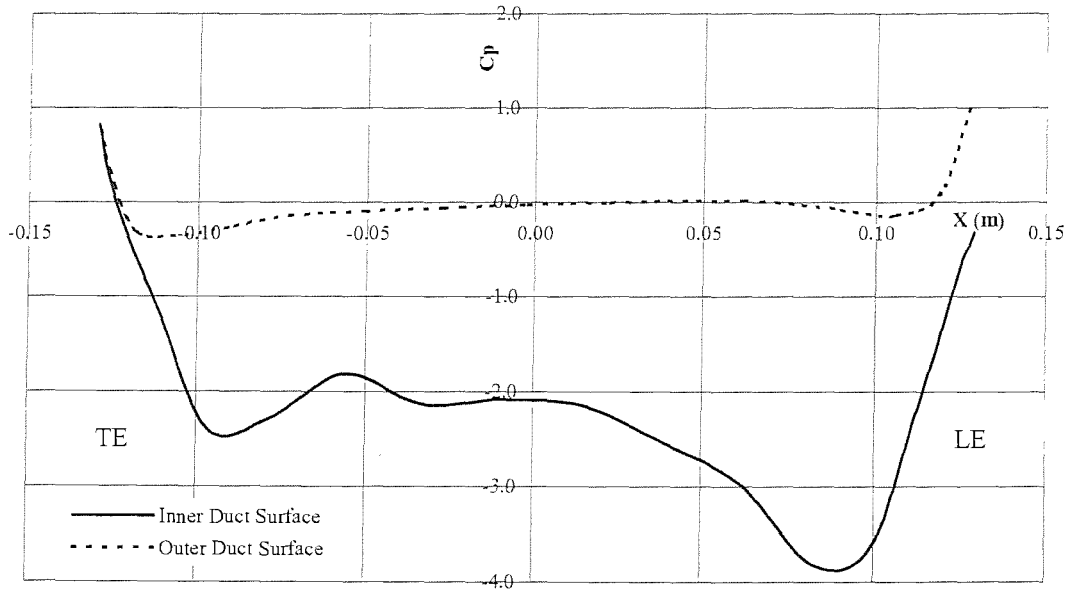

Figure A5.21 - Cp distribution along symmetrical duct s2637 with symmetrical propeller.

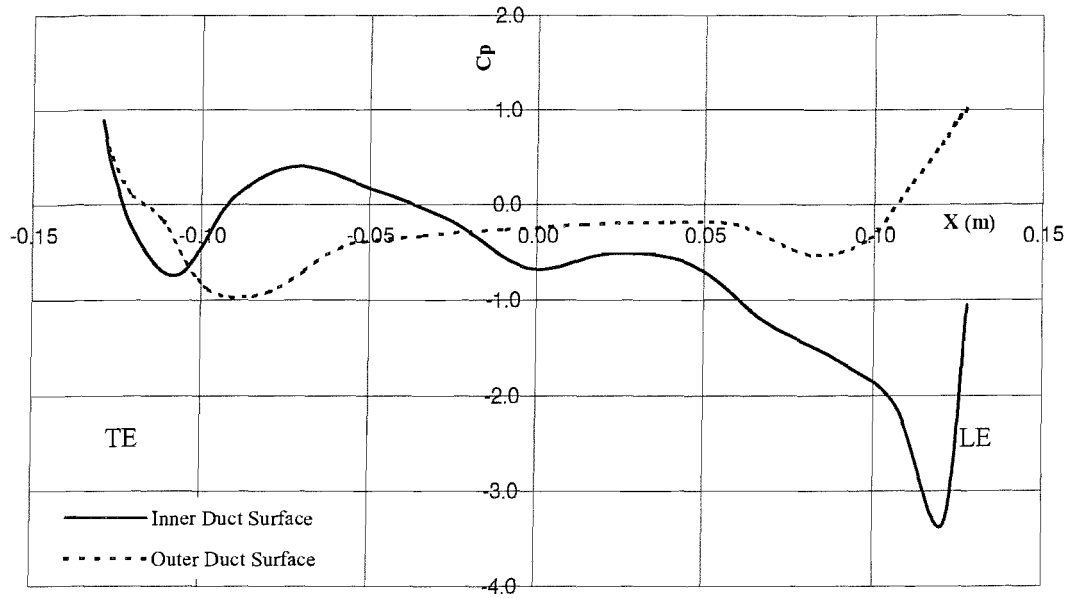

Figure A5.22 - Cp distribution along symmetrical duct f2637 with symmetrical propeller.

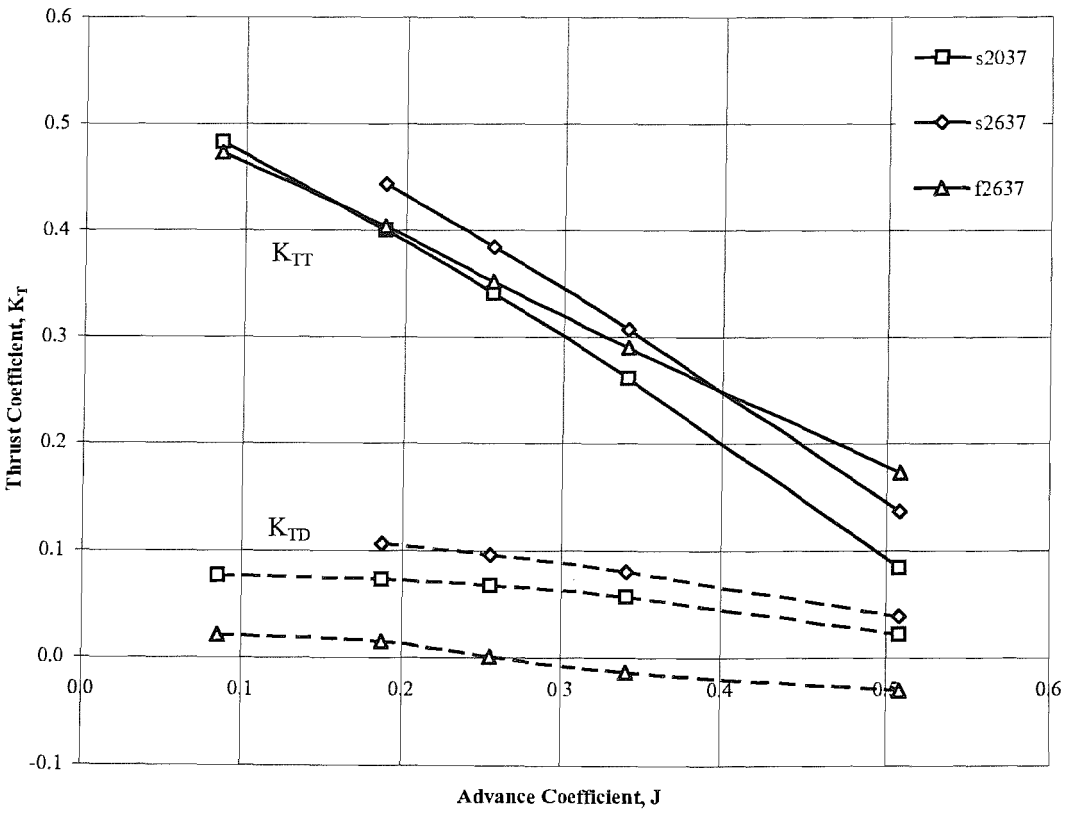

Figure A5.23 - K_T, J chart for symmetrical propeller, showing proportion of duct thrust.

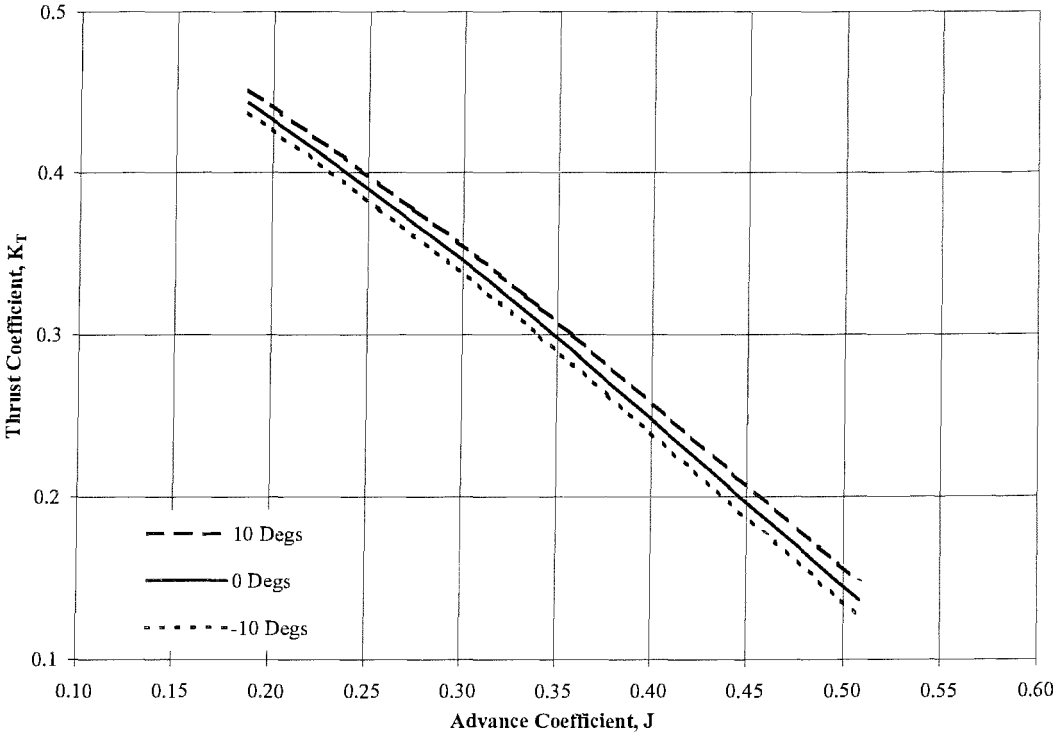

Figure A5.24 - K_T, J chart for s2637 showing predicted effect of stator angle of attack.

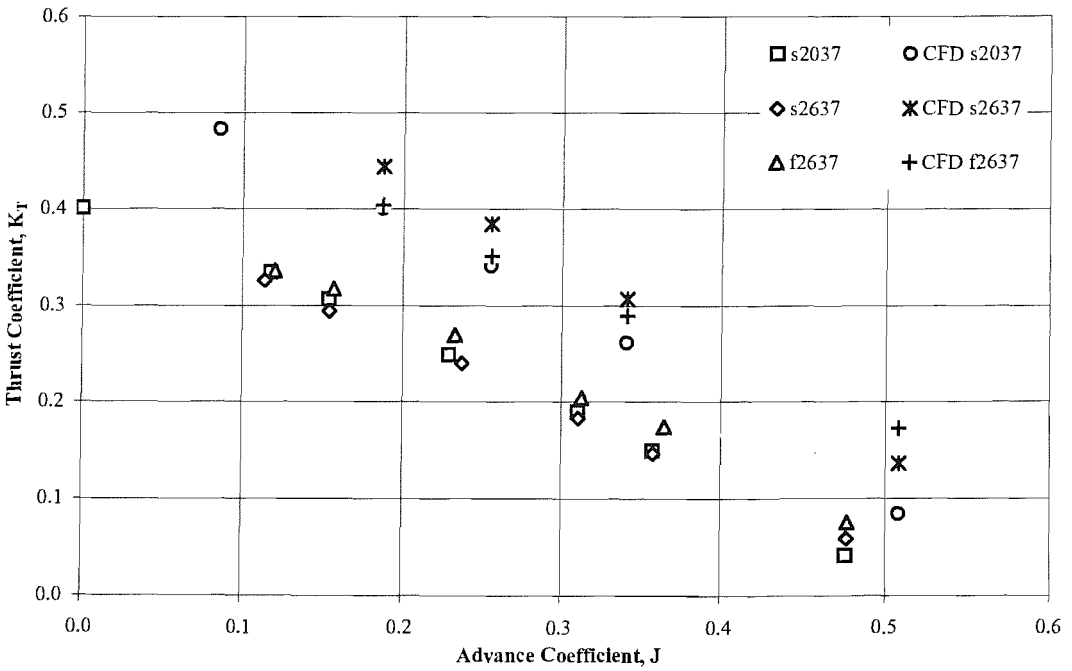

Figure A5.25 - Thrust predictions for TDP at speeds of advance.

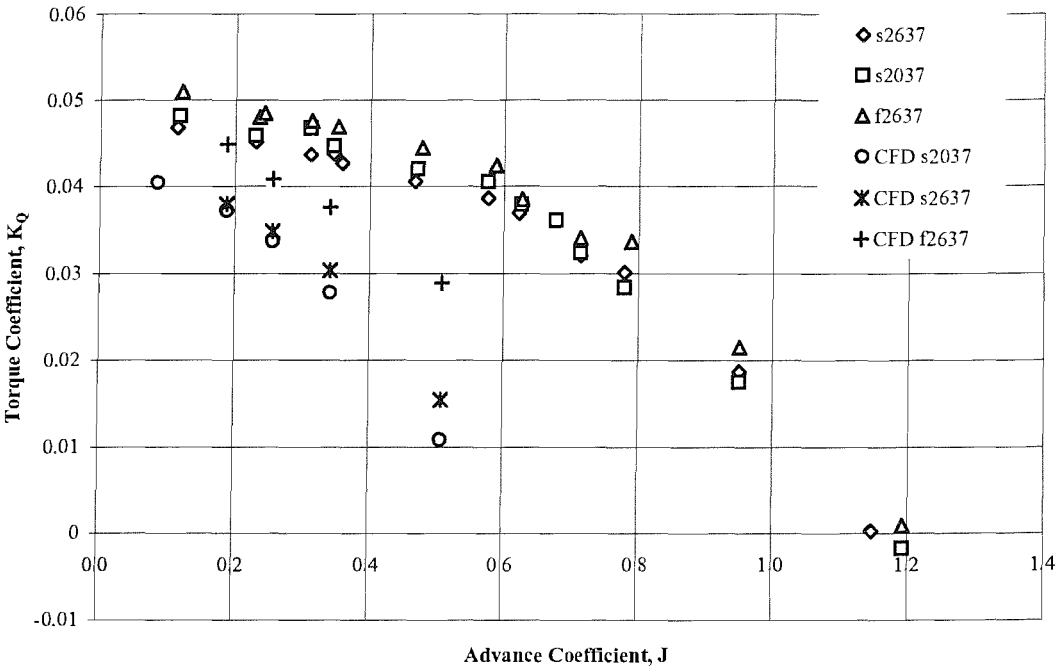

Figure A5.26 - Torque predictions for TDP at speeds of advance.

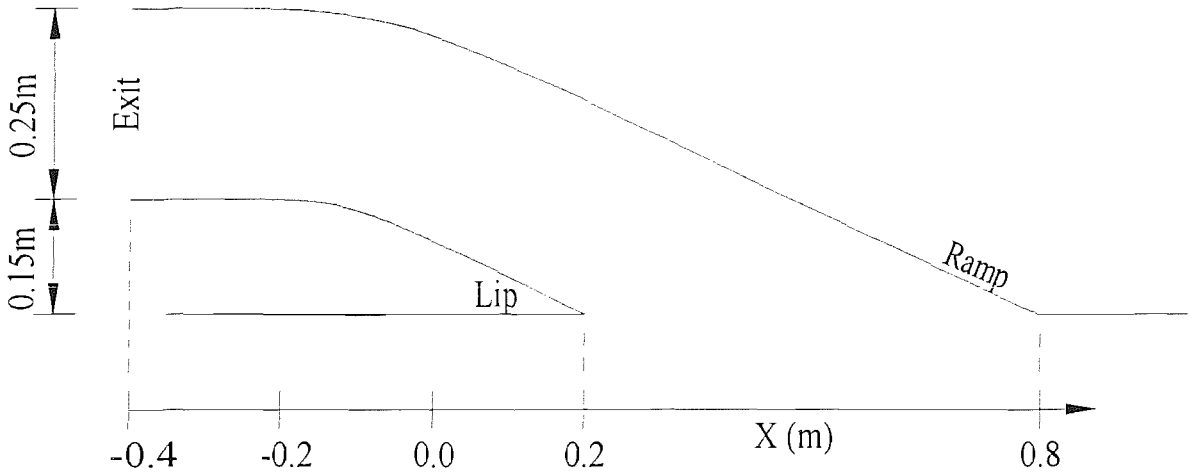

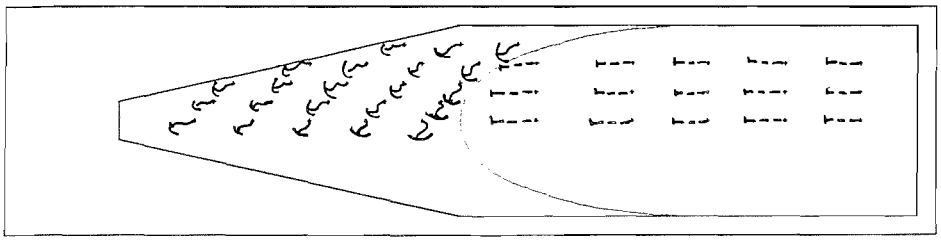

IVR = 1.41

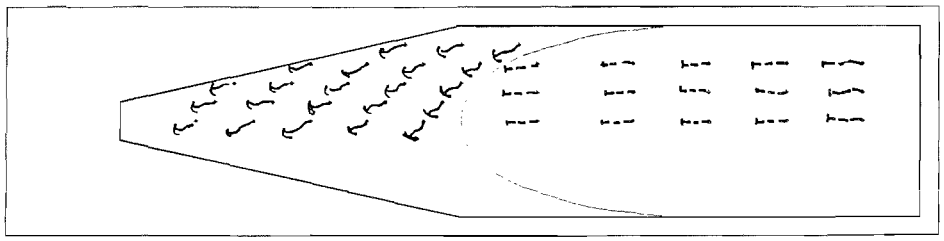

IVR = 1.17

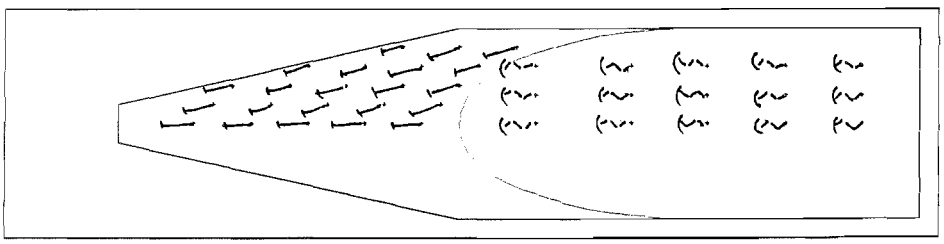

IVR = 0.88

= Upper wall of duct.

= Lower wall of duct.

Figure A6.1 - Representation of wool tuft patterns during different waterjet duct flow regimes.

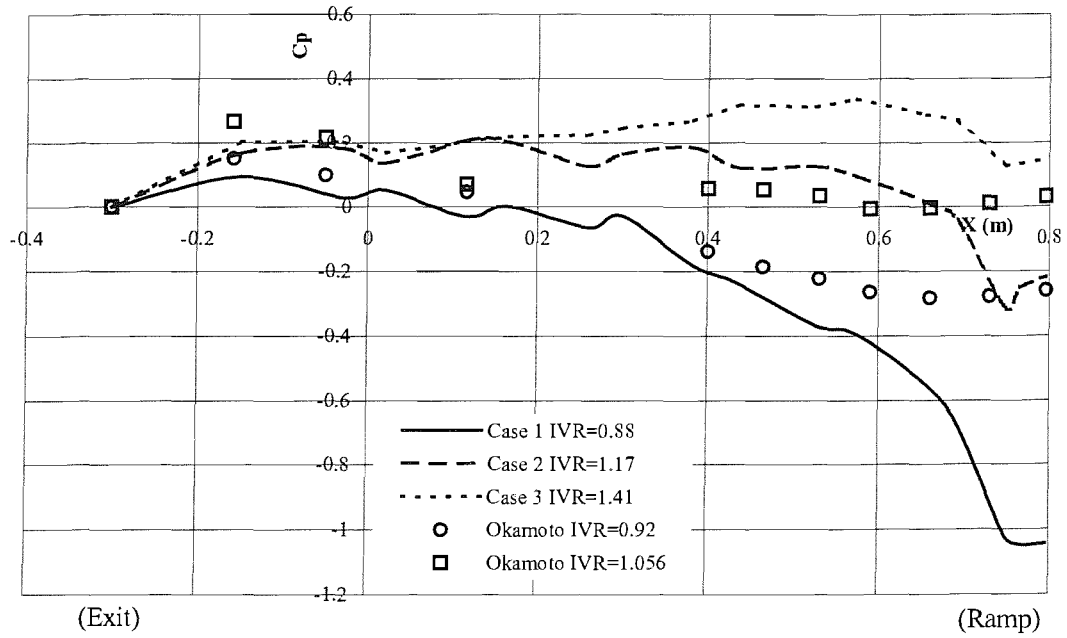

Figure A6.2 - Pressure coefficient distribution along the duct top centreline.

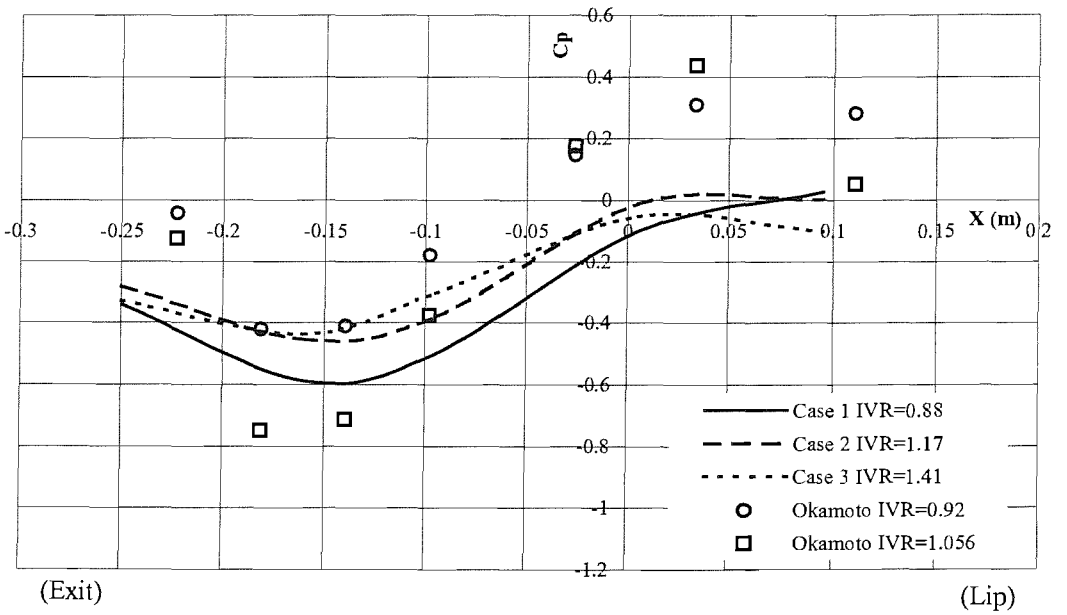

Figure A6.3 - Pressure coefficient distribution along the duct bottom centreline.

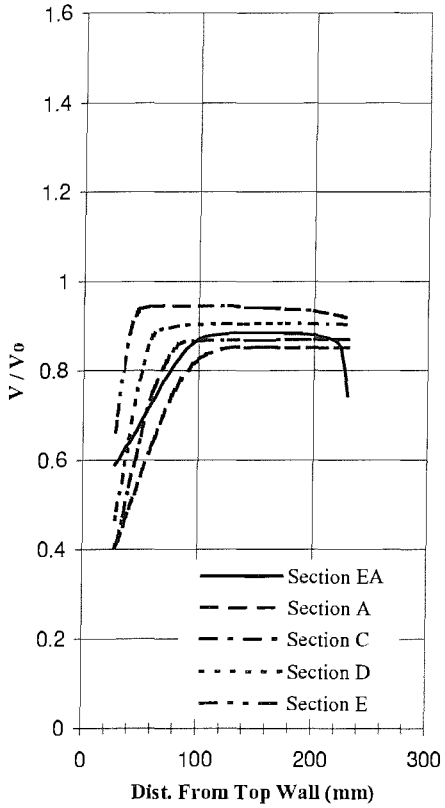

Figure A6.4 - Velocity profiles for Case 1, IVR=0.88.

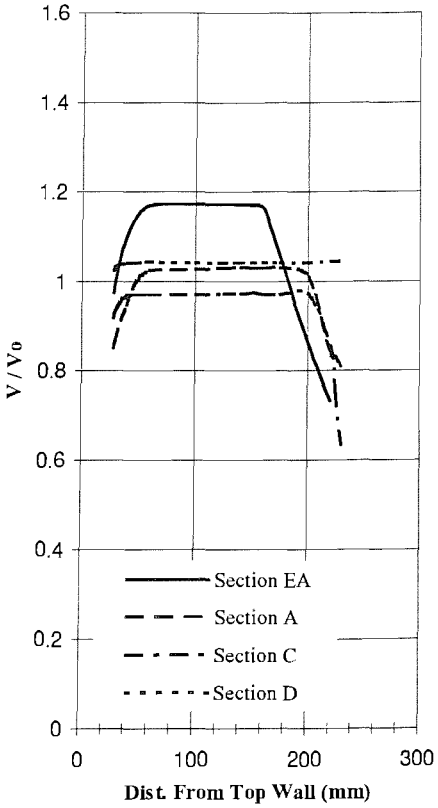

Figure A6.5 - Velocity profiles for Case 2, IVR=1.17.

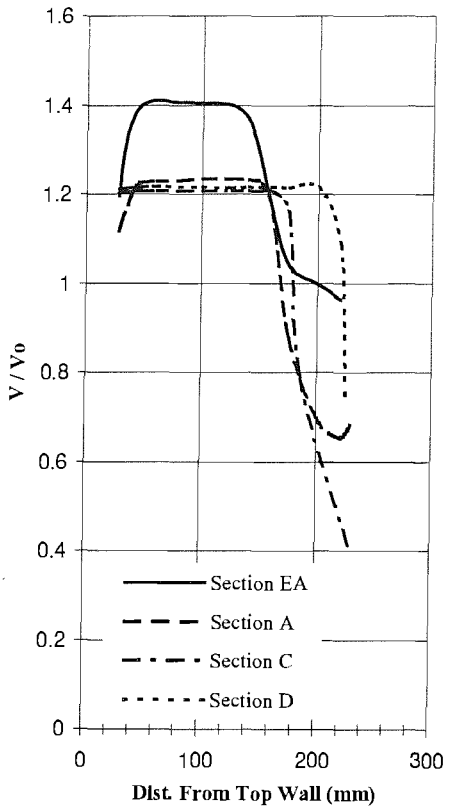

Figure A6.6 - Velocity profiles for Case 3, IVR=1.41.

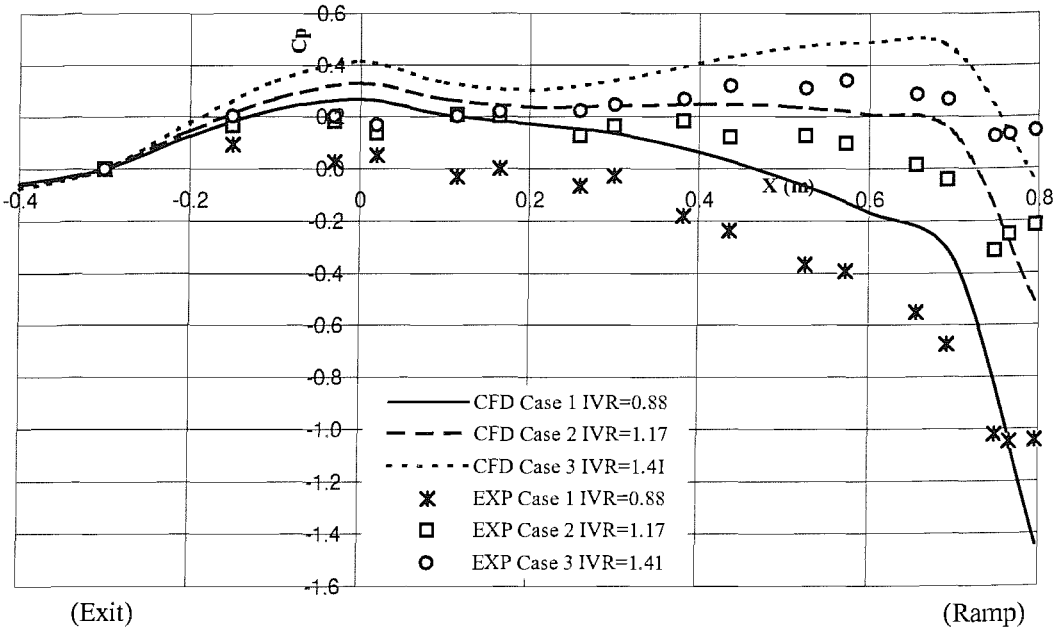

Figure A7.1 - Cp distribution along top centreline vs experimental results.

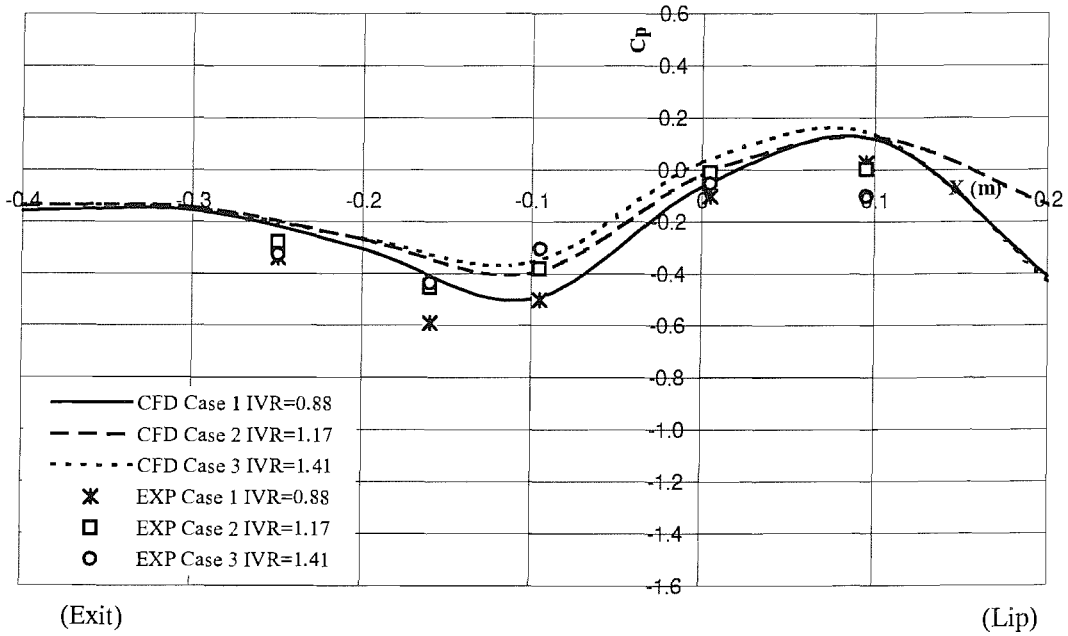

Figure A7.2 - Cp distribution along bottom centreline vs experimental results.

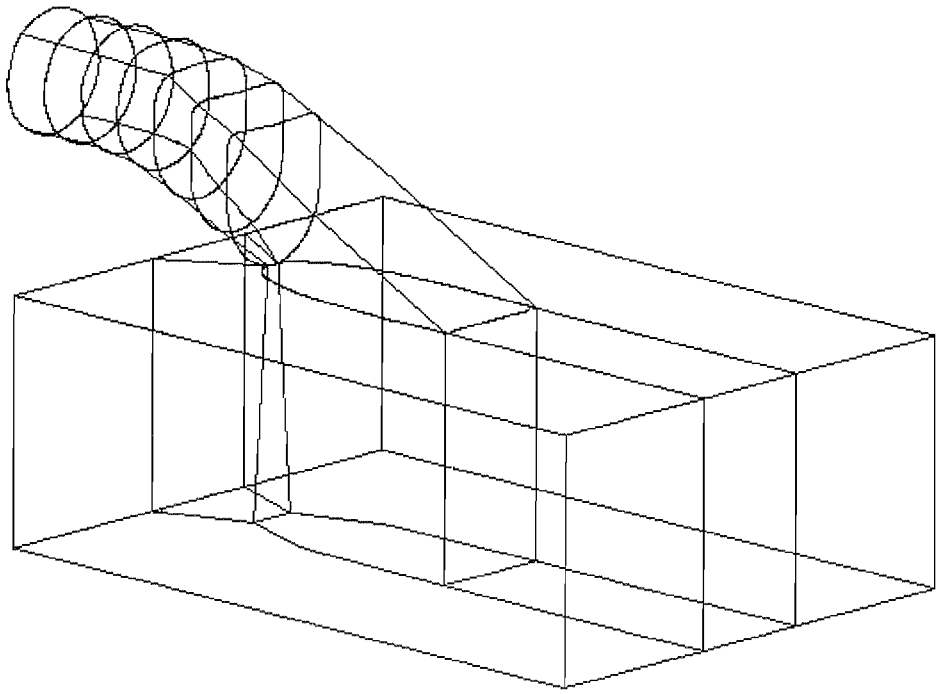

Figure A7.3 - Waterjet duct and flat plate model for trim and drift conditions.

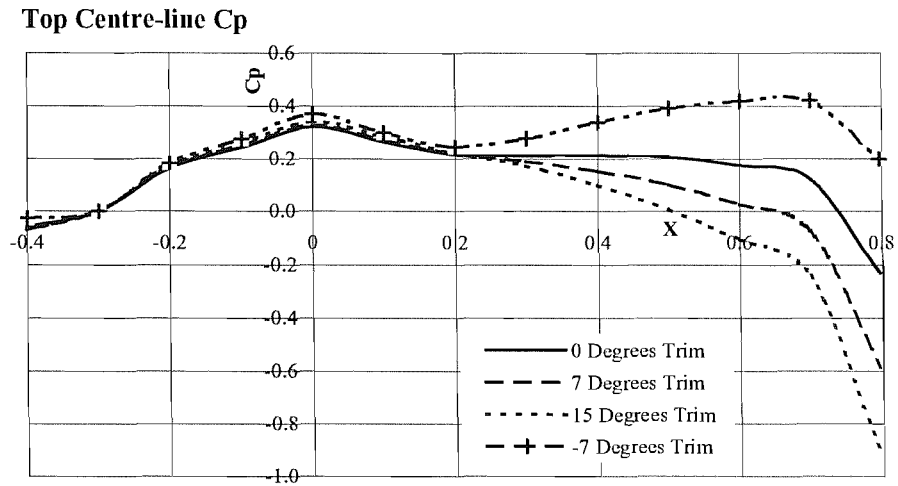

Figure A7.4 - Influence of trim on top centreline Cp distribution (IVR=1.17).

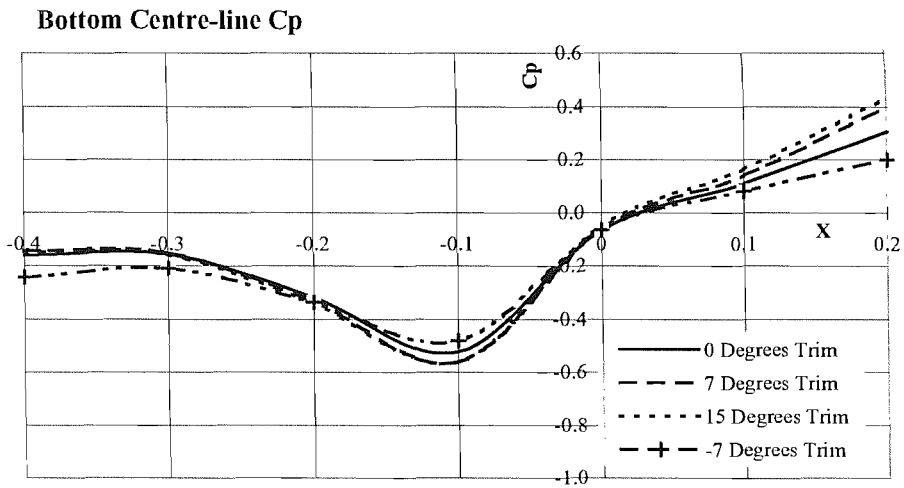

Figure A7.5 - Influence of trim on bottom centreline Cp distribution (IVR=1.17).

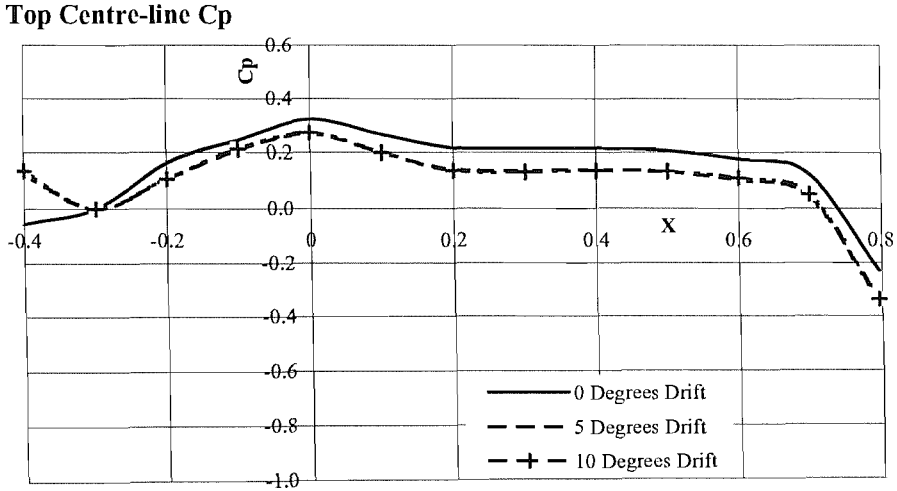

Figure A7.6 - Influence of drift on top centreline Cp distribution (IVR=1.17).

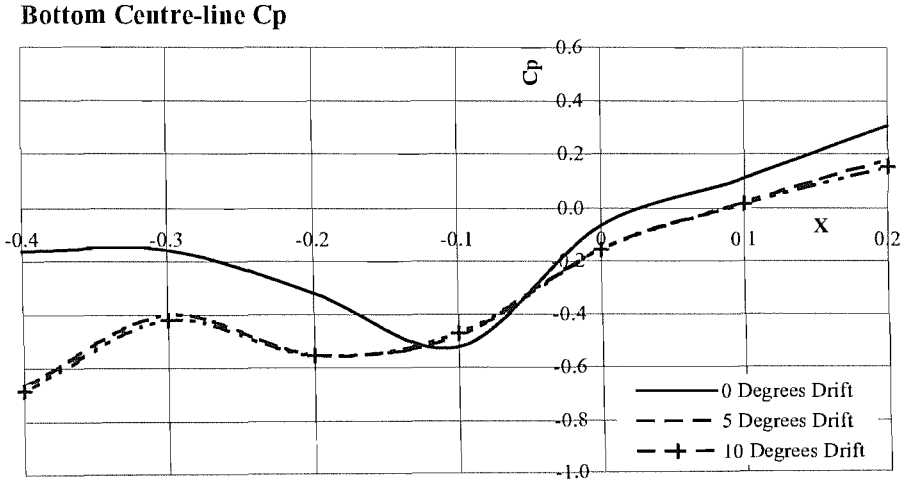

Figure A7.7 - Influence of drift on bottom centreline Cp distribution (IVR=1.17).

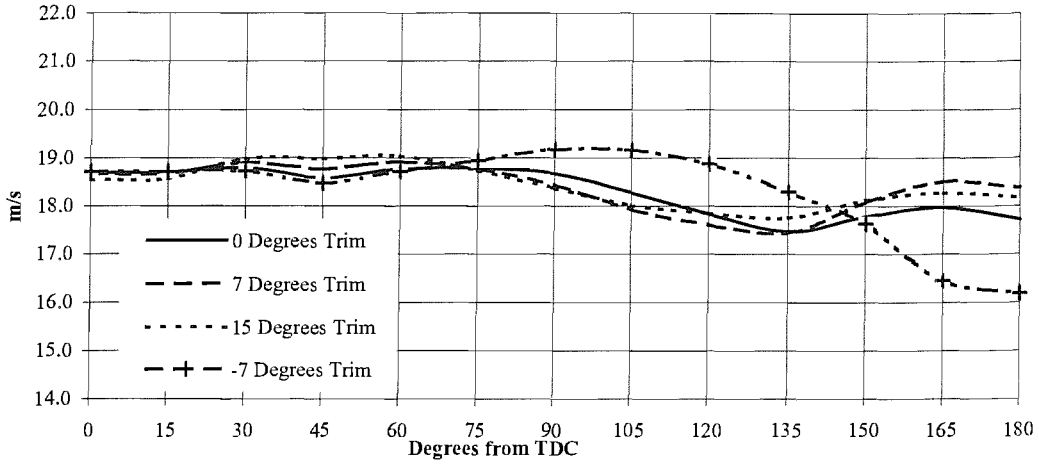

Figure A7.8 - Influence of trim on axial velocity at 0.7R at exit plane (IVR=1.17).

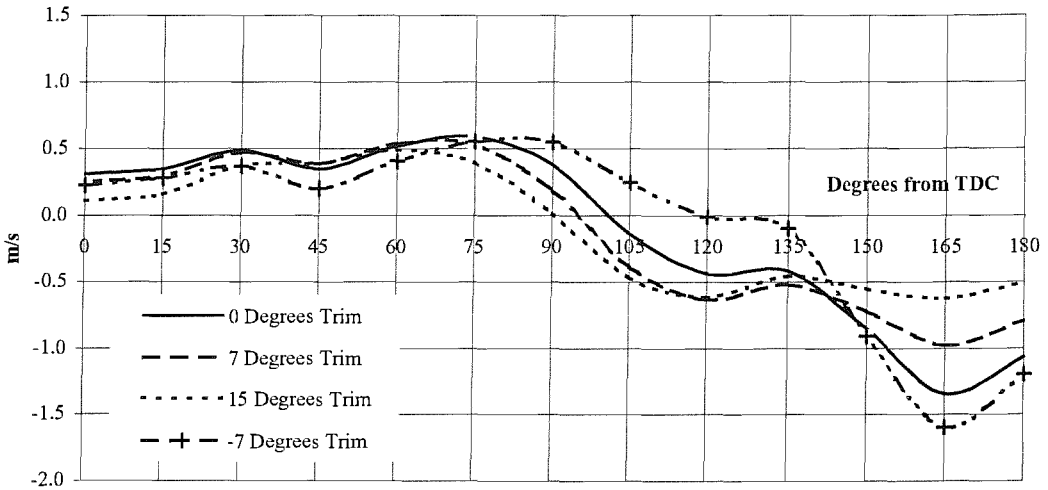

Figure A7.9 - Influence of trim on radial velocity at 0.7R at exit plane (IVR=1.17).

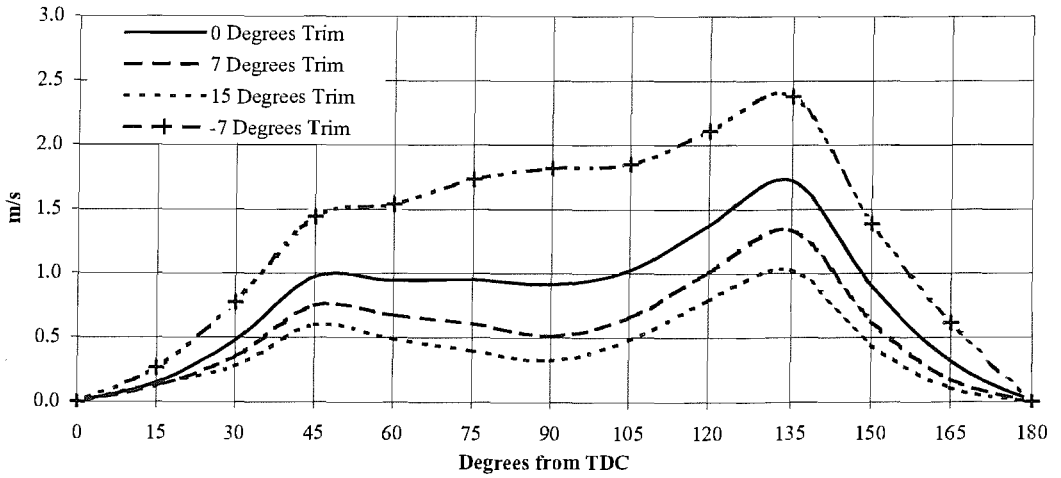

Figure A7.10 - Influence of trim on angular velocity at 0.7R at exit plane (IVR=1.17).

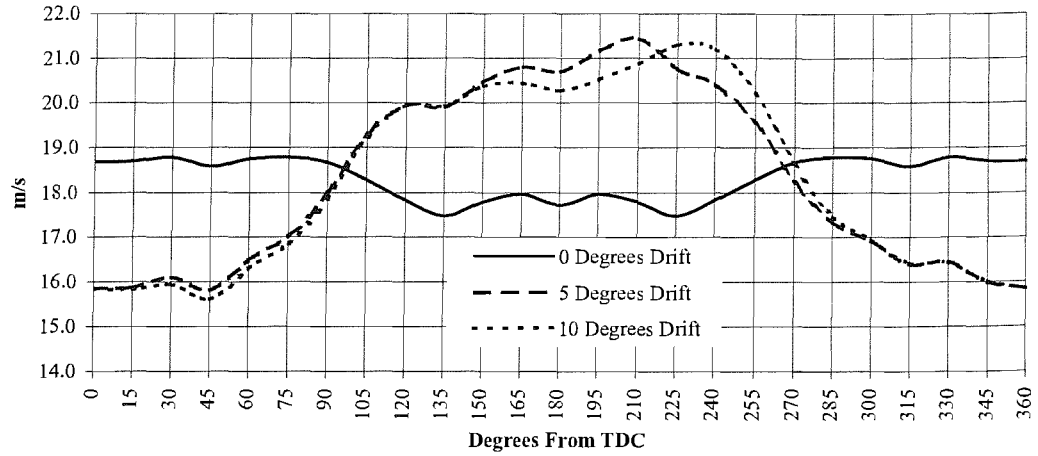

Figure A7.11 - Influence of drift on axial velocity at 0.7R at exit plane (IVR=1.17).

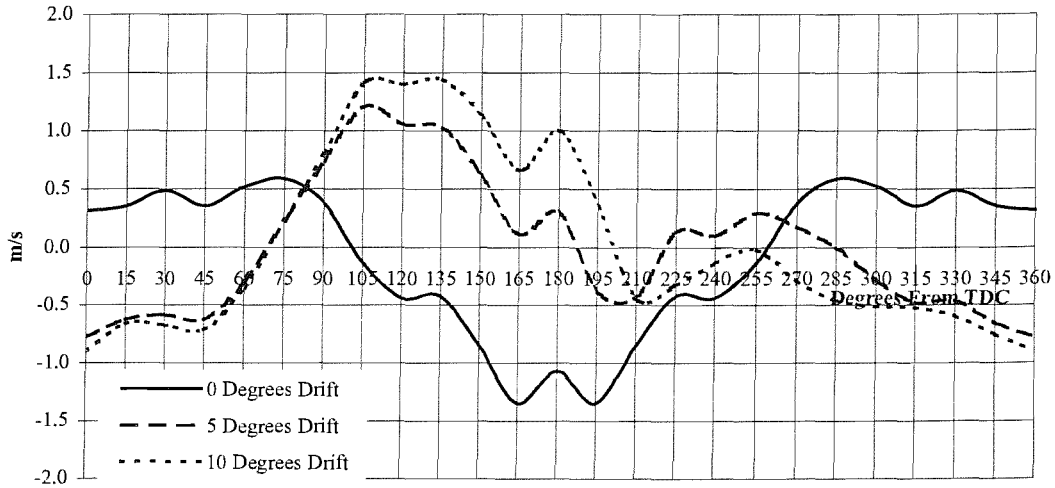

Figure A7.12 - Influence of drift on radial velocity at 0.7R at exit plane (IVR=1.17).

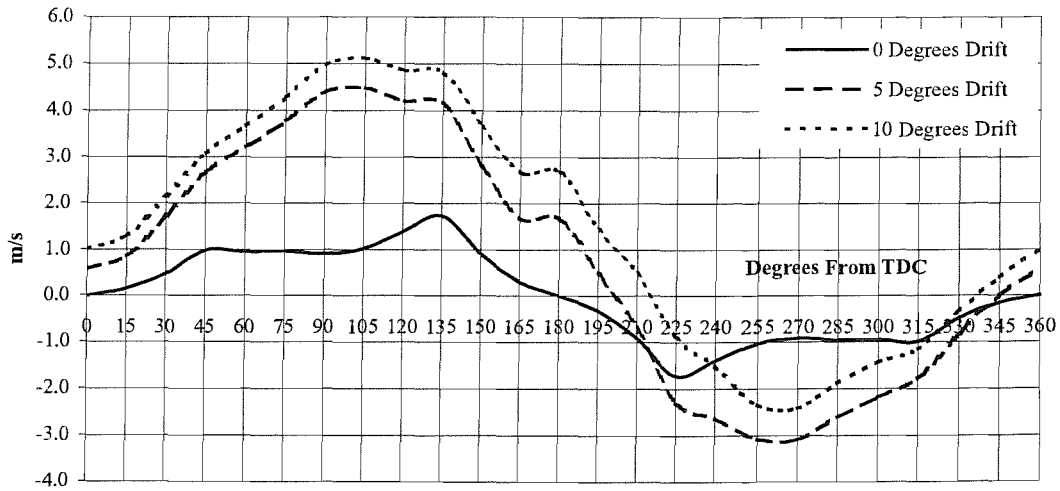

Figure A7.13 - Influence of drift on angular velocity at 0.7R at exit plane (IVR=1.17).

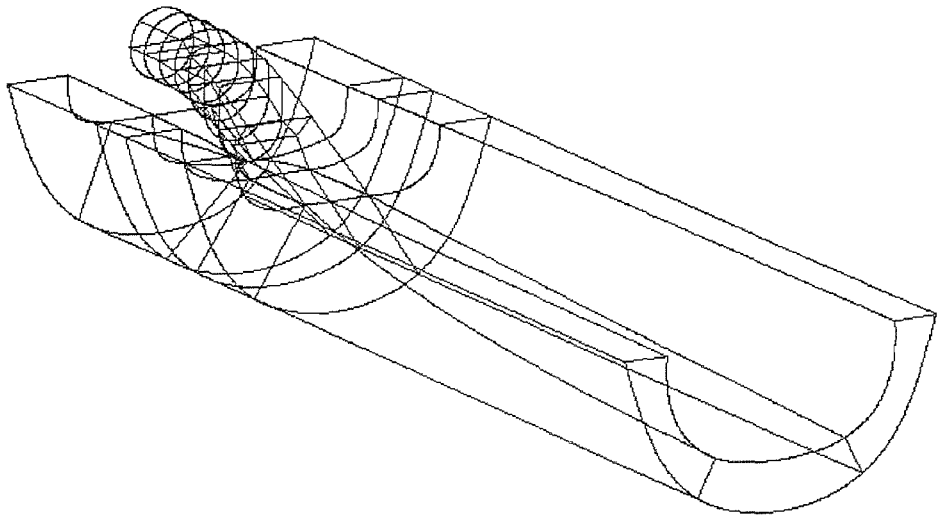

Figure A7.14 - Block structure of waterjet duct in aft half of series 64 hull.

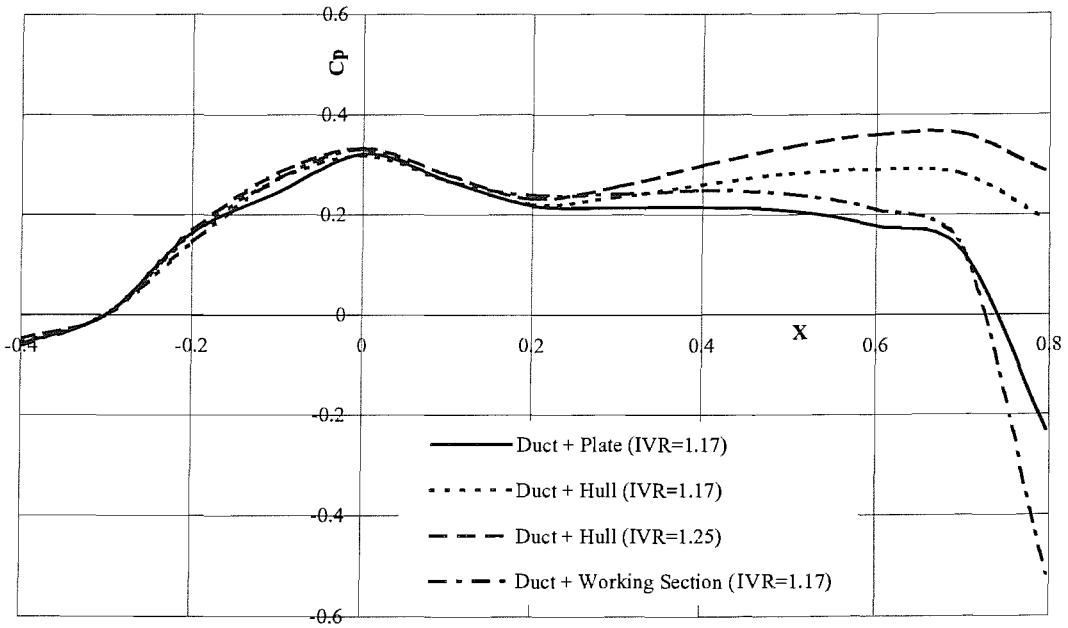

Figure A7.15 - Hull influence on top centreline Cp distribution.

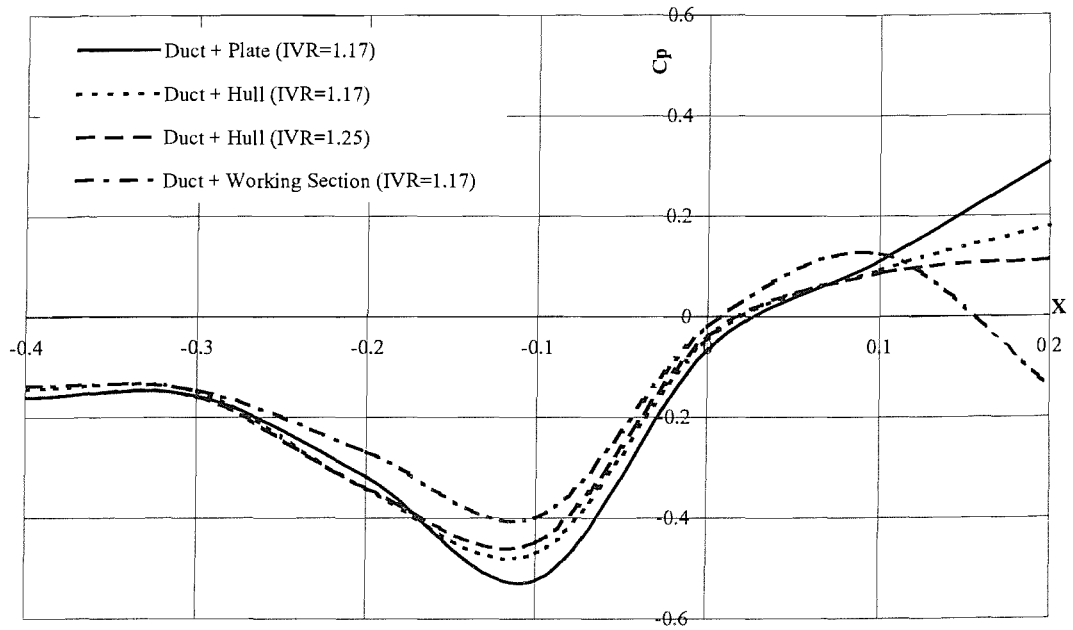

Figure A7.16 - Hull influence on bottom centreline Cp distribution.

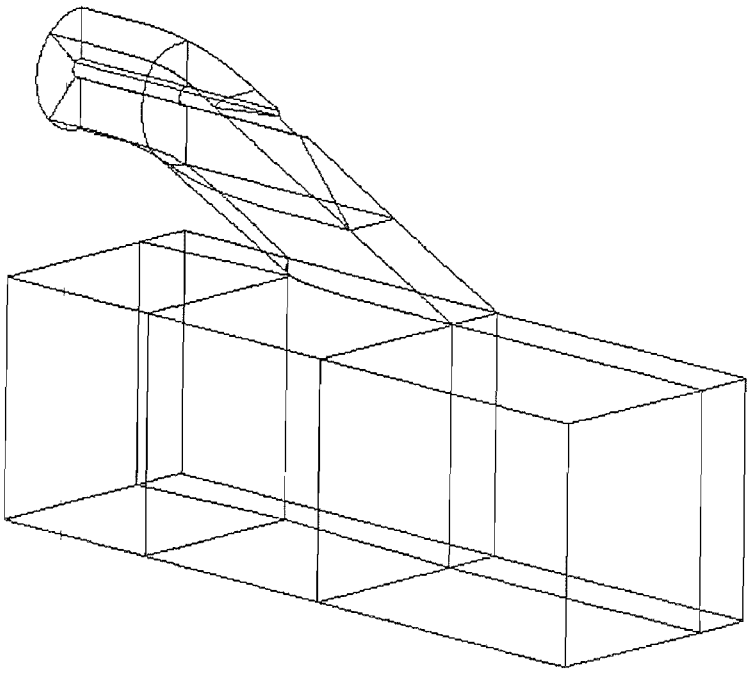

Figure A8.1 - New CFX duct geometry including drive shaft.

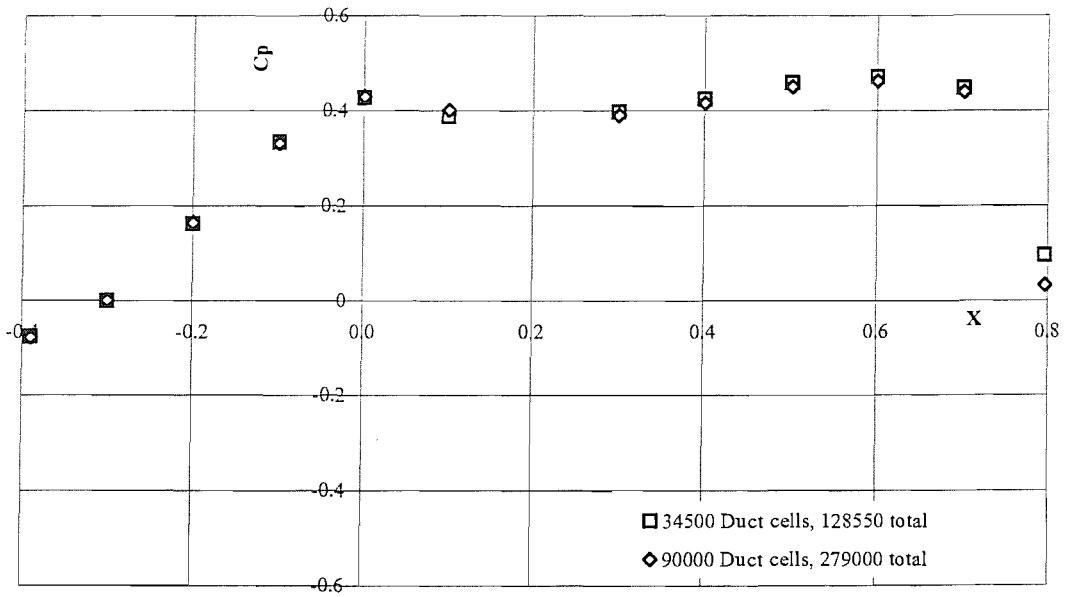

Figure A8.2 - CFX shaft geometry grid dependency, Top centreline Cp distribution.

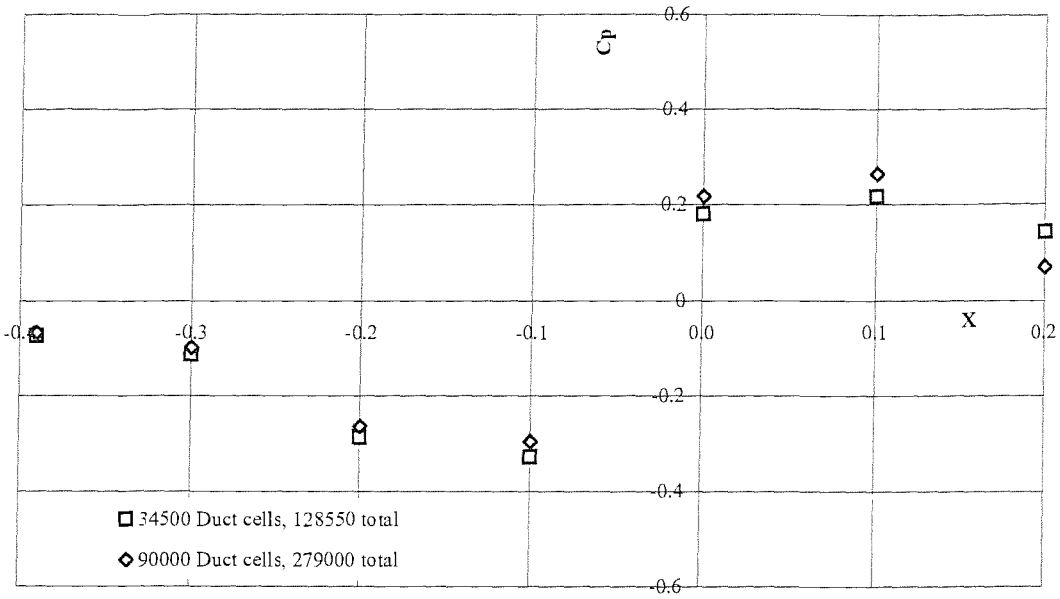

Figure A8.3 - CFX shaft geometry grid dependency, Bottom centreline Cp distribution.

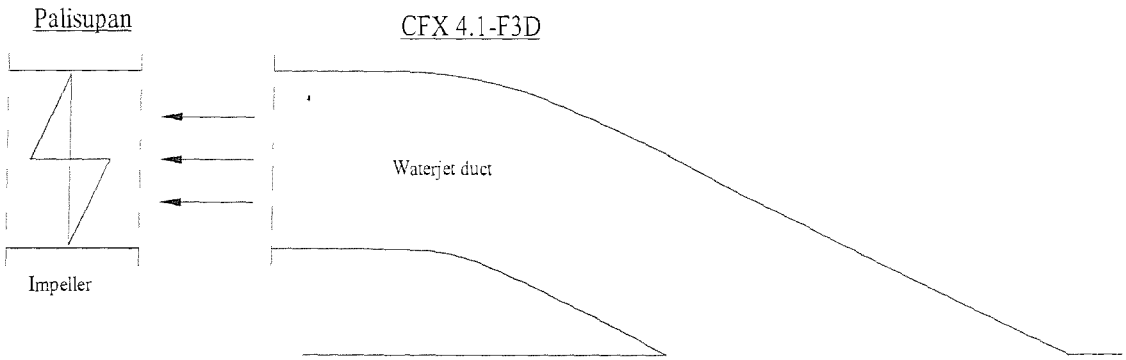

Figure A8.5 - Coupling of CFX4.1 model and Palisupan model.

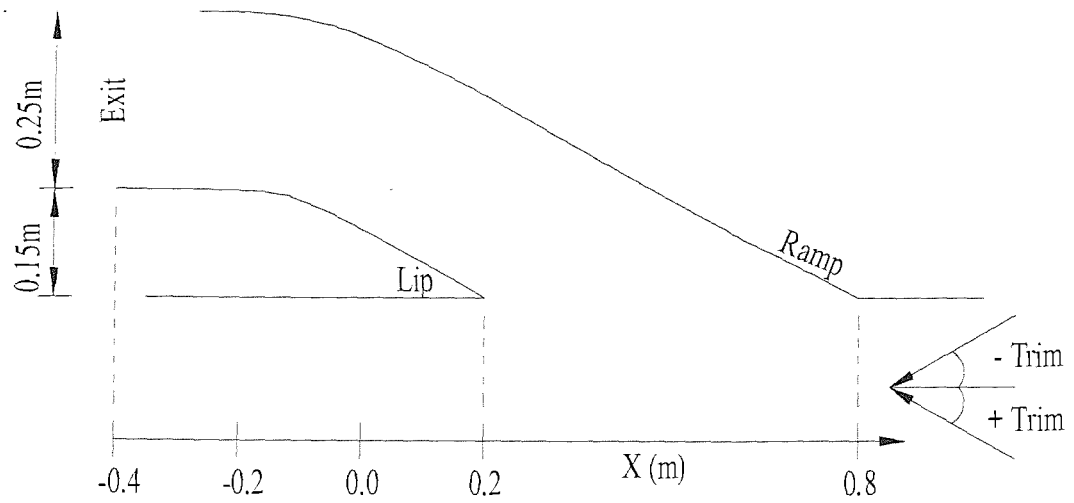

Figure A8.6 - Trim orientation.

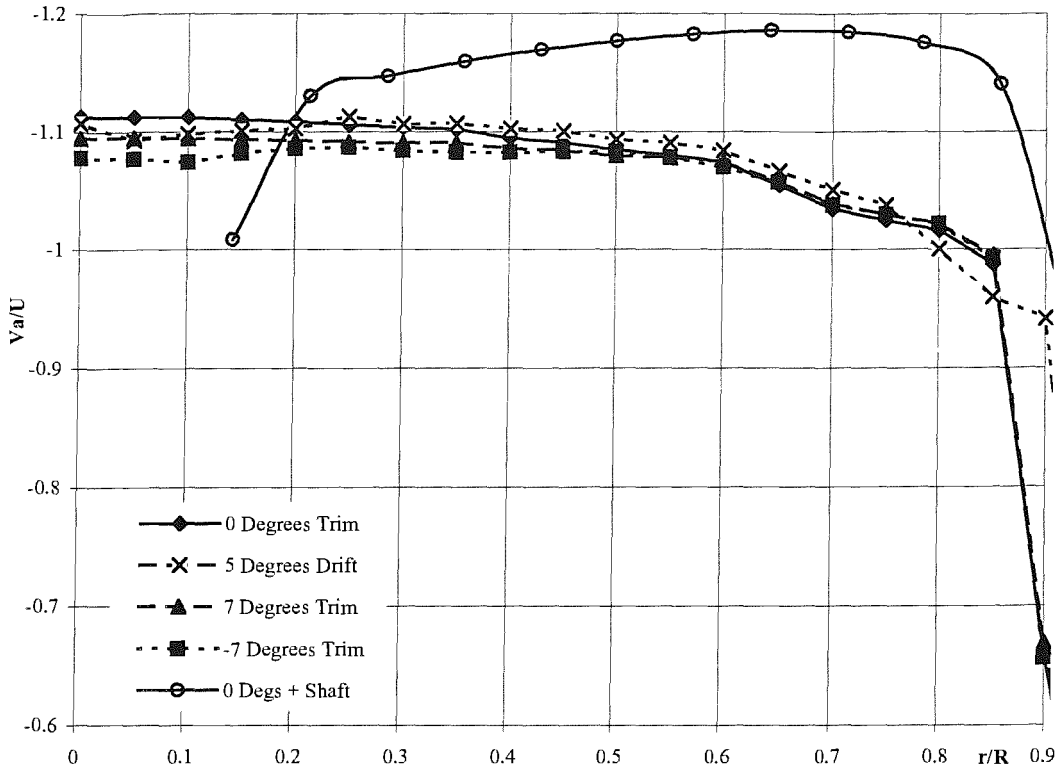

Figure A8.7 - Axial velocity variation across impeller plane.

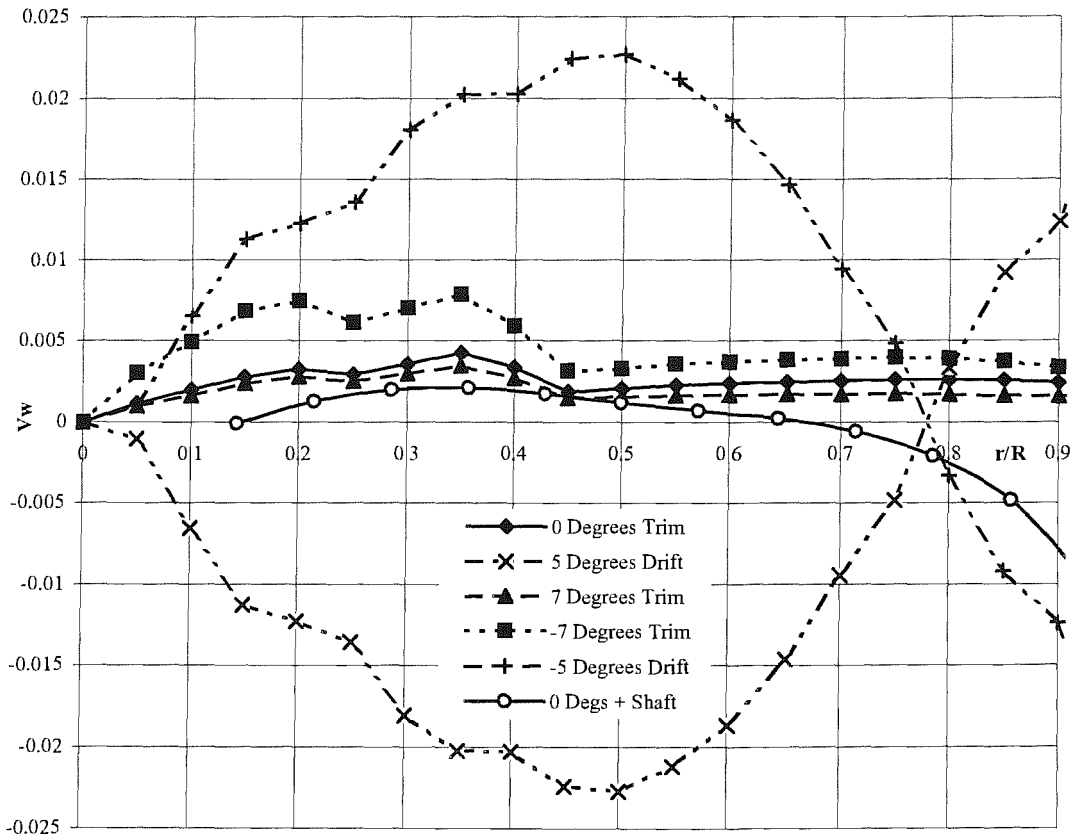

Figure A8.8 - Angular velocity variation across impeller plane.

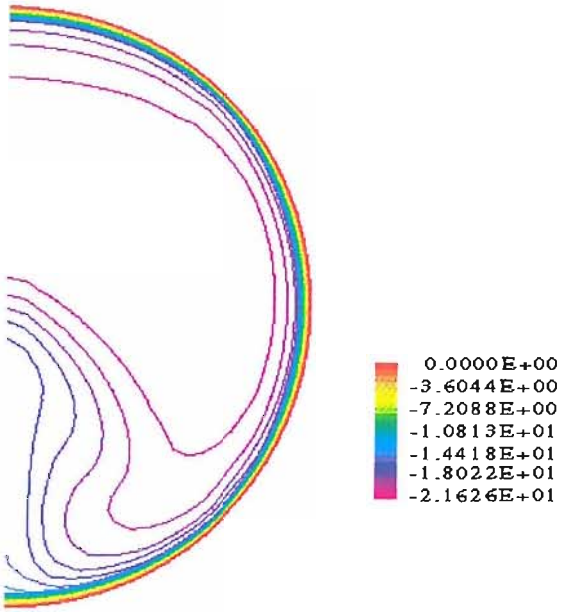

Figure A8.9 - Axial velocities at waterjet duct exit plane, zero trim, IVR=1.17.

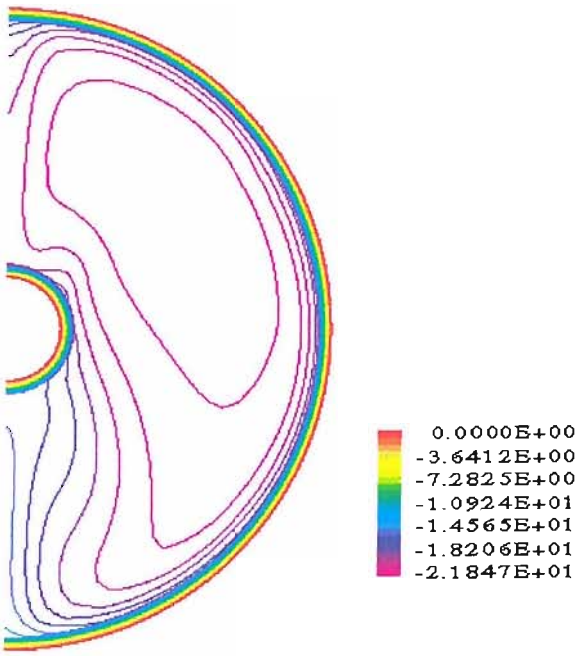

Figure A8.10 - Axial velocities at waterjet duct exit plane, zero trim + shaft, IVR=1.17.

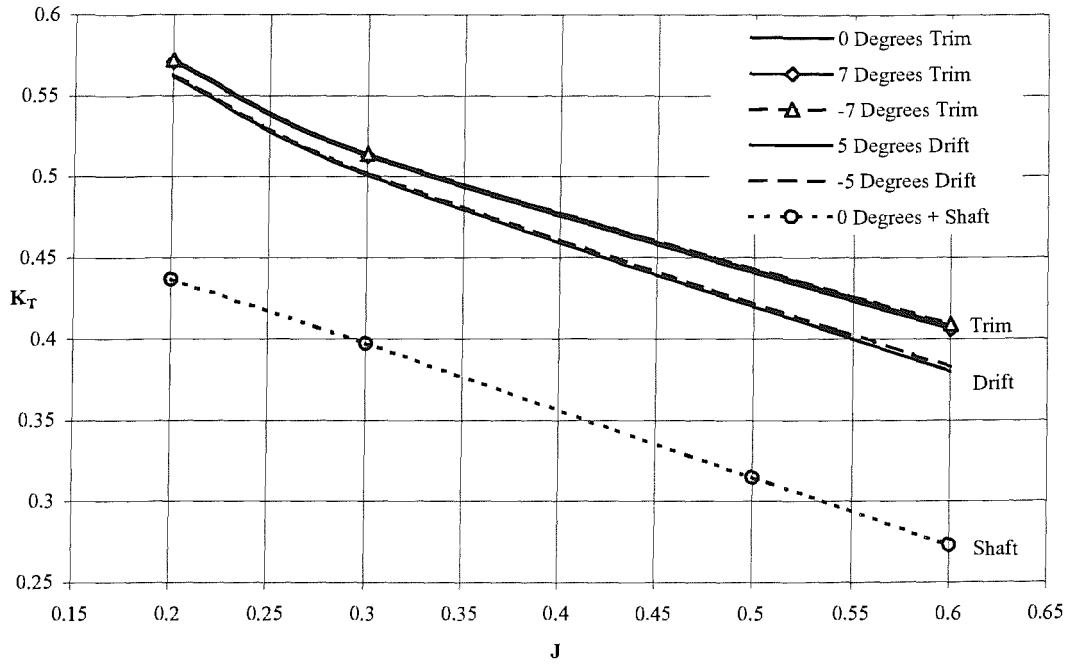

Figure A8.11 - Panel code impeller thrust results - using radially averaged inflow velocity field.

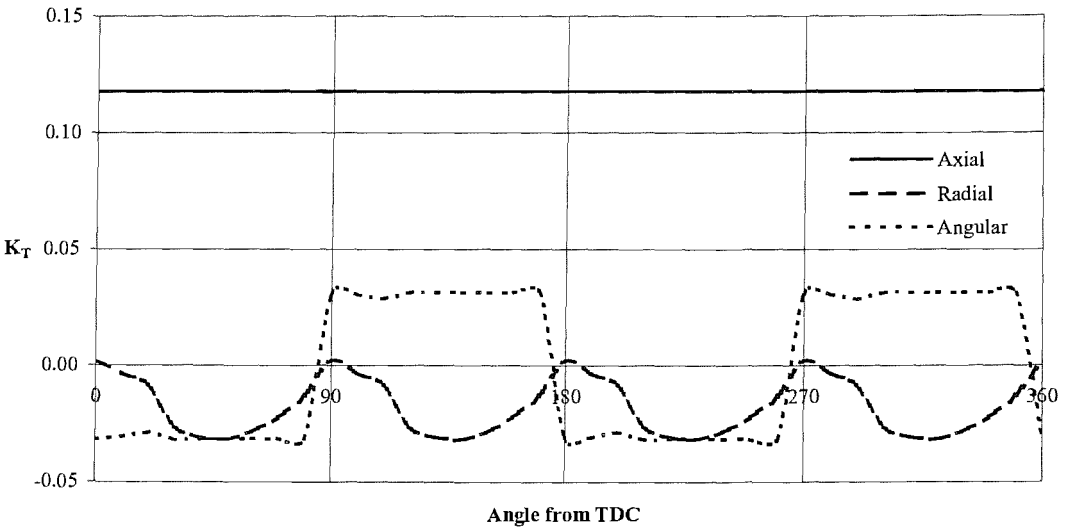

Figure A8.12 - Blade loadings in uniform velocity field.

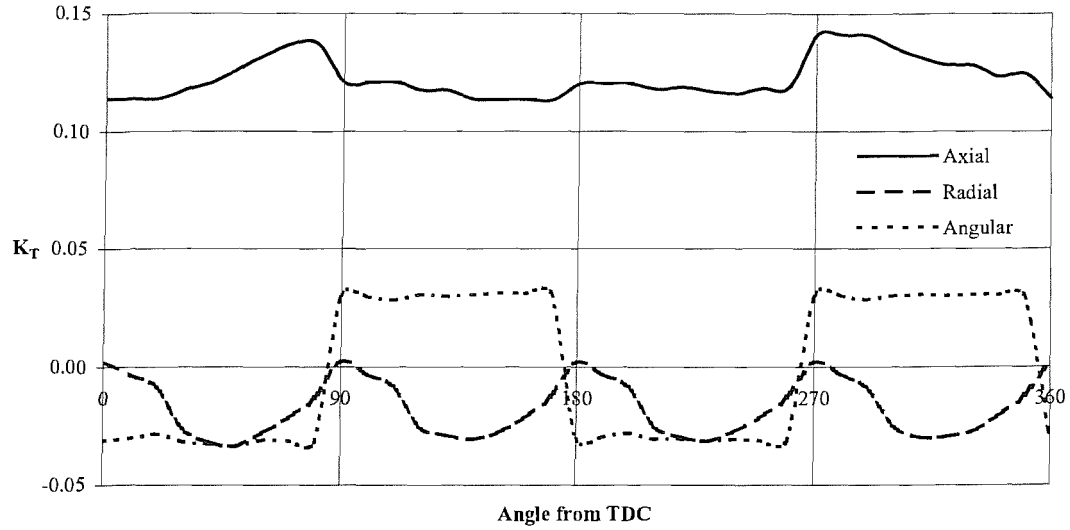

Figure A8.13 - Blade loadings - duct at 0 degrees trim.

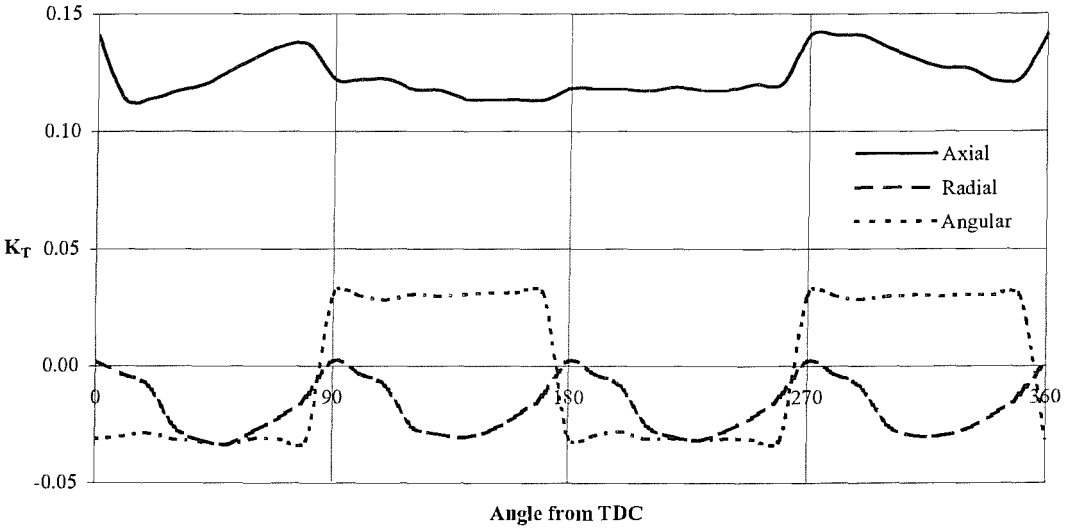

Figure A8.14 - Blade loadings - duct at 7 degrees trim.

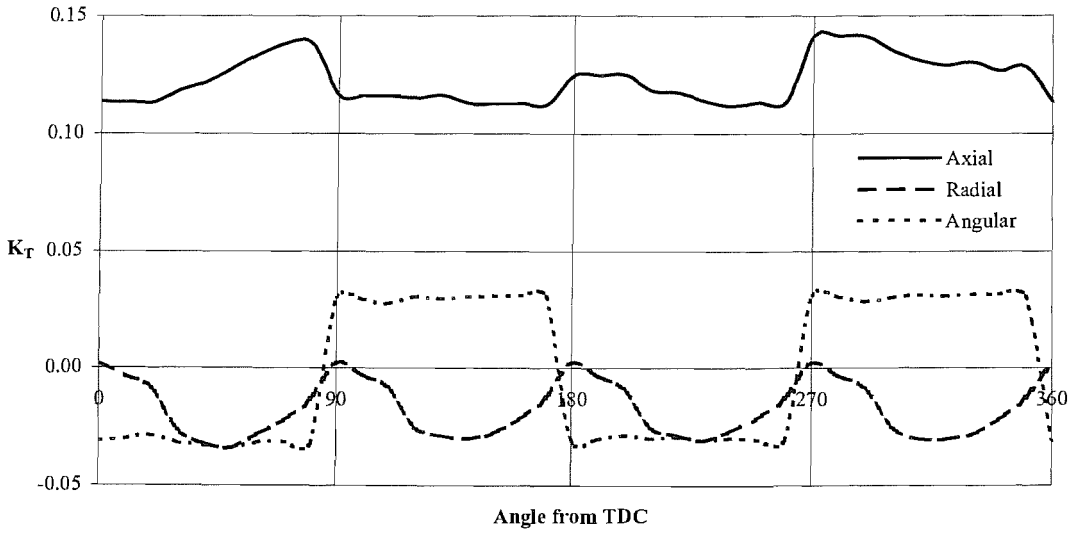

Figure A8.15 - Blade loadings - duct at -7 degrees trim.

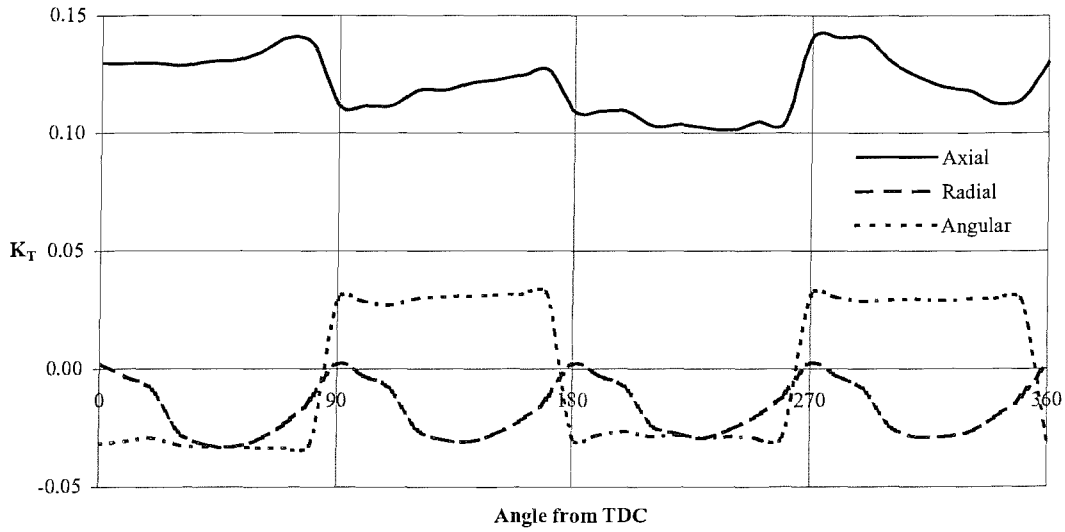

Figure A8.16 - Blade loadings - duct at 5 degrees drift.

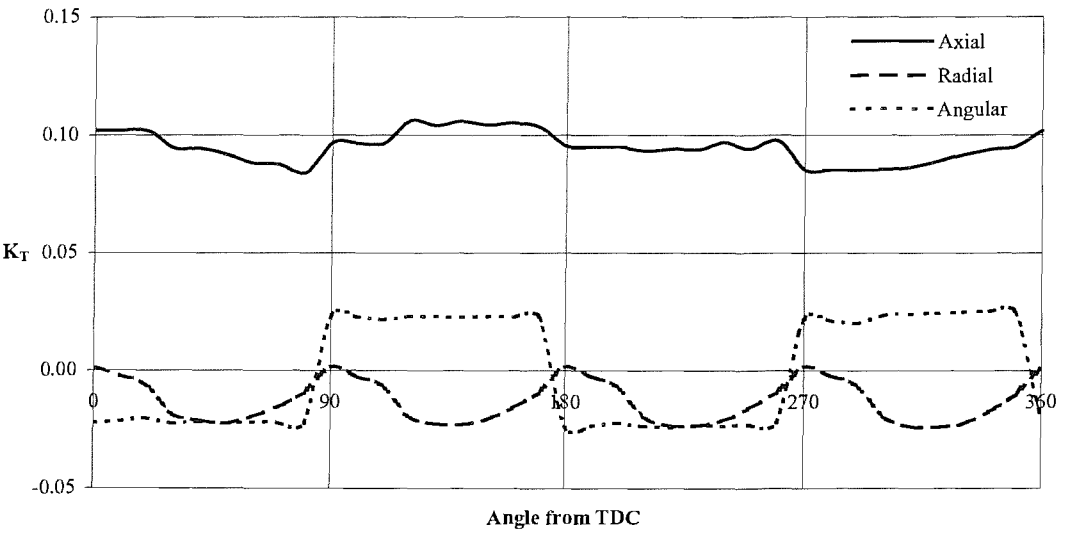

Figure A8.17 - Blade loadings - duct at 0 degrees trim with drive shaft.

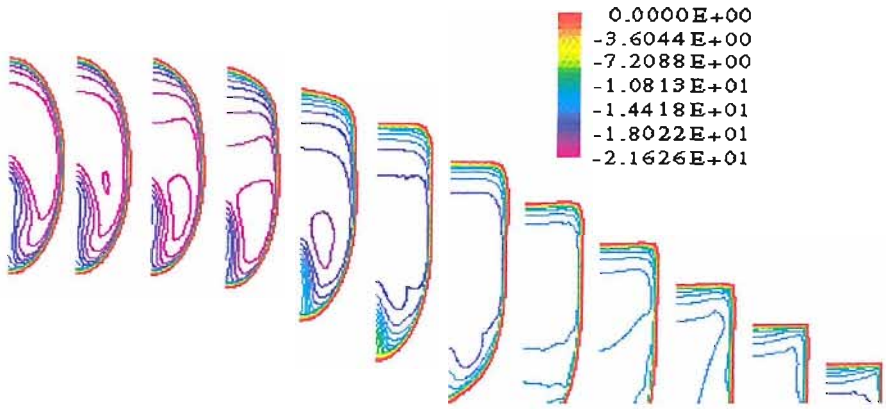

Figure A8.18 - Axial velocities through waterjet duct, zero trim, IVR=1.17.

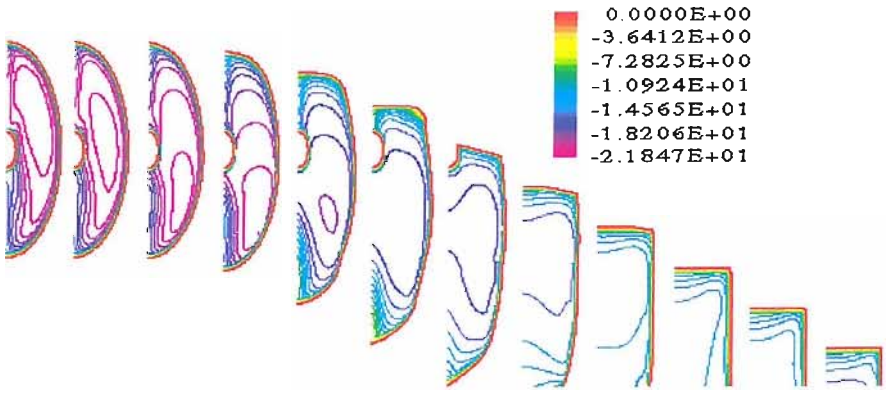

Figure A8.19 - Axial velocities through waterjet duct, zero trim + shaft, IVR=1.17.

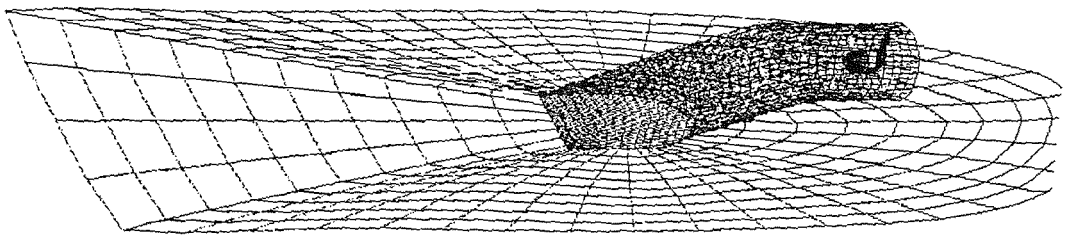

Figure A8.20 - Panel model of the waterjet inlet duct.

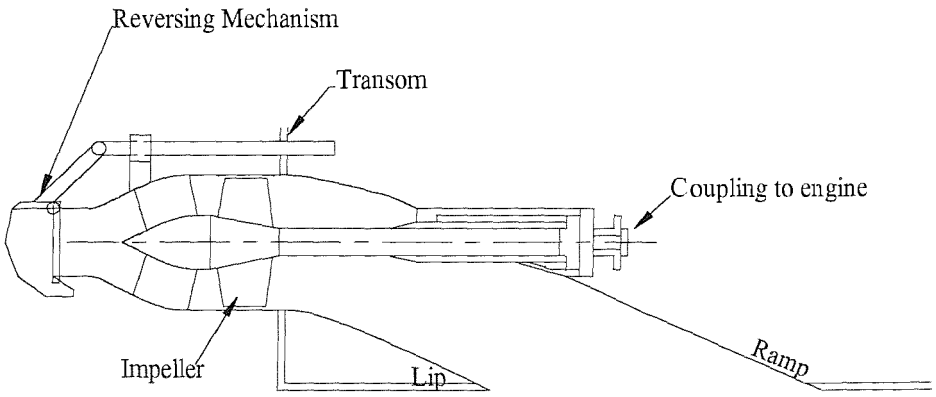

Figure A9.1 – Schematic axial flow waterjet pump installation.

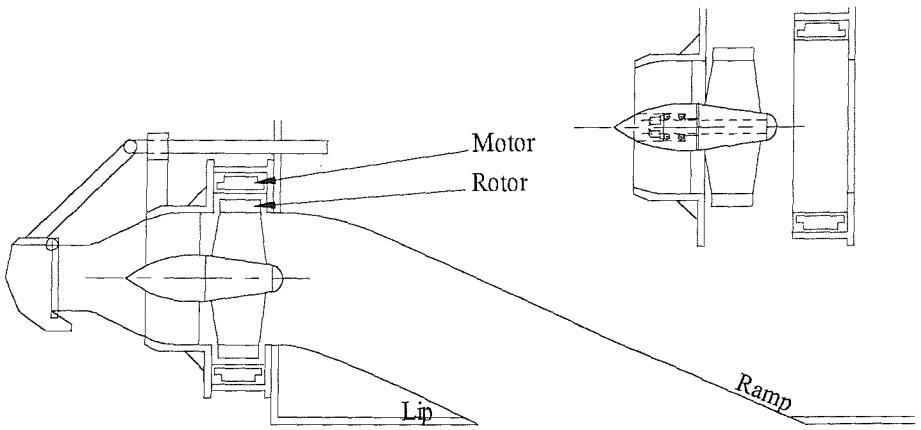

Figure A9.2 – Schematic ETDI waterjet installation.

APPENDIX B: MOMENTUM THEORY APPLIED TO A PROPELLER [B1,B2]

ASSUMPTIONS

1. The propeller is considered as an actuator disc with an infinite number of blades.
2. The propeller imparts a uniform acceleration to the fluid passing through the propeller disc. The thrust generated is uniformly distributed over the propeller disc.
3. The total energy in the flow is increased abruptly at the propeller disc. Pressure at the propeller disc is discontinuous.
4. The flow is frictionless.
5. There is unlimited inflow into the propeller.
6. The region of fluid that the propeller acts on forms a circular column. The centreline of this column is assumed to be horizontal.

In the simple momentum theory the fluid motion is considered relative to the propeller disc, and the speed of advance of the propeller V_A is represented by an axial velocity far ahead of the propeller. Consider the following diagram representing the fluid flow past the propeller disc;

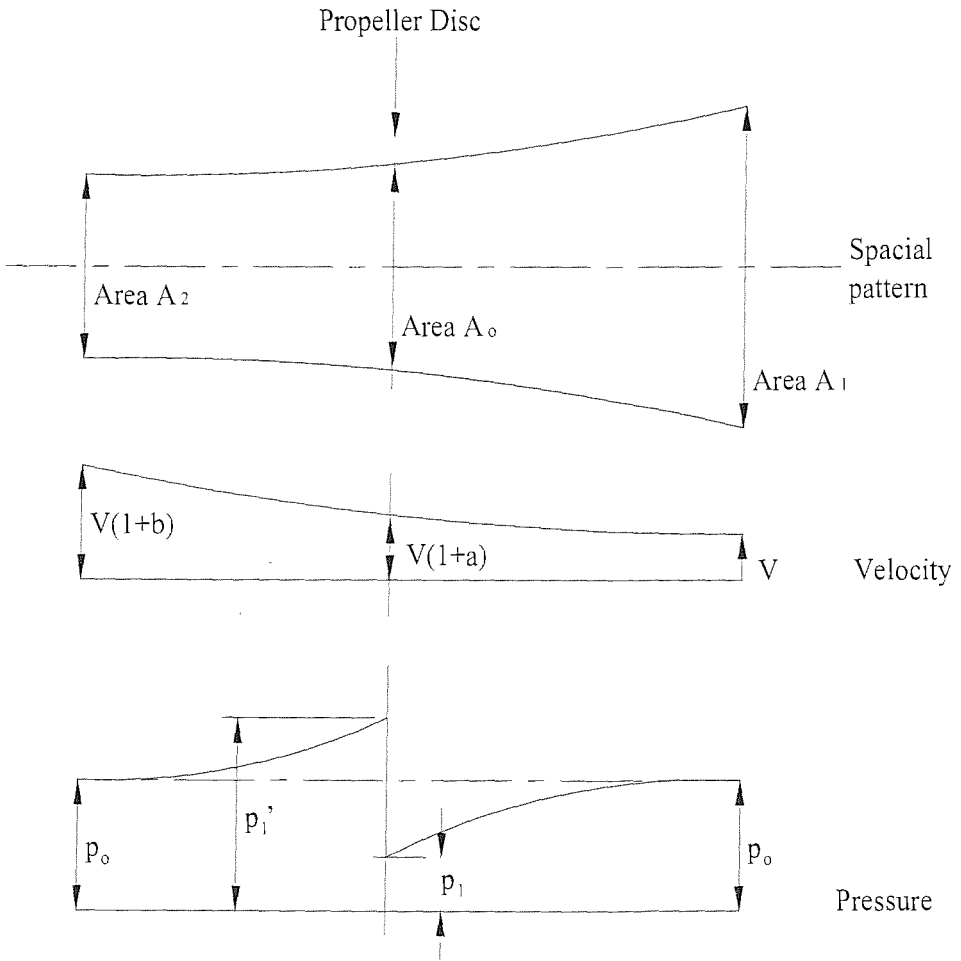

Figure B1 - Spacial, velocity and pressure patterns past the propeller disc.

Where: A_o = Area of the propeller disc.
V = Advance speed of the propeller.
p_1 = Pressure at inlet to disc.
p_1' = Pressure at exit of disc.
p_o = Pressure in streamtube at planes A_1 and A_2.

The propeller imparts an increase in pressure

$$\Delta p = p_1' - p_1 \tag{B1}$$

to the water flowing through the disc A_o. The force exerted by the propeller on the fluid or the reaction force (the propeller thrust T) is then

$$T = \Delta p A_o \tag{B2}$$

In accordance with the momentum law, this force is equal to the rate of change of momentum, which in turn is equal to the mass flow rate times the velocity.

$$\dot{T} = \rho A_o V(1+a)[V(1+b)-V]$$

$$\therefore \quad T = \rho A_o V(1+a)Vb \tag{B3}$$

Applying Bernoulli's principle upstream of the propeller disc,

$$p_o + \rho\frac{V^2}{2} = p_1 + \rho\frac{V^2}{2}(1+a)^2 \tag{B4}$$

and downstream

$$p_o + \rho\frac{V^2}{2}(1+b)^2 = p_1' + \rho\frac{V^2}{2}(1+a)^2. \tag{B5}$$

Using Equations B4 and B5, subtracting

$$p_1' - p_1 = \rho\frac{V^2}{2}(1+b)^2 - \rho\frac{V^2}{2} \tag{B6}$$

$$\therefore \quad p_1' - p_1 = \frac{\rho}{2}V^2(2b+b^2) \tag{B7}$$

Hence, from Equation B2

$$T = \frac{\rho}{2}A_o V^2(2b+b^2) \tag{B8}$$

and from Equation B3

$$\therefore \qquad T = \rho A_0 V(1+a)bV = \frac{\rho}{2} A_0 V^2 (2b + b^2) \tag{B9}$$

Comparing the terms in Equation B9, it is seen that

$$a = b/2. \tag{B10}$$

I.e. half the velocity increase experienced in the screw race is caused by the suction created by the propeller disc. This factor of increase, a, is known as the axial inflow factor. This factor controls the propeller efficiency that can be obtained since

$$\text{Propeller efficiency} = \frac{\text{useful work done by the propeller}}{\text{power absorbed by the propeller}}$$

$$= \frac{\text{thrust} \times \text{propeller speed}}{\text{overall change in kinetic energy}} \tag{B11}$$

$$= \frac{\rho A_0 V^2 2a(1+a)V}{\frac{1}{2}\rho A_0 V\ (1+a)V^2[(1+2a)^2 - 1]} \tag{B12}$$

$$= \frac{2\rho A_0 V^3 a(1+a)}{\frac{1}{2}\rho A_0 V^3 (1+a)(4a^2 + 4a)} \tag{B13}$$

$$= \frac{1}{1+a} \tag{B14}$$

Which shows that even for this ideal case, high propeller efficiency is only possible with a small inflow factor, i.e. with a large diameter propeller.

The thrust loading coefficient is defined as [B2]

$$C_T = \frac{T}{\frac{1}{2}\rho A_0 V^2} \tag{B15}$$

and substituting for T from Equation B3

$$C_T = \frac{\rho A_0 V^2 (1+a)b}{\frac{1}{2}\rho A_0 V^2} \Rightarrow 4a^2 + 4a \tag{B16}$$

$$\therefore \qquad a = \frac{-4 \pm \sqrt{16 + 16C_T}}{8} \Rightarrow \frac{1}{2} \pm \frac{1}{2}\sqrt{1 + C_T} \tag{B17}$$

So, using Equation B14,

$$\text{Ideal efficiency} = \frac{1}{1+a} = \frac{2}{1+\sqrt{1+C_T}}. \tag{B18}$$

From this equation it is evident that high thrust loading gives low efficiency and low thrust loading gives high efficiency. The thrust loading coefficient will be low if the propeller disc area, and hence the propeller diameter is large. Therefore, if a high efficiency is wanted, the propeller diameter must be as large as possible.

REFERENCES

B1. RAWSON KJ, TUPPER EC - "*Basic Ship Theory.*" Vol.2. 3rd edition. Published by Longman Scientific & Technical.

B2. HARVALD SA - "*Resistance and Propulsion of Ships.*" Published by John Wiley & Sons, 1983. pp198-218.

APPENDIX C: DYNAMOMETER CALIBRATION

C.1 DYNAMOMETER CALIBRATION MEASUREMENTS

The dynamometer system took the form of the arrangement shown in Figure C1 below.

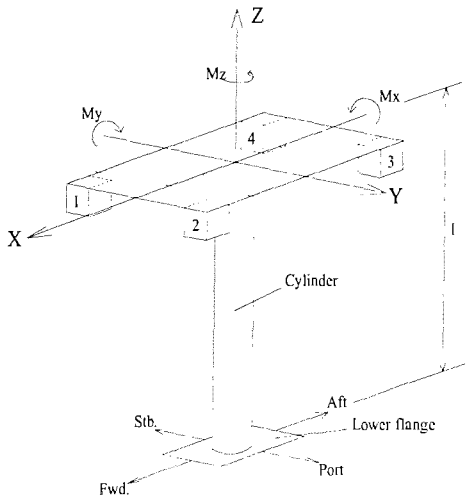

Figure C1 - Dynamometer system.

Where blocks 1 to 4 represent the individual dynamometer cages, and the thruster unit would ultimately be secured to the lower flange. The lift and drag responses of each dynamometer were measured and recorded individually.

Loads were applied to the structure through the use of weights on hooks, attached to wire ropes hanging over pulleys. Loads of up to 820N were applied in both positive and negative directions for both lift and drag force components. Due to the thruster being mounted at the end of the cylinder an effective moment would be produced about the dynamometers, causing possible moment interaction effects within the system. In order to highlight these effects and take them into account, the loads were also applied at different heights on the cylinder.

In addition, the response of the system to pure moments or pure shear forces was also investigated. Consider two forces, F_1 and F_2, applied at distances l_1 and l_2 from the top plate, as shown schematically in Figure C2.

If the magnitude of F_1 is equal to that of F_2, upon resolving the forces the resultant shear force loading is zero because the loads act in opposite directions. However, a moment, M, does exist;

$$M = F_1 l_1 - F_2 l_2 \neq 0 \qquad \text{(C1)}$$

and the dynamometer response to a pure moment can be obtained.

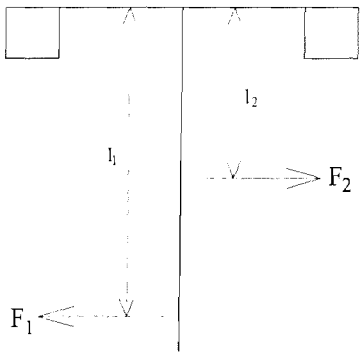

Figure C2 - Schematic diagram of applied loads.

Alternatively, if the moments $F_1 l_1$ and $F_2 l_2$ are of equal magnitude, the resultant moment loading is zero, but the net shear force, F_x, is

$$F_x = F_1 - F_2 \neq 0 \qquad \text{(C2)}$$

Hence, the response to pure forces can also be measured.

Finally, loads were applied in the negative Z direction, from the lower flange, to represent the mass of the thruster. It was seen that a load in this direction had negligible effect on any of the dynamometer voltage offset readings, maximum changes being ±1%.

C.2 DYNAMOMETER CALIBRATION MATRIX

From the calibration measurements dynamometer responses were obtained for loads at different heights, pure moment loads and pure force loads, all in the lift and drag directions. The results were plotted as graphs of voltage response versus applied load or moment and, using lines of best fit, equations relating the individual dynamometer responses to the various imposed conditions were obtained.

It is worth noting that some of the results indicated a non-linear response, possibly due to a certain degree of asymmetry in the manufacture of the framework. However, the relationships remained consistent over repeated tests and were therefore assumed adequate for calibration purposes.

Firstly, consider the calibration of the lift components. The components of drag were calibrated in the same manner, but with the relevant forces and directions changed. From the application of forces in the lift direction, F_x, at distances l on the cylinder, a relationship was derived whereby;

$$VL_i = A_i F_x \qquad \text{(C3)}$$

where VL_i = Lift component voltage offset for dynamometer i.
A_i = Constant for dynamometer i.

And from the response due to a pure force (when the moments cancelled)

$$VLF_i = B_i F_x \tag{C4}$$

where VLF_i = Lift component voltage offset for dynamometer i under a pure force.
B_i = Constant for dynamometer i.

It was assumed that, when subject to a load in the X or lift direction, the offset voltages recorded on the drag flexures did not measure any effect of the shear force. Their offset values were purely a result of the moment effect and were a function of the lever arm, l;

$$VD_i = C_i F_x l \tag{C5}$$

where VD_i = Drag component voltage offset for dynamometer i.
C_i = Constant for dynamometer I.

This assumption was confirmed by the numerical results.

It was also assumed that the total voltage offset, VL_i, consisted of an offset due to the pure shear force (when moments cancelled), VLF_i, plus an offset due to the moment effect, VLM_i. Hence,

$$VL_i = VLF_i + VLM_i \tag{C6}$$

$$\therefore \quad VLM_i = VL_i - VLF_i \tag{C7}$$

Again, the numerical results indicated that this was an acceptable assumption.

Knowing the pure shear force responses, VLF_i, the moment responses were calculated using Equation C7, and new relationships were obtained from Equation C6;

$$\begin{aligned} VL_i &= E_i F_x + G_i F_x l \\ VD_i &= C_i F_x l \end{aligned} \tag{C8}$$

where E_i and G_i are constants for dynamometer i.

Similar assumptions were employed when considering the system under forces in the drag, or Y, direction, F_y. These led to pairs of equations defining the response to a force, F_y, in the form of;

$$\begin{aligned} VD_i &= H_i F_y + J_i F_y^2 l + K_i F_y l \\ VL_i &= M_i F_y^2 l + N_i F_y l \end{aligned} \tag{C9}$$

where H_i, J_i, K_i, M_i and N_i are all constants for dynamometer i.

The extra $F_y^2\, l$ terms in Equation C9, although small, were present because of slight non-linear responses in the system. It was thought more prudent to include these non-linearities rather than fit a straight line through a non-linear set of data. However, as the results were successfully repeatable, this was considered to be a valid method.

Finally it was assumed that a nominal load, having components in both the lift and drag directions, would result in a response being the summation of Equations C8 and C9, giving,

$$\begin{aligned} VL_i &= E_i F_x + G_i F_x l + M_i F_y^2 l + N_i F_y l \\ VD_i &= C_i F_x l + H_i F_y + J_i F_y^2 l + K_i F_y l \end{aligned} \tag{C10}$$

A system of eight equations (two for each dynamometer) was therefore obtained for four unknowns. From these eight equations, a calibration matrix was calculated which allowed an accurate and reliable prediction of the forces in the system, based on measured dynamometer voltage offsets.

$$\begin{bmatrix} VL_1 \\ VD_1 \\ VL_2 \\ VD_2 \\ VL_3 \end{bmatrix} = \begin{bmatrix} E_1 & 0 & N_1 & G_1 & M_1 \\ 0 & H_1 & K_1 & C_1 & J_1 \\ E_2 & 0 & N_2 & G_2 & M_2 \\ 0 & H_2 & K_2 & C_2 & J_2 \\ E_3 & 0 & N_3 & G_3 & M_3 \end{bmatrix} . \begin{bmatrix} F_x \\ F_y \\ M_x \\ M_y \\ F_y^2 l \end{bmatrix} \tag{C11}$$

where $M_x=F_y l$ and $M_y=F_x l$, and upon inversion of the 5×5 matrix,

$$\begin{bmatrix} VL_1 \\ VD_1 \\ VL_2 \\ VD_2 \\ VL_3 \end{bmatrix} . \begin{bmatrix} S_{11} & S_{12} & S_{13} & S_{14} & S_{15} \\ S_{21} & S_{22} & S_{23} & S_{24} & S_{25} \\ S_{31} & S_{32} & S_{33} & S_{34} & S_{35} \\ S_{41} & S_{42} & S_{43} & S_{44} & S_{45} \\ S_{51} & S_{52} & S_{53} & S_{54} & S_{55} \end{bmatrix} = \begin{bmatrix} F_x \\ F_Y \\ M_x \\ M_y \\ F_y^2 l \end{bmatrix} \tag{C12}$$

from which forces can be obtained using measured voltage offsets. Equations C11 and C12 use the voltage offsets (*VL* and *VD*) for dynamometer numbers *1, 2* and *3*. Further matrices may be obtained using various combinations of *1, 2, 3* and *4*. For an ideal system, the results should yield the same forces. However, it is possible to use several matrices and take an average of the results.

APPENDIX D: CALCULATION OF ELECTROMAGNETIC MOTOR POWER AND SPEED

D.1 CALCULATION OF MOTOR SPEED [D1]

The measurements detailed in this section were carried out by the Department of Electrical Engineering, however, this information has been included for completeness.

The speed of the motor was calculated from the motor frequency using;

$$N = \frac{120f}{N_p} \tag{D1}$$

where N = motor speed (rpm),
N_p = number of poles, which is 24 for this motor,
f = motor frequency (Hz).

The frequency was measured from the Hall signal, as well as the terminal voltage. The latter was conveniently measured using the Voltech wattmeter.

D.2 BEARING FRICTION AND CORE LOSS

The no-load core loss and bearing friction loss were estimated from previous air tests of the thruster. A dynamometer rig was connected to the propeller shaft and the unit was driven as a generator. Input power was obtained by measuring the driving torque and speed.

These losses were also estimated again by measuring the input power to the thruster in air (no-load) while driven as a motor using the six-step inverter. Core and bearing losses were then calculated by subtracting the copper loss ($=3\ I_m^2\ R_{ph}$, which is very small) from the measured power. The two measurements produced very similar results, however, it must be noted that both measurements neglected the small propeller friction loss component, which was estimated to be of the order of 2W at full speed.

Core loss increases slightly on load due to armature flux. Full-load core losses still need to be evaluated using air tests on a dynamometer rig. However, for the time being it was assumed that the core loss on-load was equal to the no-load core loss.

Studying the results, bearing and no-load core loss P_{bc} in Watts were found to be given by the following empirical equation:

$$P_{bc} = 0.00369N^{1.4} \tag{D2}$$

where N = motor speed in rpm.

D.3 CALCULATION OF MOTOR OUTPUT POWER

Motor output power (or propeller input power P_p) was calculated by subtracting the bearing and core loss and motor copper loss from the measured motor input power P_m as follows:

$$P_p = P_m - P_{bc} - 3I_m^2 R_{ph} \qquad \text{(D3)}$$

where I_m = motor rms phase current (amps),
R_{ph} = phase resistance of the motor at the operating temperature
(R_{ph} was measured on many occasions as 1.25 Ω).

REFERENCES

D1. ABU SHARKH S, HUGHES AW, TURNOCK SR, BATTEN W – "*First 2kW Prototype – Test Results.*" Prototype Integrated Electric Thrusters for Work-Class Underwater Vehicles. University of Southampton, School of Engineering Sciences. Technical Note ITM04, Nov.1999.

APPENDIX E: PANEL CODE THEORY PANEL CODE EXAMPLE FILES GEOMETRY DEFINITION FILES

E.1 PANEL CODE THEORY [E1]

In a lifting surface panel formulation the approximation of the full Navier-Stokes equation assumes that the flow is inviscid, incompressible and irrotational and satisfies Laplace's potential equation:

$$\nabla^2 \phi = 0 \tag{E1}$$

A detailed description of the method and a review of its historical development is given by Hess[E2]. Lamb[E3] showed that a quantity satisfying Laplace's equation can be written as an integral over the bounding surface S of a source distribution per unit area s and a normal dipole distribution per unit area m distributed over S. If **v** represents the disturbance velocity field due to the bounding surface (or body) and is defined as the difference between the local velocity at a point and that due to the free-stream velocity then:

$$\underline{v} = \nabla \phi \tag{E2}$$

where ϕ is defined as the disturbance potential. This can be expressed in terms of a surface integral as:

$$\phi = \iint_{S_B} \left[\frac{1}{r}\sigma + \frac{\partial}{\partial n}\left(\frac{1}{r}\right)\mu \right] dS + \iint_{S_W} \frac{\partial}{\partial n}\left(\frac{1}{r}\right)\mu dS \tag{E3}$$

where S_B is the surface of the body and S_W a trailing wake sheet. In the expression r is the distance from the point for which the potential is being determined to the integration point on the surface and $\partial/\partial n$ is a partial derivative in the direction normal to the local surface. A dipole distribution is used to represent the wake sheet. Hess[E4] showed this can be directly related to the vorticity distribution used in vortex lattice methods (VLM).

The conditions imposed on the disturbance potential are that (from Hess[E2]):

1) the velocity potential satisfies Laplace's equation everywhere outside of the body and wake;
2) the disturbance potential due to the body vanishes at infinity;
3) the normal component of velocity is zero on the body surface;
4) the Kutta-Joukowsky condition of a finite velocity at the body trailing edge is satisfied.
5) the trailing wake sheet is a stream surface with equal pressure either side.

For a steady-state solution the wake dipole strength distribution is uniquely determined by the application of the Kutta condition at the body trailing edge. As conditions (1) and (2) are satisfied as functions of μ and σ, conditions (3) and (4) are used to determine μ and σ on the

body. The Kutta condition only applies at the trailing edge and some other relationship has to be used to uniquely determine the distribution of μ and σ over the body. The numerical resolution of this non-uniqueness is referred to as the singularity mix of the lifting-surface method.

Lee[E5] carried out a two-dimensional investigation into four possible schemes for the solution of Lamb's equation. The conclusion of that study was, that for lifting surfaces which have both thin and thick sections (e.g. propeller blades), the perturbation potential method taken from the work by Morino and Kuo[E6] was the most suitable. The principal advantages of this method are that because panel potential (scalar) rather than velocity (vector) influence coefficients are calculated, only a third of the memory requirement for the method is needed. Also, the perturbation potential influence coefficient is an order less singular. Kerwin and Lee[E7] used this method and found it robust in their investigation of ducted propellers.

Morino's numerical procedure is based on representing the body surface by a series of N quadrilateral panels each with an unknown but constant dipole strength per unit area. The vertices of these panels are located on the actual surface of the body. The wake sheet is represented by M panels placed on the stream-surface from the trailing edge of the body surface. Its dipole strength per unit area is related to the difference in dipole potential at the trailing edge. In Morino's work the wake strength m_w was equated to the difference in potential between the upper and lower surface at the trailing edge.

That is:

$$\mu_w = \phi_u - \phi_l \tag{E4}$$

On the body surface the source strength per unit area is prescribed by satisfying the condition for zero normal velocity at the panel centroid:

$$\sigma_S = \overline{U}.\overline{n} \tag{E5}$$

where **n** is the unit normal outward from the panel surface and U the specified inflow velocity at the panel centroid.

The numerical discretisation of Equation E3 gives the potential at the centroid of panel i as:

$$\phi_i = \frac{1}{2\pi}\sum_{j=1}^{N}\left(\left(U_\infty . n_j\right)S_{ij} - \phi_j D_{ij}\right) + \sum_{k=1}^{M}\Delta\phi_k W_{ik} \tag{E6}$$

where for panel j:
S_{ij} is the source influence coefficient of a unit strength panel;
D_{ij} the dipole influence coefficient;
W_{ik} the influence of the constant strength wake strip extending to infinity.

As there are N independent equations corresponding to the N body surface panel centroids, Equation E6 is closed and can be evaluated. Expressed in matrix form it becomes:

$$\left[D_{ij}\right]\phi+\left[W_{ik}\right]\Delta\phi=\left[S_{ij}\right]\left(U_{\infty}.n\right) \qquad \text{(E7)}$$

For Morino's original trailing edge Kutta condition, which directly relates $\Delta\phi$ to the difference in trailing edge panel potential, the matrix Expression E7 can then be directly solved to give the vector of dipole potentials ϕ. Numerical differentiation of dipole potential along the body surface allows the surface velocity and hence pressures on the surface to be evaluated.

E.2 EXAMPLE OF A COMMAND FILE, **.cmd*, TO MODEL THE TDP

Four geometry files are used to define the prototype TDP: the propeller, the duct, the forward stators and bearing casings, and the aft stators and bearing casings. For this reason, the example file shown here uses four geometry files, and defines the various parameters for each individually.

4 1 1 100 0.0001 50.0	No.of geometries (4) and overall program control variables.
250.0 0.5 5 0 0 0 8	**Start of first geometry** and its control variables.
1 1 0 0 0 1	Boolean switches to determine which parameters to record.
prop.pan	Name of geometry file defining the propeller.
prop.dij	Name of dipole matrix file, created by and used by the solver.
prop.sij	Name of source matrix file, created by and used by the solver.
prop.wik	Name of wake matrix file, created by and used by the solver.
prop.nde	Name of velocity field file, used to obtain velocities at specified points.
prop	Name of output log file, created by the solver.
0 2 1 4 100.0 0.1 1.0 0.1	Interaction velocity field data.
1.0 0.0 0.0 0.0 0.0 0.0	Interaction axis and origin data.
2	Number of geometry variations (e.g. offset, scale, or pivot).
0 0 3 0 -30.0	Body 0, Position 0, Parameter code, Reference code, Value (e.g. angle).
0 1 3 0 -30.0	Body 0, Position 1, Parameter code, Reference code, Value (e.g. angle).
250.0 0.02 5 0 0 0 8	**Start of second geometry** and its control variables.
1 1 0 0 0 1	Boolean switches to determine which parameters to record.
duct.pan	Name of geometry file defining the duct.
duct.dij	---}
duct.sij	---}
duct.wik	---}
duct.nde	---}--- As 'first geometry'.
duct	---}
0 1 1 3 100.0 0.1 1.0 0.1	---}
1.0 0.0 0.0 0.0 0.0 0.0	---}
1	Number of geometry variations (e.g. offset, scale, or pivot).
0 0 3 2 0.0	Body 0, Position 0, Parameter code, Reference code, Value (e.g. angle).
30.0 0.03 9 0 0 0 8	**Start of third geometry** and its control variables.
1 1 0 0 0 1	Boolean switches to determine which parameters to record.
fstat.pan	Name of geometry file defining the forward stators and bearing.
fstat.dij	---}
fstat.sij	---}
fstat.wik	---}
fstat.nde	---}--- As 'first geometry'
fstat	---}
0 0 1 1 100.0 0.1 1.0 0.05	---}
1.0 0.0 0.0 0.0 0.0 0.0	---}
1	Number of geometry variations (e.g. offset, scale, or pivot).
0 0 3 2 0.0	Body 0, Position 0, Parameter code, Reference code, Value (e.g. angle).

30.0 0.03 9 0 0 0 8	**Start of fourth geometry** and its control variables.
1 1 0 0 0 1	Boolean switches to determine which parameters to record.
astat.pan	Name of geometry file defining the aft stators and bearing.
astat.dij	---}
astat.sij	---}
astat.wik	---}
astat.nde	---}--- As 'first geometry'
astat	---}
0 0 1 1 100.0 0.1 1.0 0.05	---}
1.0 0.0 0.0 0.0 0.0 0.0	---}
1	Number of geometry variations (e.g. offset, scale, or pivot).
0 0 3 2 0.0	Body 0, Position 0, Parameter code, Reference code, Value (e.g. angle).

E.3 EXAMPLE OF A GEOMETRY, **.pan*, FILE FOR A PROPELLER

In this case two geometries are defined, the propeller blade (a lifting body) and a portion of the propeller hub (a non-lifting body). The hub sections include additional panel distribution data to align the panels along the hub with those on the propeller blade.

1 1 0		No. of Non-lifting bodies, No. of Lifting bodies, Dummy.
0.0 0.0 0.0		Reflection plane origin.
0.0 0.0 0.0		Reflection plane normal.
0.0 0.0 0.0		Dummy.
0.0 0.0 0.0		Origin of axis of rotation.
1499.6 0.0 0.0		Angular rotation (rads/s) about X, Y, Z axis.
30		Free-stream velocity (m/s)
1 1 1		Nx, Ny, Nz. }
0.0 0.0 0.0		Origin of cuboid (xo, yo, zo). }---Defining velocity input.
0.0 0.0 0.0		Increments (dx, dy, dz) }
-1.0 0.0 0.0		Scaled velocity.
28 7 5 4	**HUB**	No. of panels around chord, span. No. of sections. No. of images.
8 0 0 0		Panel distribution patterns around chord and span directions.
0.0 0.0 0.0		Pivot vector.
0.0 0.0 0.0		Offset vector.
1.0 1.0 1.0		X, Y, Z Scale vectors.
0.0 0.0 0.0		Angles.
21		**Start of first Hub section**. No. of co-ordinates defining section.
-0.03000 -0.01289 0.02709		X, Y, Z co-ordinates.
-0.02782 -0.01463 0.02619		--
-0.02563 -0.01632 0.02517		--
-0.02345 -0.01794 0.02405		--
-0.02127 -0.01917 0.02308		--
-0.01904 -0.02008 0.02229		--
-0.01628 -0.02090 0.02153		--
-0.01292 -0.02168 0.02074		--
-0.00915 -0.02255 0.01978		--
-0.00056 -0.02514 0.01637		--
0.00448 -0.02693 0.01322		--
0.00992 -0.02882 0.00834		--
0.01583 -0.02999 0.00069		--
0.02127 -0.02783 -0.01120		--
0.02345 -0.02704 -0.01300		--
0.02563 -0.02613 -0.01474		--
0.02782 -0.02511 -0.01642		--
0.03000 -0.02397 -0.01803		--
4 13 17		Panel distribution information.

6 23 27	Panel distribution information.
0 1 0	Panel distribution information.
21	**Start of second Hub section**. No. of co-ordinates defining section.
-0.03000 -0.00154 0.02996	X, Y, Z co-ordinates.
-0.02782 -0.00350 0.02980	--
-0.02563 -0.00544 0.02950	--
-0.02345 -0.00737 0.02908	--
-0.02127 -0.00888 0.02866	--
-0.01904 -0.01115 0.02785	--
-0.01628 -0.01317 0.02696	--
-0.01292 -0.01496 0.02601	--
-0.00915 -0.01670 0.02492	--
-0.00056 -0.02064 0.02177	--
0.00448 -0.02300 0.01926	--
0.00992 -0.02565 0.01556	--
0.01583 -0.02833 0.00986	--
0.02127 -0.03000 0.00031	--
0.02345 -0.02995 -0.00166	--
0.02563 -0.02978 -0.00362	--
0.02782 -0.02948 -0.00557	--
0.03000 -0.02905 -0.00749	--
5 14 17	Panel distribution information.
6 23 27	Panel distribution information.
0 0 0	Panel distribution information.
21	**Start of third Hub section**. No. of co-ordinates defining section.
-0.03000 0.01004 0.02827	X, Y, Z co-ordinates.
-0.02782 0.00817 0.02887	--
-0.02563 0.00626 0.02934	--
-0.02345 0.00432 0.02969	--
-0.02127 0.00276 0.02987	--
-0.01904 -0.00086 0.02999	--
-0.01628 -0.00413 0.02971	--
-0.01292 -0.00702 0.02917	--
-0.00915 -0.00973 0.02838	--
-0.00056 -0.01501 0.02598	--
0.00448 -0.01775 0.02419	--
0.00992 -0.02071 0.02171	--
0.01583 -0.02394 0.01808	--
0.02127 -0.02760 0.01176	--
0.02345 -0.02831 0.00993	--
0.02563 -0.02890 0.00805	--
0.02782 -0.02936 0.00614	--
0.03000 -0.02970 0.00420	--
5 14 17	Panel distribution information.
6 23 27	Panel distribution information.
0 0 0	Panel distribution information.
21	**Start of fourth Hub section**. No. of co-ordinates defining section.
-0.03000 0.02010 0.02227	X, Y, Z co-ordinates.
-0.02782 0.01859 0.02354	--
-0.02563 0.01701 0.02471	--
-0.02345 0.01535 0.02577	--
-0.02127 0.01398 0.02654	--
-0.01904 0.00954 0.02844	--
-0.01628 0.00532 0.02953	--
-0.01292 0.00148 0.02996	--
-0.00915 -0.00209 0.02993	--
-0.00056 -0.00855 0.02875	--
0.00448 -0.01147 0.02772	--
0.00992 -0.01433 0.02635	--

```
 0.01583 -0.01723  0.02456      --
 0.02127 -0.02099  0.02143      --
 0.02345 -0.02235  0.02001      --
 0.02563 -0.02362  0.01850      --
 0.02782 -0.02478  0.01691      --
 0.03000 -0.02584  0.01525      --
 5  14  17                      Panel distribution information.
 6  23  27                      Panel distribution information.
 0  0   0                       Panel distribution information.
21                              Start of fifth Hub section. No. of co-ordinates defining section.
-0.03000  0.02709  0.01289      X, Y, Z co-ordinates.
-0.02782  0.02619  0.01463      --
-0.02563  0.02517  0.01632      --
-0.02345  0.02405  0.01794      --
-0.02127  0.02308  0.01917      --
-0.01904  0.01877  0.02340      --
-0.01628  0.01424  0.02641      --
-0.01292  0.00986  0.02833      --
-0.00915  0.00568  0.02946      --
-0.00056 -0.00163  0.02996      --
 0.00448 -0.00454  0.02965      --
 0.00992 -0.00697  0.02918      --
 0.01583 -0.00886  0.02866      --
 0.02127 -0.01120  0.02783      --
 0.02345 -0.01300  0.02704      --
 0.02563 -0.01474  0.02613      --
 0.02782 -0.01642  0.02511      --
 0.03000 -0.01803  0.02397      --
 4  13  17                      Panel distribution information.
 6  23  27                      Panel distribution information.
 0  1   0                       Panel distribution information.
35  13  9  4            BLADE  No. of panels around chord, span. n sections. No. of images.
100  20                         No. of wake panels (lifting bodies only).
4  0  1  0                     Panel distribution patterns around chord and span directions.
0.0  0.0  0.0                  Pivot vector.
0.0  0.0  0.0                  Offset vector.
1.0  1.0  1.0                  X, Y, Z Scale vectors.
0.0  0.0  0.0                  Angles.
19                              Start of first blade section. No. of co-ordinates defining section.
-0.02127  0.02308  0.01917     X, Y, Z co-ordinates.
-0.01904  0.01877  0.02340      --
-0.01628  0.01424  0.02641      --
-0.01292  0.00986  0.02833      --
-0.00915  0.00568  0.02946      --
-0.00056 -0.00163  0.02996      --
 0.00448 -0.00454  0.02965      --
 0.00992 -0.00697  0.02918      --
 0.01583 -0.00886  0.02866      --
 0.02127 -0.01120  0.02783      --
 0.01911 -0.00533  0.02952      --
 0.01628  0.00002  0.03000      --
 0.01292  0.00478  0.02962      --
 0.00922  0.00907  0.02860      --
 0.00062  0.01573  0.02555      --
-0.00441  0.01814  0.02389      --
-0.00992  0.02000  0.02236      --
-0.01583  0.02141  0.02101      --
-0.02127  0.02308  0.01917      --
19                              Start of second blade section. No. of co-ordinates defining section
```

-0.02357 0.02699 0.02516	X, Y, Z co-ordinates.
-0.02118 0.02200 0.02963	--
-0.01807 0.01690 0.03280	--
-0.01452 0.01175 ----	--
---- ---- ----	--
---- etc ----	--
---- ---- ----	--
19	**Start of nth blade section**. No. of co-ordinates defining section.
-0.02368 0.03192 0.03744	X, Y, Z co-ordinates.
-0.02149 0.02597 0.04178	--
-0.01858 0.01994 0.04498	--
-0.01512 0.01393 0.04719	--
-0.01126 0.00799 ----	--
---- ---- ----	--
---- etc ----	--
---- ---- ----	--
71	**Start of first blade wake section**. No. of co-ordinates defining section
-0.02130 0.02310 0.01920	X, Y, Z co-ordinates.
-0.03176 0.02787 0.01111	--
-0.04376 0.02994 0.00195	--
-0.05576 0.02907 -0.00739	--
-0.06776 0.02537 -0.01602	--
-0.07976 0.01918 -0.02307	--
-0.09176 0.01111 -0.02787	--
-0.10376 0.00195 -0.02994	--
-0.11576 -0.00739 -0.02907	--
-0.12776 -0.01602 -0.02537	--
-0.13976 -0.02307 -0.01918	--
-0.15176 -0.02787 ----	--
---- ---- ----	--
---- etc ----	--

E.4 PROPELLER DEFINITION PROGRAM, *makeprop.f*

Makeprop.f is a program, written in Fortran, which generates a propeller blade geometry, propeller hub and blade wake sheet for input into the lifting panel code, Palisupan. Three input files (*ka1.dat* , *ka2.dat* , *ka3.dat*) which define the propeller blade section shapes are used as a starting point for the program. The format of these files has been based on the propeller data which was presented by Oosterveld [E8] on the Kaplan series.

The program also requires the user to input the number of blades (*BLAD*), the propeller diameter (*D*), the blade area ratio (*BAR*), the distance the blade wake should extend downstream as a multiple of the propeller diameter (*MD*), and the average pitch of the wake sheet (*WPav*).

E.4.1 Input Files

ka1.dat provides details of the blade section general dimensions. It is written in the form;

9						
0.2	0.85	30.21	36.94	67.15	4.00	34.98
0.3	0.9	36.17	40.42	76.59	3.52	39.76
0.4	0.95	41.45	43.74	85.19	3.00	46.02
0.5	0.99	45.99	47.02	93.01	2.45	49.13
0.6	1.00	49.87	---	---	---	---

0.7	---	---	---	etc	---	---
0.8	---	---	---	---	---	---
0.9	---	---	---	---	---	---
1.0	1.00	56.44	56.44	112.88	0.50	50.00

where: Line 1 = NS = Number of blade sections.
Column 1 = RR = Section radius (r/R).
Column 2 = PD = Pitch ratio (P/D).
Column 3 = CTOTE = Section length from centreline to TE as a %age of $C_{0.6R}$.
Column 4 = CTOLE = Section length from centreline to LE as a %age of $C_{0.6R}$.
Column 5 = PC = Total section chord length as a %age of $C_{0.6R}$.
Column 6 = PTmax = Max. section thickness as a %age of prop diameter D.
Column 7 = PHT = Distance of Tmax from LE as a %age of section length C.

ka2.dat provides the offset details for each section at different lengths between the TE and point of maximum thickness. It is written in the form;

5
45

1	1	0.2	100	20.21	20.21
2	1	0.2	80	38.23	7.29
3	1	0.2	60	63.65	1.77
4	1	0.2	40	82.40	0.10
5	1	0.2	20	95.00	0.00
1	2	0.3	100	13.85	13.85
2	2	0.3	80	39.05	4.62
3	2	0.3	60	66.63	1.07
4	2	0.3	40	84.14	0.00
5	2	0.3	20	95.86	0.00
1	3	0.4	100	9.170	9.17
2	3	0.4	80	40.56	2.36
3	3	0.4	60	66.94	0.56
4	3	0.4	40	85.69	0.00
5	3	0.4	20	96.25	0.00
1	4	0.5	100	---	---
2	4	0.5	80	---	---
3	4	0.5	60	---	---
4	4	0.5	---	etc	---
---	---	---	---	---	---
---	---	---	---	---	---
4	9	1.0	40	88.00	0.00
5	9	1.0	20	97.00	0.00

where: Line 1 = TPN = Number of positions per section.
Line 2 = TNUM = Total number of data lines in the file (= NSxTPN).
Column 1 = PN = Point number along line.
Column 2 = N = Section number.
Column 3 = RR = Section radius (r/R).
Column 4 = PTDIST = %age of the distance from Tmax to TE.
Column 5 = TBPOFF = Offset for Back face as a %age of Tmax.
Column 6 = TFPOFF = Offset for Front face as a %age of Tmax.

ka3.dat provides the offset details for each section at different lengths between the LE and point of maximum thickness. It is written in a similar form to *ka2.dat* i.e.;

7					
63					
1	1	0.2	100	33.33	33.33
2	1	0.2	95	27.40	20.62
3	1	0.2	90	38.75	16.04
4	1	0.2	80	55.00	10.52
5	1	0.2	60	77.19	4.37
6	1	0.2	40	90.83	1.46
7	1	0.2	20	97.92	0.21
1	2	0.3	100	21.18	21.18
2	2	0.3	95	27.57	10.3
3	2	0.3	90	37.87	8.28
4	2	0.3	80	---	---
5	2	0.3	---	etc	---
---	---	---	---	---	---
---	---	---	---	---	---
6	9	1.0	40	88.00	0.00
7	9	1.0	20	97.00	0.00

where: Line 1 = LPN = Number of positions per section.
Line 2 = LNUM = Total number of data lines in the file (= NSxLPN).
Column 1 = PN = Point number along line.
Column 2 = N = Section number.
Column 3 = RR = Section radius (r/R).
Column 4 = PLDIST = %age of the distance from Tmax to LE.
Column 5 = LBPOFF = Offset for Back face as a %age of Tmax.
Column 6 = LFPOFF = Offset for Front face as a %age of Tmax.

E.4.2 Program Structure

Having read the data given in the three files listed above, the program initially converts all percentage values into actual values and then calculates the X Y Z co-ordinates which define each individual blade section on a flat plane at TDC. In this case, the X axis is located axially through the centre of the propeller (following the line of a drive shaft) with X=0.0 positioned half way through the propeller hub. The Z axis starts at X=0.0 and runs vertically through the blade at TDC (at TDC Z is equivalent to the radius). The Y axis is then defined using the left hand rule.

The co-ordinates defining the initial blade sections are firstly rotated about the relevant pitch angle, and then mapped onto a circular arc at the relevant radii in order to define the propeller blade at TDC. A surface representing the propeller hub between two propeller blades is then calculated using the 0.2R blade section co-ordinates, which have been rotated about a pitch angle. Consequently, the hub surface is calculated as a flat plane at the relevant Z value and subsequently mapped onto a circular arc.

A helical propeller blade wake sheet extending from each section trailing edge is modelled. By default, this is defined initially as the blade geometric pitch for a short distance downstream, followed by an average pitch, based on the average pitch of the blade sections.

Finally, an 'endcap' was defined which was positioned on the upstream side of the propeller hub. This 'endcap' represents the bearing casing in the integrated thruster, and has the same diameter as the propeller hub. Several circular sections define the endcap, which was modelled as a parallel cylinder with a spherical leading edge.

It must be noted that this program calculates the defining geometry for a single blade located at TDC, with a wake sheet and a fraction of the propeller hub surface. The remainder of the propeller is modelled within the panel code by defining the correct number of images.

The output file "*prop.dat*" provides the co-ordinates for the blade/hub/wake model, centred around the origin (0,0,0), in the order;

1. Hub section data.
2. Endcap section data.
3. Propeller blade section data
4. Wake sheet section data.

Before running with Palisupan, *prop.dat* must be edited to include the relevant parameter details for the panel code, and its name changed to *prop.pan*.

E.5 DUCT DEFINITION PROGRAM, *makeduct.f*

Makeduct.f is a program, written in Fortran, which generates a duct geometry file for input into the panel code, Palisupan. One input file (*ductsect.dat*) which defines the two-dimensional section shape of the duct is used as a starting point for the program. The file format simply defines the section offsets at several lengths along the duct, additional parameters are provided by the user. The program requires the user to input the duct length, internal diameter and duct section thickness. It is therefore possible to model ducts of different sizes with the same generic section profile.

E.5.1 Input Files

Below is a typical *ductsect.dat* file, used as an input file by *makeduct.f*. Note the co-ordinates are defined from the trailing edge, along the section lower surface, around the leading edge, along the section upper surface and back to the trailing edge point. This order complies with the order necessary to define the duct section shapes in the panel code geometry files.

40	No. of offsets defining duct section shape.
-0.102 0.03130	X, Y co-ordinates defining duct section shape.
-0.093 0.02190	Y co-ordinates are measured from the base-line (y=0.0).
-0.088 0.01710	
-0.083 0.01350	
-0.078 0.01070	
-0.068 0.00650	
-0.058 0.00360	
-0.048 0.00160	
-0.038 0.00060	
-0.028 0.00010	
-0.018 0.00000	
0.002 0.00000	
0.022 0.00000	
0.032 0.00010	
0.042 0.00060	
0.052 0.00160	
0.062 0.00360	
0.072 0.00650	

0.082	0.01070
0.087	0.01350
0.092	0.01710
0.097	0.02190
0.102	0.03130
0.1007	0.03530
0.0976	0.03700
0.08	0.03700
0.07	0.03700
0.06	0.03700
0.052	0.03700
0.04	0.03700
0.02	0.03700
0.002	0.03700
-0.02	0.03700
-0.048	0.03700
-0.06	0.03700
-0.07	0.03700
-0.08	0.03700
-0.0936	0.03700
-0.0967	0.03530
-0.102	0.03130

E.5.2 Program Structure

Makeduct.f reads the input file, *ductsect.dat*, and before carrying out any further calculations, it centres the section around X=0.0. The section data is then scaled to the sizes input by the user (i.e. the length and thickness), and the Y co-ordinates of the section are offset by the value of the duct internal radius, hence the co-ordinates now define the duct section at top dead centre (TDC). Using straightforward trigonometry, a further 11 sections are calculated around the circumference of the duct, at intervals of 30^{o}. The resultant section co-ordinates are output in the form of a panel code geometry file, which defines the duct centred about the origin (0,0,0). This duct generation program was only used for cases when no stators were included in the model. If stators are included, the points of intersection with the duct have to be calculated, this method is described in Section E.6.

E.6 STATOR DEFINITION PROGRAM, *stator.f*

Stator.f is a geometry definition program, written in Fortran, which is used when the stators and bearing casings are required to be included in the ducted propeller model. In addition to generating panel code geometry files for the stators and bearing casings, both forward and aft of the propeller, it also creates a file defining the portion of the duct between two stators.

Two input files are required. One, which defines the two-dimensional section shape of the duct (*ductsect.dat*), Section E.5, and a second which defines both the section co-ordinates and the section twist angle of the stators (*stator.dat*). Additional parameters, provided by the user include the duct length, internal diameter and duct section thickness, base point of the stator from centreline, and angle of stator rake. During the program, the stator co-ordinates were calculated, and if they existed outside the dimensions of the duct, or clashed with the propeller plane (due to an incorrectly defined rake angle or base point), the program terminated and informed the user of the region where the problem existed.

E.6.1 Input Files

The input file *ductsect.dat* is described in the previous section. *Stator.dat*, which defines the stator characteristics, takes the form of:

```
21                                  No. of offsets defining stator section shape.
-0.010   0.0000                     X, Y co-ordinates defining stator section shape.
-0.008  -0.0021                        Y co-ordinates are measured from the base-line (y=0.0).
-0.006  -0.0028
-0.004  -0.0032
-0.002  -0.0034
 0.000  -0.0035
 0.002  -0.0034
 0.004  -0.0032
 0.006  -0.0028
 0.008  -0.0021
 0.010   0.0000
 0.008   0.0021
 0.006   0.0028
 0.004   0.0032
 0.002   0.0034
 0.000   0.0035
-0.002   0.0034
-0.004   0.0032
-0.006   0.0028
-0.008   0.0021
-0.010   0.0000
11                                  No, of stator sections.
0.0  0.00                           Position of section (r/R) and Angle of section twist (degs).
0.1  0.00
0.2  0.00
0.3  0.00
0.4  0.00
0.5  0.00
0.6  0.00
0.7  0.00
0.8  0.00
0.9  0.00
1.0  0.00
```

Note how again, the section co-ordinates are defined from the trailing edge point, along the lower surface, around the leading edge and back to the trailing edge, along the upper surface. At present, only a constant section shape can be used along the length of the stator, however, it would not be difficult to modify the program, and *stator.dat* file, in order to model different section profiles. Similarly, each stator is assumed to have the same angles of twist. In addition, the program has been written specifically for the prototype TDP geometry, and as such, it uses three stators on each side of the propeller. However, this is also a relatively simple parameter to change if necessary.

E.6.2 Program Structure

Having read the input files, the program calculates the duct section co-ordinates at TDC in a similar manner to that in Section E.5.2. In order for an intersection to exist between the duct and a stator, a duct section must be defined at the same angle from TDC as the location of the stator. Therefore, knowing the number of stators, which are assumed to be

equally spaced, the program calculates the necessary angles at which to define the duct sections.

The stator section co-ordinates are initially calculated for a basis stator in the TDC position, with no angle of twist. The values are subsequently adjusted for twist and rake and then rotated and/or reflected into the position of the final six stators, located around the thruster. In addition, the outer section co-ordinates of the basis stator (at TDC) are compared with the duct section co-ordinates at TDC, which are then adjusted to follow the stator section. It is assumed that the stator section remains constant for radii greater than the internal diameter of the duct. Finally, the new duct section co-ordinates are rotated and/or reflected to the necessary positions around the duct, where the stators are located. In order to make the computation simpler, because the thruster is an axisymmetric body, only one third of the duct needed to be defined.

The bearing casing at the root of the stators was defined in a similar manner to that of the propeller hub, Section E.4.2, and had a fixed diameter of 60mm, again specific to the prototype TDP.

E.7 PANEL DEFINITIONS OF THE REPRESENTATIVE BODIES

E.7.1 Propeller

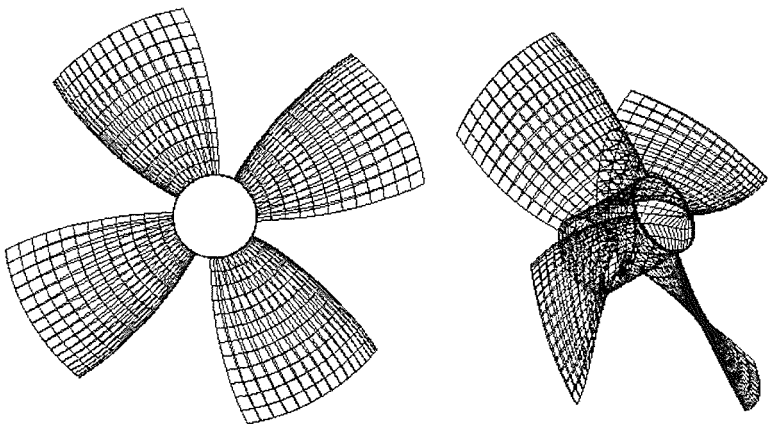

E.7.2 Duct

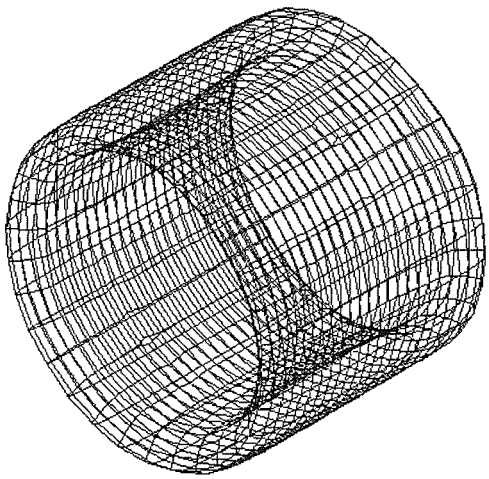

E.7.3 Forward Stators and Bearing Casing

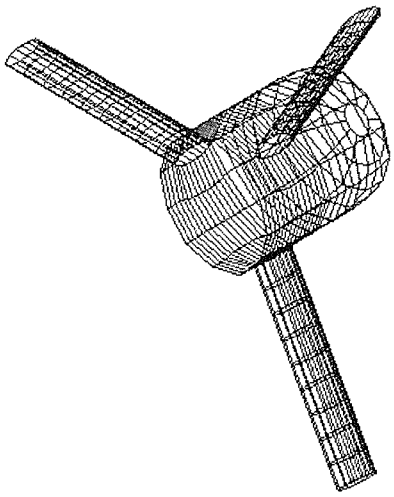

E.7.4 Aft Stators and Bearing Casing

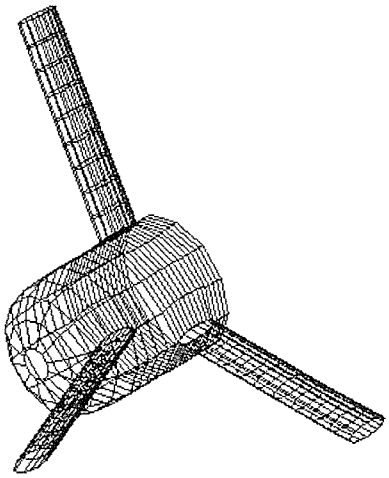

REFERENCES

E1. TURNOCK SR - "*Technical Manual and User Guide for the Surface Panel Code: Palisupan.*" University of Southampton, Ship Science Report No.100. Oct.1997.

E2. HESS JL - "*Panel Methods in Computational Fluid Dynamics.*" Annual Review of Fluid Mechanics 1990. Vol 22, pp255-274.

E3. LAMB H - "*Hydrodynamics.*" Cambridge University Press, sixth edition 1932.

E4. HESS JL - "*The Problem of Three-dimensional Lifting Flow and its Solution by Means of a Surface Singularity Distribution.*" Computational Methods Applied Mechanical Engineering 4:283-319, also 1972, Rep. MDC-J5679, McDonnell Douglas Aircraft Co. Long Beach, Calif.

E5. LEE T-J - " *A Potential Based Method for the Analysis of Marine Propellers in Steady Flow.*" Ph.D. thesis, M.I.T. Dept. of Ocean Engineering. Aug. 1987.

E6. MORINO L, KUO C-C - "*Subsonic Potential Aerodynamics for Complex Configurations: A General Theory.*" AIAA Journal, Vol.12, No.2. Feb.1974.

E7. KERWIN JE, KINNAS SA, LEE J-T, SHIH WZ - "*A Surface Panel Method for the Hydrodynamic Analysis of Ducted Propellers.*" SNAME Transactions Vol.95, 1987.

E8. OOSTERVELD MWC - "*Ducted Propeller Characteristics.*" RINA Symposium on Ducted Propellers 1973. Paper No.4, pp35-69.

APPENDIX F: BOUNDARY LAYER APPROXIMATION - THEORY, STRUCTURE AND PROGRAM.

F.1 THWAITES' LAMINAR BOUNDARY LAYER APPROXIMATION

Consider the thin shear layer equations for two-dimensional, steady, laminar flows. It has been shown [F1];

$$\frac{\partial u}{\partial x}+\frac{\partial v}{\partial y}=0 \tag{F1}$$

$$u\frac{\partial u}{\partial x}+v\frac{\partial u}{\partial y}=-\frac{1}{\rho}\frac{dp}{dx}+\nu\frac{\partial^2 u}{\partial y^2} \tag{F2}$$

where p is a known function of x independent of y, so that;

$$\frac{dp}{dx}=-\rho u_e\frac{du_e}{dx}$$

Let the momentum integral equation be written as,

$$\frac{d\theta}{dx}+\frac{\theta}{u_e}(H+2)\frac{du_e}{dx}=\frac{c_f}{2} \tag{F3}$$

If H and c_f are known as functions of θ or of some suitable combination of θ and u_e, Equation F3 can be integrated. Such functions were found in Thwaites' method by writing the following boundary conditions for Equation F2,

$$y=0 \quad , \quad \frac{\partial^2 u}{\partial y^2}=-\frac{u_e}{\theta^2}\lambda \quad , \quad \frac{\partial u}{\partial y}=\frac{u_e}{\theta}l \tag{F4}$$

It was found that the variable l adhered reasonably closely to a universal function of λ, which Thwaites denoted by $l(\lambda)$. In the same way, a reasonably valid universal function for H was also found, $H(\lambda)$.

By putting $y=0$ into Equation F2, and using Equation F4;

$$\lambda=\frac{\theta^2}{\nu}\frac{du_e}{dx} \tag{F5}$$

$$\frac{c_f}{2}=\frac{\tau_w}{\rho u_e^2}=\frac{\nu}{u_e^2}\left(\frac{\partial u}{\partial y}\right)_w=\frac{\nu l(\lambda)}{u_e\theta} \tag{F6}$$

The assumptions that l or c_f and H were functions of λ were only quasi-similarity assumptions. Falkner-Skan[F2] solutions could be used to give $l(\lambda)$ and $H(\lambda)$. With these results, Equation F3 could be written as;

$$\frac{u_e}{\nu}\frac{d\theta^2}{dx} = 2\{-[H(\lambda)+2]\lambda + l(\lambda)\} \equiv F(\lambda) \tag{F7}$$

Thwaites derived an expression for $F(\lambda)$, chosen to fit known solutions of Equation F2 as well as possible;

$$F(\lambda) = 0.45 - 6\lambda = 0.45 - 6\frac{\theta^2}{\nu}\frac{du_e}{dx} \tag{F8}$$

Substituting Equation F8 into F7 and multiplying the resultant equation by u_e^5 , after some rearranging,

$$\frac{1}{\nu}\frac{d}{dx}\left(\theta^2 u_e^6\right) = 0.45.u_e^5$$

which upon integration, leads to,

$$\frac{\theta^2 u_e^6}{\nu} = 0.45\int_0^x u_e^5 dx + \left(\theta^2\frac{u_e^6}{\nu}\right)_0 \tag{F9}$$

Using dimensionless quantities defined by

$$x^* \equiv \frac{x}{L} \quad , \quad u^* \equiv \frac{u}{u_{ref}} \quad , \quad u_e{}^* \equiv \frac{u_e}{u_{ref}} \quad , \quad R_L = \frac{u_{ref}L}{\nu} \tag{F10}$$

Equation F9 can be written as;

$$\left(\frac{\theta}{L}\right)^2 R_L = \frac{0.45}{(u_e{}^*)^6}\int_0^{x^*}(u_e{}^*)^5 dx^* + \left(\frac{\theta}{L}\right)^2 R_L\left(\frac{u_{e_0}{}^*}{u_e{}^*}\right)^6 \tag{F11}$$

And for a stagnation point flow, $u_{e_0}{}^* = 0$, so

$$\left(\frac{\theta}{L}\right)^2 R_L = \frac{0.075}{\left(du_e{}^*/dx^*\right)_0} \tag{F12}$$

where $\left(du_e{}^*/dx^*\right)_0$ denotes the slope of the velocity distribution for stagnation point flow.

Once θ has been calculated for a given velocity distribution, the other boundary layer parameters H and c_f can be determined using the following relationships;

For $0 \leq \lambda \leq 0.1$

$$l = 0.22 + 1.57\lambda - 1.8\lambda^2$$
$$H = 2.61 - 3.75\lambda + 5.24\lambda^2 \qquad \text{(F13)}$$

For $-0.1 \geq \lambda \geq 0$

$$l = 0.22 + 1.402\lambda + \frac{0.018\lambda}{0.107 + \lambda}$$
$$H = \frac{0.0731}{0.14 + \lambda} + 2.088 \qquad \text{(F14)}$$

F.2 HEAD'S TURBULENT BOUNDARY LAYER APPROXIMATION

Head offered a successful integral method for determining the growth of the turbulent boundary layer, assuming the dimensionless entrainment velocity v_E/u_e was a function of the shape factor, H_1 *[F1]*.

$$\frac{v_E}{u_e} = \frac{1}{u_e}\frac{d}{dx}[u_e(\delta - \delta^*)] = F(H_1) \qquad \text{(F15)}$$

where H_1 is defined as $H_1 = \dfrac{\delta - \delta^*}{\theta}$ (F16)

Using Equation F16, Equation F15 can be written as

$$\frac{d}{dx}(u_e \theta H_1) = u_e F \qquad \text{(F17)}$$

Head also assumed that H_1 was related to the shape factor H by

$$H_1 = G(H) \qquad \text{(F18)}$$

The functions of F and G were determined from experiments. A best fit to several sets of data is [F1];

$$F = 0.0306\,(H_1 - 3.0)^{-0.6169} \qquad \text{(F19)}$$

$$G = 0.8234\,(H - 1.1)^{-1.287} + 3.3 \quad \text{when } H \leq 1.6$$
$$G = 1.55001\,(H - 0.6778)^{-3.064} + 3.3 \quad \text{when } H \geq 1.6 \qquad \text{(F20)}$$

Writing the momentum integral equation as

$$\frac{d\theta}{dx}+\frac{\theta}{u_e}(H+2)\frac{du_e}{dx}=\frac{c_f}{2} \qquad \text{(F21)}$$

we see there are three unknowns; θ, H and c_f for a given external velocity distribution. Equation F17, with F, H, and G defined by Equations F18-F20, provides a relationship between θ and H. A further equation relating c_f to θ and/or H is also needed. Head used the c_f law given by Ludwieg and Tillmann[F3];

$$c_f = 0.246 \times 10^{-0.678H} R_\theta^{-0.268} \qquad \text{(F22)}$$

$$\text{where } R_\theta = \frac{\theta u_e}{\nu}$$

The method includes two ordinary differential equations, which can be solved numerically for a specified external velocity distribution to obtain the boundary layer development.

Note, the start the calculations, initial values of two of the three quantities θ, H and c_f must be specified, the third following from Equation F22.

From this method the shape factor, H, can be used as the criterion for separation. Equation F22 predicts $c_f=0$ as H tends to infinity. An exact value of H corresponding to separation cannot be specified, but a range between 1.8 and 2.4 is commonly quoted [F1]. The difference between the lower and upper limits of H makes only little difference in locating the separation point, since close to separation dH/dx is large.

F.3 FLOW CHART OF PANEL CODE - Blayer.f INTERACTION PROCESS

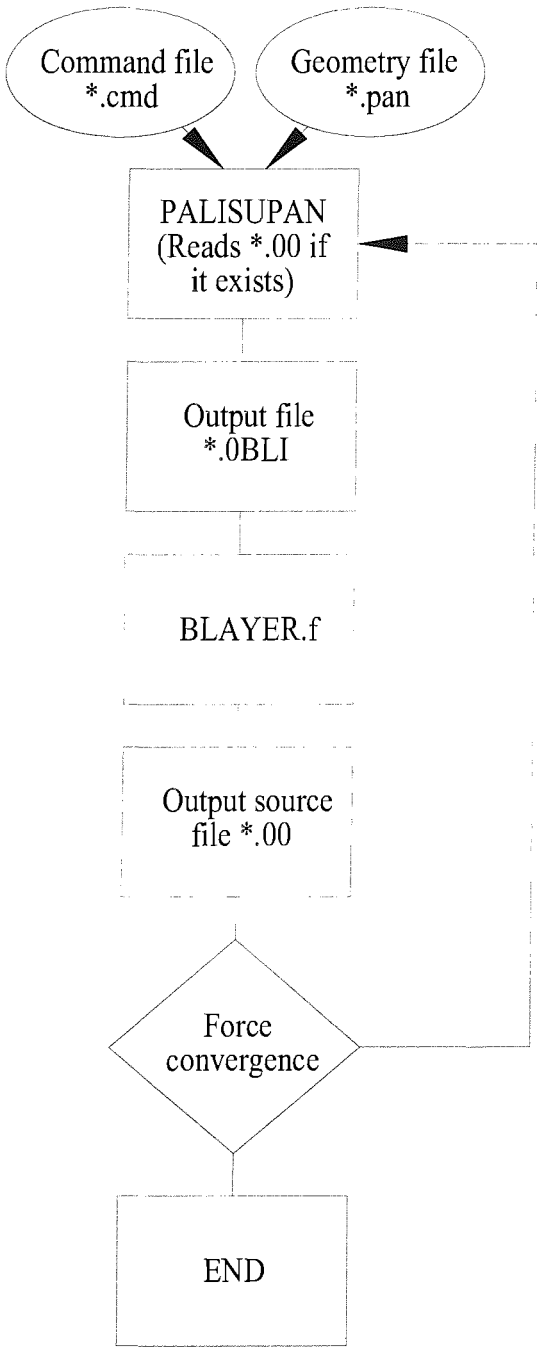

F.4 FLOW CHART OF Blayer.f PROGRAM STRUCTURE

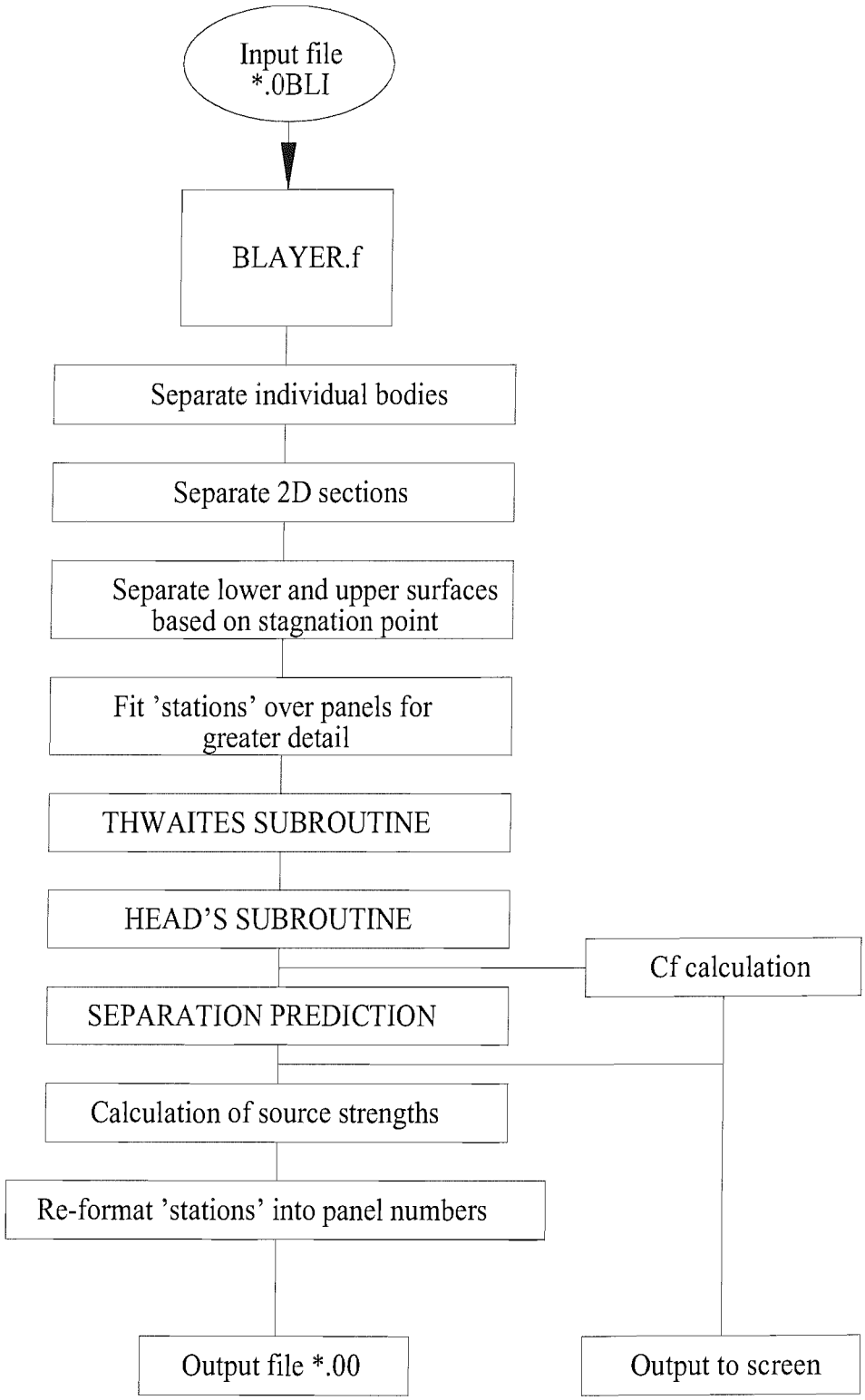

F.5 Blayer.f PROGRAM

```
c A.W.Hughes. (30th June 1998)
c
c adam/panels/blayer/blayer4.f
c
c Latest Update = 7th Dec.1999.
c
c This program takes the output file "foil.OBLI" from Palisupan,
c calculates various parameters at panel centres and imposes a
spline
c through the points. This spline is then used to find values of the
c variables at local 'stations' rather than panel centres.
c
c Based on the calculated 'Cf' a condition for predicting
c the point of flow separation is also included.
c
c Additions now mean a value for the viscous drag, or skin friction
c can be obtained.
c
c23456
      PROGRAM BLSPLINE
      REAL X(5000,3),Y(5000,3),Z(5000,3),CP(5000,3),U(5000,3),
     $V(5000,3),W(5000,3),SPEED,AirNU,Uref,RNtrans,X2(5000),
     $Y2(5000),Z2(5000),CP2(5000),U2(5000),V2(5000),NCP(5000),
     $W2(5000),T(5000),NU(5000),NV(5000),NewT(5000),NW(5000)
      REAL NREN(5000),TOTALV(5000),L,THETA(5000),H(5000),
     $RTHETA(5000),CF(5000),DELS(5000),Q(5000),PanQ(5000),
     $WQ(5000),FileQ(5000,3),SplinT(5000),SplinU(5000),SplinV(5000),
     $SplinW(5000),SplinCP(5000),SplinX(5000),NX(5000),INND(100)
      REAL OUTD(100),INNL(100),OUTL(100)
      INTEGER BOD,NT(3),PANTOT(3),B,PAN,INNPAN(200,3),M,N,NoSECTS,
     $STAR,FIN,NSTATS,NXT,NP,I,K,SEPNODE,SEP,SEP2,SURF

c Kinematic Viscosity of air
      AirNU=0.0000142
c Transition Reynolds Number
      RNtrans=500000

      WRITE(*,*)' ------------------'
      WRITE(*,*)'      blayer4.f '
      WRITE(*,*)' ------------------'

      CALL READPANFILE(BOD,SPEED,NT,PANTOT,X,Y,Z,CP,U,V,W)

      DO 30 B=1,BOD,1
        PAN=NT(B)
        Uref=SPEED
        NoSECTS=PANTOT(B)/NT(B)

c Inner Surface of the Foil
c-------------------------
        CALL INNERPAN(B,PANTOT,PAN,U,V,W,CP,INNPAN)

c INNPAN is the nth panel around the section,
c not an actual panel number

       DO 20 I=1,NoSECTS,1

        WRITE(*,*)' '
        WRITE(*,*)' *** SECTION',I,'   SURFACE 1 (IN) ***'
        SURF=1
        N=(I-1)*PAN
        M=N+INNPAN(I,B)

         CALL REORDER(B,I,INNPAN,PAN,N,M,X,Y,Z,CP,U,V,W,NP,X2,Y2,
     $Z2,CP2,U2,V2,W2,STAR,FIN)
         CALL FINDT(U2,X2,Y2,Z2,STAR,FIN,T,L)

c To know the X value at the stations
c-----------------------------------
        CALL SPLINEPREP(STAR,FIN,T,X2,NP,NSTATS,SplinT,SplinX,NewT)
        CALL SPLINE(NSTATS,NP,SplinT,SplinX,NewT,NX)
c-----------------------------------

         CALL SPLINEPREP(STAR,FIN,T,U2,NP,NSTATS,SplinT,SplinU,NewT)
         CALL SPLINE(NSTATS,NP,SplinT,SplinU,NewT,NU)
         CALL SPLINEPREP(STAR,FIN,T,V2,NP,NSTATS,SplinT,SplinV,NewT)
         CALL SPLINE(NSTATS,NP,SplinT,SplinV,NewT,NV)
         CALL SPLINEPREP(STAR,FIN,T,W2,NP,NSTATS,SplinT,SplinW,NewT)
         CALL SPLINE(NSTATS,NP,SplinT,SplinW,NewT,NW)
         CALL SPLINEPREP(STAR,FIN,T,CP2,NP,NSTATS,SplinT,SplinCP,NewT)
         CALL SPLINE(NSTATS,NP,SplinT,SplinCP,NewT,NCP)
         CALL REYNOLDS(AirNU,NSTATS,NewT,NU,NV,NW,TOTALV,NREN)
         CALL TRANSITION(NX,NSTATS,RNtrans,NREN,NXT)
         CALL THWAITES(NSTATS,AirNU,Uref,TOTALV,L,NewT,NREN,NXT,THETA,
     $H,RTHETA,CF,DELS)
         CALL
HEADS(I,NX,NSTATS,L,NXT,NewT,CF,THETA,H,RTHETA,TOTALV,DELS)
         CALL SEPARATION(NX,NSTATS,CF,H,SEP,SEP2)
         CALL
SECDRAG(I,SURF,NX,Uref,L,SEP,SEP2,THETA,NSTATS,INND,OUTD,
     $INNL,OUTL)
         CALL SOURCE(I,SEP,SEP2,NSTATS,L,NewT,TOTALV,DELS,Q)
         CALL PANELBACK(I,STAR,FIN,NSTATS,NewT,Q,T,PanQ)
         CALL ORDERAGAIN(STAR,FIN,PanQ,WQ)

         DO 40 K=STAR,FIN,1
           FileQ(K,B)=WQ(K)
```

```
c       WRITE(*,*)'FileQ ',K,' =',FileQ(K,B)
40      CONTINUE

c Outer Surface of the Foil
c-------------------------

        STAR=M
        FIN=N+PAN
c       WRITE(*,*)'Outer STAR=',STAR,' FIN=',FIN
        WRITE(*,*)' '
        WRITE(*,*)' *** SECTION',I,'   SURFACE 2 (OUT) ***'
        SURF=0

c For when there is more than one body in foil.OBLI
c-------------------------------------------------
      DO 100 INT=(M),FIN,1
        X2(INT)=X(INT,B)
        Y2(INT)=Y(INT,B)
        Z2(INT)=Z(INT,B)
        CP2(INT)=CP(INT,B)
        U2(INT)=U(INT,B)
        V2(INT)=V(INT,B)
        W2(INT)=W(INT,B)
c
        WRITE(*,15)INT,X2(INT),Y2(INT),Z2(INT),CP2(INT),U2(INT),V2(IN
T),
c     $W2(INT)
c15     FORMAT(I3,F8.4,F8.4,F8.4,F8.4,F8.4,F8.4,F8.4)
100     CONTINUE
c-------------------------------------------------

        CALL FINDT(U2,X2,Y2,Z2,STAR,FIN,T,L)
        CALL SPLINEPREP(STAR,FIN,T,X2,NP,NSTATS,SplinT,SplinX,NewT)
        CALL SPLINE(NSTATS,NP,SplinT,SplinX,NewT,NX)
        CALL SPLINEPREP(STAR,FIN,T,U2,NP,NSTATS,SplinT,SplinU,NewT)
        CALL SPLINE(NSTATS,NP,SplinT,SplinU,NewT,NU)
        CALL SPLINEPREP(STAR,FIN,T,V2,NP,NSTATS,SplinT,SplinV,NewT)
        CALL SPLINE(NSTATS,NP,SplinT,SplinV,NewT,NV)
        CALL SPLINEPREP(STAR,FIN,T,W2,NP,NSTATS,SplinT,SplinW,NewT)
        CALL SPLINE(NSTATS,NP,SplinT,SplinW,NewT,NW)
        CALL SPLINEPREP(STAR,FIN,T,CP2,NP,NSTATS,SplinT,SplinCP,NewT)
        CALL SPLINE(NSTATS,NP,SplinT,SplinCP,NewT,NCP)
        CALL REYNOLDS(AirNU,NSTATS,NewT,NU,NV,NW,TOTALV,NREN)
        CALL TRANSITION(NX,NSTATS,RNtrans,NREN,NXT)
        CALL THWAITES(NSTATS,AirNU,Uref,TOTALV,L,NewT,NREN,NXT,THETA,
     $H,RTHETA,CF,DELS)
        CALL
HEADS(I,NX,NSTATS,L,NXT,NewT,CF,THETA,H,RTHETA,TOTALV,DELS)
        CALL SEPARATION(NX,NSTATS,CF,H,SEP,SEP2)
        CALL
SECDRAG(I,SURF,NX,Uref,L,SEP,SEP2,THETA,NSTATS,INND,OUTD,
     $INNL,OUTL)
        CALL SOURCE(I,SEP,SEP2,NSTATS,L,NewT,TOTALV,DELS,Q)
        CALL PANELBACK(I,STAR,FIN,NSTATS,NewT,Q,T,PanQ)

        DO 50 K=STAR,FIN,1
          FileQ(K,B)=PanQ(K)
c       WRITE(*,*)'FileQ ',K,' =',FileQ(K,B)
50      CONTINUE

c-------------------------

20      CONTINUE
30    CONTINUE

      CALL TOTALDRAG(I,SURF,Uref,INND,OUTD,INNL,OUTL,NoSECTS)
      CALL WRITEFILE(BOD,PANTOT,FileQ)

      WRITE(*,*)'---------------------'
      WRITE(*,*)'  blayer4.f Finished'
      WRITE(*,*)'---------------------'

      STOP
      END

c---------------------------------------------------------------------
c SUBROUTINE READPANFILE reads the data output from Palisupan given
c in file "foil.OBLI".
c---------------------------------------------------------------------
      SUBROUTINE READPANFILE(BOD,SPEED,NT,PANTOT,X,Y,Z,CP,U,V,W)
      REAL ONE(5000,3),TWO(5000,3),THREE(5000,3),FOUR(5000,3),
     $X(5000,3),Y(5000,3),Z(5000,3),Q(5000,3),CP(5000,3),U(5000,3),
     $V(5000,3),W(5000,3),SPEED
      INTEGER NODE(5000,3),N,PANTOT(3),NT(3),NS(3),BOD

c      WRITE(*,*)' Subroutine READPANFILE.'

      OPEN(1, FILE='foil.0BLI', STATUS='OLD')
c     For inner surface of duct.

c      WRITE(*,*)'I      X       Y       Z        Cp       U
V
c     $  W'
      READ(1,*)BOD,SPEED
      DO 10 I=1,BOD,1
       READ(1,*)NT(I),NS(I)
       PANTOT(I)=NT(I)*NS(I)
       DO 20 N=1,PANTOT(I),1
         READ(1,*)NODE(N,I),X(N,I),Y(N,I),Z(N,I),Q(N,I),CP(N,I),
```

```
     $U(N,I),V(N,I),W(N,I),ONE(N,I),TWO(N,I),THREE(N,I),FOUR(N,I)
c       WRITE(*,15)NODE(N,I),I,X(N,I),Y(N,I),Z(N,I),CP(N,I),U(N,I),
c     $V(N,I),W(N,I)
c15     FORMAT(I4,I3,F8.4,F8.4,F8.4,F8.4,F8.4,F8.4,F8.4)
20     CONTINUE
10     CONTINUE
       CLOSE(1)

       RETURN
       END

c-----------------------------------------------------------------
--
c SUBROUTINE INNERPAN reads the data from Readpanfile and calculates
c       the nearest panel to the stagnation point at the leading edge
c       - hence the number of panels defining the inner surface, P,
c       is known for each section.
c-----------------------------------------------------------------
--
       SUBROUTINE INNERPAN(B,PANTOT,PAN,U,V,W,CP,INNPAN)
       REAL
U(5000,3),V(5000,3),W(5000,3),VEL(5000,3),STAGV,CP(5000,3),
     $STAGCP
       INTEGER NoSECTS,PANTOT(3),I,J,K,STAG,INNPAN(200,3),B,PAN

c       WRITE(*,*)' Subroutine INNERPAN'

c Using Cp values to find stagnation point
c---------------------------------------
       NoSECTS=PANTOT(B)/PAN
       DO 200 I=1,NoSECTS,1
c Integers to help define panel numbers around each section.
        L=I*PAN
        K=(L+1)-PAN
        STAGCP=CP((K+3),B)
        STAG=(K+3)
        DO 175 J=(K+4),(L-1),1
          IF (CP(J,B).GE.CP((J-1),B)) THEN
           IF (CP(J,B).GE.CP((J+1),B)) THEN
            IF (CP(J,B).GT.STAGCP) THEN
              STAGCP=CP(J,B)
               STAG=J
            ENDIF
           ENDIF
          ENDIF
175     CONTINUE
        INNPAN(I,B)=STAG-(K-1)
        WRITE(*,*)'Start=',K,' Fin=',L,' Cp STAG=',STAG,' P',I,'=',
     $INNPAN(I,B)
200    CONTINUE
```

```
c---------------------------------------


c The value (K+3) has been used above because otherwise the program
c would assume the panel with the highest pressure to be at the
c trailing edge - a result from the potential flow solver. The
integer
c K is measured from the trailing edge.
c The GE conditions are used rather than GT conditions to take
account
c of modelling a symmetrical foil with an even number of Nt panels
at
c zero degrees angle of attack (i.e. the two LE panels would have
the
c same pressures).

       RETURN
       END

c-----------------------------------------------------------------
--
c SUBROUTINE REORDER takes the log file data for the inner surface
of
c       the duct sections, which is defined from the trailing edge to
c       leading edge and re-orders it to read from the leading edge
to
c       the trailing edge - as required for the following
subroutines.
c-----------------------------------------------------------------
--
       SUBROUTINE
REORDER(B,CONT,P,PAN,N,M,X,Y,Z,CP,U,V,W,NP,X2,Y2,Z2,
     $CP2,U2,V2,W2,STAR,FIN)
       REAL X(5000,3),Y(5000,3),Z(5000,3),CP(5000,3),U(5000,3),
     $X2(5000),Y2(5000),Z2(5000),CP2(5000),U2(5000)
       REAL V(5000,3),W(5000,3),V2(5000),W2(5000)
       INTEGER B,P,PAN,NP,N,M,INT,STAR,FIN,CONT,K

c       WRITE(*,*)' Subroutine REORDER'

c       WRITE(*,*)'Node    X        Z       U        W'
c       DO I=1,P,1
c        WRITE(*,11)I,B,X(I,B),Z(I,B),U(I,B),W(I,B)
c11     FORMAT(I3,I3,F8.4,F8.4,F8.4,F8.4)
c       ENDDO
       NP=P
       STAR=N+1
       FIN=M
c        WRITE(*,*)'STAR=',STAR,' FIN=',FIN
c        WRITE(*,*)'CONT=',CONT
```

```
c      WRITE(*,*)'INT     X     Y     Z     Cp     U     V     W'
       DO 10 I=(N+1),M,1
c       WRITE(*,*)'U',I,'=',U(I,B)
        K=I-(PAN*(CONT-1))
        INT=ABS(K-(M+1))
        X2(INT)=X(I,B)
        Y2(INT)=Y(I,B)
        Z2(INT)=Z(I,B)
        CP2(INT)=CP(I,B)
        U2(INT)=U(I,B)
        V2(INT)=V(I,B)
        W2(INT)=W(I,B)
c
        WRITE(*,5)INT,X2(INT),Y2(INT),Z2(INT),CP2(INT),U2(INT),V2(INT
),
c      $W2(INT)
c5      FORMAT(I3,F8.4,F8.4,F8.4,F8.4,F8.4,F8.4,F8.4)
10     CONTINUE

       RETURN
       END

c-----------------------------------------------------------------------
--
c SUBROUTINE FINDT calculates the straight line distance along the
c panels and non-dimensions them with respect to the farthest panel
c distance.
c-----------------------------------------------------------------------
--
       SUBROUTINE FINDT(U2,X2,Y2,Z2,STAR,FIN,T,L)
       REAL X2(5000),Y2(5000),Z2(5000),INC,LENGTH(5000),T(5000),L,
      $U2(5000)
       INTEGER STAR,FIN,I

c       WRITE(*,*)' Subroutine FINDT'

       LENGTH(STAR)=0.0
       T(STAR)=LENGTH(STAR)
       DO 100 I=(STAR+1),FIN,1
         INC=((X2(I)-X2(I-1))**2)+((Y2(I)-Y2(I-1))**2)+((Z2(I)-
      $Z2(I-1))**2)
       LENGTH(I)=LENGTH(I-1)+SQRT(INC)
       T(I)=LENGTH(I)
c       WRITE(*,*)I,' X=',X2(I),' Y=',Y2(I),' Z=',Z2(I)
100    CONTINUE
       L=T(FIN)

c       WRITE(*,*)' T1=',T(STAR),' U=',U2(STAR)
c       WRITE(*,*)' T2=',T(STAR+1),' U=',U2(STAR+1)
c       WRITE(*,*)' T3=',T(STAR+2),' U=',U2(STAR+2)

c Normalising T
c--------------

       IF (T(FIN).GT.0.0) THEN
         DO 110 I=STAR,FIN,1
           T(I)=T(I)/T(FIN)
110      CONTINUE
         T(FIN)=1.0
       ENDIF

c       DO 120 I=STAR,FIN,1
c        WRITE(*,*)'T',I,' = ',T(I)
c120    CONTINUE

       RETURN
       END

c-----------------------------------------------------------------------
--
c SUBROUTINE SPLINEPREP Prepares some data necessary for the spline
c subroutines to process.
c NSTATS = Number of points (stations) for the new values.
c NP = Number of points defining the old values.
c OldT = Old distance values.
c OldS = Old variable values.
c NewT = New distance values.
c-----------------------------------------------------------------------
--
       SUBROUTINE SPLINEPREP(STAR,FIN,OldT,OldS,NP,NSTATS,SplinT,
      $SplinS,NewT)
       REAL OldT(5000),OldS(5000),NewT(5000),DT,Splint(5000),
      $SPlinS(5000)
       INTEGER STAR,FIN,NP,OFFSET,NSTATS,I,J

c       WRITE(*,*)' Subroutine SPLINEPREP'

c Converting values from Star to Fin into 1 to NP
c------------------------------------------------
       NP=(FIN+1)-STAR
       OFFSET=STAR-1.0
       DO 100 I=STAR,FIN,1
         J=I-OFFSET
         SplinS(J)=OldS(I)
         SplinT(J)=OldT(I)
c        WRITE(*,*)I,' OldT=',OldT(I),' OldS=',OldS(I)
100    CONTINUE

c Number of new points (= No.of stations over each surface)
c----------------------
```

```
      NSTATS=200
      DT=1.0/(NSTATS-1)
      DO 200 I=1,NSTATS,1
        NewT(I)=DT*(I-1)
200   CONTINUE

c       WRITE(*,*)'NewT 1=',NewT(1)
c       WRITE(*,*)'NewT 2=',NewT(2)
c       WRITE(*,*)'NewT 3=',NewT(3)

      RETURN
      END

c-----------------------------------------------------------------------
--
c-----------------------------------------------------------------------
--
c SUBROUTINE SPLINE places a spline between the points. Along with
c Subroutine Newvalue, it can be used to find new values of the
c variables between the given points.
c Subroutine Station and Subroutine Newvalue are called from within
c this subroutine. The three subroutines produce new values of the
c variable along the spline.
c NSTATS = Number of points defining for the new values.
c NP = Number of points defining the old values.
c OldT = Old distance values.
c OldS = Old variable values.
c NewT = New distance values.
c NewS = New variable values.
c-----------------------------------------------------------------------
--
      SUBROUTINE SPLINE(NSTATS,NP,OldT,OldS,NewT,NewS)
      REAL OldT(5000),OldS(5000),S2(5000),DUM(5000),SIG,P,THI(5000),
     $TLO(5000),SHI(5000),SLO(5000),S2HI(5000),S2LO(5000),NewT(5000),
     $NewS(5000)
      INTEGER I,J,NP,NSTATS

c       WRITE(*,*)' Subroutine SPLINE'

       IF (OldT(NP).GT.0.0) THEN
         S2(1)=0.0
         DUM(1)=0.0
         DO 120 I=(2),(NP-1),1
           SIG=(OldT(I)-OldT(I-1))/(OldT(I+1)-OldT(I-1))
           P=(SIG*S2(I-1))+2.0
           S2(I)=(SIG-1.0)/P
           DUM(I)=((6.0*((((OldS(I+1)-OldS(I))/(OldT(I+1)-OldT(I)))-
     $((OldS(I)-OldS(I-1))/(OldT(I)-OldT(I-1))))/(OldT(I+1)-
     $OldT(I-1))))-(SIG*DUM(I-1)))/P
c         WRITE(*,*)'DUM',I,' = ',DUM(I)
120    CONTINUE

       DUM(NP)=0.0
       S2(NP)=0.0

       DO 130 I=1,(NP-2),1
         J=(NP-1)-I
         S2(J)=(S2(J)*S2(J+1))+DUM(J)
130    CONTINUE

      ELSE

       DO 140 I=1,NP,1
         S2(I)=0.0
140    CONTINUE

      ENDIF

      CALL STATION(NSTATS,NewT,OldT,OldS,S2,NP,THI,TLO,SHI,SLO,S2HI,
     $S2LO)
      CALL NEWVALUE(NSTATS,NewT,THI,TLO,OldS,SHI,SLO,S2HI,S2LO,NewS)

c       WRITE(*,*)'NSTATS =',NSTATS
c      WRITE(*,*)'I     NewT     NewS'
c      DO 150 I=1,NSTATS,1
c       WRITE(*,149)I,NewT(I),NewS(I)
c149   FORMAT(I3,F8.4,F8.4)
c150   CONTINUE

      RETURN
      END

c-----------------------------------------------------------------------
--
c SUBROUTINE STATION calculates the normalised distance position of
c a set number of Stations. It records the higher and lower values
c of T, S, S2 which lie at the Panel positions either side of the
c station position.
c-----------------------------------------------------------------------
--
      SUBROUTINE STATION(NSTATS,NewT,OldT,OldS,S2,NP,THI,TLO,SHI,
     $SLO,S2HI,S2LO)
      REAL OldT(5000),OldS(5000),S2(5000),THI(5000),TLO(5000),
     $SHI(5000),SLO(5000),S2HI(5000),S2LO(5000),NewT(5000)
      INTEGER I,NP,NSTATS

c       WRITE(*,*)' Subroutine STATION'

c       WRITE(*,*)'NP= ',NP,' NSTATS= ',NSTATS,' DT= ',DT
```

```
      DO 220 I=1,NSTATS,1
        DO 210 J=1,NP,1
          TOL=ABS(NewT(I)-OldT(J))
          IF (TOL.LT.0.00001) THEN
            THI(I)=OldT(J)
            TLO(I)=OldT(J)
            SHI(I)=OldS(J)
            SLO(I)=OldS(J)
            S2HI(I)=S2(J)
            S2LO(I)=S2(J)
          ELSE
            IF (NewT(I).LT.OldT(J)) THEN
            IF (NewT(I).GT.OldT(J-1)) THEN
             THI(I)=OldT(J)
             TLO(I)=OldT(J-1)
             SHI(I)=OldS(J)
             SLO(I)=OldS(J-1)
             S2HI(I)=S2(J)
             S2LO(I)=S2(J-1)
            ENDIF
            ENDIF
          ENDIF
210     CONTINUE
220   CONTINUE

      RETURN
      END

c-----------------------------------------------------------------------
--
c SUBROUTINE NEWVALUE calculates the values of the variables at the
c Station positions rather than at the Panel positions using
c natural cubic splines.
c-----------------------------------------------------------------------
--
      SUBROUTINE
NEWVALUE(NSTATS,NewT,THI,TLO,OldS,SHI,SLO,S2HI,S2LO,
     $NewS)
      REAL NewT(5000),THI(5000),TLO(5000),OldS(5000),SHI(5000),
     $SLO(5000),S2HI(5000),S2LO(5000),H,A,B,NewS(5000)
      INTEGER NSTATS,I

c      WRITE(*,*)' Subroutine NEWVALUE'

c      WRITE(*,*)'NSTATS = ',NSTATS
c      WRITE(*,*)'I      NewT       THI     TLO      SHI       SLO
S2HI
c     $  S2LO'
c      DO 290 I=1,NSTATS,1
c       WRITE(*,280)I,NewT(I),THI(I),TLO(I),SHI(I),SLO(I),S2HI(I),
c     $S2LO(I)
c280    FORMAT(I3,F8.4,F8.4,F8.4,F8.3,F8.3,F10.3,F10.3)
c290   CONTINUE

      DO 300 I=1,NSTATS,1
        H=THI(I)-TLO(I)
        IF (H.EQ.0.0) THEN
          NewS(I)=SLO(I)
        ELSE
          A=(THI(I)-NewT(I))/H
          B=(NewT(I)-TLO(I))/H
          NewS(I)=((A*SLO(I))+(B*SHI(I)))+(((((A**3)-A)*S2LO(I))+
     $(((B**3)-B)*S2HI(I)))*((H**2)/6))
        ENDIF
300   CONTINUE

      RETURN
      END

c-----------------------------------------------------------------------
--
c-----------------------------------------------------------------------
--
c-----------------------------------------------------------------------
--
c SUBROUTINE REYNOLDS calculates the Reynolds Number at each station
c point based on the station distance NT and the total velocity.
c-----------------------------------------------------------------------
--
      SUBROUTINE REYNOLDS(AirNU,NSTATS,NT,NU,NV,NW,TOTALV,NREN)
      REAL NT(5000),NU(5000),NV(5000),NW(5000),TOTALV(5000),AirNU,
     $NREN(5000)
      INTEGER NSTATS,I

c      WRITE(*,*)' Subroutine REYNOLDS'

      DO 400 I=1,NSTATS,1
        TOTALV(I)=SQRT((NU(I)**2)+(NV(I)**2)+(NW(I)**2))
        NREN(I)=(TOTALV(I)*NT(I))/AirNU
400   CONTINUE
c      WRITE(*,*)'Spline 1 NT= ',NT(1),' Totvel= ',TOTALV(1)
c      WRITE(*,*)'Spline 2 NT= ',NT(2),' Totvel= ',TOTALV(2)
c      WRITE(*,*)'Spline 3 NT= ',NT(3),' Totvel= ',TOTALV(3)


c      WRITE(*,*)'I      NT      NREN'
c      DO 410 I=1,NSTATS,1
c       WRITE(*,405)I,NT(I),NREN(I)
c405    FORMAT(I3,F8.4,F13.3)
```

```
c410   CONTINUE


      RETURN
      END

c-----------------------------------------------------------------------
--
C SUBROUTINE TRANSITION calculates the node at which the boundary
c layer changes from laminar to turbulent - based on a specified
c Reynolds number.
c-----------------------------------------------------------------------
--
      SUBROUTINE TRANSITION(NX,NSTATS,RNtrans,NREN,NXT)
      REAL RNtrans,NREN(5000),NX(5000)
      INTEGER NSTATS,I,NXT

c      WRITE(*,*)' Subroutine TRANSITION'

      DO 450 I=2,NSTATS,1
        IF (NREN(I-1).LT.RNtrans) THEN
        IF (NREN(I).GT.RNtrans) THEN
         NXT=(I-1)
        ELSE
         NXT=NSTATS
        ENDIF
        ENDIF
450   CONTINUE

      WRITE(*,*)' Trans node, NXT= ',NXT,' X=',NX(NXT)

      RETURN
      END


c-----------------------------------------------------------------------
--
c SUBROUTINE THWAITES calculates the solution of a laminar boundary
c       layer using the method proposed by Thwaites.
c       The Trapezoidal Rule is used to find
c       the value of the integral.
c THETA = Momentum thickness
c DELS = Displacement thickness
c-----------------------------------------------------------------------
--
      SUBROUTINE THWAITES(NSTATS,AirNU,Uref,UE,L,NT,RN,NXT,THETA,H,
     $RTHETA,CF,DELS)
      REAL L,RL,Uref,AirNU,UE(5000),NDUE(5000),NT(5000),DUEDS(5000),
     $DT,F1,F2,URSUM(5000),CONST(5000),TLR(5000),THETA(5000)
      REAL
 RS(5000),RN(5000),LAMDA(5000),H(5000),CL(5000),DELS(5000),
     $T(5000),CF(5000),ENDADD(5000),RTHETA(5000),RAD
      INTEGER I,J,NSTATS

c      WRITE(*,*)' Subroutine THWAITES'

      DT=1.0/(NSTATS-1)

c      WRITE(*,*)' Uref = ',Uref
c      WRITE(*,*)'AirNU=',AirNU
c      WRITE(*,*)'L=',L

      RL=(Uref*L)/AirNU
      DO 40 I=1,NSTATS,1
        NDUE(I)=UE(I)/Uref
40    CONTINUE

      DUEDS(1)=((NDUE(2))-NDUE(1))/NT(2)
c      WRITE(*,*)'DUEDS(1)=',DUEDS(1)
      TLR(1)=0.056/DUEDS(1)
c      WRITE(*,*)'UE 1=',UE(1),' UE 2=',UE(2)
c      WRITE(*,*)'TLR 1=',TLR(1)

      F1=0.0
      URSUM(1)=0.0
      DO 45 I=(2),NXT,1
        F2=NDUE(I)**5
        URSUM(I)=URSUM(I-1)+((0.5*(F1+F2))*(NT(I)-NT(I-1)))
        DUEDS(I)=(NDUE(I+1)-NDUE(I-1))/(NT(I+1)-NT(I-1))
        IF (NXT.EQ.NSTATS) THEN
          DUEDS(NXT)=(NDUE(NXT)-NDUE(NXT-1))/(NT(NXT)-NT(NXT-1))
        ENDIF
        CONST(I)=0.45/(F2*NDUE(I))
        ENDADD(I)=TLR(1)*((NDUE(1)/NDUE(I))**6)
        TLR(I)=(CONST(I)*URSUM(I))+ENDADD(I)
c       TLR(I)=CONST(I)*URSUM(I)
        F1=F2
c         WRITE(*,*)'TLR',I,'=',TLR(I),'  DUEDS',I,'=',DUEDS(I)
45    CONTINUE

      DO 50 I=1,NXT,1
        THETA(I)=SQRT(TLR(I)/RL)*L
        RTHETA(I)=(THETA(I)*NDUE(I)/AirNU)*Uref
        RS(I)=(NDUE(I)*NT(I)/AirNU)*Uref*L
c       LAMDA(I)=TLR(I)*DUEDS(I)
        LAMDA(I)=((THETA(I)**2)/AirNU)*DUEDS(I)

        IF (LAMDA(I).LT.0.0) THEN
          H(I)=(0.0731/(0.14+LAMDA(I)))+2.088

CL(I)=0.22+(1.402*LAMDA(I))+(0.018*LAMDA(I))/(LAMDA(I)+0.107)
```

```
        ENDIF

        IF (LAMDA(I).GT.0.0) THEN
          H(I)=2.61-(3.75*LAMDA(I))+(5.24*(LAMDA(I)**2))
          CL(I)=0.22+(1.57*LAMDA(I))-(1.8*(LAMDA(I)**2))
        ENDIF

        DELS(I)=THETA(I)*H(I)
c       WRITE(*,*)'Lamda',I,'=',LAMDA(I),'  H',I,'=',H(I),'
CL',I,'=',CL(I)

50     CONTINUE

          DO 52 J=1,NXT,1
c           CF(J)=2.0*CL(J)/(NDUE(J)*(THETA(J)/L)*RL)
            CF(J)=(2.0*AirNU*CL(J))/(UE(J)*THETA(J))
52        CONTINUE

       DO 55 I=1,NSTATS,1
         UE(I)=NDUE(I)*Uref
         T(I)=NT(I)*L
55     CONTINUE


c Short section to calculate BL thickness' at Stagnation
c point - based on HIEMENZ equations (Cebeci & Bradshaw).
c-------------------------------------------------------
c Setting nose radius (for initial trials on naca2415)
       RAD=0.0248
       THETA(1)=0.29234*(SQRT((RAD*AirNU)/(2.0*Uref)))
       DELS(1)=0.64791*(SQRT((RAD*AirNU)/(2.0*Uref)))
C-------------------------------------------------------

c       WRITE(*,*)'  '
c       WRITE(*,*)' APPROXIMATE SOLUTION FOR A LAMINAR BOUNDARY
LAYER'
c       WRITE(*,*)' USING THWAITES METHOD IS AS FOLLOWS.'
c       WRITE(*,*)'  '
c       WRITE(*,*)' Transition node= ',NXT
c       WRITE(*,*)'  '
c       WRITE(*,*)'Node  T       Ue       Dels     Theta       H       Cf
c      $ Rtheta      Rn'
c       DO 65 I=1,NSTATS,1
c
        WRITE(*,60)I,T(I),UE(I),DELS(I),THETA(I),H(I),CF(I),RTHETA(I)
,
c      $RN(I)
c60     FORMAT(I2,F8.4,F9.4,F9.6,F9.6,F8.4,F8.4,F10.4,F11.2)
c65     CONTINUE

        RETURN
        END

c-------------------------------------------------------------------
-----
c SUBROUTINE HEADS calculates the solution of the turbulent boundary
c       layer using a method proposed by Head. The initial values are
c       taken from the final values (at the transition point) found
c       by using Thwaites method.
c THETA = Momentum thickness
c DELS = Displacement thickness
c DEL = Boundary layer thickness (Usually @ U=0.99*Uref)
c-------------------------------------------------------------------
-----
        SUBROUTINE HEADS(SECT,NX,NSTATS,L,NXT,NT,CF,THETA,H,RTHETA,UE,
      $DELS)
        REAL THETA(5000),H(5000),RTHETA(5000),UE(5000),DT,NX(5000),
      $DUDS(5000),NU,HS(5000),NT(5000),T(5000),L,F(5000),CF(5000)
        REAL USS(5000),DELS(5000),DEL(5000),DUSDS(5000),DTDS(5000)
        INTEGER NSTATS,NXT,I,SECT

c       WRITE(*,*)' Subroutine HEADS'

        DO I=1,NSTATS,1
         T(I)=NT(I)*L
        ENDDO
        DT=ABS(T(2)-T(1))

c        WRITE(*,*)' NXT= ',NXT,' L= ',L,' DT= ',DT
c        WRITE(*,*)'I       T        UE     THETA      H        RTHETA
c       $ CF'
c         DO 10 I=1,NSTATS,1
c        WRITE(*,15)I,T(I),UE(I),THETA(I),H(I),RTHETA(I),CF(I)
c15       FORMAT(I3,F8.4,F8.4,F10.6,F8.4,F10.2,F8.4)
c10      CONTINUE

        NU=(UE(NXT)*THETA(NXT))/RTHETA(NXT)
c        WRITE(*,*)'NU= ',NU

        DO 72 I=NXT,(NSTATS-1),1
          DUDS(I)=(UE(I+1)-UE(I-1))/(T(I+1)-T(I-1))
c         WRITE(*,*)'DUDS',I,'= ',DUDS(I)
72      CONTINUE
c         DUDS(NSTATS)=(UE(NSTATS)-UE(NSTATS-1))/(T(NSTATS)-T(NSTATS-
1))
        DUDS(NSTATS)=(1.0/DT)*((0.5*UE(NSTATS-2))-(2*UE(NSTATS-1))+
      $(1.5*UE(NSTATS)))
c         WRITE(*,*)'DUDS',NSTATS,' =',DUDS(NSTATS)

        IF(H(NXT).GE.1.6) THEN
```

```
        HS(NXT)=(1.5501*((H(NXT)-0.6778)**-3.064))+3.3
      ENDIF
      IF(H(NXT).LE.1.6) THEN
        HS(NXT)=(0.8234*((H(NXT)-1.1)**-1.287))+3.3
      ENDIF

      DO 80 I=NXT,(NSTATS-1),1
c       WRITE(*,*)'DUDS',I,' =',DUDS(I)

        F(I)=0.0306*((ABS(HS(I)-3.0))**(-0.6169))
        DTDS(I)=(CF(I)/2.0)-((H(I)+2.0)*DUDS(I)*(THETA(I)/UE(I)))
        DUSDS(I)=F(I)*UE(I)
        USS(I)=HS(I)*UE(I)*THETA(I)
        THETA(I+1)=THETA(I)+(DTDS(I)*((T(I+1)-T(I))))
        USS(I+1)=USS(I)+(DUSDS(I)*((T(I+1)-T(I))))
        HS(I+1)=USS(I+1)/(THETA(I+1)*UE(I+1))
        H(I+1)=(((ABS(HS(I+1)-3.3))/0.8234)**(-0.777))+1.1
        RTHETA(I+1)=(THETA(I+1)*UE(I+1))/NU
        CF(I+1)=(0.246/(10**(0.678*H(I+1))))/(RTHETA(I+1)**(0.268))

c Making sure method doesn't 'blow up' after separation.
c-------------------------------------------------------
        IF (CF(I).LT.0.0001) THEN
          CF(I+1)=0.0
        ENDIF
c-------------------------------------------------------

80     CONTINUE

c       DO I=(NXT+1),NSTATS,1
c        DELS(I)=THETA(I)*(H(I)+1.0)
c       ENDDO

        DO 100 I=1,NSTATS,1
          DELS(I)=THETA(I)*(H(I))
          DEL(I)=(THETA(I)*HS(I))+DELS(I)
100      CONTINUE

       IF (SECT.EQ.1) THEN
       WRITE(*,*)'Node    NX      Ue      Dels     Theta     H       Cf
Rtheta
      $         HS       DEL'
        DO 90 I=1,NSTATS,1

WRITE(*,85)I,NX(I),UE(I),DELS(I),THETA(I),H(I),CF(I),RTHETA(I),
     $HS(I),DEL(I)
85       FORMAT(I3,F8.4,F8.4,F8.5,F9.6,F7.4,F7.4,F10.3,F7.4,F9.6)
90      CONTINUE
       ENDIF

      RETURN
      END
c-----------------------------------------------------------------
------
c SUBROUTINE SEPARATION determines the point of separation based on
the
c values of Cf obtained from both Thwaites' and Head's procedures.
It has
c been assumed the flow is near enough to separation when Cf<0.0004.
c-----------------------------------------------------------------
------
      SUBROUTINE SEPARATION(NX,NSTATS,CF,H,SEP,SEP2)
      REAL NX(5000),CF(5000),H(5000)
      INTEGER NSTATS,I,SEP,SEP2

c      WRITE(*,*)' Subroutine SEPARATION.'

      SEP=0
      SEP2=0

c Separation based on Cf values
c------------------------------
      DO 100 I=1,NSTATS,1
        IF (CF(I).LE.0.0004) THEN
          SEP=I
          GOTO 150
        ENDIF
100   CONTINUE

150   IF (SEP.LT.NSTATS) THEN
        DO 200 I=(SEP+1),NSTATS,1
          IF (CF(I).LT.0.0004) THEN
            IF (CF(I-1).GE.0.0004) THEN
              SEP2=I
              GOTO 250
            ENDIF
          ENDIF
200     CONTINUE
250     ENDIF
      WRITE(*,*)' Using Cf values:'

c Alternative Separation based on H values
c----------------------------------------
c       DO 100 I=1,NSTATS,1
c        IF (H(I).GT.2.3) THEN
c          SEP=I
c          GOTO 150
c        ENDIF
c100    CONTINUE
c
```

```
c150    IF (SEP.LT.NSTATS) THEN
c        DO 200 I=(SEP+1),NSTATS,1
c          IF (H(I).GT.2.3) THEN
c           IF (H(I-1).LT.2.3) THEN
c            SEP2=I
c            GOTO 250
c           ENDIF
c          ENDIF
c200     CONTINUE
c250     ENDIF
c       WRITE(*,*)' Using H values:'

       WRITE(*,*)'    SEP= ',SEP,' X= ',NX(SEP)
       WRITE(*,*)'    SEP2= ',SEP2,' X= ',NX(SEP2)

       RETURN
       END

c-------------------------------------------------------------------
-----
c SUBROUTINE SECDRAG Performs a simple calculation of the viscous
c drag of EACH SECTION based on flat plate theory and the momentum
c thickness, THETA. See "Schlichting - 'Boundary Layer Theory' pages
115
c and 535."
c-------------------------------------------------------------------
-----
       SUBROUTINE
SECDRAG(I,SURF,NX,Uref,L,SEP,SEP2,THETA,NSTATS,INND,
     $OUTD,INNL,OUTL)
       REAL NX(5000),Uref,THETA(5000),DTDX(5000),F1,F2,RHO,L,CD(100),

$SUM(5000),AREA,TAU(5000),INND(100),OUTD(100),INNL(100),OUTL(100)
       INTEGER NSTATS,I,SURF,K,SEP2,FIN,SEP

c       WRITE(*,*)' Subroutine SECDRAG'
c       WRITE(*,*)' SECTION',I

c Density of air (~15degreesC)
       RHO=1.225

       FIN=NSTATS
       DTDX(1)=(THETA(2)-THETA(1))/(NX(2)-NX(1))
         DTDX(FIN)=(THETA(FIN)-THETA(FIN-1))/(NX(FIN)-NX(FIN-1))
       DO 100 K=2,(FIN-1),1
         DTDX(K)=(THETA(K+1)-THETA(K-1))/(NX(K+1)-NX(K-1))
100    CONTINUE

       DO 200 K=1,FIN,1
         TAU(K)=RHO*(Uref**2)*DTDX(K)
```



```
200    CONTINUE

c Simple trapezoidal integration
       F1=TAU(1)
       SUM(1)=0.0
       DO 300 K=2,FIN,1
         F2=TAU(K)
         AREA=0.5*(F1+F2)*(NX(K)-NX(K-1))
         SUM(K)=SUM(K-1)+AREA
         F1=F2
300    CONTINUE

       IF (SURF.EQ.1) THEN
         INND(I)=SUM(FIN)
         INNL(I)=L
         CD(I)=INND(I)/(0.5*1.225*(Uref**2)*1)
         WRITE(*,*)' INND= ',INND(I),' Cd= ',CD(I)
c        WRITE(*,*)' INNL= ',INNL(I)
       ENDIF
       IF (SURF.EQ.0) THEN
         OUTD(I)=SUM(FIN)
         OUTL(I)=L
         CD(I)=OUTD(I)/(0.5*1.225*(Uref**2)*1)
         WRITE(*,*)' OUTD= ',OUTD(I),' Cd= ',CD(I)
c        WRITE(*,*)' OUTL= ',OUTL(I)
       ENDIF

       RETURN
       END

c-------------------------------------------------------------------
-----
c SUBROUTINE SOURCE Calculates the source strength for each panel
and
c       creatres the output file necessary for input back into
Palisupan.
c-------------------------------------------------------------------
-----
       SUBROUTINE SOURCE(SECT,SEP,SEP2,NSTATS,L,NT,UE,DELS,Q)
       REAL
NT(5000),T(5000),UE(5000),DELS(5000),Q(5000),UDELS(5000),L
       INTEGER NODESEP,NSTATS,I,LOW,HIGH,J,K,SEP,SEP2,SECT

c        WRITE(*,*)' Subroutine SOURCE'

       DO 120 I=1,NSTATS,1
         T(I)=NT(I)*L
120    CONTINUE

       DO 200 I=1,NSTATS,1
```

```
      UDELS(I)=(UE(I)*DELS(I))
200   CONTINUE

c Making source strengths after separation equal
c those at separation. Otherwise, this blows up.
c-----------------------------------------------

      IF (SEP.GT.SEP2) THEN
       NODESEP=SEP
      ENDIF
      IF (SEP2.GT.SEP) THEN
       NODESEP=SEP2
       IF (SEP.GT.1) THEN
        NODESEP=SEP
       ENDIF
      ENDIF
      IF (SEP.EQ.SEP2) THEN
       NODESEP=SEP
      ENDIF

      Q(1)=(UDELS(2)-UDELS(1))/(T(2)-T(1))
      Q(NSTATS)=(UDELS(NSTATS)-UDELS(NSTATS-1))/(T(NSTATS)-T(NSTATS-
1))
      DO 250 I=2,(NSTATS-1),1
       Q(I)=(UDELS(I+1)-UDELS(I-1))/(T(I+1)-T(I-1))
       IF (I.GT.NODESEP) THEN
         IF (NODESEP.GT.0) THEN
          Q(I)=Q(NODESEP-1)
         ENDIF
       ENDIF
250   CONTINUE

DO 275 I=1,NSTATS,1
       Q(I)=Q(I)*(-1)
275    CONTINUE

c Checking resultant values.
c---------------------------
       IF (SECT.EQ.0) THEN
        WRITE (*,*)'I     T      UE       DELS    UDELS      Q'
        DO 350 I=1,NSTATS,1
         WRITE(*,300)I,T(I),UE(I),DELS(I),UDELS(I),Q(I)
300      FORMAT(I3,F8.4,F8.4,F8.4,F8.4,F8.4)
350     CONTINUE
       ENDIF

      RETURN
      END
```

```
c-----------------------------------------------------------------
------
c SUBROUTINE PANELBACK takes the source strength values for each
station
c point and, using the Spline subroutines, calculates the source
strength
c value for each panel point.
c-----------------------------------------------------------------
------
      SUBROUTINE PANELBACK(SECT,STAR,FIN,NSTATS,NT,Q,T,NewPanQ)
      REAL
NT(5000),Q(5000),PanT(5000),PanQ(5000),T(5000),NewPanT(5000),
     $NewPanQ(5000)
      INTEGER SECT,STAR,FIN,NSTATS,NOld,NNew,I,J,OFFSET

c      WRITE(*,*)' Subroutine PANELBACK'

c      WRITE(*,*)'STAR=',STAR,' FIN=',FIN

      NOld=NSTATS
      NNew=(FIN+1)-STAR
c      WRITE(*,*)'NOld=',NOld,' NNew=',NNew

c Converting values from Star to Fin into 1 to NP
c------------------------------------------------
      OFFSET=STAR-1
      DO 100 I=STAR,FIN,1
       J=I-OFFSET
       PanT(J)=T(I)
c      WRITE(*,*)'T',I,'=',T(I)
c      WRITE(*,*)J,' PanT=',PanT(J)
100   CONTINUE

      CALL SPLINE(NNew,NOld,NT,Q,PanT,PanQ)

c      IF (SECT.EQ.1) THEN
c       DO 150 I=1,NNew,1
c      WRITE(*,*)I,' PanT=',PanT(I),' PanQ=',PanQ(I)
c150    CONTINUE
c      ENDIF

      DO 200 I=1,NNew,1
       J=I+OFFSET
       NewPanT(J)=PanT(I)
       NewPanQ(J)=PanQ(I)
c      IF (SECT.EQ.1) THEN
c       WRITE(*,*)J,' NewPanT=',NewPanT(J),' NewPanQ=',NewPanQ(J)
c      ENDIF
200   CONTINUE
```

```
c Values for the inner surface of the section are still defined
c from LE to TE. They now need to be rearranged into the original
c order from TE to LE.

      RETURN
      END

c-----------------------------------------------------------------
------
c SUBROUTINE ORDERAGAIN reorders the values along the inner surface,
c which are from LE to TE, into the original panel code definition
which
c is from TE to LE.
c-----------------------------------------------------------------
------
      SUBROUTINE ORDERAGAIN(STAR,FIN,LT1,TL1)
      REAL LT1(5000),TL1(5000)
      INTEGER STAR,FIN,I,J,K

c      WRITE(*,*)' Subroutine ORDERAGAIN'

      DO 100 I=STAR,FIN,1
        K=I-(STAR-1)
        J=FIN-(K-1)
        TL1(J)=LT1(I)
c       WRITE(*,*)'LT1',I,'=',LT1(I),'  TL1',J,'=',TL1(J)
100   CONTINUE

      RETURN
      END
c-----------------------------------------------------------------
------
c SUBROUTINE TOTALDRAG takes the individual sectional drag values
from
c Subroutine SECDRAG and calculates the overall viscous drag (or
skin
c friction) for the entire foil. N.b. This works for FOIL-TYPE
BODIES ONLY
c at the moment, and the PANEL WIDTH is defined in this subroutine.
c-----------------------------------------------------------------
------
      SUBROUTINE TOTALDRAG(I,SURF,Uref,INND,OUTD,INNL,OUTL,NoSECTS)
      REAL
INND(100),OUTD(100),INNL(100),OUTL(100),F1,F2,SUM(100),AREA,

$DRAG,UNITD(100),SUMINNL,SUMOUTL,SUMLEN,SURFLEN(100),AVINNL,AVOUTL,
     $AVLEN,DRAGCOEF,Uref,PANWIDTH,DRAGCOF1
      INTEGER I,SURF,NoSECTS,K

c      WRITE(*,*)' Subroutine TOTALDRAG'

      PANWIDTH=0.04

      DO 100 K=1,NoSECTS,1
       UNITD(K)=INND(K)+OUTD(K)
       IF (K.EQ.1) THEN
        DRAGCOF1=UNITD(1)/(0.5*1.225*(PANWIDTH*1.0)*(Uref**2))
        WRITE(*,*)' '
        WRITE(*,*)' '
        WRITE(*,*)'*********************************************'
        WRITE(*,*)'1st Section Drag = ',UNITD(1)
        WRITE(*,*)'1st Section Drag CoefF (actual area) = ',DRAGCOF1
       ENDIF
100   CONTINUE

c Integrating of UNITDs over the sections
      F1=UNITD(1)
      SUM(1)=0.0
      DO 200 K=2,NoSECTS,1
        F2=UNITD(K)
        AREA=0.5*(F1+F2)*PANWIDTH
        SUM(K)=SUM(K-1)+AREA
        F1=F2
200   CONTINUE

c Total Viscous Drag (or skin friction)
      DRAG=SUM(NoSECTS)
      DRAGCOEF=DRAG/(0.5*1.225*0.667*(Uref**2))

c Summary of surface lengths
      SUMINNL=0.0
      SUMOUTL=0.0
      SUMLEN=0.0
      DO 300 K=1,NoSECTS,1
        SURFLEN(K)=INNL(K)+OUTL(K)
        SUMINNL=SUMINNL+INNL(K)
        SUMOUTL=SUMOUTL+OUTL(K)
        SUMLEN=SUMLEN+SURFLEN(K)
300   CONTINUE
      AVINNL=SUMINNL/NoSECTS
      AVOUTL=SUMOUTL/NoSECTS
      AVLEN=SUMLEN/NoSECTS

      WRITE(*,*)'*********************************************'
      WRITE(*,*)'*********************************************'
      WRITE(*,*)' TOTAL FOIL VISCOUS DRAG IN AIR= ',DRAG
      WRITE(*,*)' Drag coefficient (area 0.667) = ',DRAGCOEF
      WRITE(*,*)' Inner surface length (m) = ',AVINNL
      WRITE(*,*)' Outer surface length (m) = ',AVOUTL
```

```
      WRITE(*,*)' Total surface length (m) = ',AVLEN
      WRITE(*,*)' '

      RETURN
      END

c-----------------------------------------------------------------
------
c SUBROUTINE WRITEFILE writes the source strength data obtained
using the
c above program into a file ready for input back into Palisupan.
This
c file is called 'foil.00'.
c-----------------------------------------------------------------
------
      SUBROUTINE WRITEFILE(BOD,PANTOT,FileQ)
      REAL FileQ(5000,3),V,W
      INTEGER BOD,PANTOT(3),I,J,PANEL

c      WRITE(*,*)' Subroutine WRITEFILE'

      OPEN(2, FILE='foil.00',STATUS='UNKNOWN')
       V=0.0
       W=0.0
       PANEL=0
c For body number 1
         WRITE(2,10)PANTOT(1)
         DO 90 J=1,PANTOT(1),1
            WRITE(2,30)(J-1),FileQ(J,1),V,W
30          FORMAT(I4,F10.3,F5.2,F5.2)
            PANEL=PANEL+1
90       CONTINUE

c For subsequent bodies
        IF (BOD.GT.1) THEN
         DO 100 I=2,BOD,1
           WRITE(2,10)PANTOT(I)
10         FORMAT(I4)
           DO 150 J=1,PANTOT(I),1
             WRITE(2,20)(PANEL),FileQ(J,I),V,W
20           FORMAT(I4,F10.3,F5.2,F5.2)
             PANEL=PANEL+1
150        CONTINUE
100      CONTINUE
        ENDIF
       CLOSE(2)

       RETURN
       END

c-----------------------------------------------------------------
------
c END OF PROGRAM
c-----------------------------------------------------------------
------
```

REFERENCES

F1. CEBECI T, BRADSHAW P - "*Momentum Transfer in Boundary Layers.*" Published by Mcgraw-Hill.

F2. FALKNER VG, SKAN SW - "*Some Approximate Solutions of the Boundary Layer Equations.*" ARC R&M 1314, 1930. (Also see Phil.Mag. Vol.12, pp865, 1931).

F3. LUDWIEG H , TILLMANN W - "*Investigations of the Wall Shearing Stress in Turbulent Boundary Layers.*" NACA Report TM 1285, 1949.

APPENDIX G: WATERJET INTAKE DUCT GEOMETRY

Section 1

X (m)	Y (m)	Z (m)
-0.4	0.1500	0.0000
-0.4	0.1507	0.0131
-0.4	0.1527	0.0260
-0.4	0.1561	0.0386
-0.4	0.1608	0.0508
-0.4	0.1667	0.0625
-0.4	0.1738	0.0735
-0.4	0.1821	0.0836
-0.4	0.1914	0.0929
-0.4	0.2015	0.1012
-0.4	0.2125	0.1083
-0.4	0.2242	0.1142
-0.4	0.2364	0.1189
-0.4	0.2490	0.1223
-0.4	0.2619	0.1243
-0.4	0.2750	0.1250
-0.4	0.2821	0.1229
-0.4	0.2983	0.1195
-0.4	0.3198	0.1133
-0.4	0.3428	0.1034
-0.4	0.3633	0.0883
-0.4	0.3784	0.0678
-0.4	0.3883	0.0448
-0.4	0.3945	0.0233
-0.4	0.3979	0.0071
-0.4	0.4000	0.0000

Section 2

X (m)	Y (m)	Z (m)
-0.3	0.1500	0.0000
-0.3	0.1507	0.0131
-0.3	0.1527	0.0260
-0.3	0.1561	0.0386
-0.3	0.1608	0.0508
-0.3	0.1667	0.0625
-0.3	0.1738	0.0735
-0.3	0.1821	0.0836
-0.3	0.1914	0.0929
-0.3	0.2015	0.1012
-0.3	0.2125	0.1083
-0.3	0.2242	0.1142
-0.3	0.2364	0.1189
-0.3	0.2490	0.1223
-0.3	0.2619	0.1243
-0.3	0.2750	0.1250
-0.3	0.2908	0.1233
-0.3	0.3089	0.1190
-0.3	0.3281	0.1180
-0.3	0.3467	0.1017
-0.3	0.3633	0.0883
-0.3	0.3767	0.0717
-0.3	0.3868	0.0531
-0.3	0.3940	0.0339
-0.3	0.3983	0.0158
-0.3	0.4000	0.0000

Section 3

X (m)	Y (m)	Z (m)
-0.2	0.1493	0.0000
-0.2	0.1500	0.0131
-0.2	0.1521	0.0260
-0.2	0.1555	0.0386
-0.2	0.1601	0.0508
-0.2	0.1661	0.0625
-0.2	0.1732	0.0735
-0.2	0.1814	0.0836
-0.2	0.1907	0.0929
-0.2	0.2009	0.1012
-0.2	0.2119	0.1083
-0.2	0.2236	0.1142
-0.2	0.2358	0.1189
-0.2	0.2484	0.1223
-0.2	0.2614	0.1243
-0.2	0.2744	0.1250
-0.2	0.2937	0.1235
-0.2	0.3125	0.1190
-0.2	0.3305	0.1117
-0.2	0.3472	0.1018
-0.2	0.3621	0.0895
-0.2	0.3750	0.0748
-0.2	0.3854	0.0581
-0.2	0.3930	0.0399
-0.2	0.3976	0.0207
-0.2	0.3993	0.0010
-0.2	0.3994	0.0004
-0.2	0.3994	0.0000

Section 4

X (m)	Y (m)	Z (m)
-0.1	0.1351	0.0000
-0.1	0.1358	0.0131
-0.1	0.1380	0.0260
-0.1	0.1414	0.0386
-0.1	0.1462	0.0508
-0.1	0.1523	0.0625
-0.1	0.1597	0.0735
-0.1	0.1681	0.0836
-0.1	0.1776	0.0929
-0.1	0.1881	0.1012
-0.1	0.1886	0.1015
-0.1	0.1993	0.1083
-0.1	0.2113	0.1142
-0.1	0.2237	0.1189
-0.1	0.2366	0.1223
-0.1	0.2498	0.1243
-0.1	0.2631	0.1250
-0.1	0.2798	0.1242
-0.1	0.2965	0.1219
-0.1	0.3128	0.1179
-0.1	0.3285	0.1124
-0.1	0.3434	0.1052
-0.1	0.3602	0.0928
-0.1	0.3723	0.0773
-0.1	0.3805	0.0591
-0.1	0.3852	0.0388
-0.1	0.3869	0.0167
-0.1	0.3874	0.0134
-0.1	0.3878	0.0100
-0.1	0.3883	0.0067
-0.1	0.3887	0.0033
-0.1	0.3892	0.0000

Section 5

X (m)	Y (m)	Z (m)
0	0.0952	0.0000
0	0.0960	0.0131
0	0.0982	0.0260
0	0.1020	0.0386
0	0.1038	0.0434
0	0.1071	0.0508
0	0.1137	0.0625
0	0.1215	0.0735
0	0.1306	0.0836
0	0.1394	0.0917
0	0.1409	0.0929
0	0.1521	0.1012
0	0.1642	0.1089
0	0.1771	0.1142
0	0.1905	0.1189
0	0.1976	0.1208
0	0.2045	0.1223
0	0.2186	0.1243
0	0.2329	0.1250
0	0.2485	0.1250
0	0.2640	0.1248
0	0.2794	0.1244
0	0.2947	0.1236
0	0.3099	0.1224
0	0.3315	0.1156
0	0.3378	0.1117
0	0.3461	0.1037
0	0.3550	0.0876
0	0.3597	0.0677
0	0.3613	0.0444
0	0.3619	0.0355
0	0.3625	0.0266
0	0.3632	0.0177
0	0.3638	0.0088
0	0.3644	0.0000

Section 6

X (m)	Y (m)	Z (m)
0.1	0.0486	0.0000
0.1	0.0494	0.0131
0.1	0.0516	0.0260
0.1	0.0553	0.0386
0.1	0.0563	0.0411
0.1	0.0605	0.0508
0.1	0.0670	0.0625
0.1	0.0687	0.0651
0.1	0.0749	0.0735
0.1	0.0840	0.0836
0.1	0.0852	0.0848
0.1	0.0942	0.0929
0.1	0.1055	0.1012
0.1	0.1078	0.1027
0.1	0.1176	0.1083
0.1	0.1304	0.1142
0.1	0.1370	0.1167
0.1	0.1439	0.1189
0.1	0.1579	0.1223
0.1	0.1721	0.1243
0.1	0.1743	0.1245
0.1	0.1865	0.1250
0.1	0.2076	0.1250
0.1	0.2152	0.1250
0.1	0.2267	0.1250
0.1	0.2446	0.1250
0.1	0.2616	0.1250
0.1	0.2747	0.1250
0.1	0.2779	0.1250
0.1	0.2976	0.1242
0.1	0.3114	0.1183
0.1	0.3198	0.1076
0.1	0.3240	0.0927
0.1	0.3251	0.0738
0.1	0.3251	0.0591
0.1	0.3251	0.0444
0.1	0.3251	0.0296
0.1	0.3251	0.0148
0.1	0.3251	0.0000

Section 7

X (m)	Y (m)	Z (m)
0.2	0.0000	0.0000
0.2	0.0027	0.0131
0.2	0.0050	0.0260
0.2	0.0083	0.0375
0.2	0.0087	0.0386
0.2	0.0139	0.0508
0.2	0.0178	0.0582
0.2	0.0204	0.0625
0.2	0.0283	0.0735
0.2	0.0285	0.0737
0.2	0.0374	0.0836
0.2	0.0404	0.0866
0.2	0.0476	0.0929
0.2	0.0538	0.0977
0.2	0.0588	0.1012
0.2	0.0691	0.1073
0.2	0.0709	0.1083
0.2	0.0838	0.1142
0.2	0.0870	0.1155
0.2	0.0973	0.1189
0.2	0.1084	0.1217
0.2	0.1112	0.1223
0.2	0.1255	0.1243
0.2	0.1348	0.1249
0.2	0.1399	0.1250
0.2	0.1630	0.1250
0.2	0.1670	0.1250
0.2	0.1908	0.1250
0.2	0.1953	0.1250
0.2	0.2123	0.1250
0.2	0.2322	0.1250
0.2	0.2359	0.1250
0.2	0.2510	0.1250
0.2	0.2620	0.1244
0.2	0.2702	0.1214
0.2	0.2759	0.1159
0.2	0.2793	0.1081
0.2	0.2810	0.0981
0.2	0.2810	0.0785
0.2	0.2810	0.0590
0.2	0.2810	0.0394
0.2	0.2810	0.0197
0.2	0.2810	0.0000

Section 8

X (m)	Y (m)	Z (m)
0.3	0.0000	0.0921
0.3	0.0010	0.0929
0.3	0.0112	0.1005
0.3	0.0122	0.1012
0.3	0.0237	0.1080
0.3	0.0243	0.1083
0.3	0.0372	0.1142
0.3	0.0375	0.1144
0.3	0.0507	0.1189
0.3	0.0529	0.1195
0.3	0.0646	0.1223
0.3	0.0703	0.1232
0.3	0.0789	0.1243
0.3	0.0904	0.1250
0.3	0.0933	0.1250
0.3	0.1177	0.1250
0.3	0.1207	0.1250
0.3	0.1458	0.1250
0.3	0.1482	0.1250
0.3	0.1740	0.1250
0.3	0.1756	0.1250
0.3	0.2022	0.1250
0.3	0.2029	0.1250
0.3	0.2240	0.1250
0.3	0.2259	0.1242
0.3	0.2276	0.1231
0.3	0.2291	0.1218
0.3	0.2305	0.1203
0.3	0.2318	0.1186
0.3	0.2318	0.0949
0.3	0.2318	0.0712
0.3	0.2318	0.0475
0.3	0.2318	0.0237
0.3	0.2318	0.0000

Section 9

X (m)	Y (m)	Z (m)
0.4	0.0000	0.1176
0.4	0.0040	0.1189
0.4	0.0136	0.1214
0.4	0.0180	0.1223
0.4	0.0286	0.1239
0.4	0.0322	0.1243
0.4	0.0452	0.1250
0.4	0.0466	0.1250
0.4	0.0686	0.1250
0.4	0.0741	0.1250
0.4	0.1001	0.1250
0.4	0.1016	0.1250
0.4	0.1282	0.1250
0.4	0.1290	0.1250
0.4	0.1564	0.1250
0.4	0.1839	0.1250
0.4	0.1839	0.1146
0.4	0.1839	0.1048
0.4	0.1839	0.0946
0.4	0.1839	0.0845
0.4	0.1839	0.0744
0.4	0.1839	0.0595
0.4	0.1839	0.0446
0.4	0.1839	0.0298
0.4	0.1839	0.0149
0.4	0.1839	0.0000

Section 10

X (m)	Y (m)	Z (m)
0.5	0.0000	0.1250
0.5	0.0166	0.1250
0.5	0.0276	0.1250
0.5	0.0369	0.1250
0.5	0.0550	0.1250
0.5	0.0624	0.1250
0.5	0.0825	0.1250
0.5	0.0951	0.1250
0.5	0.1099	0.1250
0.5	0.1373	0.1250
0.5	0.1373	0.1000
0.5	0.1373	0.0750
0.5	0.1373	0.0500
0.5	0.1373	0.0250
0.5	0.1373	0.0000

Section 11

X (m)	Y (m)	Z (m)
0.6	0.0000	0.1250
0.6	0.0085	0.1250
0.6	0.0213	0.1250
0.6	0.0360	0.1250
0.6	0.0473	0.1250
0.6	0.0635	0.1250
0.6	0.0798	0.1250
0.6	0.0909	0.1250
0.6	0.0909	0.1000
0.6	0.0909	0.0750
0.6	0.0909	0.0500
0.6	0.0909	0.0250
0.6	0.0909	0.0000

Section 12

X (m)	Y (m)	Z (m)
0.7	0.0000	0.1250
0.7	0.0170	0.1250
0.7	0.0259	0.1250
0.7	0.0445	0.1250
0.7	0.0445	0.1000
0.7	0.0445	0.0750
0.7	0.0445	0.0500
0.7	0.0445	0.0250
0.7	0.0445	0.0000

Section 13

X (m)	Y (m)	Z (m)
0.8	0.0000	0.1250
0.8	0.0000	0.1000
0.8	0.0000	0.0000

APPENDIX H: CFX4.1-F3D GOVERNING EQUATIONS CFX EXAMPLE COMMAND FILE

NOMENCLATURE

B	Body force.
H	Total enthalpy.
h	Static enthalpy.
p	Pressure.
R_n	Reynolds number.
S	Source or sink term representing creation or destruction of Φ.
T	Temperature.
t	Time.
U	Overall fluid velocity.
u	Fluid velocity in the x direction.
v	Fluid velocity in the y direction.
w	Fluid velocity in the z direction.
Γ	Diffusion coefficient.
λ	Thermal conductivity.
μ	Absolute viscosity.
υ	Kinematic viscosity.
ρ	Density.
σ	Stress.
Φ	A function of either mass, momentum or heat.

H.1 GOVERNING EQUATIONS [H1,H2]

There is a basic set of equations which the program solves for laminar flows. These are the Navier Stokes equations, which comprise of formulae for the conservation of mass, momentum and energy:

Let the operator $$\nabla = i\frac{\partial}{\partial.x} + j\frac{\partial}{\partial.y} + k\frac{\partial}{\partial.z} = \left(\frac{\partial}{\partial.x}, \frac{\partial}{\partial.y}, \frac{\partial}{\partial.z}\right) \quad \text{(H1)}$$

$$\frac{\partial.\rho}{\partial.t} = -\left[\frac{\rho.u}{\partial.x} + \frac{\rho.v}{\partial.y} + \frac{\rho.w}{\partial.z}\right] \quad \text{(H2)}$$

$$\therefore \quad \frac{\partial.\rho}{\partial.t} + \nabla.(\rho.U) = 0 \quad \text{(H3)}$$

and $$\frac{\partial.\rho.U}{\partial.t} + \nabla.(\rho.U \otimes U) = B + \nabla\sigma \quad \text{(H4)}$$

and $$\frac{\partial.\rho.H}{\partial.t} + \nabla.(\rho.UH) - \nabla.(\lambda.\nabla.T) = \frac{\partial.p}{\partial.t} \quad \text{(H5)}$$

In addition there is a relationship between the stress and rate of strain, and two algebraic equations of state relating density to temperature and pressure, and one relating static enthalpy to temperature and pressure:

$$\sigma = -\rho.\delta + \mu.\left(\nabla.U + (\nabla.U)^T\right) \tag{H6}$$

$$\rho = \rho_{(T,p)} \qquad h = h_{(T,p)} \qquad H = h + \frac{1}{2}U^2 \tag{H7}$$

The seven equations above plus boundary and initial conditions define the seven unknown functions, ρ, u, v, w, p, h, T.

If the flow is incompressible and μ is a constant, the number of equations can be reduced to four involving four unknown functions, u, v, w, p.

$$\frac{\partial \rho U}{\partial .t} + \nabla\left(\rho U \otimes U - \mu \nabla U\right) = B - \nabla p$$
$$\nabla U = 0 \tag{H8}$$

The equations for laminar flow are also valid for turbulent flow. However, we are limited in solving these equations accurately for high Reynolds numbers and we have to resort to turbulence modelling.

$$\text{Reynolds number } R_n = \frac{\rho.Ux}{\mu} = \frac{Ux}{\upsilon} \tag{H9}$$

where $\upsilon = \dfrac{\mu}{\rho}$ = kinematic viscosity $\left(m^2/s\right)$.

H.1.1 Reynolds-averaged Navier Sokes equations [H2]

All the above transport equations can be expressed as a scalar advection-diffusion equation:

$$\frac{\partial .\rho.\Phi}{\partial .t} + \nabla.\left(\rho.U.\Phi - \Gamma.\nabla.\Phi\right) = S \tag{H10}$$

where Γ = Diffusion coefficient.

Φ = A function of either mass, momentum, or heat.

S = Source or sink term representing the creation or destruction of Φ.

This equation is called the generic equation. For an example, take the case of the momentum in the y direction. The generic form of the equation can be written as:

$$\frac{\partial .\rho.V}{\partial .t} + \nabla.\left(\rho.U.V - \mu.\nabla.V\right) = B_y - \frac{\partial .p}{\partial .y} \tag{H11}$$

Turbulent flows are extremely complex time-dependent flows governed by the laminar flow equations [H1]. Applying Reynolds time averaging to the continuity equation, the momentum equation and the scalar equation for incompressible flow, we obtain:

$$\frac{\partial .\rho}{\partial .t} + \nabla.\left(\rho.U\right) = 0 \tag{H12}$$

$$\frac{\partial.\rho.U}{\partial.t} + \nabla.\left(\rho.U \otimes U\right) = B + \nabla.\left(\sigma - \rho.\overline{u \otimes u}\right) \quad \text{(H13)}$$

$$\frac{\partial.\rho.\Phi}{\partial.t} + \nabla.\left(\rho.U.\Phi\right) = \nabla.\left(\Gamma\nabla\Phi - \rho.\overline{u.\phi}\right) + S \quad \text{(H14)}$$

The momentum and scalar transport equations contain additional terms. These are:

Reynolds Stress = $\rho.\overline{u \otimes u}$

Reynolds Flux = $\rho.\overline{u\phi}$

These terms arise from the non-linear corrective term in the unaveraged equations.

In addition to the above equations, complex eddy viscosity models are also used to express the Reynolds stress and Reynolds fluxes in terms of the mean quantities.

The default turbulent model in CFX4.1 is the k-ε model and there are three versions available:

- The standard k-ε model.
- The low Reynolds number k-ε model - a modification of the standard k-ε model to allow calculation of turbulent flows at low Reynolds numbers, typically in the range 5000 to 30,000.
- The RNG k-ε model - an alternative to the standard k-ε model for high Reynolds number flows. It has a modification to the equation for ε and uses a different set of model constraints [H1,H2].

H.2 CFX4.1-F3D STRATEGIES

H.2.1 Differencing schemes

The numerical accuracy of the modelled equations to be solved to a large extent depend upon the method of discretization chosen for their advection terms. Various discretization methods are available in the software ranging from robust but relatively inaccurate hybrid and upwind schemes to more accurate but less robust higher order schemes. Hybrid differencing is the default scheme used to model the convective terms of all transport equations.

All equations except k and ε were left as hybrid schemes. The k and ε equations were set to use the CCCT scheme, a third order accurate method. Some higher order methods can suffer from non-physical overshoots, for example, turbulent kinetic energy could become negative. The CCCT method is bounded in order to eliminate these overshoots.

H.2.2 Variable Iterations

To aid convergence it is sometimes necessary to alter the standard strategy by iterating on a subset of variables within each global iteration. This was done for the turbulence equations. Rather than the default one iteration, these were set to three iterations per global iteration. This did mean the solver required more CPU time but the solution was more accurate.

H.2.2 Under-Relaxation

Under-relaxation has several interlinked purposes in the solution process. Principally, the amount by which a variable would change if its discrete transport equation were solved as

it stands is reduced. In this way difficulties caused by instability due, among other factors, to non-linearity are overcome. Under-relaxation for all the transport equations is implemented by scaling the coefficient of the variable in the current cell by an under-relaxation factor (URF) in the range 0<URF<1. The smaller the factor, the more under-relaxation.

H.2.3 Deferred Correction

One of the most common causes of lack of convergence of turbulence flow calculations within CFX is due to the cross-derivative diffusion terms in the k and ε equations on non-orthogonal grids. There is a facility for under-relaxing these terms during the course of the calculation. A start iteration before which the terms are omitted and an end iteration after which the terms are included can be set. This was done for the first 250 iterations.

H.3 EXAMPLE OF A CFX COMMAND FILE

This is an example of a CFX command file, which was used to run a model of the waterjet intake half-duct at IVR=0.88. Further descriptions of the defined parameters can be found in the CFX user manual [H1].

```
/*                              */
/*awh1/newjet/m15.fc            */
/*created 17-6-99               */
/*                              */
>>CFX4
  >>OPTIONS
    THREE DIMENSIONS
    BODY FITTED GRID
    CARTESIAN COORDINATES
    TURBULENT FLOW
    INCOMPRESSIBLE FLOW
    STEADY STATE
>>MODEL DATA
  >>DIFFERENCING SCHEME
    U VELOCITY 'HYBRID'
    V VELOCITY 'HYBRID'
    W VELOCITY 'HYBRID'
    PRESSURE 'HYBRID'
    K 'CCCT'
    EPSILON 'CCCT'
  >>TITLE
    PROBLEM TITLE 'COMMAND FOR NEW HALF-JET'
  >>PHYSICAL PROPERTIES
    >>STANDARD FLUID
      FLUID 'AIR'
      STANDARD FLUID REFERENCE TEMPERATURE 2.8500E+02
>>SOLVER DATA
  >>PROGRAM CONTROL
    MAXIMUM NUMBER OF ITERATIONS 1000
    MAXIMUM CPU TIME 50300
    PRESSURE REFERENCE POSITION -3.900000E-01 3.100000E-01 0.000000E+00
    OUTPUT MONITOR POSITION -3.900000E-01 3.100000E-01 0.000000E+00
    MASS SOURCE TOLERANCE 1.0000E-05
    ITERATIONS OF TURBULENCE EQUATIONS 3
  >>DEFERRED CORRECTION
    K START 1
    K END 250
    EPSILON START 1
    EPSILON END 250
>>CREATE GRID
  >>INPUT GRID
    READ GRID FILE
    FORMATTED
```

```
>>MODEL BOUNDARY CONDITIONS
  >>MASS FLOW BOUNDARY CONDITIONS
    FLUXES 1.47285E+00 4.4185E+00
    MASS FLOW SPECIFIED
  >>SET VARIABLES
    PATCH NAME 'INLET'
    U VELOCITY -2.1060E+01
>>OUTPUT OPTIONS
  >>LIMITS
    MAXIMUM NUMBER OF DUMP FILE OPTIONS 100
    MAXIMUM NUMBER OF PRINT OPTIONS 50
    MAXIMUM NUMBER OF ANIMATION FILES 10
    MAXIMUM NUMBER OF LINE GRAPHS 50
    BUFFER SIZE FOR DYNAMIC DATA 10
  >>LINE GRAPH DATA
    XYZ -3.900000E-01 3.100000E-01 0.000000E+00
    EACH ITERATION
    FILE NAME 'EXIT'
    U VELOCITY
    PRESSURE
  >>LINE GRAPH DATA
    XYZ -3.000000E-01 4.000000E-01 0.000000E+00
    EACH ITERATION
    FILE NAME 'BSTATIC'
    PRESSURE
  >>LINE GRAPH DATA
    XYZ -3.900000E-01 3.990000E-01 0.000000E+00
    EACH ITERATION
    FILE NAME 'TA'
    PRESSURE
  >>LINE GRAPH DATA
    XYZ -3.000000E-01 3.990000E-01 0.000000E+00
    EACH ITERATION
    FILE NAME 'TB'
    U VELOCITY
    ---   ---   ---
    ---   ---   ---
    ---   etc   ---
    ---   ---   ---
    ---   ---   ---
   >>LINE GRAPH DATA
    XYZ -3.900000E-01 1.900000E-01 0.000000E+00
    EACH ITERATION
    FILE NAME 'E5'
    U VELOCITY
    PRESSURE
>>STOP
```

REFERENCES

H1. "*Environment User Guide*", "*CFDS-Flow3d User Guide*" and "*CFX4.1 User Guide.*" UK AEA TECHNOLOGY, Harwell. 1995.

H2. TAN M Y - "*Application of CFD to Marine Dynamics.*" University of Southampton, Department of Ship Science, Lecture notes, 1996.

APPENDIX I: ELECTROMAGNETIC TIP-DRIVEN PROPELLER DESIGN DRAWINGS

Section AA

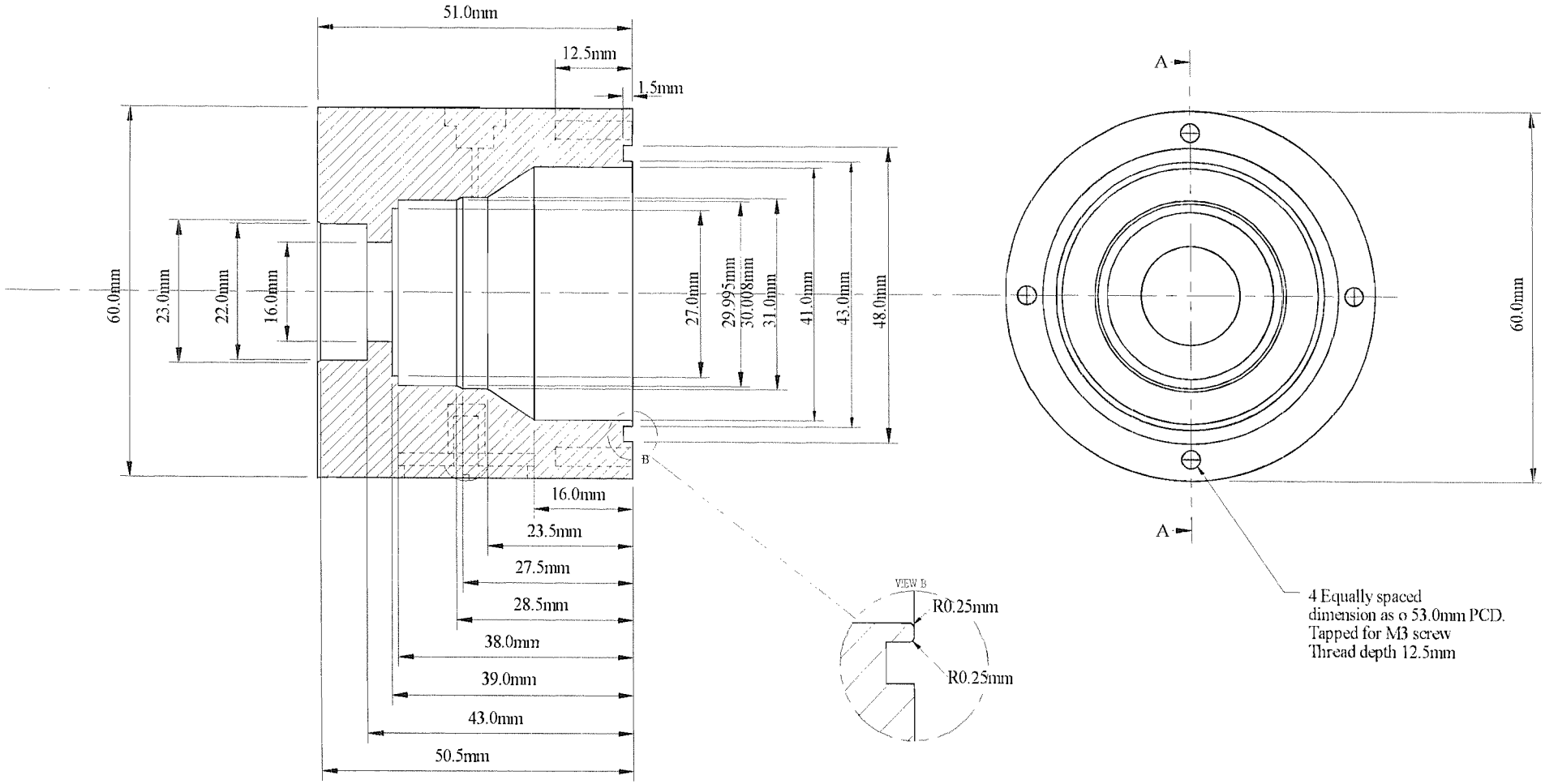

NOTES

Quantity = 2

See Drawing P1-43 for further details

Material = aluminium alloy

Page 1 of 2

CONTRACT NO. C31 R201	DATE	TUUV Prototype Integrated Thrusters	
DRAWN BY: A.W.Hughes	15-7-98		
CHECKED BY: S.R.Turnock	21-7-98	TITLE: Bearing Casing- Main Dimensions	
DESIGNED BY:		SIZE: A4 / FSCM NO. / DWG NO. / FILE NAME: P1-42 / casing.skd	
DESIGN ACTIVITY: Prototype 1			
CUSTOMER		SCALE: 1mm = 1mm / DATE: 15-7-1998 / SHEET: 1 of 1	

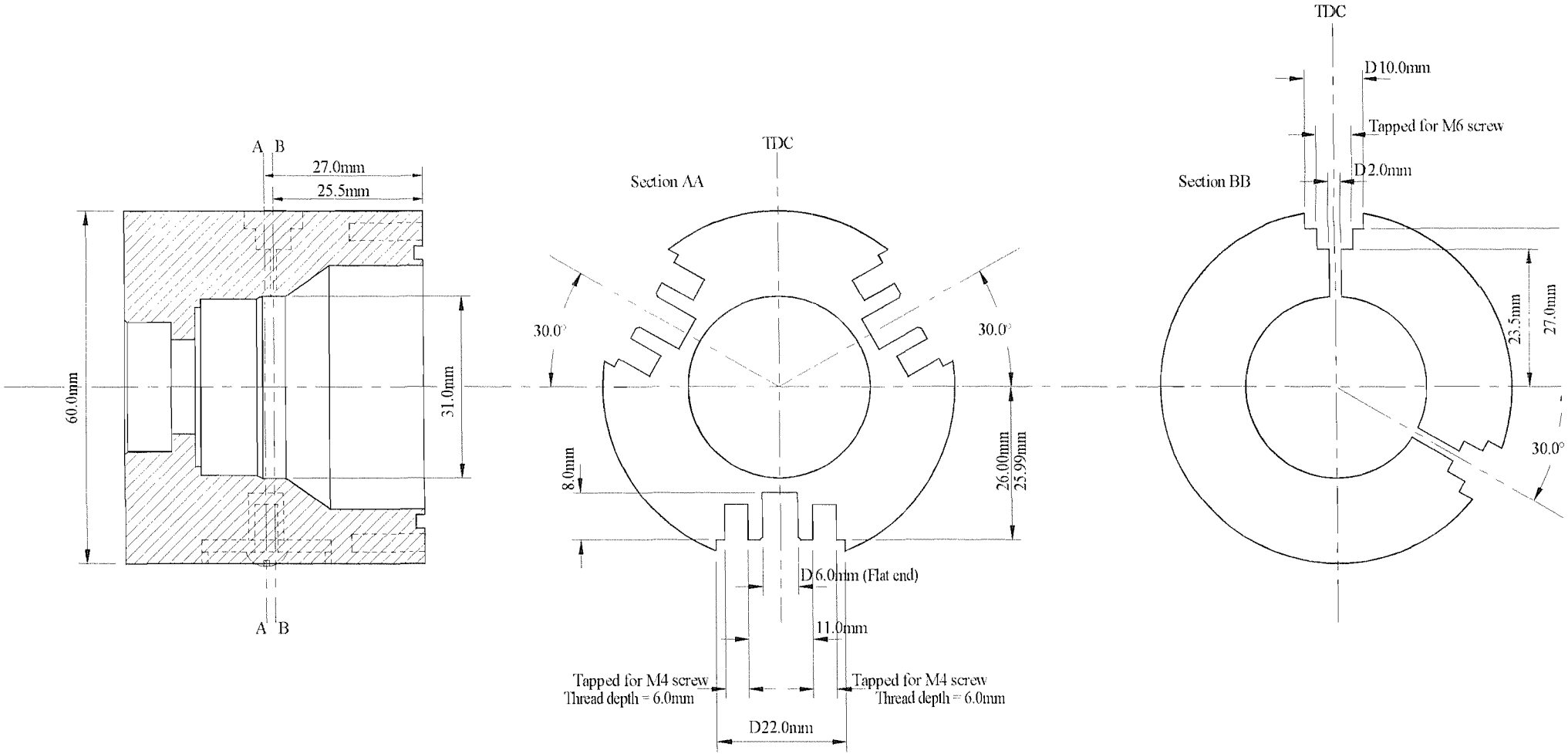

NOTES

Illustrated are two sections through the bearing casing where it is drilled/tapped into.

Page 2 of 2

CONTRACT NO. C31 R201	DATE	TUUV Prototype Integrated Thrusters
DRAWN BY: A.W.Hughes	15-7-98	
CHECKED BY: S.R.Turnock	21-7-98	TITLE: Bearing Casing
DESIGNED BY:		SIZE: A4 / FSCM NO. / DWG NO. / FILE NAME: P1-43 / casing2.skd
DESIGN ACTIVITY: Prototype 1		
CUSTOMER		SCALE: 1mm = 1mm / DATE: 15-7-1998 / SHEET: 1 of 1

Section AA

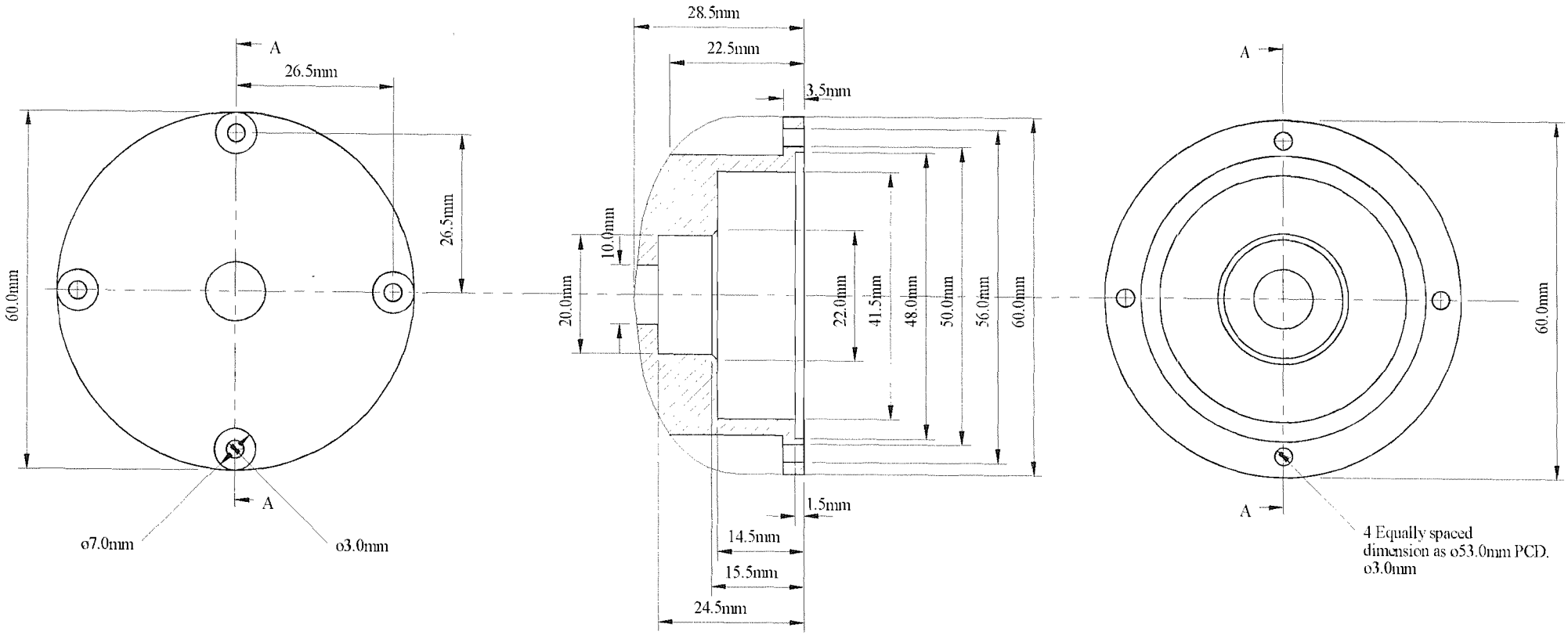

NOTES

Quantity = 2

Material = aluminium alloy

For profile see Drawing P1-46

Page 1 of 2

CONTRACT NO. C31 R201	DATE	TUUV Prototype Integrated Thrusters
DRAWN BY: A.W.Hughes	16-7-98	
CHECKED BY: S.R.Turnock	21-7-98	TITLE: Bearing Casing Endcap
DESIGNED BY:		SIZE: A4 / FSCM NO. / DWG NO. / FILE NAME: P1-45 / endcap.skd
DESIGN ACTIVITY: Prototype 1		
CUSTOMER		SCALE: 1mm = 1mm / DATE: 16-7-1998 / SHEET: 1 of 1

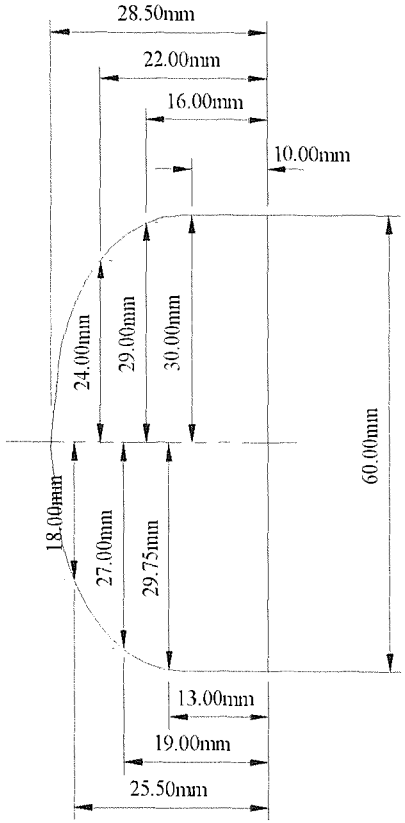

NOTES

Quantity = 2
Material = aluminium alloy

Page 2 of 2

CONTRACT NO. C31 R201	DATE	TUUV Prototype Integrated Thrusters
DRAWN BY: A.W.Hughes	16-7-98	
CHECKED BY: S.R.Turnock	21-7-98	TITLE: Bearing Casing Endcap - Profile
DESIGNED BY:		SIZE: A4 / FSCM NO. / DWG NO. / FILE NAME: P1-46 / endcap2.skd
DESIGN ACTIVITY: Prototype 1		
CUSTOMER		SCALE: 1mm = 1mm / DATE: 16-7-1998 / SHEET: 1 of 1

Section AA

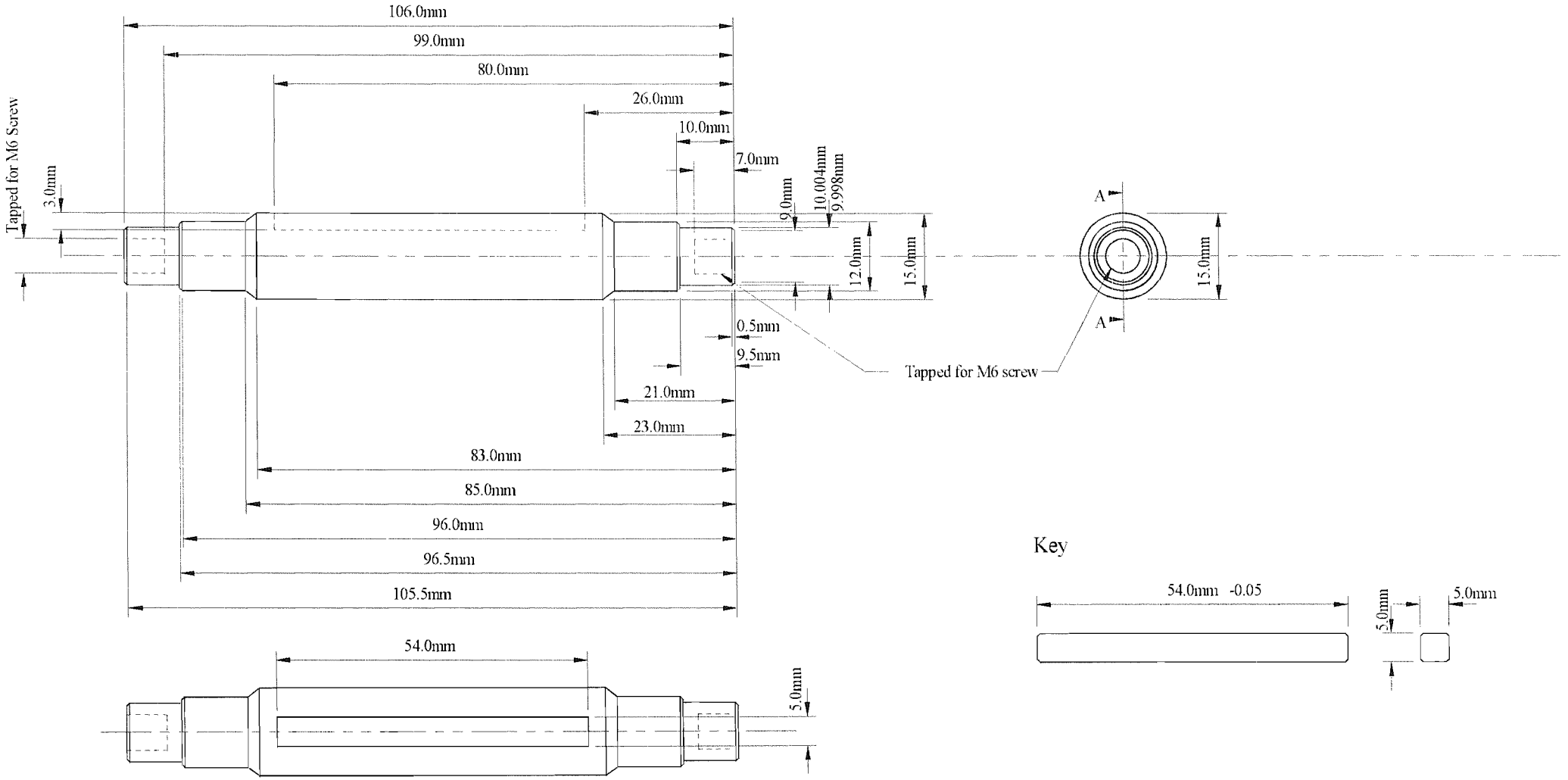

Key

NOTES

Material = Stainless steel

CONTRACT NO	C31 R201	DATE	TUUV Prototype Integrated Thrusters
DRAWN BY:	A.W.Hughes	15-7-98	
CHECKED BY:	S.R.Turnock	21-7-98	TITLE: Propeller Shaft
DESIGNED BY:			SIZE: A4 / FSCM NO. / DWG NO. / FILE NAME: P1-44 / shaft.skd
DESIGN ACTIVITY	Prototype 1		
CUSTOMER			SCALE: 1mm = 1mm / DATE: 15-7-1998 / SHEET: 1 of 1

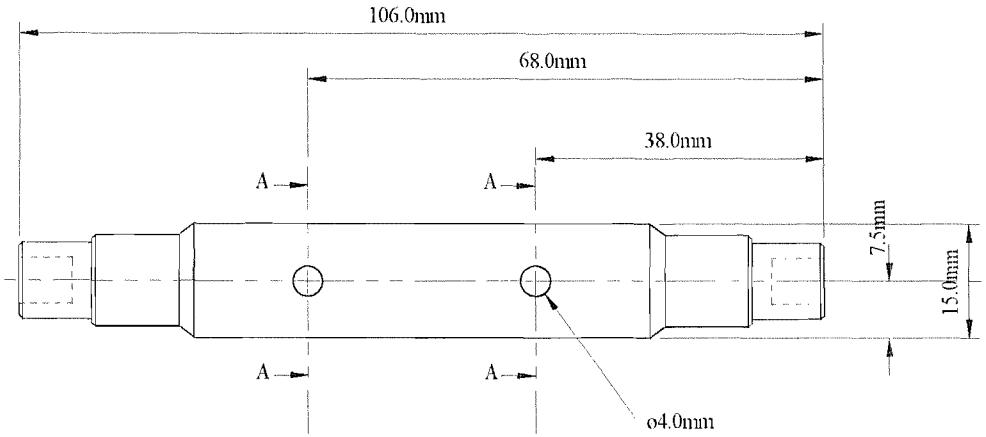

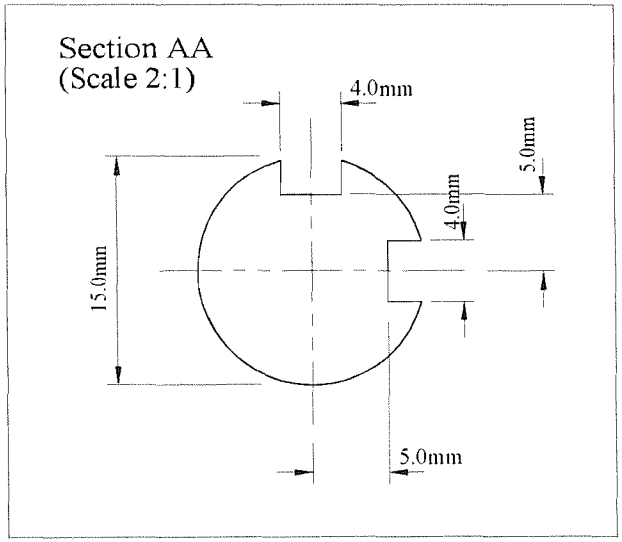

NOTES

Material = Stainless steel

CONTRACT NO. C31 R201	DATE	TUUV Prototype Integrated Thrusters	
DRAWN BY: A.W.Hughes	13-10-98		
CHECKED BY:		TITLE: Propeller Shaft Pin Locations	
DESIGNED BY:			
DESIGN ACTIVITY: Prototype 1		SIZE: A4 / FSCM NO. / DWG NO. / FILE NAME: P1- / shaftpin.skc	
CUSTOMER		SCALE: 1mm = 1mm / DATE: 13-10-1998 / SHEET: 1 of 1	

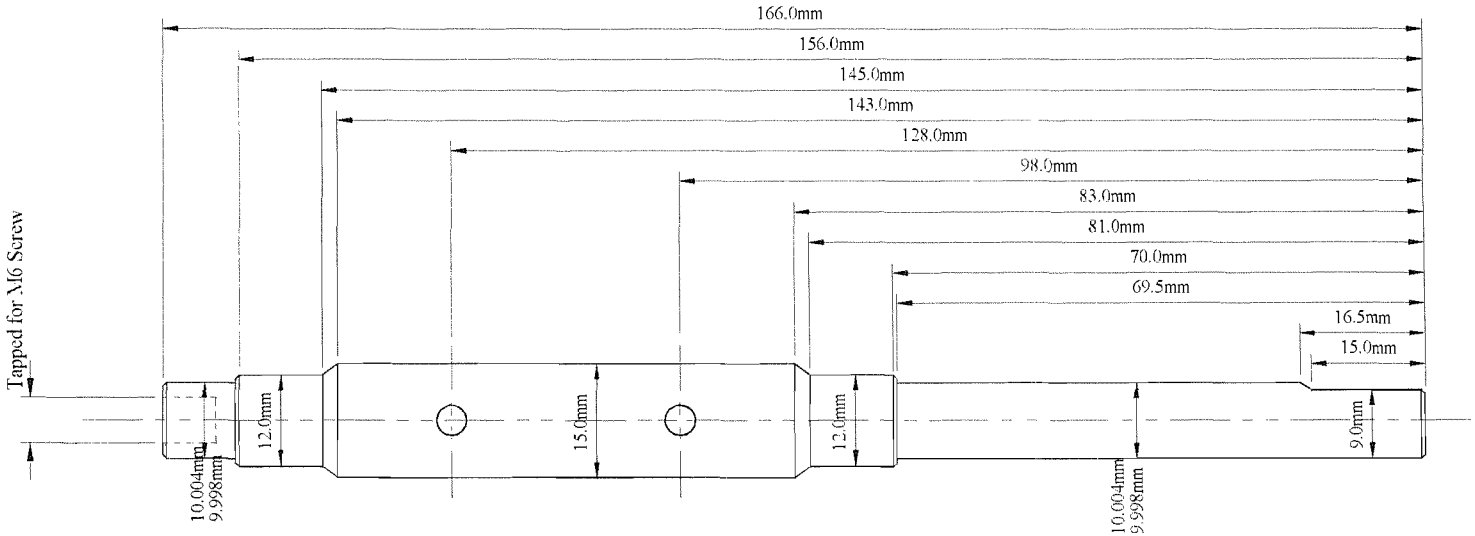

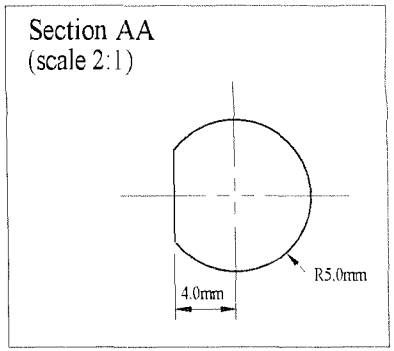

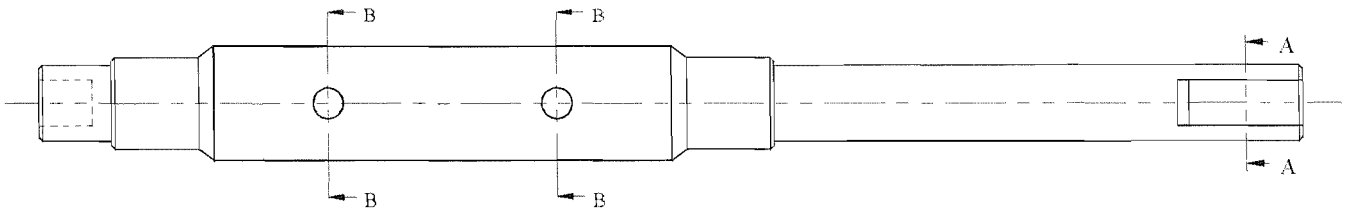

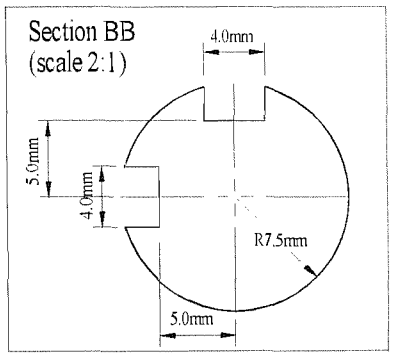

NOTES

Material = Stainless steel

CONTRACT NO.	C31 R201	DATE
DRAWN BY:	A.W.Hughes	15-7-98
CHECKED BY:	S.R.Turnock	21-7-98
DESIGNED BY:		
DESIGN ACTIVITY	Prototype 1	
CUSTOMER		

TUUV Prototype Integrated Thrusters

TITLE

Extended Propeller Shaft

SIZE	FSCM NO.	DWG NO. / FILE NAME
A4		P1- / longshaf.sk

SCALE	DATE	SHEET
1mm = 1mm	15-7-1998	1 of 1

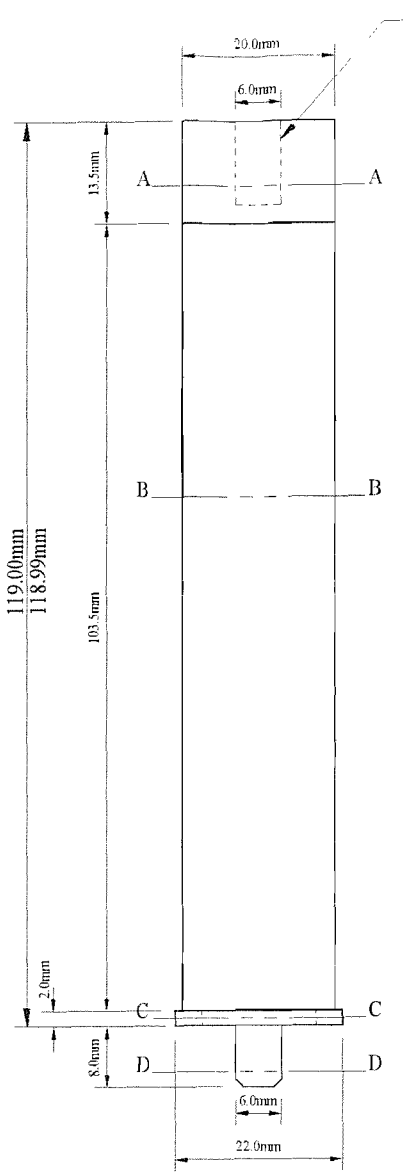

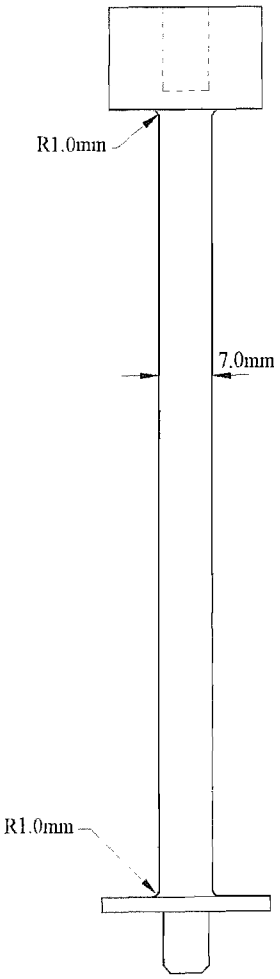

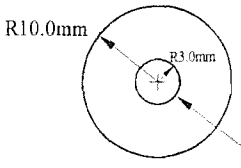

Section through AA

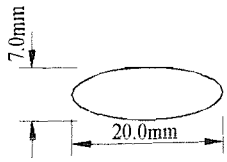

Section through BB

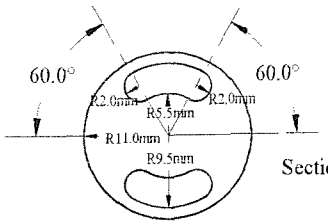

Section through CC

Section through DD

NOTES

Quantity = 6
Material = aluminium alloy
Top hole tapped for M6 screw

CONTRACT NO. C31 R201	DATE	TUUV Prototype Integrated Thrusters	
DRAWN BY: A.W.Hughes	10-7-98		
CHECKED BY: S.R.Turnock	21-7-98	TITLE: Hydrodynamic stator	
DESIGNED BY:		SIZE: A4 / FSCM NO. / DWG NO. / FILE NAME: P1-41 / stat4.skd	
DESIGN ACTIVITY: Prototype 1			
CUSTOMER		SCALE: 1mm = 1mm / DATE: 10-7-1998 / SHEET: 1 of 1	

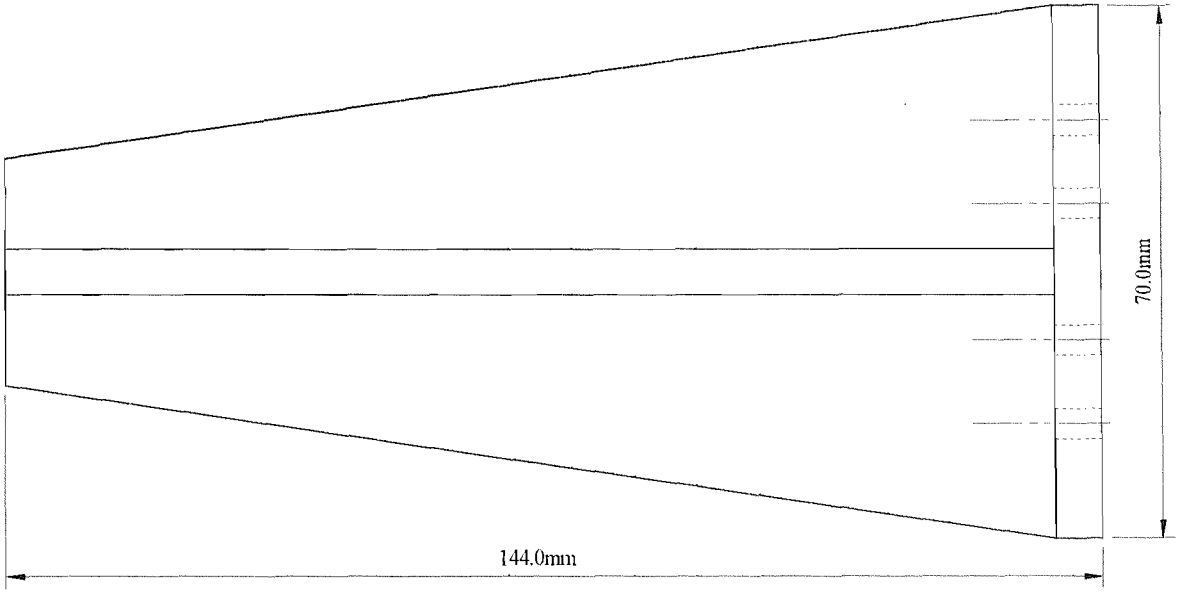

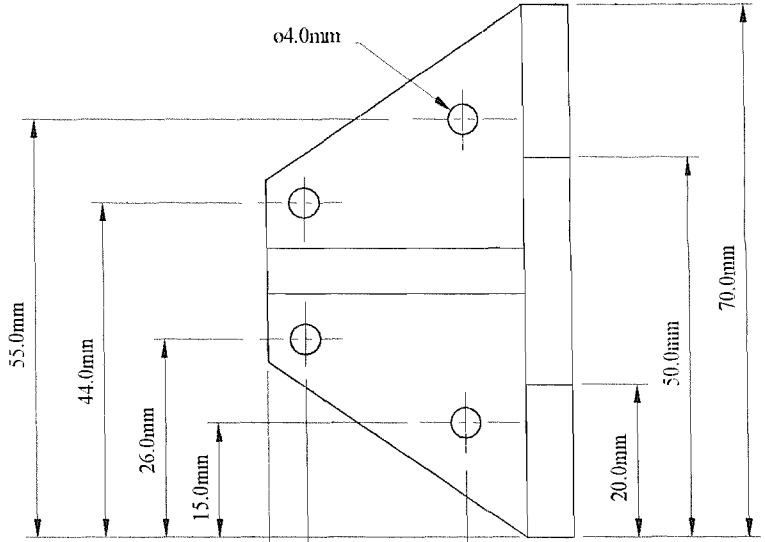

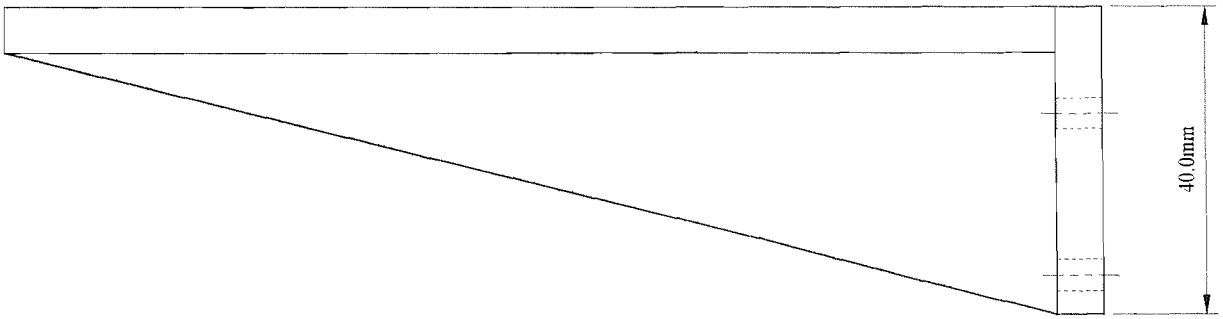

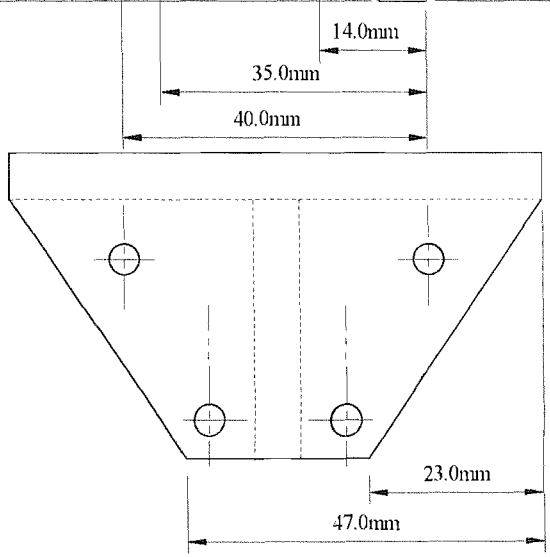

NOTES

Material = Aluminium plate (1/4 inch)

Quantity = 3 Off

(To be lined with 1/2 inch nylon)

CONTRACT NO. C31 R201	DATE	TUUV Prototype Integrated Thrusters
DRAWN BY: A.W.Hughes	13-10-98	
CHECKED BY:		TITLE: Guides
DESIGNED BY:		
DESIGN ACTIVITY: Prototype 1		SIZE: A4 / FSCM NO. / DWG NO. / FILE NAME: P1- / tguide.skd
CUSTOMER		SCALE: 1mm = 1mm / DATE: 13-10-1998 / SHEET: 1 of 1

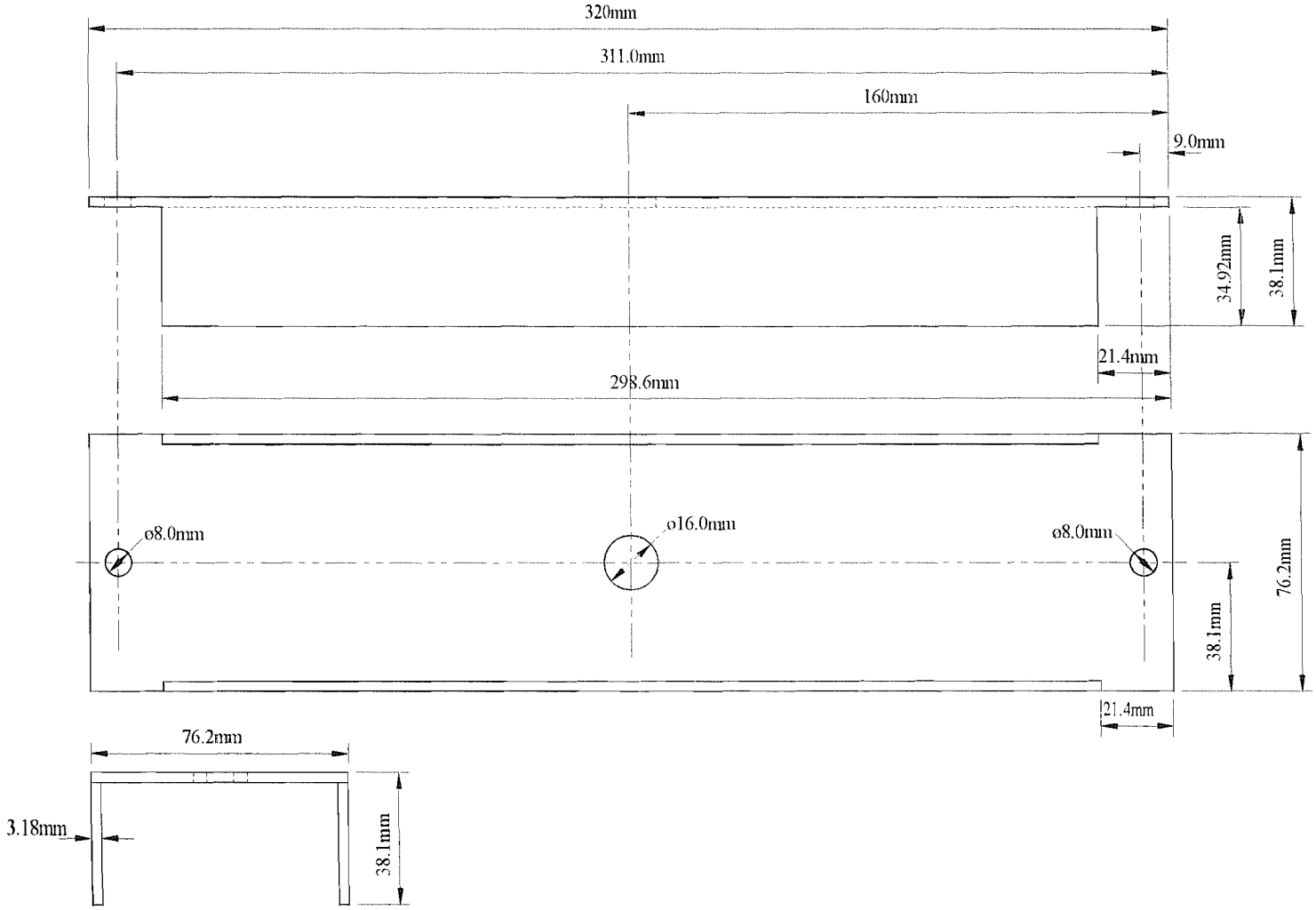

NOTES

Material = Aluminium channel 76.2 x 38.1 x 3.18 mm

Quantity = 1 Off

CONTRACT NO. C31 R201	DATE	TUUV Prototype Integrated Thrusters	
DRAWN BY: A.W.Hughes	13-10-98		
CHECKED BY:		TITLE	
DESIGNED BY:		SIZE A4 / FSCM NO.	DWG NO. / FILE NAME P1- / ubeam1.skd
DESIGN ACTIVITY Prototype 1			
CUSTOMER		SCALE 1mm = 2mm / DATE 13-10-1998	SHEET 1 of 1

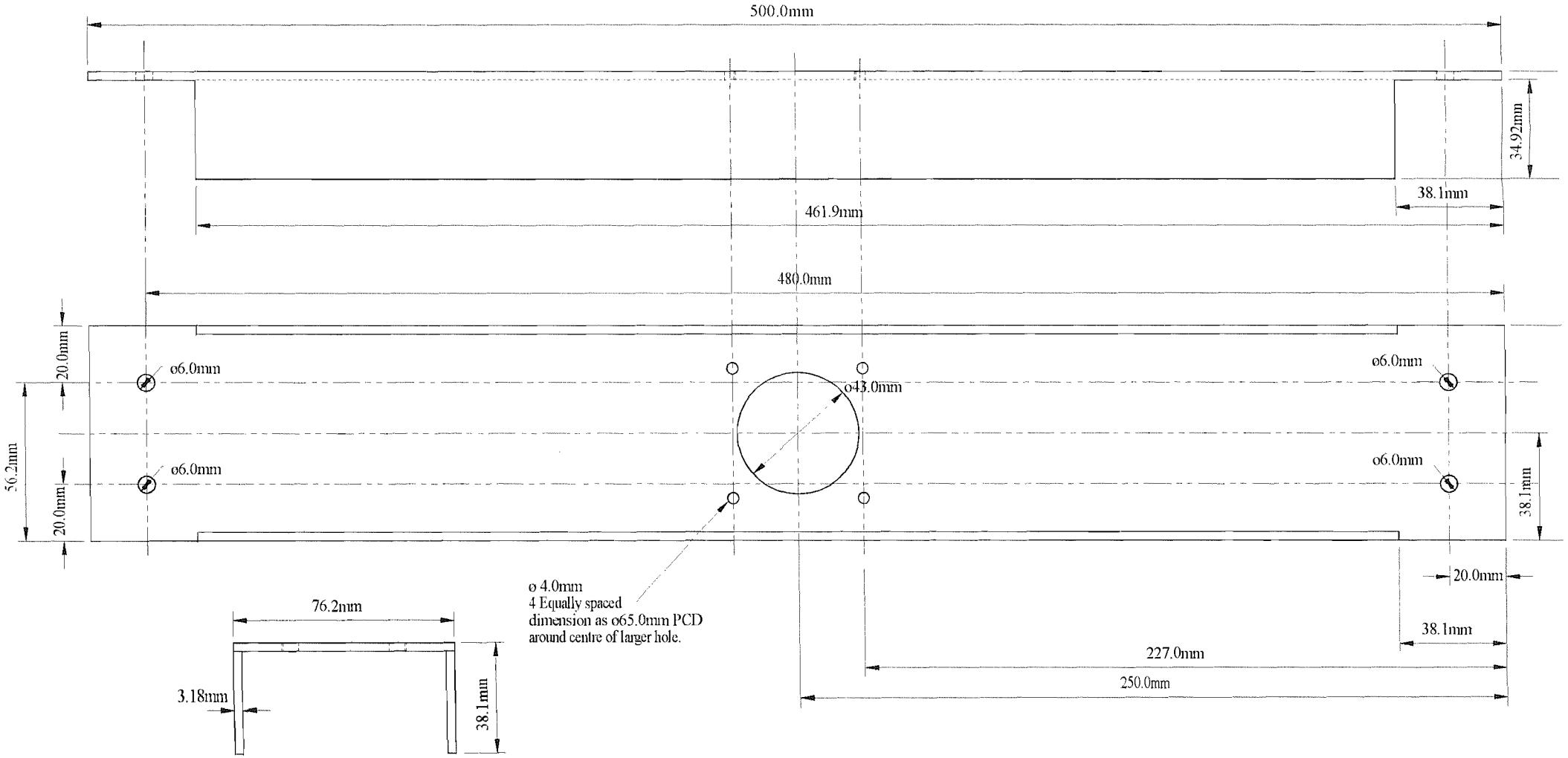

NOTES

Material = Aluminium Channel 76.2mm x 38.1mm x 3.18mm

Quantity = 1 Off

CONTRACT NO. C31 R201	DATE	TUUV Prototype Integrated Thrusters	
DRAWN BY: A.W.Hughes	13-10-98		
CHECKED BY:		TITLE: Cross Beam	
DESIGNED BY:			
DESIGN ACTIVITY: Prototype 1		SIZE: A4	FSCM NO.
CUSTOMER		DWG NO. / FILE NAME: P1- / ubeam2.skd	
		SCALE: 1mm = 2mm	DATE: 13-10-1998
		SHEET: 1 of 1	

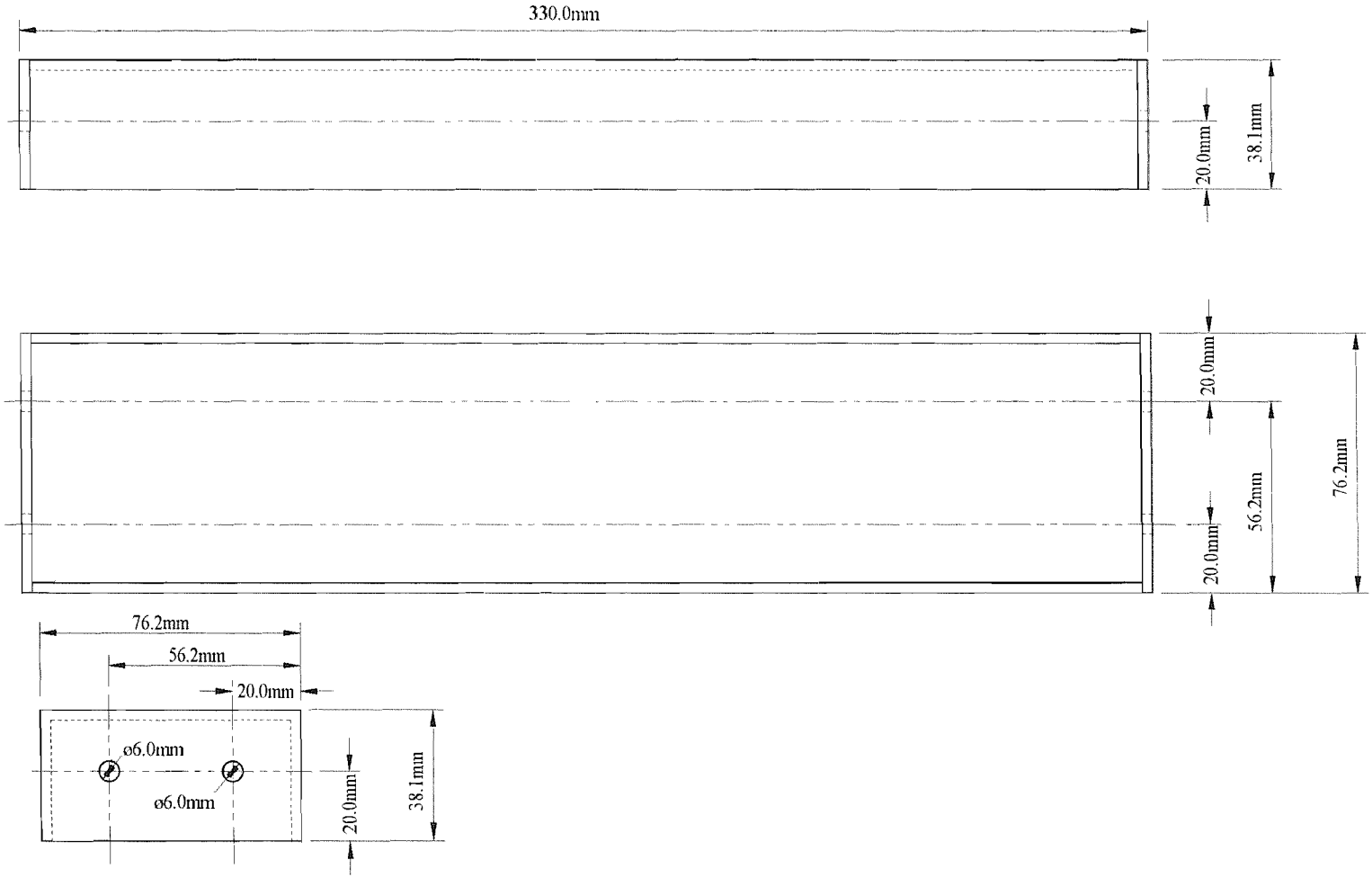

NOTES

Material = Aluminium Camel 76.2 x 38.1 x 3.18mm

Quantity = 2 Off

CONTRACT NO. C31 R201	DATE	TUUV Prototype Integrated Thrusters	
DRAWN BY: A.W.Hughes	13-10-98		
CHECKED BY:		TITLE: Cross Beam Supports	
DESIGNED BY:			
DESIGN ACTIVITY: Prototype 1		SIZE: A4 / FSCM NO. / DWG NO. / FILE NAME: P1- / ubeam3.skd	
CUSTOMER:		SCALE: 1mm = 2mm / DATE: 13-10-1998 / SHEET: 1 of 1	

Section AA

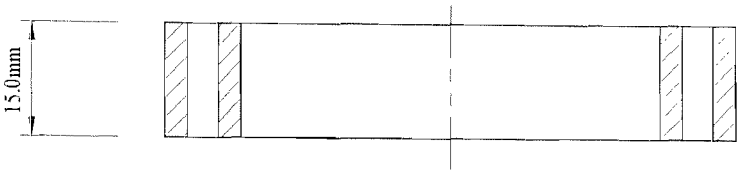

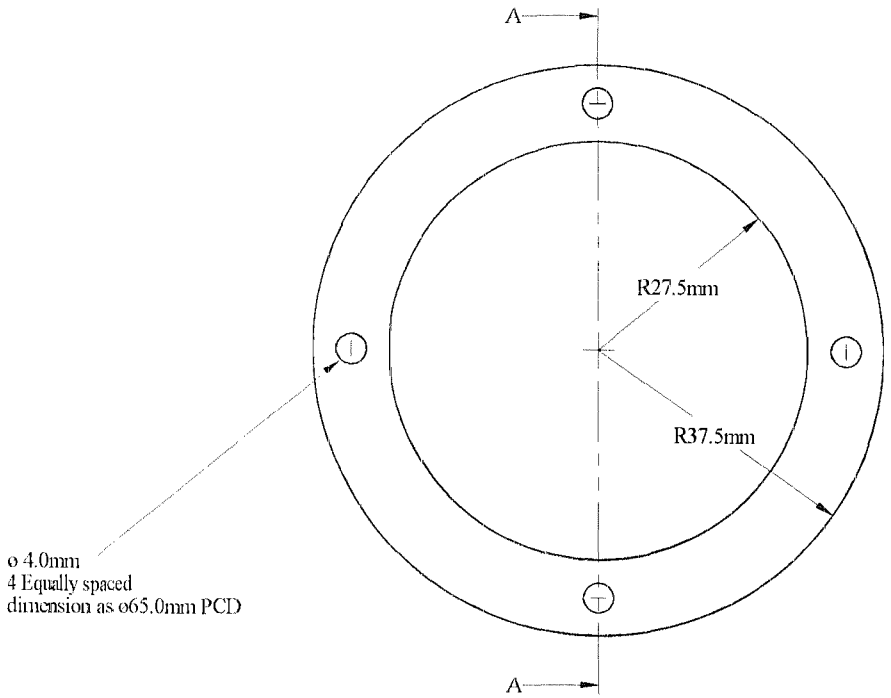

NOTES

Material = Aluminium

Quantity = 1 Off

CONTRACT NO. C31 R201	DATE	TUUV Prototype Integrated Thrusters	
DRAWN BY: A.W.Hughes	13-10-98		
CHECKED BY:		TITLE: Bearing Locator	
DESIGNED BY:			
DESIGN ACTIVITY: Prototype 1		SIZE: A4 / FSCM NO. / DWG NO. / FILE NAME: P1- / bushring.sk	
CUSTOMER		SCALE: 1mm = 1mm / DATE: 13-10-1998 / SHEET: 1 of 1	

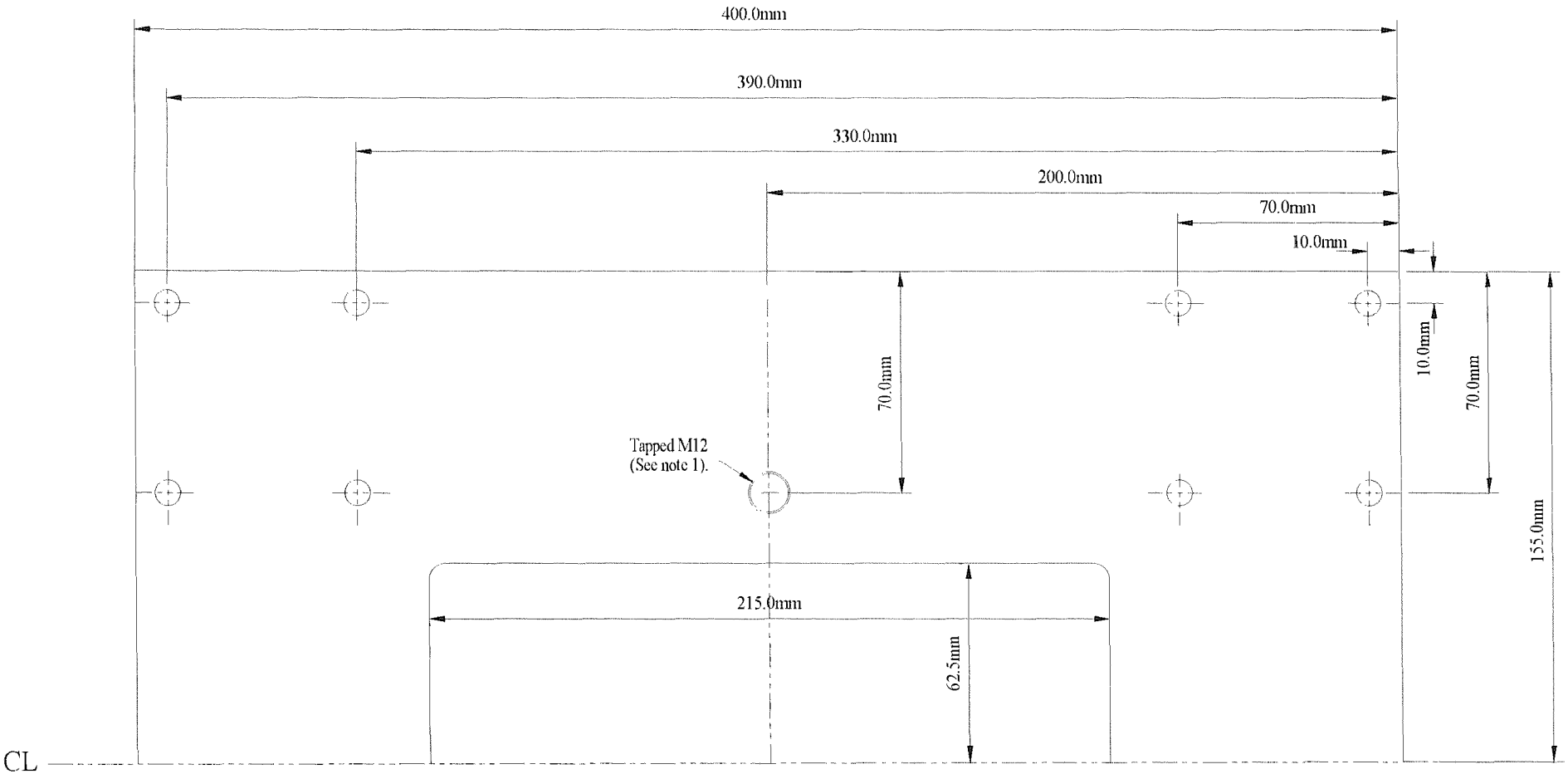

Note 1:
(scale 1:1)

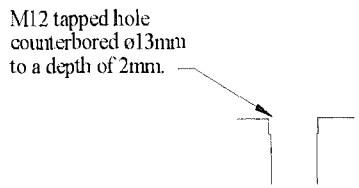

NOTES

Material = Steel (1 inch plate).

Quantity = 1 Off

All holes tapped M8 unless shown otherwise.

Upper and lower surfaces skimmed parallel.

CONTRACT NO. C31 R201	DATE	TUUV Prototype Integrated Thrusters	
DRAWN BY: A.W.Hughes	13-10-98		
CHECKED BY:		TITLE: Force Block Angle Plate	
DESIGNED BY:			
DESIGN ACTIVITY: Prototype 1		SIZE: A4 / FSCM NO. / DWG NO. / FILE NAME: P1- / angplat2.skd	
CUSTOMER		SCALE: 1mm = 2mm / DATE: 13-10-1998 / SHEET: 2 of 2	

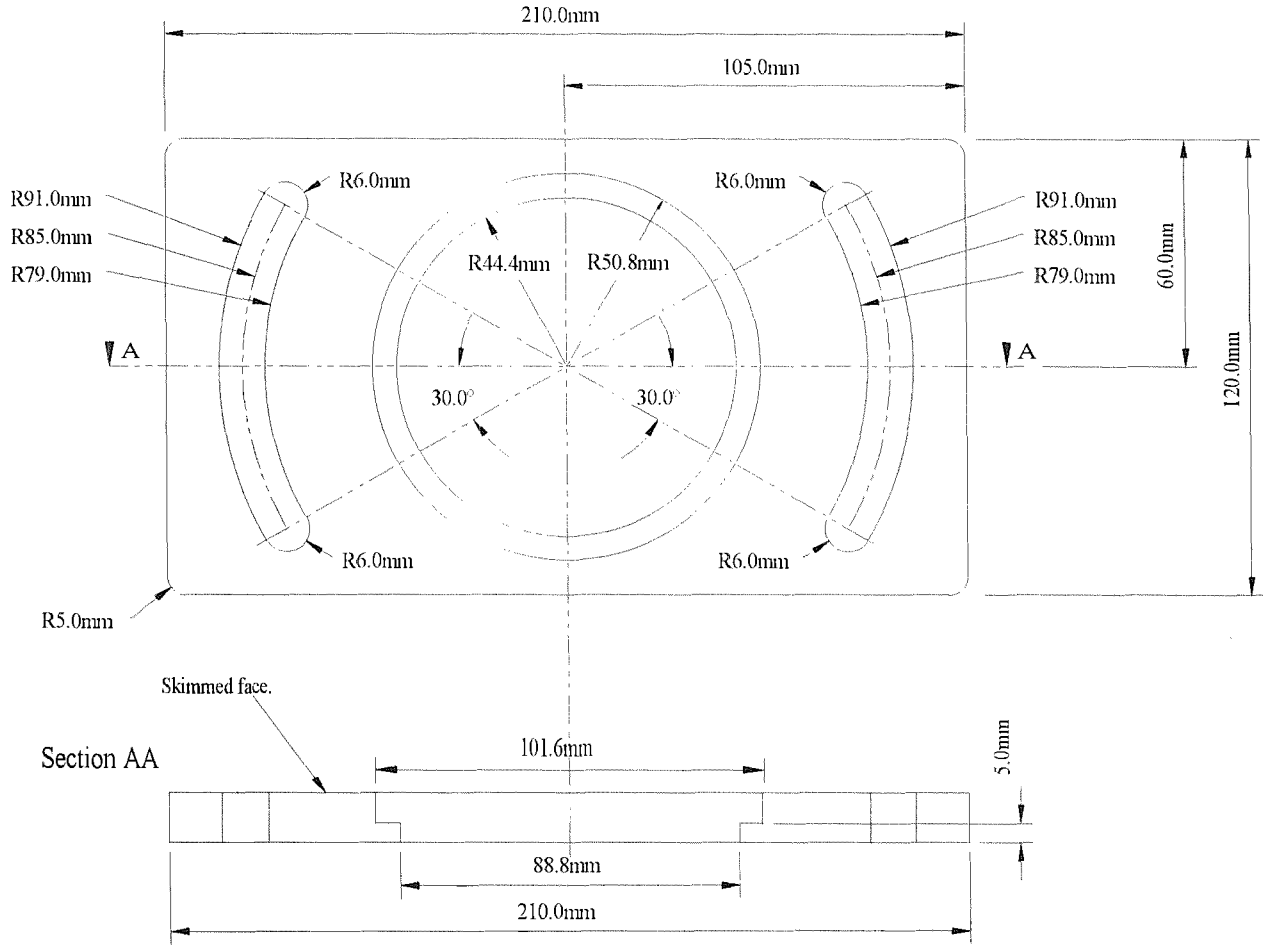

NOTES

Material = Steel (3/4 inch plate)

Quantity = 1 Off

CONTRACT NO.	DATE	Prototype Integrated Thrusters
DRAWN BY: A.W.Hughes	13-10-98	
CHECKED BY:		TITLE: Upper Bracket Plate
DESIGNED BY:		
DESIGN ACTIVITY: Prototype 1		SIZE: A4 / FSCM NO. / DWG NO. / FILE NAME: P1- / topplat.skd
CUSTOMER		SCALE: 1mm = 2mm / DATE: 13-10-1998 / SHEET: 1 of 1

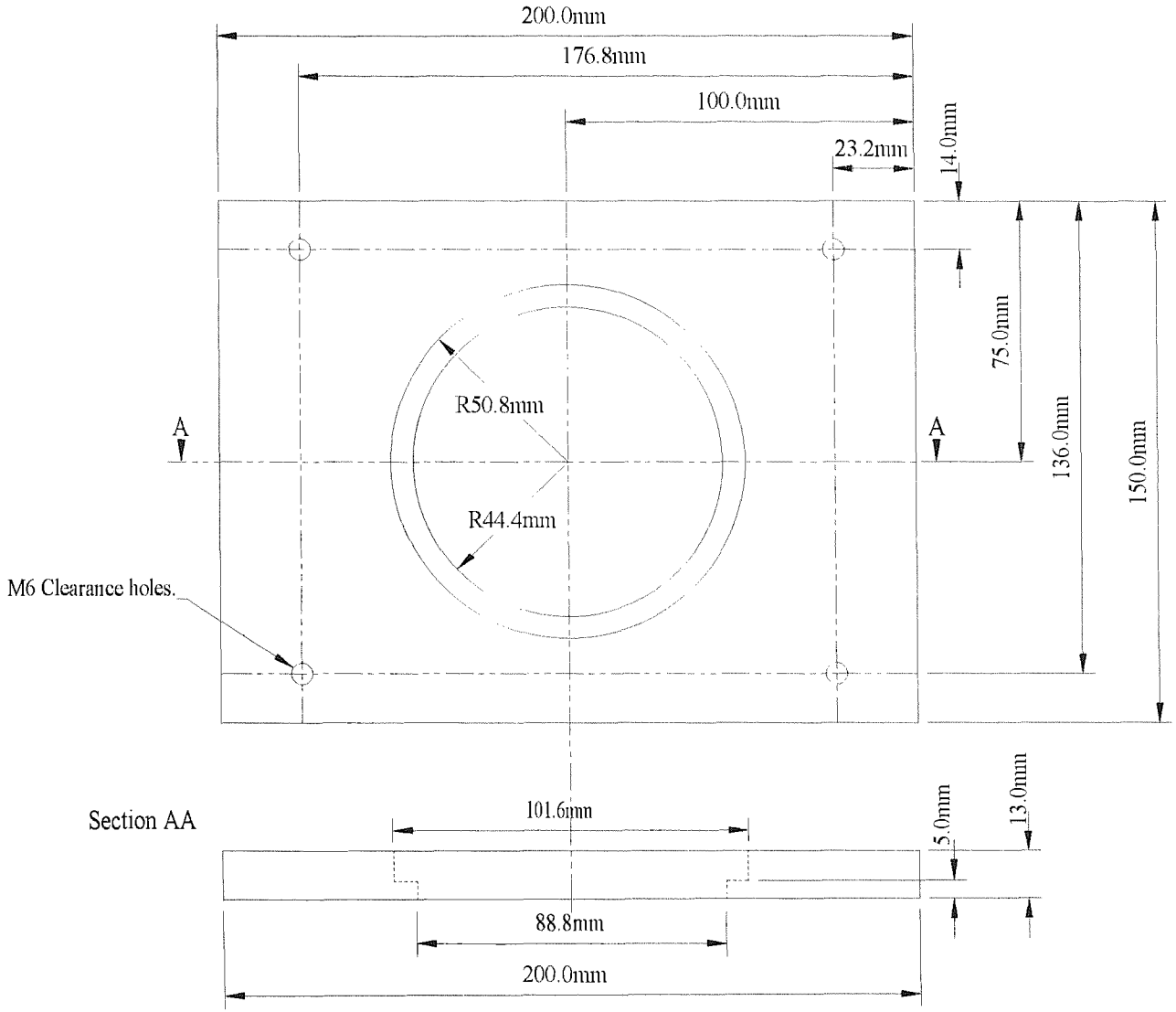

NOTES

Material = Steel (1/2 inch plate).

Quantity = 1 Off

CONTRACT NO. C31 R201	DATE	TUUV Prototype Integrated Thruste	
DRAWN BY: A.W.Hughes	13-10-98		
CHECKED BY:		TITLE: Lower Bracket Plate	
DESIGNED BY:			
DESIGN ACTIVITY: Prototype 1		SIZE: A4	FSCM NO.
CUSTOMER		DWG NO. / FILE NAME: P1- / bracplat.skd	
		SCALE: 1mm = 2mm	DATE: 13-10-1998
		SHEET: 1 of 1	

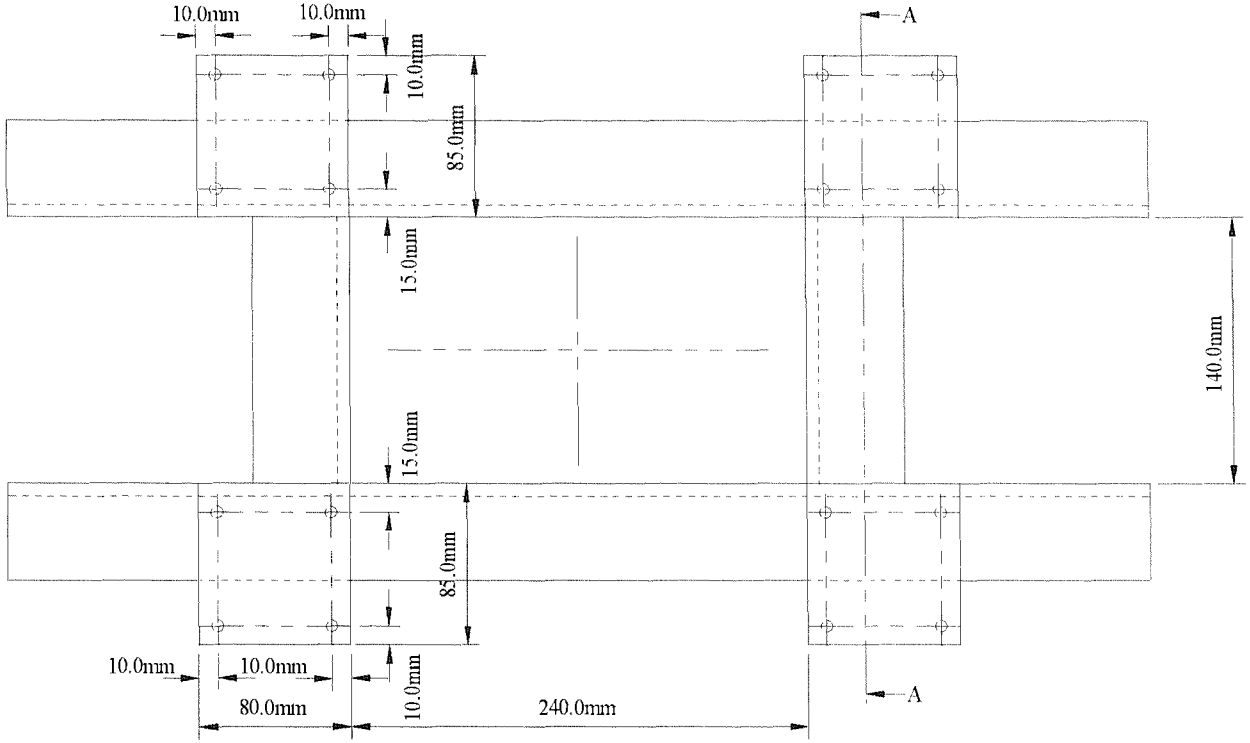

Section AA

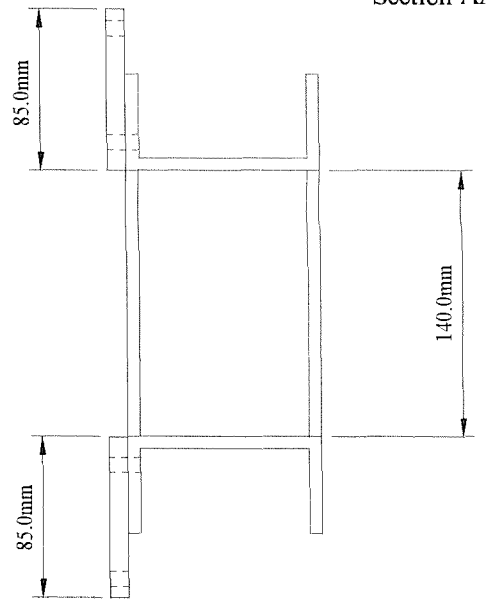

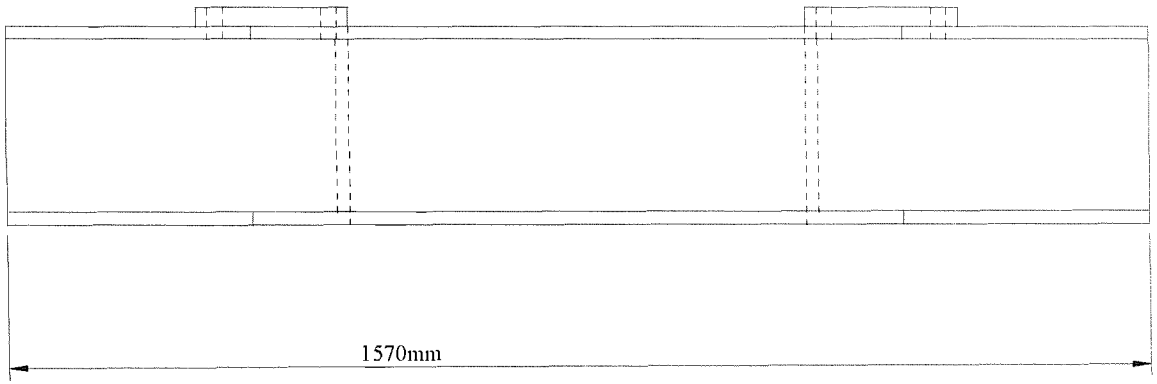

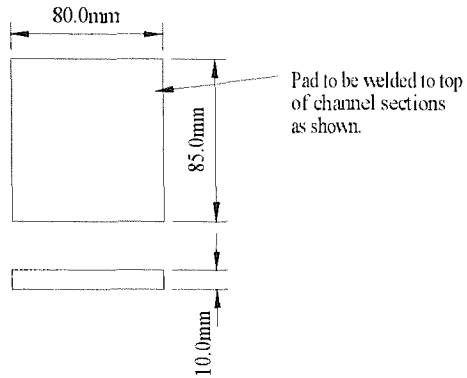

NOTES

Material = Steel
(Channel section 102mm x 51mm x 10.42Kg/m).

All holes clearance M8 unless shown otherwise.

Quantity = 1 Off

CONTRACT NO. C31 R201	DATE	TUUV Prototype Integrated Thrusters	
DRAWN BY: A.W.Hughes	13-10-98		
CHECKED BY:		TITLE: Cross Beams to Support Force Blocks	
DESIGNED BY:			
DESIGN ACTIVITY: Prototype 1		SIZE: A4	FSCM NO.
CUSTOMER		DWG NO. / FILE NAME: P1- / beams.skd	
		SCALE: 1mm = 4mm	DATE: 13-10-1998
			SHEET: 1 of 1

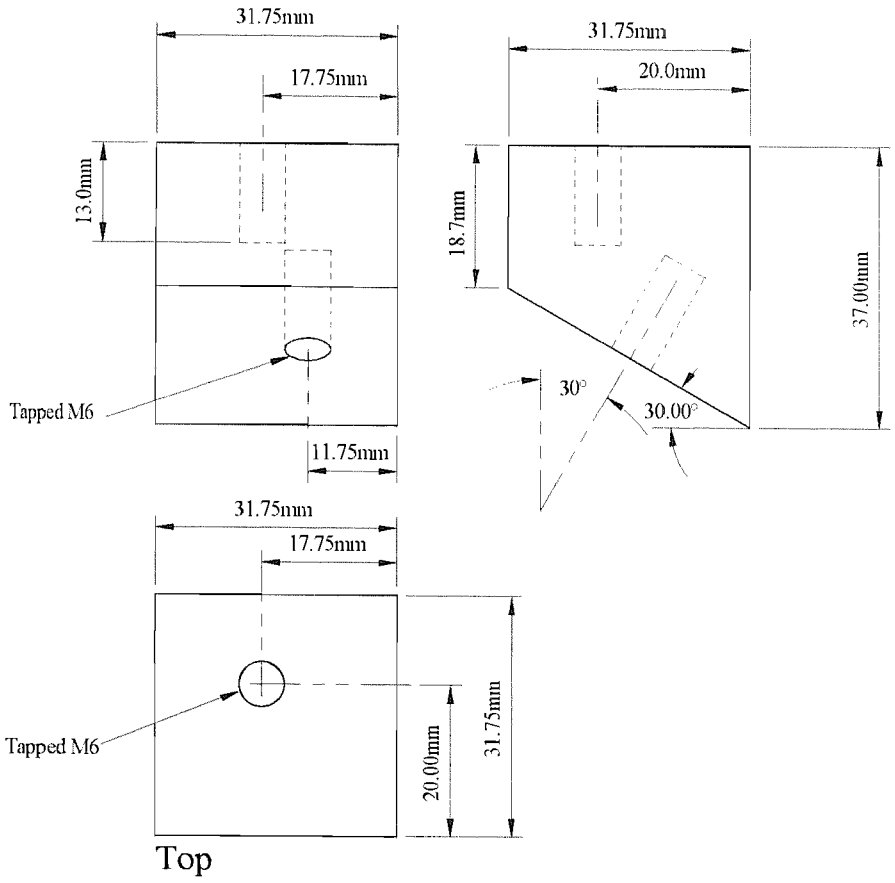

Quantity = 2 Off

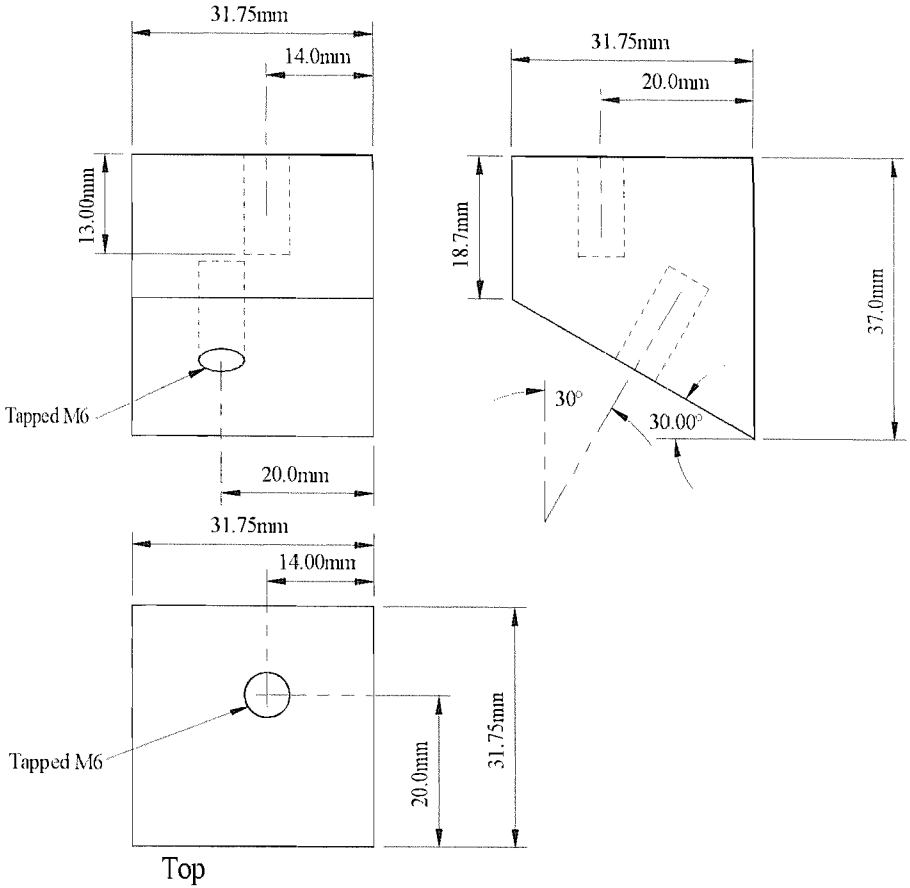

Quantity = 2 Off

NOTES

Material = 1,1/4 x 1,1/4 inch mild steel.

Quantity = 2 Off each design

CONTRACT NO. C31 R201	DATE	TUUV Prototype Integrated Thrusters	
DRAWN BY: A.W.Hughes	13-10-98		
CHECKED BY:		TITLE: Bracket Stubs	
DESIGNED BY:			
DESIGN ACTIVITY: Prototype 1		SIZE: A4 / FSCM NO. / DWG NO. / FILE NAME: P1- / bracstub.skd	
CUSTOMER		SCALE: 1mm = 1mm / DATE: 13-10-1998 / SHEET: 1 of 1	

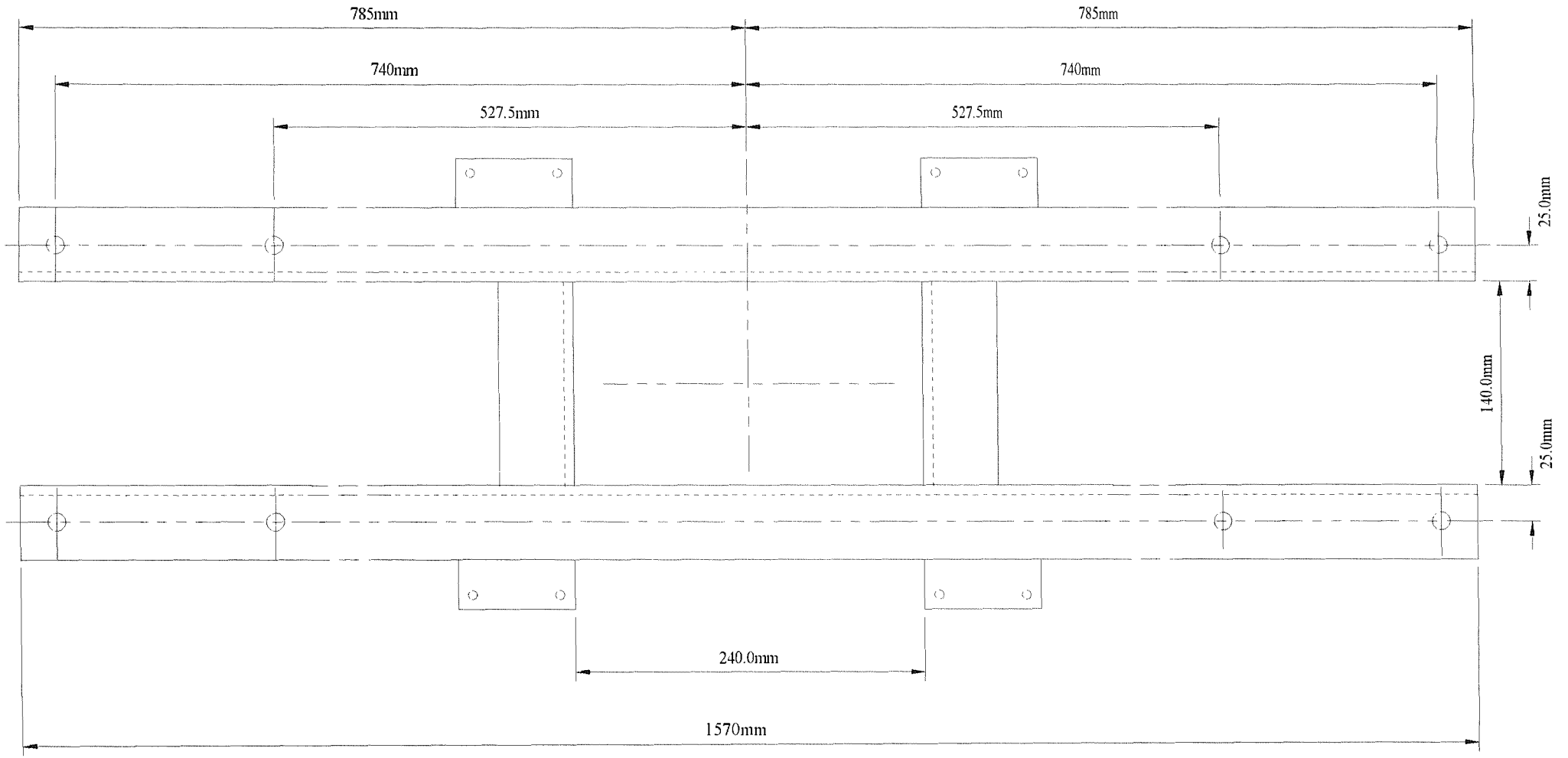

NOTES

Material = Steel
(Channel section 102mm x 51mm x 10.42Kg/m).

All holes clearance M12 unless shown otherwise.

Quantity = 1 Off

CONTRACT NO. C31 R201	DATE	TUUV Prototype Integrated Thrusters	
DRAWN BY: A.W.Hughes	13-10-98		
CHECKED BY:		TITLE: Cross Beams to Support Force Blocks	
DESIGNED BY:			
DESIGN ACTIVITY: Prototype 1		SIZE: A4	FSCM NO.
CUSTOMER		DWG NO. / FILE NAME: P1- / beams.skd	
		SCALE: Not to scale	DATE: 13-10-1998
			SHEET: 1 of 1